INVESTIGATING BIOLOGICALLY-RELEVANT SMALL MOLECULES USING NEW APPROACHES IN MASS SPECTROMETRY

by

Lekha Sleno

Submitted in partial fulfillment of the requirements
for the degree of Doctor of Philosophy

at

Dalhousie University
Halifax, Nova Scotia
March 2006

Your file Votre référence
ISBN: 978-0-494-16693-2
Our file Notre référence
ISBN: 978-0-494-16693-2

DALHOUSIE UNIVERSITY

To comply with the Canadian Privacy Act the National Library of Canada has requested that the following pages be removed from this copy of the thesis:

Preliminary Pages
- Examiners Signature Page (pii)
- Dalhousie Library Copyright Agreement (piii)

Appendices
- Copyright Releases (if applicable)

TABLE OF CONTENTS

List of Figures vii
List of Tables xi
Abstract xiii
List of Abbreviations xiv
Acknowledgements xvi
Chapter I. Introduction 1
Research Objectives 1
Background 3
Sample Preparation 3
High Performance Liquid Chromatography 6
Ionization Techniques 9
Mass Analyzers 14
Ion Activation Techniques 32
Chapter II. Structural Study on Spirolide Marine Toxins 40
Introduction 40
Experimental 44
Chemicals 44
Culture and Sample Preparation 44
In vitro Microsomal Incubations 45
High Performance Liquid Chromatography 45
Mass-Triggered Fraction Collection 45
Mass Spectrometry 46
Results and Discussion 49
LC/MS Analysis of Phytoplankton Extract 49
MS-Triggered Fraction Collection 50
Collision-Induced Dissociation 53
FT-ICR-MS 57
Fragmentation Pathways of 13-desmethyl Spirolide C 59
Structural Elucidation of Unknown Spirolides 61

In vitro Metabolism of Spirolide Toxins 66
Conclusions 69
Future Work 70
Chapter III. Paralytic Shellfish Poisons 72
A. Gas Phase Dissociation Reactions of Protonated Saxitoxin and Neosaxitoxin 72
Introduction 72
Experimental 76
Chemicals 76
Triple Quadrupole and Ion Trap Mass Spectrometry 76
FT-ICR-MS 76
Computational Calculations of Absolute Proton Affinities 77
Results and Discussion 79
Collisional Activation of Protonated PSPs 80
Elemental Formula Assignment from Accurate Mass Measurements 86
Proton Affinities of STX and NEO 89
Dissociation Pathways and Mechanisms 92
Conclusions 97
B. Assigning Product Ions from Complex MS/MS Spectra: The Importance of Mass Uncertainty and Resolution 98
Introduction 98
Experimental 101
Chemicals 101
Quadrupole-Time-of-Flight MS/MS 101
Fourier Transform-Ion Cyclotron Resonance MS/MS 102
Results and Discussion 103
General Considerations for Mass Accuracy Comparison 105
Comparison of QqTOF and FT-ICR 105
The Refined Approach: Monoisotopic Activation Cycles 113
A Few Interesting Observations in the QqTOF Spectra of STX and NEO 114
Prospects for Automated Formula Assignment 117
Conclusions 120

Chapter IV. Dissociation Reactions of Protonated Anthracycline Antibiotics .122
Introduction 122
Experimental 125
Chemicals 125
Mass Spectrometry 125
In vitro Microsomal Incubations and LC/MS Analysis 126
Results and Discussion 127
General Fragmentation Behavior of Doxorubicin and its Analogs 127
Comparison of MS/MS of Doxorubicin Analogs 133
MS Characterization of Doxorubicin Metabolites 135
Conclusions 138
Chapter V. Quantitative Small Molecule MALDI 139
Introduction 139
Experimental 143
Chemicals 143
Sample Preparation 143
MALDI Mass Spectrometry 144
LC/MS Analyses 146
Light Microscope Images 146
Scanning Electron Microscope Images 146
log D, pK_a Calculations 147
Results and Discussion 148
Quantitative MALDI of Pharmaceutical Drugs 148
Assessing Properties of Internal Standards 157
Screening of Toxin Samples using MALDI-QqQ 168
Conclusions 179
Chapter VI. Conclusion 181
References 183
Appendix 1- Student Contribution to Manuscripts in Thesis Forms 206

List of Figures

1.1 Process of Eddy diffusion within particle-packed HPLC column 7

1.2 van Deemter plot relating plate height and linear mobile phase velocity for HPLC columns 8

1.3 The electrospray ionization process 11

1.4 Schematic representation of the MALDI process 13

1.5 A linear time-of-flight mass analyzer 15

1.6 Quadrupole mass filter 19

1.7 Schematic representation of a triple quadrupole mass spectrometer 21

1.8 Diagram of a quadrupole ion trap 23

1.9 The events during an ion trap microscan 25

1.10 Image current produced following ion activation of neosaxitoxin (*m/z* 316) in the FT-ICR cell. The transient FID is transformed into the frequency-domain and subsequently into a resulting mass spectrum 29

1.11 Diagram of a FT-ICR cell 29

1.12 Schematic representation of IRMPD ion activation in a FT-ICR cell 37

2.1 a) Structures of known spirolides found in *Alexandrium ostenfeldii.* b) Structures of structurally-related marine toxins, pinnatoxin A (left) and gymnodimine (right) 42

2.2 SIM traces of MH^+ ions of various known and unknown spirolide species in a crude *Alexandrium* extract 51

2.3 LC-preparative mass-triggered fraction collection experiment from crude phytoplankton extract 52

2.4 LC/MS quantitative analysis of 13-desmethyl spirolide C with gymnodimine (internal standard) for quantitation of spirolide fractions 53

2.5 CID spectra of 13-desmethyl spirolide C on the triple quadrupole instrument 54

2.6 Proposed fragmentation scheme for 13-desmethyl spirolide C 55

2.7 MS/MS spectra of various spirolide species in collected fractions 56

2.8 FT-ICR mass spectrum of the MH^+ region of 13-desmethyl spirolide C 57

2.9 Enlarged 694.5^+ region of the FT-ICR-MS spectrum of the crude spirolide extract 63

2.10 Proposed structures for important fragment ions and MH^+ for component labelled 694.5(a) 64

2.11 Enlarged 708.5^+ region of the FT-ICR-MS spectrum of the crude spirolide extract 65

2.12 Proposed structures for important fragment ions and MH^+ for component labelled 708.5(a) 65

2.13 Detoxification of spirolide A through hydrolysis of imine group, forming spirolide E 67

2.14 Extracted ion chromatograms for 13-desmethyl spirolide C and detected metabolites from human liver microsomal incubations 68

3.1 Chemical structures and nominal molecular weights of saxitoxin and neosaxitoxin 73

3.2 Triple quadrupole CID spectra of STX and NEO 81

3.3 Ion trap product ion spectrum (MS^4) of the 3rd generation precursor ion at *m/z* 265, from the MH^+ ion of STX (*m/z* 300) 82

3.4 Proposed principal dissociation reactions of the MH^+ ion of STX 85

3.5 Proposed principal dissociation reactions of the MH^+ ion of NEO 86

3.6 IRMPD/FT-ICR spectrum of the MH^+ ion of STX 89

3.7 Structures of the investigated protonated guanidinium species for proton affinity calculations 90

3.8a Proposed principal dissociation mechanisms for STX and NEO (*m1-m8*) 95

3.8b Proposed principal dissociation mechanisms for STX and NEO (*m9-m18*) 96

3.9 Two different mass calibration protocols used in QqTOF experiments 102

3.10 Two isobaric NEO product ions at *m/z* 203 111

3.11 Isobaric $^{12}C_9$ and $^{13}C_1{}^{12}C_8$ species at *m/z* 222 in STX product ion spectra 112

3.12 Proposed dissociation mechanisms for several interesting fragmentation reactions in the product ion spectra of NEO 115

3.13 Two isobaric species differing by CO vs. N_2 (0.01123 Da) at *m/z* 137 in product ion spectra of STX 115

3.14 Four isobaric species at *m/z* 178 in the IRMPD product ion spectrum of NEO 116

3.15 IRMPD spectrum of NEO near *m/z* 238 revealing four isobaric species 117

4.1 Structures of doxorubicin and three structurally-similar anthracycline drugs 122

4.2 CID spectra of four anthracycline drugs 129

4.3 Proposed fragmentation scheme for doxorubicin 132

4.4 Proposed fragmentation scheme for the formation of ions at *m/z* 361 and 333 of doxorubicin 132

4.5 Breakdown curves showing differences between pathways of doxorubicin analogs 134

4.6 Specific dissociation reactions for idarubicin under investigated energy regime 135

4.7 Representative chromatograms for mouse liver microsomal incubations with 50 μM doxorubicin 136

4.8 Triple quadrupole CID spectra for doxorubicin metabolites and accurate mass data from ESI-TOF analyses 137

4.9 Proposed fragmentation scheme for doxorubicin metabolites 137

5.1 Schematic representation of quantitative MALDI-triple quadrupole assay 148

5.2 Effect of laser energy/pulse (a) and pulse frequency (b) on % ablation in MALDI traces 149

5.3 The effect of laser energy/pulse on precursor ion current for the four internal standards used in the quantitative assays 150

5.4 Scanning electron microscope (SEM) and light microscope images of a MALDI sample spot on an uncoated stainless steel target 151

5.5 Chemical structures and nominal molecular weights of the investigated drug molecules and their internal standards, as well as the structures proposed for the chosen product ions for MRM analyses 153

5.6 Light microscope images of crystal spots of three different MALDI matrix solutions at 1 mg/ml and comparison of the measurement reproducibilities for the three matrices at two different concentration levels. Structures of three matrices shown on the right. 153

5.7 Product ion spectra of the investigated drug molecules and their internal standards obtained from MALDI-QqQ analyses 155

5.8 Chemical structure and nominal molecular weight of hydroquinine 4-methyl-2-quinolyl ether 155

5.9 Acylcarnitine structures with corresponding *m/z* values and common product ion (*m/z* 85) monitored in MRM experiments 159

5.10 Average %RSD values (a) and linearities (R^2) (b) for calibration curves in the quantitation of acetyl-carnitine (M_n 203) plotted as a function of relative change in nominal mass between the analyte and the internal standard used 160

5.11 Average %RSD values (a) and linearities (R^2) (b) for calibration curves in the quantitation of hexanoyl-carnitine (M_n 259) plotted as a function

of relative change in nominal mass between the analyte and the internal standard used 161

5.12 Representative ion current traces for three spots from vertical rastering down a MALDI plate for acetyl-carnitine with d_3-acetyl-carnitine (a) and octadecanoyl-carnitine (b) as internal standards 162

5.13 Structures of fluoroquinolone antibiotics (1-14) and other pharmaceutical drugs (15-22) employed in the quantitation study of ciprofloxacin 164

5.14 Results from ciprofloxacin quantitation study 167

5.15 Optimization of MALDI quantitation of 13-desmethyl spirolide C. SIM detection with constant matrix concentration (a, inset without IS) and with constant analyte:matrix ratio (b, inset without IS). MRM detection with constant matrix concentration (c) 170

5.16 Product ion spectra following CID in triple quadrupole instrument with MALDI (a) and electrospray ionization (b) 171

5.17 Quantitative results from MALDI and ESI experiments. Calibration curves are shown for MALDI (a) and electrospray (b) analyses 173

5.18 Representative chromatogram from electrospray MRM experiment for the quantitation of 13-desmethyl spirolide C 174

5.19 Cross-correlation diagram comparing MALDI and ESI quantitation results and accuracy of methods 174

5.20 MALDI experiments on crude phytoplankton extract. Full scan experiments (a), precursor ion scans (b) for fragment ions at i) *m/z* 164 (at 60 V) and ii) *m/z* 444 (at 45 V) and neutral loss scans (c) of i) 528 Da and ii) 248 Da 177

5.21 a) Full scan experiment (*m/z* 500-750) from purified fraction of phytoplankton extract. b) Product ion scans from individual spirolide components at *m/z* 692, 694, 706 and 708 178

List of Tables

2.1 Accurate mass IRMPD data of *m/z* 692.5 ion in crude extract 58

2.2a The protonated molecules, elemental formulae and the fragment ion masses of the spirolide compounds at known *m/z* values 62

2.2b The protonated molecules, elemental formulae and the fragment ion masses of the unknown spirolide-related compounds 63

3.1 The relationships between several *n*th order precursor and product ions of STX from ion-trap MS^n experiments 83

3.2 The relationships between several *n*th order precursor and product ions of NEO from ion-trap MS^n experiments 84

3.3 The nominal, measured and theoretical masses, mass measurement errror (ppm), product ion identity and ion intensity for product ions observed in the IRMPD FT-ICR-MS experiments on STX 87

3.4 The nominal, measured and theoretical masses, mass measurement error (ppm), product ion identity, and ion intensity for product ions observed in the IRMPD FT-ICR-MS experiments on NEO 88

3.5 The calculated proton affinities of the various investigated guanidinium species 91

3.6 The chemical structures of selected product ions of STX and NEO for mass accuracy comparison 104

3.7a The measured and theoretical masses, mass measurement errors (ppm), elemental formulae, and resolving powers for product ions observed in the internal calibration QqTOF CID and IRMPD FT-ICR experiments for STX 107

3.7b The measured and theoretical masses, mass measurement errors (ppm), elemental formulae, and resolving powers for product ions observed in the internal calibration QqTOF CID and IRMPD FT-ICR experiments for NEO 108

3.8 The theoretical resolving power, $m/\Delta m_{50\%}$ required to separate several important interfered species in the MS/MS spectra of STX and NEO 109

3.9 The measured masses, elemental formulae and mass measurement uncertainties (ppm) for product ions observed in STX (a) and NEO (b) spectra from 7 Tesla IRMPD FT-ICR and QqTOF CID instruments 119

4.1 Corresponding fragment ion masses for doxorubicin and its three analogs 128

4.2 Summary of MS^3 results for doxorubicin 129

4.3 Accurate mass data for doxorubicin product ions 130

5.1 Summary of quantitation results for the investigated pharmaceutical drugs 156

5.2 Physicochemical properties of compounds used in quantitative analysis of ciprofloxacin 166

5.3 Quantitation results for acidic quinolones 167

5.4 Summary of quantitative results for unknown samples from MALDI and ESI experiments 173

Abstract

A strategy for the structural elucidation of selected biological molecules has been devised using several mass spectrometry (MS) techniques. A combination of tandem MS and high-resolution, accurate mass measurements has been employed in the study of spirolide marine toxins and paralytic shellfish poisons (PSPs). The toxin profiling of a crude algal extract containing several known and unknown spirolides provided a good example for the use of mass spectrometry in the structural characterization of small molecules. Through the detailed study of the fragmentation behavior of these compounds, some structures of unknown compounds were proposed. In addition, several other compounds were recognized as having similar structural features, thus potentially possessing a biogenetic link to the spirolides. Two PSP toxins, saxitoxin and neosaxitoxin, exhibit extremely complex collision-induced dissociation spectra and their fragmentation patterns were elucidated with ion trap MS^n and high-resolution mass spectrometry. A detailed understanding of gas-phase dissociation behavior was afforded by the collection of MS data as well as computational calculations of their gas-phase proton affinities. The PSP toxins also provided an excellent example for the comparison of mass resolution and accuracy requirements of complex spectra. High-resolution Fourier transform-ion cyclotron resonance and medium-resolution quadrupole-time-of-flight instruments were compared for elemental formula assignments from these measurements. Likewise, the study of anthracycline antibiotics involved the detailed study of the fragmentation behavior of doxorubicin and three structural analogs, supported by accurate mass measurements. Furthermore, using the information gained from these experiments, metabolites of doxorubicin were elucidated.

Additionally, growing interest in the ability to conduct rapid quantitative assays for small molecules by matrix-assisted laser desorption/ionization (MALDI) has been the driving force for several recent studies. The combination of a high repetition rate MALDI source with a triple quadrupole has been employed in several fundamental studies involving some technical aspects of high-throughput quantitative MALDI. Also, certain physicochemical properties were assessed for understanding the importance of internal standard selection. The potential of the MALDI-triple quadrupole system has been further demonstrated in a study of the spirolides, both in utilizing its abilities as a high-throughput quantitative instrument and a rapid screening tool.

List of Abbreviations

APA	Absolute proton affinity
APCI	Atmospheric pressure chemical ionization
ASP	Amnesic shellfish poison
BIRD	Blackbody infrared radiative dissociation
CE	Capillary electrophoresis
CHCA	α-cyano-4-hydroxycinnamic acid
CI	Chemical ionization
CID	Collision-induced dissociation
com	Center of mass reference frame
dc	Direct current
DHB	2,5-dihydroxy benzoic acid (gentisic acid)
DSP	Diarrhetic shellfish poison
ECD	Electron capture dissociation
EI	Electron ionization
ELSD	Evaporative light scattering detector
ESI	Electrospray ionization
FAB	Fast atom bombardment
FT-ICR	Fourier transform-ion cyclotron resonance
FWHM	Full width at half maximum
GC	Gas chromatography
GYM	Gymnodimine
HPLC	High performance liquid chromatography
IP	Intraperitoneal
IR	Infrared
IRMPD	Infrared multiphoton dissociation
IS	Internal standard
IT	Quadrupole ion trap
LC	Liquid chromatography
LD_{50}	Dose with 50% death rate
LIT	Linear ion trap
LLE	Liquid-liquid extraction
LLOQ	Lower limit of quantitation
LOD	Limit of detection
MALDI	Matrix-assisted laser desorption/ionization

MH^+	Protonated molecule
MRM	Multiple reaction monitoring
MS	Mass spectrometry
MS/MS	Tandem mass spectrometry
MS^n	Tandem mass spectrometry in an ion trap (*n*th generation MS/MS)
NEO	Neosaxitoxin
NMR	Nuclear magnetic resonance
NSP	Neurotoxic shellfish poison
PSP	Paralytic shellfish poison
QET	Quasi equilibrium theory
Q	Quadrupole
q	Collision quadrupole (operated in rf-only mode)
QqQ	Triple quadrupole
QqLIT	Quadrupole-linear ion trap
QqTOF	Quadrupole-time-of-flight
RDA	Retro-Diels-Alder
RETOF	Reflectron time-of-flight
rf	Radio frequency
RSD	Relative standard deviation
SA	Sinapinic acid
SEM	Scanning electron microscope
SIM	Selected-ion monitoring
SORI	Sustained off resonance irradiation
SPE	Solid-phase extraction
SSI	Sonic spray ionization
STX	Saxitoxin
SWIFT	Stored waveform inverse Fourier transform
TFA	Trifluoroacetic acid
TOF	Time-of-flight
TOF/TOF	Tandem time-of-flight
UPLC	Ultra-high pressure liquid chromatography
UV	Ultraviolet

ACKNOWLEDGEMENTS

Many thanks to Dr. Dietrich Volmer for his excellent supervision and invaluable discussions and support throughout the progress of my research. All group members at IMB, past and present, are also mentioned for their support. I would like to specifically acknowledge Dr. Anthony Windust for his help with culture preparations and general toxin knowledge. Additionally, several discussions on fragmentation mechanisms with Dr. Stuart Grossert were quite useful. Helpful collaborations with Dr. Alan Marshall and Dr. Michael Chalmers, at the National High Magnetic Field Laboratory (NHMFL) in Tallahassee, Florida, supported some of the FT-ICR experiments. Dr. Ken Renton from the Pharmacology Department at Dalhousie is thanked for useful discussions on metabolism studies and the general use of laboratory space and equipment for some experiments. Dr. Kevin Bateman, from Merck Frosst's Centre for Therapeutic Research, is mentioned for his help with my decision to pursue grad studies in the field of small molecule mass spectrometry under Dr. Volmer's supervision as well as for the use of instrumentation for the fractionation experiments. MDS Sciex is recognized for instrumental support as well as Dr. Jay Corr for his help with the troubleshooting and operation of the MALDI-QqQ instrument. Dr. Chris Lock from MDS Sciex is also thanked for QqTOF measurements. Dr. Kevin Crellin and Dr. Robert Williams from IonSpec supplied FT-ICR data, from a 7 Tesla instrument demonstration. Some experimental results were obtained as part of a collaboration with Dr. Julie Marr from Agilent Technologies. Summer students, Suzanne Bos and Brendan McIntosh, were helpful during some of the MALDI experiments. Dr. David O'Neil (NRC-IMB) is acknowledged for providing SEM images. I would also like to thank my committee members, Dr. Bruce Grindley, Dr. Robert Guy and Dr. Robert White and my external examiner, Dr. Gilles Lajoie, from the University of Western Ontario. I thank Dalhousie University and the NRC-IMB for allowing me to conduct such stimulating research during my PhD. Financial support from FCAR, NSERC, the Killam Trust, the Walter C. Sumner Foundation and the National Research Council's GSSSP scholarships are also recognized. Also, I would like to acknowledge support on a more personal level from all of my friends and family, both near and far.

Chapter I. Introduction

Research Objectives

Mass spectrometry, over the past 20 years, has evolved into what is now considered one of the most important analytical techniques for studying biological systems. The introduction of electrospray ionization (ESI) and matrix-assisted laser desorption/ionization (MALDI) has allowed the analysis of very small quantities of biological molecules such as proteins, peptides, DNA and metabolites, in their native state. Previously, such molecules had to be derivatized for gas chromatography/mass spectrometry analysis, as most of them are very polar and of low volatility. Since then, a multitude of instrument configurations has been proposed and developed, with different ionization, mass analysis and ion activation techniques. Some of the more important ones, used for the collection of results presented in this work, are briefly described in the Background section of this thesis.

Researchers in the drug and biotechnology industries are increasingly relying on mass spectrometry to support their ambitious research goals. For example, the requirement for higher throughput, increased sensitivity, and mass accuracy in the drug discovery and development process has been a major driving force toward the development of new MS technologies. Especially at the discovery stage, applications such as combinatorial library screening, metabolism and pharmacokinetic analyses have triggered several technological advances.

The present research proposes to improve on two important limitations of current biological mass spectrometry assays. First, studies were aimed at developing tools for aiding and accelerating the structural elucidation process of biologically-relevant small molecules. Examples were chosen from the pharmaceutical and environmental fields. Experiments have been performed using novel mass spectrometric techniques for a relatively new class of marine biotoxins, the spirolides (Chapter 2), as well as for selected paralytic shellfish poisons (Chapter 3). A further section (Chapter 4) involves the analysis of anthracycline antibiotics, commonly used in cancer therapy. This study was performed

to further understand the dissociation mechanisms of these molecules in the mass spectrometer following ion activation.

This thesis also describes a novel concept for performing high-throughput analysis by mass spectrometry. Chapter 5 introduces quantitative small molecule matrix-assisted laser desorption/ionization, including some fundamental studies as well as real applications, using marine toxins and pharmaceutical drugs, using a novel MALDI- triple quadrupole mass spectrometer. The research addresses some of the physical limitations encountered in regular MALDI, which have so far prevented it from being routinely applied in these fields, despite its obvious advantage of increased speed of analysis in comparison to any other mass spectrometry technique. Results will be shown demonstrating the applicability of the technique as well as the validity of the obtained results, by comparing it to established mass spectrometry assays.

Background

Some important introductory concepts are outlined in this section, including sample preparation, high performance liquid chromatography and different mass spectrometry techniques employed in these studies.

Sample Preparation

Sample preparation represents an essential step in almost any analytical method. Its importance, however, is often undervalued. It can consist of a wide range of procedures, including simple filtration or centrifugation, for the removal of insoluble materials from solutions or sample clean-up and pre-concentration using different extraction methods, such as solid-phase extraction (SPE) or liquid-liquid extraction (LLE). Three common techniques employed routinely in bioanalytical applications are protein precipitation, SPE and LLE.

Protein precipitation

Protein precipitation is one of the most straightforward and simple procedures for sample preparation and is most often used in the high-throughput analysis of pharmaceutical plasma samples [1]. Plasma proteins are one of the major interferences in these samples and can cause several problems in the analysis of drugs or endogenous compounds. These proteins can be precipitated out of solution with either organic solvents, such as methanol, acetonitrile or acetone, or with strong acids, including trichloroacetic acid. The main advantage of this procedure is its simplicity; however, adding volume to the biological sample may become a problem for detection, and therefore an additional step of sample evaporation and reconstitution is often necessary. This technique can also be used as an initial step in more elaborate sample preparation protocols.

Solid-phase extraction

Solid phase extraction (SPE) cartridges are routinely used in the clean-up of numerous types of biological samples [2]. They consist of a short extraction column, where contaminants and other unwanted species can either be retained or, more often, rinsed off in washing steps while pre-concentrating the analytes of interest. The mechanism of SPE is based on the same theories as chromatography (see following section) for the separation of different molecular species. Several different bonding phases are available, using polarity, hydrophobicity or ionization as mechanisms for trapping molecules, and analytes can be eluted with solvents of differing polarity or pH. A major application for SPE cartridges is the extraction of pharmaceutical drugs from biological fluids. For these applications, SPE well-plates are available to process a large number of samples in high-throughput assays. This technique has largely replaced liquid-liquid extraction, primarily due to the less hazardous solvents used as well as the minimal handling of potentially infectious biological media. Furthermore, SPE methods are simple and easy to use. Environmental applications are a primary field of SPE techniques, where the main advantage is the pre-concentration of analytes, such as environmental contaminants, onto the cartridge to improve assay detection limits.

In a typical experiment, the SPE cartridge is first conditioned with suitable organic and/or aqueous media, followed by loading of the sample solution. Subsequent washing steps allow unwanted materials to be rinsed off and the final cleaned-up sample is eluted off in the final step. Different commercial SPE materials include reversed-phase chemistries (from C_2 to C_{18}) as well as some more specialized phases using, for example, cyano, phenyl, diol and amino functional groups to increase selectivity. There also exists strong or weak cation or anion exchange materials for ionizable species, as well as a combination of phases (polysorbent) within the same cartridge, causing the trapping of both hydrophilic and lipophilic compounds from the sample solution. The ideal material is obviously application-dependent and the analyte as well as the sample matrix is important in the selection of the SPE cartridge. The composition of the loading and washing solutions as well the solvent used to elute the compounds to be analyzed is also crucial for optimal recoveries.

Liquid-liquid extraction

Liquid-liquid extractions are based on differences in solubility of an analyte molecule between two immiscible solvents. The distribution of the analyte between the two phases is an equilibrium process, governed by the law of mass action. The equilibrium constant K for the analyte A's distribution between water and an organic phase is

$$K = \frac{c_{A,org}}{c_{A,aq}}, \tag{1.1}$$

with $c_{A,org}$ and $c_{A,aq}$, the activities of A in the organic and aqueous solvents, respectively. The equilibrium constant K is often called the partition coefficient, P, particularly in bioanalytical applications. Naturally, 100% extraction into the organic phase is the desired outcome of a liquid-liquid extraction method. Lower recoveries are acceptable, however, if internal standards are used for correction. Of course, an efficient extraction does not guarantee sufficient selectivity, as the extraction solvent may also extract unwanted interfering compounds at the same time. For a biological fluid, where the goal is to extract drugs and their metabolites from the aqueous biological phase, the aim obviously must be to partition the drug-related molecules into an organic phase, while the interfering endogenous materials remain in the aqueous phase. Naturally, ionization equilibria will have a strong effect on extraction efficiencies if the analyte molecule possesses ionizable sites. For example, the protonated form BH^+ of a basic analyte is much less hydrophobic than the unionized neutral form B and will not readily extract into the organic phase:

$$BH_{aq}^{+} \overset{K_a}{\rightleftharpoons} B_{aq} \overset{P}{\rightleftharpoons} B_{org} \tag{1.2}$$

Similar to the partition coefficient P, a distribution coefficient D [3] can be used, taking into account the dissociation via the Henderson-Hasselbalch equation. In these cases, adjustment of pH is then necessary to convert the analyte to the neutral form, in order to improve the extraction efficiencies.

The choice of extraction solvent for a particular analyte molecule depends on several factors, including the type of matrix the analyte is extracted from, the nature of the analyte and the experimental technique for the subsequent analysis. Typical solvents for extraction from aqueous biological materials include ethyl acetate, halogenated

hydrocarbons (chloroform, dichloromethane), or diethyl ether. Depending on the biological matrix, an appropriate solvent must be used in order not to extract interfering endogenous compounds from the sample. Furthermore, pH adjustment can increase efficiencies for many biological molecules significantly. Basic drug molecules are often extracted into organic solvents at high pH and organic acids at low pH. Finally, the volatility of the extraction solvent is of concern if extracts are to be dried down or if gas chromatography is used for analysis. Very often, mixed solvents are used to circumvent some of the described problems or a combination of SPE and LLE is applied.

High Performance Liquid Chromatography

Most bioanalytical applications in mass spectrometry involve hyphenation with chromatography. The combination of gas chromatography with mass spectrometry has been considered routine for several decades, and is probably still the most widely used hyphenated MS technique. High performance liquid chromatography (HPLC), though, was considered more difficult to combine with mass spectrometry due to the lack of an appropriate interface for LC/MS. This technique has been revolutionized by the introduction of atmospheric pressure ionization sources, such as electrospray (ESI) and atmospheric pressure chemical ionization (APCI) and what was once considered an arduous task is now a routine technique used in laboratories worldwide. LC/MS allows the separation of complex mixtures, including biological samples, prior to their analysis by mass spectrometry. This section will outline some of the features of HPLC and important factors that need to be taken into account when analyzing small polar molecules by LC/MS.

Chromatography is applied in order to separate components of a mixture using their interactions within two different phases: the stationary phase (the packed material within the column) and the mobile phase (moving in a defined direction through the column). In the case of HPLC, the mobile phase is a liquid under high pressure (up to 400 bar) and the stationary phase is a packed column stable to these types of pressures. Analytes interact with the stationary and mobile phases to different extents and thus are retained on the column for different lengths of time (retention time). If the conditions

(e.g., flow rate, temperature, mobile phase composition) remain constant, the retention time for each analyte remains stable and can be used as a basis for identification of a specific component in a mixture. HPLC columns are available in very different dimensions, from nanoscale or microscale to preparative scale columns, with correspondingly different optimal flow rates in order to keep the operating pressure of the system within the acceptable range.

HPLC columns, thus, have different performance efficiencies, based on their length, particle size and mobile phase flow rate. A measure of the chromatographic performance for packed columns is the rate of band broadening, often described using the van Deemter equation [4]:

$$H = \frac{1}{\left(C_e d_p\right)^{-1} + \left(C_m d_p^2 \mu / D_m\right)^{-1}} + \frac{C_d D_m}{\mu} + \frac{C_{sm} d_p^2 \mu}{D_m} \approx A + B/\mu + C\mu \qquad (1.3)$$

This equation relates plate height (H) to mobile phase linear velocity (μ) for a particle-packed column. Other variables are d_p, the particle diameter, D_m, the diffusion coefficient of the solute and C_e, C_m, C_d, C_{sm}, the coefficients for Eddy diffusion (see Figure 1.1), mobile-phase mass transfer, longitudinal diffusion, and mass transfer within a particle, respectively.

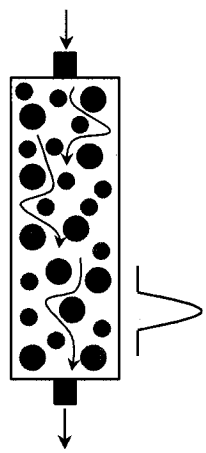

Figure 1.1 Process of Eddy diffusion within particle-packed HPLC column. Different analyte molecules can have differing diffusion paths through the column and thus lead to peak broadening.

For simplicity, the first term, based on Eddy diffusion and mobile phase transfer, is approximated as a constant, A, with no dependence on μ. A typical van Deemter plot [5] for a particle-packed column is represented in Figure 1.2. A decrease in particle size leads to increased column efficiency since the A term is decreased and the diffusion path length within a particle is shorter, thus decreasing the C term contribution to H, especially at high mobile phase flow rates [5]. However, a major limitation for these columns is the large increase in column backpressure associated with smaller particles.

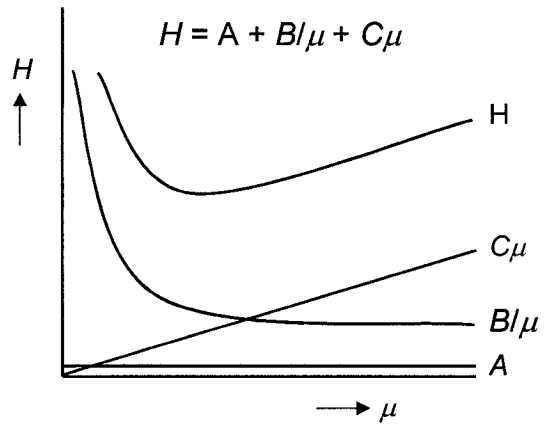

Figure 1.2 van Deemter plot relating plate height (H) and mobile phase linear velocity (μ) for HPLC columns [5].

Several methods of increasing HPLC efficiencies have been evaluated: ultra-high pressure liquid chromatography (UPLC), capillary electrochromatography, open tube chromatography and high temperature LC. However, there exists instrumental and operational difficulties associated with the use of these techniques [6]. Recently, a commercial system, based on UPLC technology has been introduced and is finding general acceptance in several pharmaceutical and metabolomics research areas, due to its improved efficiency and high-throughput nature [7]. Monolithic columns, having a continuous unitary structure based on sol-gel chemistry with macroporous channels, also show increased efficiency as well as the ability to run at much higher flow rates without deterioration in the chromatographic performance [6]. These columns are presently not produced in all sizes and chemistries that are available for conventional packed columns.

Certain factors must be accounted for when combining liquid chromatography with mass spectrometry. Conventional HPLC columns are 4.6 mm in diameter with 5 μ

sized particles and have optimal flow rates of ~1 ml/min. However, if a concentration-dependent detector, such as ESI-MS, is used, the sensitivity of the analysis increases by using a smaller diameter column, thus decreasing the flow rate into the mass spectrometer. From the van Deemter equation, keeping the linear flow rate constant should cause the absolute mobile phase flow rate to be decreased by the square of the change in column diameter. Therefore, for a 2 mm column, the optimal flow rate would be decreased to ~0.2 ml/min. It is also possible to split the effluent from the column into the MS in order to decrease the amount of liquid introduced into the system. Another important factor is the composition of the mobile phase. Atmospheric pressure ionization sources do not tolerate non-volatile buffers well, since this may cause ion suppression and could potentially block the ion source. Therefore, most LC/MS analyses utilize volatile buffer systems, such as ammonium formate and ammonium acetate, to regulate pH for better chromatography. Reversed-phase applications are most common in bioanalysis and usually use a mixture of aqueous and organic (methanol, acetonitrile) mobile phase for the separation of analytes.

Ionization Techniques

Electrospray ionization

Historically, structural studies in organic mass spectrometry (MS) have been performed with the "hard ionization" technique of electron ionization (EI). This method is quite useful, but only for a very limited number of molecules, specifically for low molecular weight, volatile compounds. Soft ionization techniques, such as fast atom bombardment (FAB) [8], electrospray ionization (ESI) [9, 10], atmospheric pressure chemical ionization (APCI) [11] and matrix-assisted laser desorption/ionization (MALDI) [12], have extended the application range of MS to polar and more thermally labile molecules. ESI, in particular, has proven to be quite useful in the analysis of a wide range of biologically relevant compounds, such as peptides and proteins [13, 14, 15], nucleic acids [16, 17], natural products [18] and pharmaceutical drugs [19]. Consequently, it has become the most routinely used ionization method in bioanalytical laboratories.

Instead of molecules being volatilized prior to ionization, as in electron ionization, ESI allows gaseous ions to be formed directly from the condensed phase [20]. This technique is therefore of high relevance, since most biological molecules can now be studied without prior derivatization. In order to achieve this type of ionization, the liquid phase is forced through a narrow metal capillary needle at a high electric potential relative to the walls of the atmospheric pressure region. This potential causes the liquid phase to explode into a fine spray of charged droplets. Depending on the polarity of the electric field, either positive or negative ions are transported into the mass spectrometer. A "Taylor cone" is initially formed and extends beyond the capillary. Eventually, the surface tension of the solution is equal to the force of Coulombic repulsion (Raleigh limit) [21]. Charged droplets then emerge from the capillary, followed by the evaporation of the solvent within the ion source and transport region of the mass spectrometer. As a result, the droplets become increasingly smaller and the total charge is now compressed into a reduced surface area. The large droplets subsequently separate into gaseous analyte ions, by one of two proposed mechanisms. The first mechanism states that charge density on the droplet increases by solvent evaporation with the eventual formation of smaller charged droplets, and finally single ions are formed (*charged residue model*) [22]. Another explanation was introduced by Iribarne and Thomson [23] as the *ion evaporation mechanism* and is similar to the mechanism explaining the creation of charged droplets from the Taylor cone. Solvent evaporation is assumed to cause such a strong Coulombic repulsion that it eventually exceeds the surface tension of the droplet, with a consequent release of ions. Figure 1.3 illustrates the electrospray ionization process. Ions are initially formed in large solvent clusters. Consequently, a drying gas helps the solvent evaporate rapidly. The analyte ions are then transferred from atmospheric pressure into the mass spectrometer through an intermediate pressure region (~ 1 Torr) to the high vacuum of the analyzer.

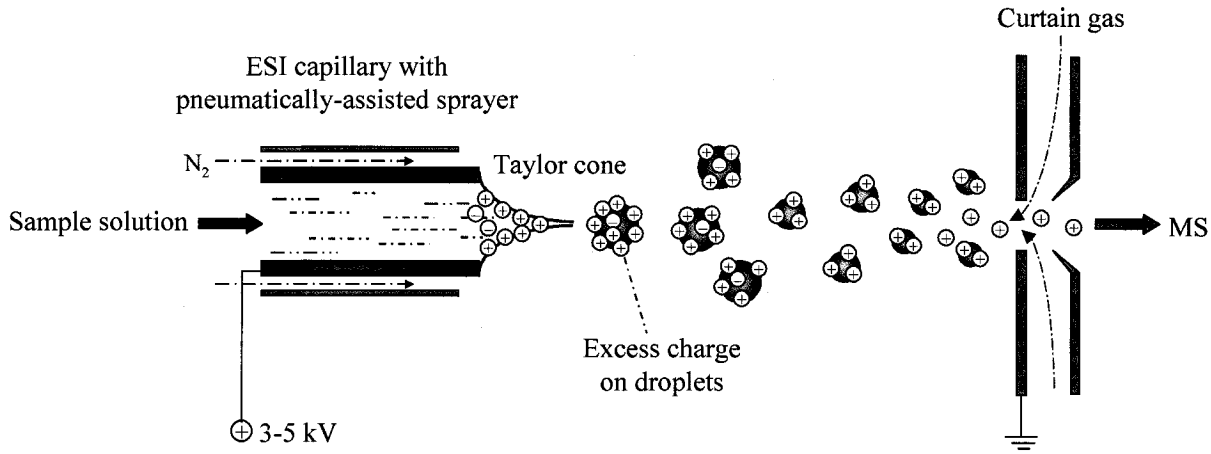

Figure 1.3 The electrospray ionization process. A solution passes through a spray needle (capillary), which is at high voltage, producing a Taylor cone and forming large charged droplets. Eventually, solvent evaporation causes individual gaseous ions to be formed for analysis by mass spectrometry.

Electrospray ionization is considered one of the softest ionization techniques available and, accordingly, the ions formed by this process often assume similar characteristics as observed in the liquid phase. Even non-covalent interactions are maintained, under careful instrument conditions, allowing studies on weakly bound multiprotein or protein-ligand complexes [24]. Also, probably the most significant advantage of ESI is the ease with which it is coupled to liquid separation techniques, such as liquid chromatography (LC) and capillary electrophoresis (CE) [25, 26]. Complex mixtures can thus be analyzed without tedious sample preparation steps.

ESI has developed into an extremely important technique in biological mass spectrometry. Its introduction, by Dr. John Fenn at Virginia Commonwealth University in 1984, was recently recognized with the Nobel Prize in Chemistry (2002) with particular emphasis on its application to the analysis of peptides and proteins [27]. The main reason that ESI is so amenable to protein analysis is that it offers the ability to form multiply charged species. Since mass spectrometers detect the mass-to-charge ratio (*m/z*) of ions and multiply charged biomolecules have relatively small *m/z* values, analyses can be performed with instruments of limited *m/z* range, such as quadrupole mass filters and ion traps. This technique is therefore widely applied for the analysis of biological molecules. ESI was initially developed using a quadrupole mass spectrometer, however it is presently available for most commercial mass spectrometers.

Matrix-assisted laser desorption/ionization

Another important ionization technique in bioanalysis, which was also recently introduced, is matrix-assisted laser desorption/ionization. MALDI has revolutionized the analysis of large biomolecules and synthetic polymers to a similar extent than electrospray ionization has modernized the analysis of peptides and proteins [12, 28]. As a result, MALDI is presently the most important technique for determining the molecular weights of peptides and proteins, carbohydrates, nucleic acids and polymers. In a MALDI experiment, a sample solution is mixed with an organic matrix solution and is then deposited onto a suitable target surface. Subsequent solvent evaporation results in co-crystallization and formation of a "solid solution" of matrix and analyte molecules on the target surface. This solid sample spot is then irradiated with a pulsed laser beam of a suitable wavelength, for example, from a nitrogen laser of 337 nm (Figure 1.4). The process can be summarized as follows:

1. **Formation of a "solid solution":** Analyte molecules are distributed throughout the matrix, completely isolated from one another.
2. **Matrix excitation**: Laser energy is absorbed by the matrix, causing vibrational excitation, and formation of clusters made up of single analyte molecules surrounded by neutral and excited matrix molecules. Matrix evaporates away from the clusters, leaving excited analyte molecules.
3. **Ionization:** Analyte molecules can be ionized by protonation via the photo-excited matrix, leading to typical MH^+ species.

The matrix compound serves as a means of absorbing light during laser irradiation. It must therefore have a strong chromophore, absorbing at the laser's wavelength [29]. Because of the pulsed nature of the laser desorption and ionization process, most instruments employ a time-of-flight (TOF) analyzer for mass analysis. The theoretical details of the MALDI process are not fully understood yet and are the subject of many ongoing investigations [30]. Experimental parameters such as laser wavelength and fluence (energy per unit area), type of organic matrix, and the concentration ratio of matrix and analyte have a strong influence on the ion formation processes [31]. It is

evident, for example, that ion production only starts after the laser fluence reaches a certain threshold. This threshold depends on both the type of matrix and its concentration relative to the analyte. MALDI analyses are therefore usually conducted at laser fluences just above the threshold, to avoid fragmentation of the formed ions [32].

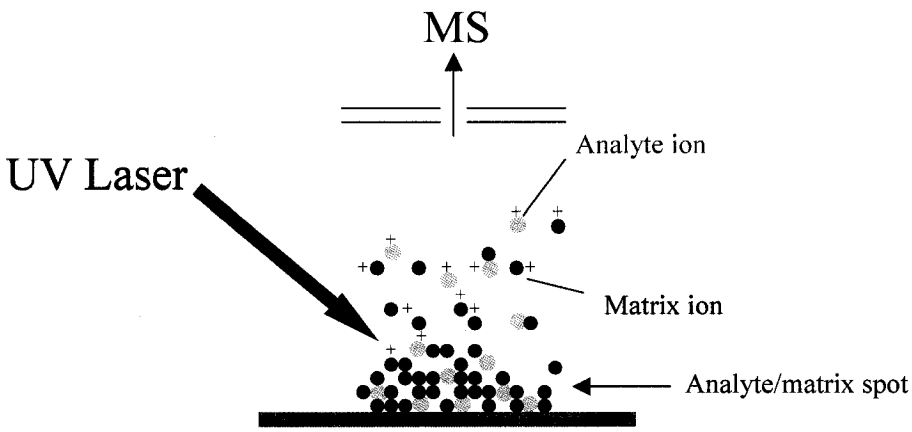

Figure 1.4 Schematic representation of the MALDI process

The selection of a suitable matrix represents a challenging experimental parameter during optimization of a MALDI method and can have a significant impact on the experimental outcome. In addition to absorbing the laser light, the chemical properties of the matrix compound must be matched to the analyte molecule of interest, as both compounds must co-crystallize for successful MALDI analysis [33]. In addition, the matrix compound is often directly involved in the subsequent ionization process of the analyte, acting, for example, as a protonating or deprotonating agent. Consequently, a wide range of matrix compounds have been utilized for MALDI analyses [31]. Generally, small organic acids are used for the analysis of basic molecules. Most researchers currently begin their analyses by using one of the three most common matrices, namely, α-cyano-4-hydroxycinnamic acid (CHCA), 2,5-dihydroxybenzoic acid (DHB) or sinapinic acid (SA).

The sample preparation and crystallization procedures are equally important for a good MALDI analysis [34]. In most analyses, the analyte solution is added to a

concentrated matrix solution, characteristically yielding a 1,000 to 10,000-fold molar excess of matrix to analyte. Typically, one microliter of the mixture is spotted onto the target surface and dried at ambient conditions. The goal is to achieve a homogeneous layer of small micro-crystals, leading to a good shot-to-shot reproducibility and mass accuracy. This simple procedure is called the *dried droplet* technique [35]. More elaborate sample preparation procedures involve the use of volatile solvents, vacuum drying, heated drying or electrospraying of the mixture. Furthermore, the application of specialized target coating materials can lead to more homogeneous sample layers. These different factors must all be taken into account for a successful analysis using the MALDI technique.

Mass Analyzers[†]

There are four basic types of mass analyzers found in modern mass spectrometry: time-of-flight (TOF), quadrupole (and a recent derivative, quadrupole linear ion trap, LIT), quadrupole ion trap (IT), and Fourier transform-ion cyclotron resonance (FT-ICR). There are also several advanced permutations of these analyzers, which through the combination of different analyzers, create enhanced tandem MS capabilities, novel scan modes or superior mass resolution and accuracy. The underlying physical principles of each mass analyzer will be explained in the following sections, while highlighting their characteristic features, limitations and some important application areas. The instruments used in the research shown will be discussed, starting with the most straightforward design for a mass spectrometer, the time-of-flight analyzer.

Time-of-flight Analyzer

A linear TOF mass spectrometer is the simplest mass analyzer, consisting only of an ion-accelerating region, a flight tube and a detector. These linear instruments are mostly used in combination with the pulsed matrix-assisted laser desorption/ionization (MALDI) technique for the analysis of large biomolecules. In theory, all ions experience

[†] Part in this section was reproduced with permission from Advanstar Communications, New York. Volmer DA, Sleno L. *Spectroscopy,* 2005; **20**: 20; *ibid.* 90.

the same potential difference during acceleration and thus have the same kinetic energy at the start of the flight tube, and different velocities depending on their mass. Therefore, their arrival time at the detector is proportional to their mass and they reach the detector in order of increasing mass. The mass-to-charge (*m/z*) ratios of the ions relate to the flight times, *t*, by the following equations:

$$mv^2/2 = zV; \qquad v = \sqrt{2zV/m} \tag{1.2}$$

$$t = l/v = l\sqrt{m/2zV}, \tag{1.3}$$

where l is the length of the flight tube, v is the velocity of the ion of mass m and charge z and V is the acceleration potential. For example, the electrosprayed antibiotic ciprofloxacin (MW = 331 g/mol; MH^+ at *m/z* 332) arrives at the detector 9.3 μsec after being accelerated with 20 kV into a 1 m flight tube, whereas the much heavier singly protonated bovine insulin molecule (*m/z* 5734) needs 65.1 μsec to reach the end of the tube. These flight times translate into the *m/z* values *via* eq. (1.3). The differences of flight times are, of course, the basis for resolving ions of different *m/z* in the TOF analyzer and the mass resolution depends on the flight time differences, which are proportional to $l(\sqrt{m_1} - \sqrt{m_2})$. Figure 1.5 shows a diagram of a linear time-of-flight instrument, with the acceleration region from the source into the drift tube with lighter ions arriving before heavier ones at the detector.

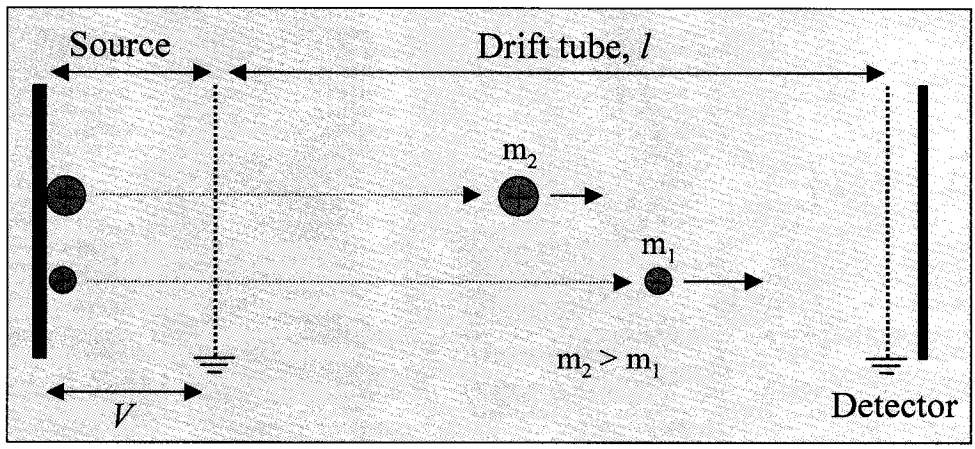

Figure 1.5 A linear time-of-flight mass analyzer.

The major deficiency of a simple linear TOF instrument is its insufficient mass resolution, resulting from flight time variations of ions of the same *m/z* ratio. First, the laser pulses used for ion generation in MALDI-TOF instruments are fairly long, resulting in a wide distribution of starting times of the same ions. Furthermore, the ionization process adds a certain amount of initial kinetic energy to the molecules prior to acceleration. Finally, the different spatial positions in the source from where the ions are formed lead to varying values of l (eq. (1.3)) and thus to flight time variations. As a result, modern TOF instruments commonly employ two techniques to enhance resolution, *reflectrons* and *delayed extraction* (for MALDI-TOF).

A reflectron TOF (RETOF) is used to focus ions of the same *m/z* but of different kinetic energy. There are different designs of reflectrons but they often consist of a series of rings or grids. It is located after the drift tube, creating a retarding field that the ions penetrate after leaving the flight tube. Depending on their kinetic energy, they will penetrate this field at different depths and are then reflected back into the flight tube, where they drift to the detector, which is now placed close to the ion source. Consider the case of ions of the same *m/z* but significant energy spread, which would be detected as broad peaks in the linear TOF. The ion with a higher kinetic energy would penetrate deeper into the reflectron and the slow ion would return to the flight tube faster, but with the same lower kinetic energy. The faster ion, thus, will catch up with the slow one at the detector, thereby greatly improving mass resolution.

The delayed extraction technique can be used on both linear and RETOF instruments, to compensate for the initial velocity distributions of ions. In this technique, ions are allowed to drift free of electric fields after formation for a certain delay time. After this time, the ions are accelerated into the flight tube. By allowing them to drift, faster ions move farther away from the sample target than the slower ions. After the delay, these faster ions will then experience less of the accelerating voltage between the sample target and the extraction plate than the slow ones. This procedure compensates for the initial energy distribution of ions with the same *m/z*.

There are several benefits that TOF analyzers offer when combined with ionization sources such as electrospray or MALDI. In addition to the high mass range that can be analyzed (with a linear TOF instrument) and the high ion transmission, there

is the unique advantage of quasi-simultaneous detection of all ions, resulting in high sensitivity 'full-scan' analyses (of course, the term 'full scan' is obviously wrong in the context of TOF-MS, as it is not a scanning device, however, it is used here for convenience). Thus, they are ideal in qualitative applications, such as the identification of unknown compounds, where the acquisition of an entire mass spectrum is required. In addition, they exhibit very fast acquisition times and are thus ideal for hyphenation with capillary electrophoresis and fast chromatography runs. Of course, the pulsed nature of TOF analysis makes the hyphenation with a continuous ion source such as electrospray more difficult than with MALDI, which is inherently compatible with TOF analysis. The necessary 'slicing' of the ion beam coming from the ESI source can be performed axially or orthogonally. For organic LC/MS, the design is usually an orthogonal acceleration (oa) TOF type. The ions are focused into the orthogonal accelerator as a narrow ion beam and a slice of it is pushed down into the TOF tube. The amount of ions entering the TOF tube (*i.e.*, the length of the 'slice') relative to the total amount of ions in the orthogonal accelerator determines the *duty cycle* of the instrument. After the heaviest ions have reached the detector, the next pulse pushes another slice of ions into the drift tube.

The downside of TOF applications is the limited dynamic range, over which a linear response is obtained from the detector. This is the direct result of the detectors that are employed for handling the large number of high-resolution spectra, making the TOF instruments less attractive for quantitative analyses. There is another weakness encountered with TOF analyzers: it is technically difficult to select a precursor ion for tandem mass spectrometry (MS/MS) experiments. In MS/MS, a specific precursor ion is isolated and then made to undergo dissociation to fragment ions, which are subsequently analyzed to obtain structural information. It is important that the precursor ion of interest be isolated from interfering species, thus one needs to be able to select a very narrow *m/z* range. In a RETOF instrument, a TOF gate can only provide a very coarse precursor selection (over several *m/z* units wide), to study metastable decompositions. This technique can be used in combination with post-source decay (PSD) and is quite popular for sequencing of peptides.

It is much more elegant, however, to have a separate mass spectrometer select the precursor ion, allowing the isolation of a single *m/z* value. One option is to use another

TOF drift tube together with a time selector. Such a design is commercially available and is usually used in specialized proteomics applications (TOF/TOF). Much more common, however, is the implementation of a quadrupole mass filter prior to the TOF tube. Adding a second, rf-only quadrupole as a collision cell can allow accurate mass data for the fragment ions to be provided by the TOF analyzer. Before this type of instrument (QqTOF) is discussed, the basic operating principles of a quadrupole will be presented.

Quadrupole mass analyzer

The quadrupole mass filter [36, 37] is the most common analyzer found in analytical laboratories today. It is the standard analyzer for GC/MS but is also part of various designs of LC/MS instruments. Quadrupoles are not only used as mass analyzers; they are also frequently implemented as ion transfer optics, collision cells and linear ion traps. This analyzer works on the basis of electric fields generated between a set of four circular, or ideally, hyperbolic, axial rods through which ions pass on their way to the detector. The voltages applied to these rods consist of direct current (dc) and radio-frequency (rf) components, which together create a quadrupolar field [38, 39], as shown in Figure 1.6, allowing only a certain *m/z* range to pass through for a given combination of potentials; ions outside that *m/z* region hit the rods and are discharged. The quadrupole therefore is also referred to as a *mass filter*, into which ions are accelerated from the ion source by a small potential. Positive ions will be attracted to negative rods, and vice versa. The rf component, however, causes the electric field to alternate at a frequency in the MHz range (usually ~10^8 Hz). The applied potential to the rods is of the form:

$$\Phi_0 = U + V\cos\omega t \qquad (1.4)$$

where U is the magnitude of the dc voltage, V is the zero-to-peak amplitude of the rf voltage and $V\cos\omega t$ is the rf potential of frequency $\omega/2\pi$. In addition, the two rf fields applied to the opposing parallel rods are 180° out of phase. As a result, the trajectory of an ion constantly fluctuates as it travels between the rods until its eventual detection.

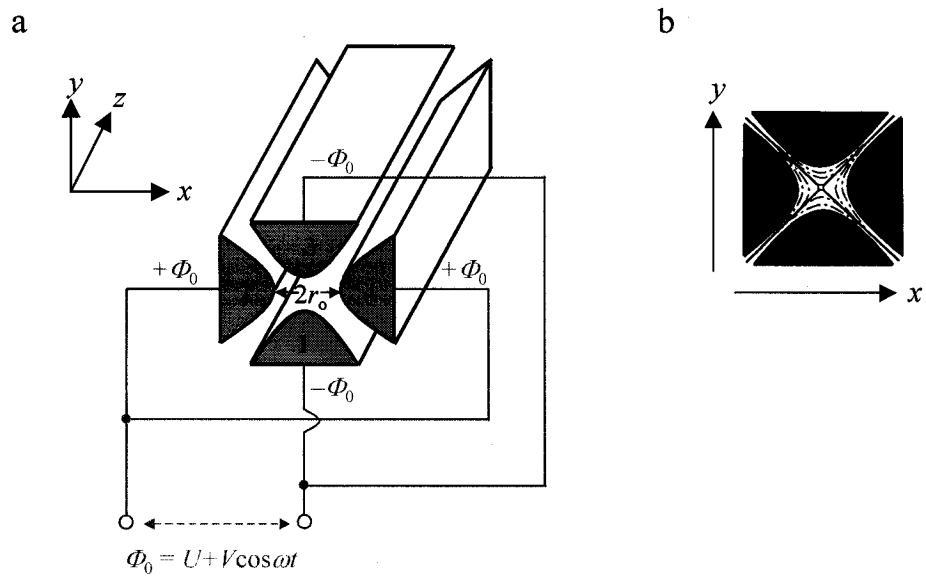

Figure 1.6 A quadrupole mass filter consists of two sets of electrically connected circular (or hyperbolic) rods. Cross section of a quadrupole showing the potentials applied on rods (a). A quadrupolar field is achieved by dc and rf voltage components (b).

In a full-scan experiment, the dc and rf components are ramped at a constant ratio and ions entering from the ion source are successively able to pass through the rod assembly. For a specific combination of dc and rf, only a very small *m/z* range can pass through, the size of which determines the resolution of the instrument. Quadrupoles are usually operated at unit resolution throughout the mass range (often up to *m/z* 4000), allowing the separation of *e.g.* *m/z* 150 and 151 or *m/z* 1500 and 1501. Higher mass resolution throughout the entire mass range, however, is available on a recent commercial quadrupole instrument [40]. The sequential detection in the full-scan mode of any quadrupole analyzer results in a low duty cycle, typically of the order of 0.1% depending on the monitored *m/z* range. The duty cycle (and the resulting sensitivity) is much higher in the *selected ion monitoring* (SIM) mode of the quadrupole (close to 100%). In this case, the dc and rf potentials are held constant, so only a specific *m/z* ratio can pass. One can also jump between different voltages, to allow more than one *m/z* ratio to be detected sequentially, with a corresponding reduction in duty cycle.

Single quadrupole instruments are usually limited to measuring intact species generated by the ionization source, resulting in limited selectivity in comparison to many

of the more advanced instrumental designs. They have nevertheless found a wide application range in LC/MS and GC/MS. Typical applications of single quadrupoles include purity assessments, molecular weight confirmations and automated mass-triggered HPLC fractionations.

In a single quadrupole instrument operating with an ESI or APCI source, selectivity can be increased when fragmentation is induced in the ion source region. This procedure refers to the activation of ions in the region between the ion source and the analyzer, where fragmentation can be initiated by collisions with residual gas molecules at intermediate pressures. The generated fragment ions may be used for limited structure elucidation or confirmation purposes. However, no precursor ion selection takes place and fragment ions cannot be specifically linked to the precursor ion of interest. Therefore, fragments could originate from several compounds for co-eluting peaks in LC/MS, making structure assignments difficult.

The most common mass analyzer for quantitative bioanalytical assays is the triple quadrupole [41]. This tandem mass spectrometer consists of three sequential quadrupoles ($Q_1q_2Q_3$; Q refers to a mass resolving quadrupole, q to an rf-only quadrupole). A simple representation of the triple quadrupole can be viewed in Figure 1.7. This configuration allows additional ion activation in q_2, after the ion of interest has been selected in Q_1. The second quadrupole, q_2, is operated in the *rf-only* mode, thus effectively becoming a wide-band pass for the ions. It can be filled with a neutral gas such as N_2 or Ar, acting as a collision gas with typical pressures of ~10^{-3} Torr. The ions leaving Q_1 are accelerated into q_2 with offset voltages typically between 0 and 100 V. Resulting collision-induced dissociation (CID) product ions can be analyzed with the third quadrupole. This is referred to as a *product ion scan.* In addition, several other selective MS/MS modes are available on a triple quadrupole, depending on which mode Q_1 and Q_3 are used in:

Scan mode	**Q_1**	**q_2**	**Q_3**
Product ion	SIM	CID	full-scan
Precursor ion	full-scan	CID	SIM
Neutral loss	full-scan	CID	full-scan
Multiple reaction monitoring (MRM)	SIM	CID	SIM

The *precursor ion scan* is essentially the reverse of the product ion scan. The third quadrupole is set to select a specific product ion formed in q_2 and the first quadrupole is scanned for all precursor ions forming the chosen fragment. An important use for precursor ion scans is seen in the pharmaceutical industry, for the identification of drug metabolites with similar fragmentation behavior to that of the parent molecule. *A neutral loss scan* experiment is also achieved in this instrument with relative ease. Neutral loss scans are routinely used to identify common functional groups present in a set of molecules. One of the most common applications conducted with triple quadrupole instruments is the quantitative analysis of small molecules in biological specimens such as plasma or urine. In these analyses, the *MRM mode* is almost always applied, allowing enhanced selectivity, and thus sensitivity, in most cases, by circumventing isobaric interferences from the biological material.

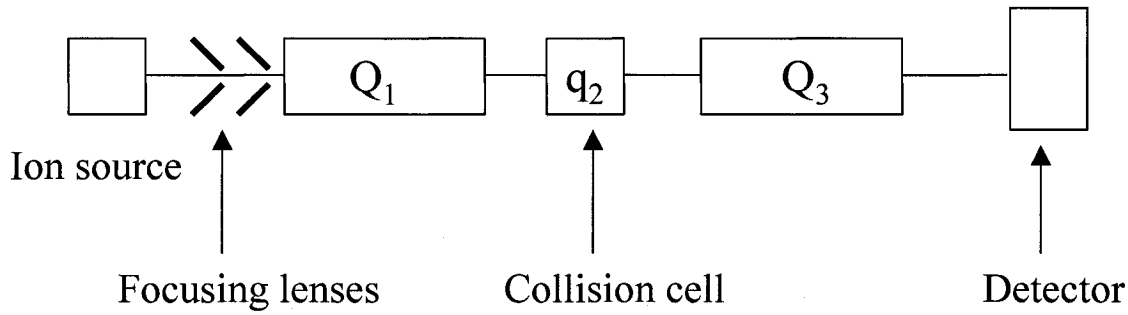

Figure 1.7 Schematic representation of a triple quadrupole mass spectrometer. Ions are first produced in the source and accelerated into the first quadrupole. Selected masses then enter the collision cell where they undergo collisional activation with neutral gas molecules. The formed product ions are separated by the third quadrupole and are subsequently detected.

Interestingly, in addition to their function as collision cells, rf-only quadrupoles are also widely used as ion transfer optics. In that application, ions passing through the quadrupole are confined in the center of the quadrupole axis at low gas pressures, thus increasing transmission efficiency. Often other multipoles such as hexapoles or octopoles are used for the same purpose. This effect is called *collisional cooling* or *focusing*. Furthermore, by adding trapping electrodes at the beginning and the end of such a

quadrupole, one can store ions in the device. These *linear ion traps* (LIT) have recently become very popular, either as a stand-alone MS, as a front-end stage prior to FT-ICR, or as Q_3 in a triple quadrupole MS (QqLIT).

Finally, one can also replace Q_3 with a completely different mass analyzer, in particular with a high-resolution device, like a TOF in the case of a QqTOF instrument.

Ion trap mass spectrometry

The analyzers described in the previous sections are ion beam-type instruments (except for the LIT). In the following text, ion trapping devices, allowing the storage of ions using electric potentials (ion trap) or magnetic fields (ion cyclotron resonance, ICR) with subsequent mass analysis in the same space, will be discussed. This first section explains the principles of quadrupole ion trap mass spectrometry.

The quadrupole ion trap (IT) mass spectrometer [42], first developed by Paul and Steinwedel [43], can be envisioned as a regular quadrupole wrapped around itself. It is composed of two end-cap electrodes and one ring electrode. By applying appropriate potentials on these electrodes, a pseudo-potential well, to which ions are confined, is formed within the trap, and ions can be stored for long intervals in this instrument. A special feature of the ion trap is that it is kept at high pressures relative to other mass analyzers. This is caused by the presence of a damping gas, usually He, which causes collisional cooling of the analyte ions with subsequent confinement in the center of the trap for an improvement in mass resolution. The pressure inside the trap is $\sim 10^{-3}$ Torr vs. 10^{-7}-10^{-10} Torr for other mass spectrometers. A diagram of an ion trap instrument is shown in Figure 1.8.

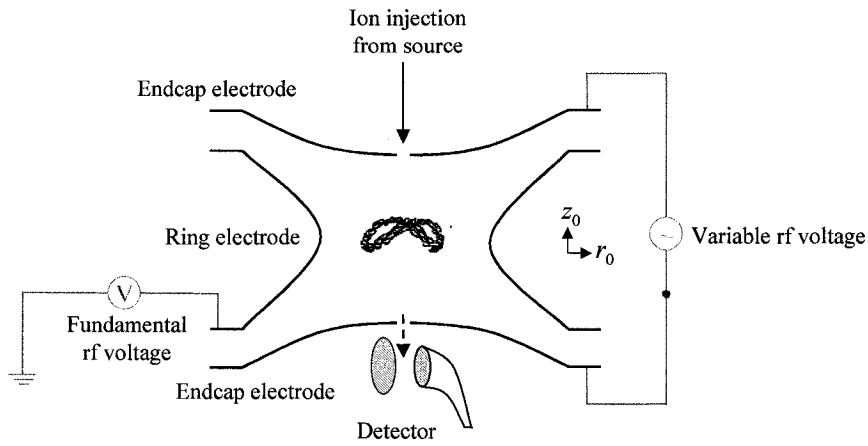

Figure 1.8 Diagram of a quadrupole ion trap. The instrument is composed of two end cap electrodes and one ring electrode. A fundamental rf frequency is applied to the ring electrode creating a pseudo-potential well to trap ions. A variable rf frequency is applied to the end cap electrode for either ion ejection or ion excitation.

Mass analysis in the ion trap is achieved by means of the so-called *mass-selective instability scan* [44] or by *resonance ejection* [45]. In the mass selective instability scan, ions of specific *m/z* values are selectively ejected from the trap by linearly increasing the rf amplitude on the ring electrode. Detection of the ions occurs following the ejection process. The resonance ejection technique extends the mass range of the ion trap by exciting the ions in the trap via a supplemental potential applied to the end caps. If the amplitude of this additional potential is large enough, ions can be ejected from the ion trap at ring electrode rf voltages lower than those required for the mass selective instability scan.

It is important to realize, that an experiment on an ion trap is composed of several steps occurring sequentially, in the same space. This chain of events is called a *microscan.* The separated time periods include ion injection, isolation, excitation and analysis. In addition, very often an initial pre-scan is performed to determine the ideal injection time, thereby reducing *space charge* effects. This is very important, because a fundamental limitation of the ion trap is the dependence of ion stabilities on the number of ions present in the trap. As the amount of ions is increased, space charging [46, 47] becomes an important factor. The electrostatic field is distorted by having too many ions in the trap, thus causing broadening of peaks, mass scale shifts, and loss in sensitivity. Eventually, ions are not trapped anymore when the ion density becomes too large.

Quadrupole linear ion traps also exhibit space charge effects, but they have larger ion storage capacities [48].

After the ions are injected into the trap from the source, a suitable rf voltage on the ring electrode confines them to stable trajectories. An isolation scan can be subsequently performed in order to selectively accumulate a specific ion or a range of ions. The next possible step is ion excitation, in the case of tandem mass spectrometry. Finally, ions are analyzed by ejection from the ion trap to the detector through an opening in the end cap. Figure 1.9 exhibits representative scan functions for a full scan, a selected-ion monitoring and an MS^n experiment in an ion trap. The type of scan dictates the length of time spent on each step. Note that for the SIM experiment, an isolation step includes an applied waveform with a notch present, corresponding to that of the secular frequency of the ion of interest, for selective accumulation. All unwanted ions are removed by resonant ejection during the accumulation period.

The analytical figures of merit of ion trap mass spectrometers are somewhat comparable to quadrupole mass analyzers. Mass ranges of up to *m/z* 4000 can be analyzed, at unit mass resolution. Higher mass resolution can be achieved with special slow scanning routines, for much smaller *m/z* ranges. The detection sensitivity, as outlined above, is generally very good in the full-scan mode because of the ion trapping abilities. The duty cycle in the SIM or MRM modes of the IT-MS is much lower than on the quadrupole MS, because of the significant overhead contributions to the microscan sequence (Figure 1.9). The sensitivity enhancements in the SIM mode in comparison to the full scan mode are therefore not very pronounced.

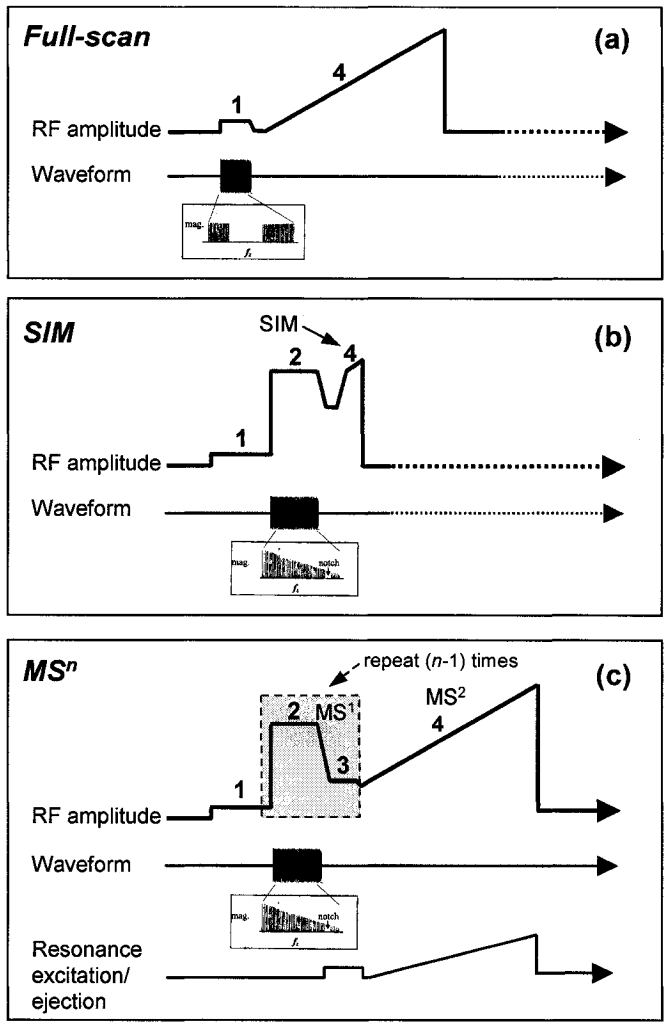

Figure 1.9 The events during an IT microscan are: *1* ion injection, *2* isolation, *3* excitation, *4* mass analysis. (**a**) Full-scan MS: a waveform is used to eject unwanted ions from the trap and to isolate a mass range of interest during ion injection (*1*); the rf voltage is ramped during mass analysis to sequentially eject the ions out of the trap (*4*). (**b**) SIM: a waveform is used to isolate a narrow *m/z* range of interest (the waveform has a notch present, corresponding to that of the secular frequency of the ion of interest, for selective accumulation. The rf ramping during mass analysis is very short for the limited *m/z* range. (**c**) MS*n*: a waveform is used to isolate only the precursor ion (*2*); the resonance excitation step (*3*) dissociates the precursor ion using an auxiliary rf voltage at the end caps. Product ions are subsequently analyzed (*4*).

The next mass analyzer, the FT-ICR-MS, is also an ion trapping device, using a strong magnetic field to confine ions and manipulate their motions.

Fourier transform-ion cyclotron resonance

Fourier transform-ion cyclotron resonance (FT-ICR) mass spectrometry has experienced a remarkable increase in use by analytical chemists recently. This instrument was historically employed for fundamental physics and physical chemistry applications [49, 50]. In recent years, though, new developments such as efficient ion-transport devices have allowed the use of external ionization sources (particularly ESI and MALDI), significantly increasing the versatility of these mass spectrometers. Furthermore, quadrupole and linear ion trap analyzers have been implemented for precursor ion selection and collisional activation, prior to FT-ICR mass analysis. Consequently, FT-ICR has become an invaluable tool for biological mass spectrometry, primarily for its extremely high-resolution and mass accuracy and its flexibility in ion activation techniques available. The most striking feature of this instrument is its outstanding mass resolution, significantly larger than any other mass spectrometry technique currently available. A basic description of the principles of ion motion in magnetic fields allows one to understand how it achieves these important advantages over other instruments.

While the principles of mass analysis by ICR date back to 1932, it was not until 1974, that Alan Marshall and Mel Comisarow added their landmark discovery to ICR, the use of Fourier transform pulse techniques [51, 52]. Combined magnetic and rf fields cause this instrument to have very unique properties, yielding some important advantages over the other instruments.

In the homogeneous magnetic field B of the ICR cell, the Lorentz force F_L subjected onto an ion of velocity v entering the magnetic field, will bend the ion's path into a circular motion, as follows [53]:

$$F_L = qvB = mv^2 / r = F_c, \tag{1.5}$$

where v and B are vectors, perpendicular to each other, m is the mass of the ion, q is the charge, r is the ion's radius, and F_c is the balancing centrifugal force. If the ion is under extremely low pressure conditions, it does not experience any collisions with residual gas molecules in the cell. Consequently, the speed of an ion in the FT-ICR cell is constant. With $\omega = v / r$, the angular velocity is given by:

$$\omega_c = \frac{qB}{m}. \tag{1.6}$$

This is the fundamental equation for FT-ICR, where the ion's *m/z* value can be directly measured by its ion cyclotron frequency, ω_c. Note that ions of the same *m/z* value have equal ω_c and no dependence on the ion's initial velocity upon injection into the cell; *i.e.*, no energy focusing is required for the precise determination of *m/z*. The ion's cyclotron frequency ranges from kHz to MHz values, depending on its mass, for small organic molecules to biomolecules in the kDa range, respectively. The radius of the cyclotron motion is given by $r = mv/qB$ (eq. (1.5)). As illustrated by Marshall and coworkers [53], cyclotron radii between 0.08 mm for *m/z* 100 and 1 cm for *m/z* 10,000 are assumed by the ions at room temperature and a magnetic field strength of 3 Tesla.

In order to measure the cyclotron frequency and thus the mass of an ion (*via* e.q. (1.6)), ions need to be coherently accelerated to a new radius. This is required, since initially not all ions are at the same point on their circular orbits. Therefore, their motions are incoherent, thus their frequencies cancel out and cannot be measured. In order for all ions of a specific *m/z* value to become coherent, an rf field, rotating with the ICR frequency of the specific ion, is applied. After this excitation, the radius of the ion no longer depends on its *m/z* value [53]:

$$r = \frac{V_{p-p} T_{excite}}{2dB}, \tag{1.7}$$

where $V_{p\text{-}p}$ is the peak-to-peak magnitude of the rf electric field, d is the distance between the flat electrode plates, and T_{excite} is the excitation time. Note that by exciting all ions of different *m/z* values with a broadband rf field, they all end up at the same radius. The resulting ions have all become spatially coherent, but ions of different *m/z* values still have a characteristic cyclotron frequency. Each *m/z* value can be differentiated based on the speed at which they orbit the common radius occupied by all ions.

A unique and quite interesting feature of these instruments is the way the frequency measurement is performed. FT-ICR analyzers do not have a detector, where ions are physically discharged, as is the case with most other mass spectrometers. Rather, detection is based on measuring the *image current* that individual ion packages induce when they pass the detector plates repeatedly, at their cyclotron frequencies. In a typical

experiment, the ions in the cell are simultaneously excited, and a composite image current for all ions is measured. This results in a time-domain ICR signal, which decays based on the number of collisions the ions undergo during detection. At extremely low pressures in the ICR cell, the signal decays slowly and we can measure the signal for longer periods and sensitivity is thus increased. This transient signal can be converted from the time domain to the frequency domain using a fast Fourier transform algorithm. The individual frequencies can then be transformed to *m/z* values by means of eq. (1.6). Figure 1.10 illustrates a typical transformation from the time-domain image current to a mass spectrum. The example shown in this figure is an MS/MS spectrum of neosaxitoxin (see Chapter 3) with certain product ion *m/z* values noted in the spectrum. Importantly, this method of detection is non-destructive and, therefore, allows for re-measurement. Ions can be measured for extended transient times, if required, thereby increasing sensitivity and mass resolution. The transient signals eventually diminish, because of collisions in the ICR cell slowing down the orbiting ions. A diagram of a FT-ICR cell is shown in Figure 1.11 [54]. Note that the ion has a combined cyclotron and magnetron motion. The magnetron motion has the larger radius and orbits around a center. This motion becomes more important as the ion becomes larger and is responsible for a loss of resolution at higher masses.

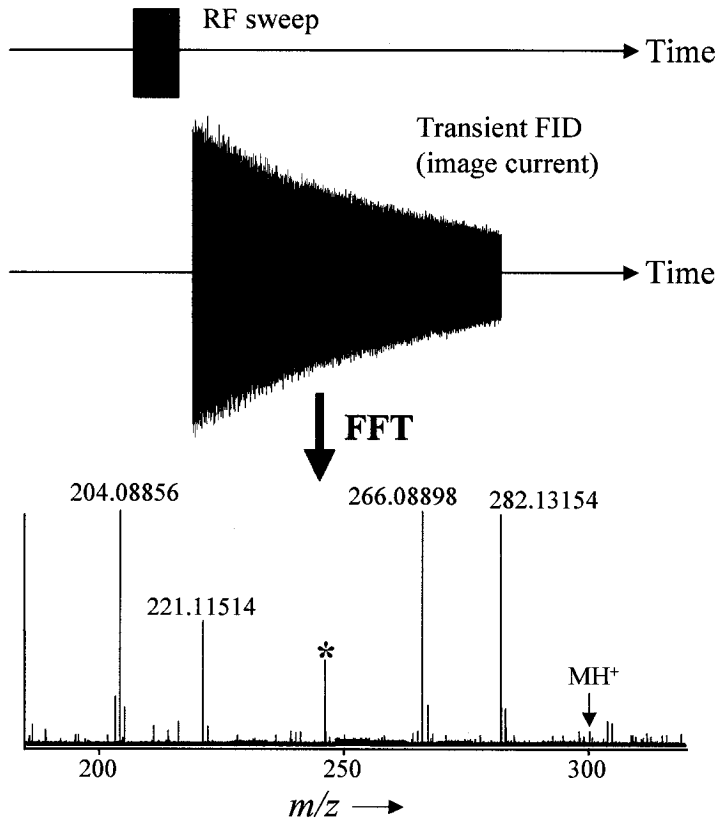

Figure 1.10 Image current produced by a broadband rf sweep following ion activation of protonated neosaxitoxin (*m/z* 316) in the FT-ICR cell. The transient FID is transformed into a frequency-domain magnitude spectrum and subsequently into a resulting mass spectrum (bottom) via eq. 1.6.

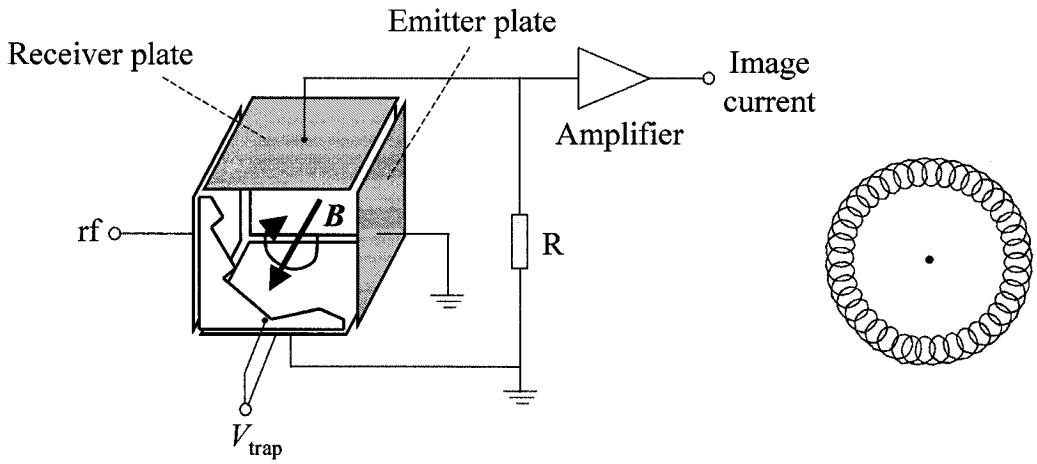

Figure 1.11 Diagram of a FT-ICR cell showing the direction of magnetic field and the motion of an ion orbiting about this field. The actual motion of an ion has two components: a cyclotron frequency, which is measured by the FT-ICR for a direct measurement of the *m/z* value of an ion, and a magnetron motion (consisting of the motion with the larger radii seen on the right of the figure).

It is evident that the strength of the magnetic field has an important influence on several properties of the ions. Firstly, the initial radius of an ion is inversely proportional to *B*, so that the higher the magnetic field, the higher the accessible mass range. Ions of larger *m/z* values occupy larger orbital radii. Consequently, there is an upper mass limit based on the size of the ICR cell and the strength of the magnetic field. Furthermore, as *B* increases, so does the cyclotron frequency of an ion, indicating that higher magnetic fields yield higher mass resolution. However, there is a reduction in the lower limit of *m/z* values with a higher magnetic field, since their frequencies become correspondingly higher and thus more difficult to measure. As seen with quadrupole ion traps, FT-ICR measurements can also be adversely affected in terms of space charge effects, when too many ions are present in the cell. The interactions between the ions can lead to dephasing of the ion cloud and peak coalescence.

As mentioned above, one of the primary advantages of FT-ICR is the flexibility in ion activation techniques available for tandem mass spectrometry experiments. Since isolation and excitation takes place in the same confined space, this instrument also belongs to the tandem-in-time category. This device enables the use of several "slow heating" ion activation methods, that are not feasible with many other mass spectrometers. Some such methods include sustained off-resonance irradiation (SORI), infrared multiphoton dissociation (IRMPD) and blackbody infrared radiative dissociation (BIRD). The SORI and IRMPD methods are covered briefly in the following section. Also, a fundamentally different technique of activation is also available on all commercial FT-ICR instruments. Electron capture dissociation (ECD) involves the capture of low-energy electrons, with charge-state reduction and subsequent fragmentation. It is therefore only applicable to multiply-charged cationic species, usually peptides or proteins, and will not be covered here.

MS/MS experiments are increasingly conducted outside the ICR cell, either with a linear ion trap or a Qq arrangement, coupled to the FT-ICR mass analyzer. They offer increased compatibility with fast chromatography runs, as ion activation experiments directly in the ICR cell often take too long to be suitable for these experiments.

Hyphenated designs

Several individual mass analyzers have been covered; namely, time-of-flight, quadrupole, ion trap and FT-ICR instruments. As illustrated above, the way these analyzers function and their characteristic features are quite different. As the demands continue to grow for mass spectrometry applications, there is an increasing trend toward hybrid designs, to increase versatility by combining the intrinsic advantages of the different analyzers. A few examples are outlined here.

In 2002, a new design of hybrid quadrupole-linear ion trap (QqLIT) was introduced. This instrument can be visualized as a triple quadrupole, in which Q_3 is replaced by a linear ion trap [55]. This configuration results in a high-sensitivity triple quadrupole-like tandem mass spectrometer with a further stage of MS/MS possible in the LIT. Importantly, this instrument maintains full QqQ capability but adds important performance enhancements, such as improved duty cycle and several novel scan modes. An illustrative example was shown by Hopfgartner and co-workers [56], who used a QqLIT for very selective identification of metabolites at the picogram level in very complex matrices.

The most successful hyphenated LC/MS/MS instrument so far has been the QqTOF mass spectrometer. QqTOF instruments have been around for several years. They have evolved significantly and are now essential to researchers in the proteomics and drug discovery fields for obtaining accurate mass information on precursor and product ions. Mass accuracies of <10 ppm have routinely been achieved, allowing the determination of a small number of possible empirical formulae [57]. The coupling of the Qq section with a TOF is achieved in exactly the same way as described in the previous section for ESI-TOF; by adding an orthogonal acceleration region after the collision cell. The TOF section now only serves to record spectra, with high resolution and mass accuracy.

More recently, new technological developments in Fourier transform-ion cyclotron resonance mass spectrometry have brought this technology back into the spotlight. FT-ICR is now a serious contender for the more established QqTOF instruments. QqFT-ICR hybrid designs allow pre-accumulation of ions in a multipole lens before the ICR cell as well as external low-energy CID experiments [58, 59].

Furthermore, various ion activation techniques to generate product ions can be applied, once the ions are trapped in the FT-ICR cell. In addition, a hybrid of a linear ion trap and a FT-ICR mass spectrometer is commercially available. The most interesting aspect of this particular instrument is the concept of method development: one can first develop and optimize the analytical methods on the ion trap portion of the instrument (which is essentially a stand-alone LIT instrument with its own detector) and then add the capability of FT-ICR, merely by switching the instrument into the high-resolution mode, thus obtaining accurate masses with appropriate mass calibration routines [60]. All MS^n experiments are conducted in the LIT portion of this instrument.

This technology is advancing at such a rapid rate that even very recently conceived instruments are finding full implementation in bioanalytical laboratories. During the past two decades, we have seen a divergence in the number and specific characteristics of instruments used in these types of analyses. However, more recently, there has been a shift toward converging to a single multi-purpose instrument through the hyphenation of different mass analyzers. The use of several of these new instruments will be discussed throughout this text.

Ion Activation Techniques[†]

Soft ionization techniques, such as ESI and MALDI, primarily yield protonated or deprotonated species with little or no fragmentation occurring in the source, therefore limiting the structural information available in a single-stage mass spectrum. As a consequence, tandem mass spectrometry (MS/MS) has emerged as an essential technique for the structural analysis of a wide range of biologically-relevant compounds. MS/MS involves the activation of a known precursor ion formed in the ion source and mass analysis of its fragmentation products. The ion activation step is crucial to the experiment and ultimately defines what types of products result. Several ion activation techniques have been developed. A description of collision-induced dissociation and its application

[†] From: Sleno L, Volmer DA. *J. Mass Spectrom.* 2004; **39**: 1091. 2004 © John Wiley & Sons Limited. Reproduced in part, with permission.

in different instrument designs as well as the technique of infrared multiphoton dissociation are covered here.

Collision-induced dissociation

Methods of ion activation cause the deposition of internal energy into precursor ions and allow for the observation of fragment ions. Collision-induced dissociation remains the most common ion activation method used in present day instruments [61, 62, 63]. Collisions between the precursor ion and a neutral target gas are accompanied by an increase in internal energy. This induces decomposition with an improved probability of fragmentation as compared to metastable unimolecular dissociations, occuring in field-free regions of sector or time-of-flight mass spectrometers. A brief review of the collision process between a fast ion and slow target is useful for understanding how the collision energy is converted into internal energy.

When an ion with a high translational energy undergoes an inelastic collision with a neutral, part of the translational energy is converted into internal energy of the ion, leading to subsequent decomposition [64]. The transfer of kinetic energy to internal energy is governed by the laws of physics involving a mobile species (ion) and a static target (gas). To simplify the description of such a process, it is more useful to work in the center-of-mass (com) framework instead of the laboratory reference frame, since in the latter, a binary collision is described by the two particles involved with their respective position and velocity vectors. A conversion to the com reference frame is easier, because the kinetic energy of the collision pair, assuming no external forces involved, is conserved throughout the collision process. Energy transfer in collisional activation and kinetic energy release during the dissociation of activated ions are deduced by applying the conservation of momentum to the process. The entire system is evaluated as a whole and velocities of the ion and neutral are stated as velocities relative to each other. The total available energy for the transfer of kinetic energy to internal energy is the relative energy (E_{com}) and depends on the collision partners' masses. The following relationship relates the center of mass and laboratory collision energies:

$$E_{com} = \left(\frac{N}{m_p + N} \right) E_{lab}, \tag{1.8}$$

where E_{lab} is the ion's kinetic energy and N, m_p represent the masses for the neutral target and precursor ion, respectively. Through the collision process, since conservation of energy is assumed, their relative energies change by an amount designated as the collision endothermicity, q_e (the amount of translational energy converted into internal energy). The maximum magnitude of q_e is seen in the case where the collision partners stick together, consisting of a totally inelastic collision. In this case, the final relative kinetic energy is zero. The value of $q_{e,max}$ thus is equal to the initial center of mass energy. E_{com} represents the maximum amount of energy to be converted into internal energy of the precursor ion. This energy, as seen in eq. (1.8), increases with the target's mass, allowing more of the ion's kinetic energy to be converted into internal energy. Furthermore, E_{com} decreases as a function of $1/m_p$, so larger precursor ions have less internal energy available for fragmentation [65]. During the collision process, collision partners approach and recede from each other with changes occurring at the molecular level. For an elastic collision (q_e=0), there is no net change in kinetic energy. When q_e>0, an inelastic process occurs with a decrease in kinetic energy (E_k) and a simultaneous increase in internal energy. Under superelastic conditions (q_e<0), there is a net increase in E_k and decrease in internal energy. Collision-induced dissociations of polyatomic ions represent inelastic collisions. Collisional activation mechanisms have been extensively studied for diatomic ions with neutral target atoms [66], but are still not well defined for polyatomic ions. In general, the quasi-equilibrium theory (QET) for unimolecular dissociations is used to explain the fragmentations of these ions [67], and the dissociations are assumed to occur by a 2-step mechanism, where excitation of the precursors and dissociation of ions at excited vibrational levels of the ground electronic state are separated in time:

$$m_p^+ + N \rightarrow m_p^{+\neq} \rightarrow m_f^+ + m_n \qquad (1.9)$$

The second part of this mechanism is, of course, a unimolecular dissociation of an excited ion, and explains why the QET can be used to rationalize CID spectra. Fragmentation of a precursor ion can occur if the collision energy is sufficiently high that the ion is excited beyond its threshold for dissociation. There exists, however, an amount of extra energy needed above and beyond that of the threshold energy, namely the *kinetic shift*, for

fragmentation to occur on the time scale of the experiment. The shorter the time scale of activation, the higher the kinetic shift necessary to observe fragments.

All CID processes occurring routinely can be separated into one of two categories based primarily on the translational energy of the precursor ion; *low-energy collisions*, common in quadrupole and ion trap instruments, occur in the 1-100 eV range of collision energy, and *high-energy collisions*, seen in sector and TOF/TOF instruments, are in the kiloelectronvolt range. Intermediate collision energies (100-1000 eV) do not occur regularly in commonly used tandem mass spectrometers. The case of low energy collisions is explained in detail below.

Low-energy collisions

Low energy collisions, in the range of 1-100 eV of laboratory collision energy, are mostly observed in triple quadrupoles and trapping devices, such as quadrupole ion traps and FT-ICR instruments. In a QqQ instrument, the collision cell is filled with a neutral inert gas, usually N_2 or Ar, and ion activation is achieved by multiple collisions. In a quadrupole ion trap, the precursor ions are isolated and accelerated by "on-resonance" excitation and product ions are detected by subsequent ejection from the trap. In on-resonance excitation, the isolated precursor is excited by applying a small (tickle) potential across the end caps, corresponding to the secular frequency of the ion. As ion activation times on the order of tens of milliseconds can be used without significant ion losses, multiple collisions occur during the excitation period. Because of this relatively long time-scale, this excitation technique falls in the category of so-called "slow heating" processes [68]. For a slow heating process, excitation in an ion trap is still quite fast, due to the high pressure of helium present in the trap (~1 mTorr). There are other slow heating methods, such as "sustained off-resonance irradiation" (SORI) with longer excitation periods.

Moreover, ion traps have the ability to perform multiple stages of tandem mass spectrometry, thus yielding MS^n CID spectra. This is quite advantageous for the elucidation of fragmentation pathways, which in turn aids in the analysis of CID spectra for proposing molecular structures for precursors as well as product ions. Ion traps offer the advantage of studying exact relationships between precursor and product ions. The

mechanism of resonance excitation causes specific precursors to be accelerated, thus only direct products are formed in an ion trap.

Similarly, in FT-ICR instruments, isolation and excitation take place in the same confined space, where the ions are trapped for a specific time in a combined magnetic and electrostatic field. The technique of sustained off-resonance irradiation is usually applied for collisional activation of precursor ions in FT-ICR instruments. In SORI, the precursor ion is excited at a frequency slightly higher than its natural cyclotron frequency. In that way, ions undergo multiple acceleration/deceleration cycles as they repeatedly increase and decrease their orbit radii in the FT-ICR cell before dissociation takes place. As the ion translational energy is small compared with on-resonance excitation, much longer activation times can be used, often in the hundreds of milliseconds, sometimes up to seconds [68] and a larger number of lower energy collisions take place. Consequently, the ion sequentially absorbs more and more collision energy until the collision threshold is reached. As a result, slow, low-energy rearrangement reactions are favored with subsequent decomposition by the lowest energy pathway [69].

For all low energy collisional activation techniques, the ions' excitation energy is mostly vibrational [70], since the interaction time is in the order of $\sim 10^{-13}$-10^{-14} s, which coincides with a bond's vibration period. The mass of the neutral target has a very important role for low energy CID. More energy is transferred with heavier targets. Even though the energy deposited is slightly lower than in high energy CID, collision yields are extremely high, since the length of the collision cell in a QqQ and the duration of IT or FT-ICR CID experiments allow for multiple collisions.

Infrared multiphoton dissociation

In FT-ICR-MS, an alternative to SORI is infrared multiphoton dissociation (IRMPD). Ion activation occurs in the ICR cell by irradiation with a low-power CO_2 infrared laser (10.6 μm) for tens to hundreds of milliseconds per experiment, resulting in the stepwise absorption of photons, followed by subsequent dissociation of the ion. A schematic of an IRMPD laser into a FT-ICR cell is represented in Figure 1.12.

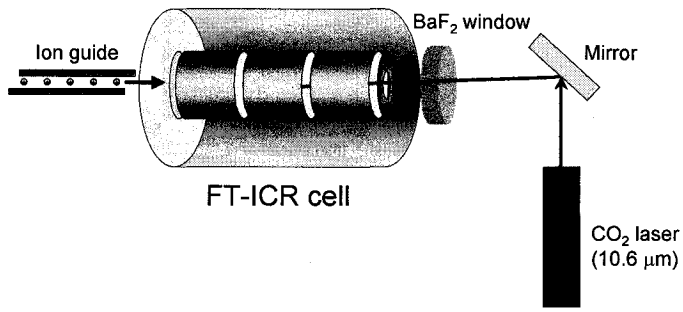

Figure 1.12 Schematic representation of IRMPD ion activation in a FT-ICR cell.

Photodissociation occurs when ions are excited and subsequently fragmented by the absorption of one or more photons. This type of activation of gaseous ions in a mass spectrometer has been performed with a range of photon energies, primarily by using lasers of different wavelengths. Historically, lasers emitting in the ultraviolet (UV), such as ArF excimer lasers (193 nm), and visible regions were used. Recently, there has been a prominent increase in the use of infrared (IR) lasers for photodissociation. These lasers are of quite low energies compared to the UV lasers, where the absorption of only one photon provides enough energy to initiate dissociation of precursor ions. In IR, multiphoton processes are consequently needed to sufficiently excite ions for efficient fragmentation.

The chemistry of small molecules has been studied by infrared multiphoton dissociation for a long time [71, 72, 73]. The recent increase of applications for IRMPD as an activation technique in tandem mass spectrometry is primarily due to the growth in popularity of trapping instruments, including quadrupole ion traps and Fourier transform-ion cyclotron resonance mass spectrometers. IRMPD is ideally suited to these instruments, given their ability to store ions for long times. Typically, ions in the ion trap or the ICR cell are activated by a low-power (<100 W) continuous-wave CO_2 (10.6 μm) laser for a selected irradiance time (usually on the order of tens to hundreds of milliseconds), followed by the detection of the resulting product ions. High-power (megawatt) pulsed lasers can also be used, but are not very common, since they are not easily implemented in most analytical laboratories.

Photodissociation can be generally viewed by the following mechanism:

$$m_p^+ \xrightarrow{nh\nu} m_p^{+\neq} \xrightarrow{k_{diss}} m_f^+ + m_n, \qquad (1.10)$$

where n describes the number of absorbed photons, $h\nu$ is the photon energy and k_{diss} is the rate constant for photodissociation. The mechanism of activation is assumed to be through the absorption of IR radiation by IR active modes present in the ion, followed by the rapid redistribution of energy over all the vibrational degrees of freedom. The outcome is a statistical internal energy distribution, similar to low energy CID. The activation is stepwise, by subsequent absorption of photons, and dissociation follows the lowest energy pathway. There are several important criteria for photodissociation to occur. The precursor ion must be able to absorb energy in the form of photons, producing excited states above the threshold of dissociation for the ion of interest, and the rate for dissociation must be relevant on the time scale of the mass spectrometer. Competitive collisional and radiative cooling of ions also occurs, partially decreasing the energy gained by photon absorption and thus lowering the overall rate for dissociation. The energy gained by the absorption of photons must consequently overcome the energy lost by photon emission from the excited ions, as well as by deactivation from collisions. The presence of gas in the activation region (storage device) increases the chances for deactivation of the excited ions. In an FT-ICR instrument, this fact does not pose a problem since extremely low pressures are maintained in the cell. Conversely, the quadrupole ion trap has a constant amount of helium gas present in the trapping region at all times to help narrow the kinetic energy distribution of the ions, so collisional deactivation can become an issue. A compromise is usually reached with a lower helium pressure than usual in the ion trap, because removing the helium altogether would cause peak shapes and resolution to suffer tremendously [74].

A very important advantage of IRMPD over CID in an ion trap comes from the fact that the trapping conditions, such as the rf voltages, do not need to be altered in the activation process. In a typical CID experiment, the precursor ion of interest is selectively accelerated by resonant excitation, causing multiple collisions and stepwise energy deposition to occur, until an energy threshold is surpassed. The necessary conditions for CID in an IT cause an inherent low-mass cut-off for the detection of product ions, so low mass fragments are not observed even if they are formed easily. A trade-off must be

made between the amount of internal energy available, which depends on the potential well depth, and the low-mass cut-off for product ions. Conversely, low-mass fragments can easily be detected by photodissociation [75]. IRMPD can thus allow for the storage of a wide *m/z* range of ions with no mass discrimination of product ions.

The advantages of IRMPD are numerous. The energy deposited from this technique is very well defined. In the case of a 10.6 μm CO_2 laser, the absorption of one photon corresponds to 0.117 eV of energy. The dissociation efficiency of this technique is high, given enough time for activation, and it can easily be implemented in routine analytical laboratories. Dissociation of precursor ions does not compete with scattering and ejection out of the trapping region and no mass discrimination is seen. In the case of FT-ICR, no gas is added to the cell, so resolution is not sacrificed and no time is needed for pumping out gas prior to MS detection, as is necessary for CID in these instruments. However, the cost of this technique is high and direct fragmentation pathways are often not easily determined, as in CID in an ion trap. The process is non-selective, therefore all trapped ions are excited and secondary product ions can also be observed. This feature of IRMPD can be convenient, since the resulting spectra are often similar to low-energy CID spectra measured on triple quadrupole instruments [76]. Recent studies have generally focused on the analysis of biomolecules by MS/MS using IRMPD. The technique has been successfully employed for proteins [77, 78], oligosaccharides [79], oligonucleotides [80, 81], and pharmaceuticals [75, 82, 83].

CHAPTER II- Structural Study on Spirolide Marine Toxins[†]

Introduction

A major concern in marine chemistry is the identification and regulation of marine toxins. These harmful secondary metabolites are produced by several strains of phytoplankton and severe outbreaks originate from "red tides" (harmful algal blooms) [84]. These microscopic plants are the basis of the marine food chain and shellfish, as well as herbivorous finfish, grazing on these algae can cause bioaccumulation of toxins. This can therefore result in human toxicity. Marine algal toxins represent an enormous health risk with over 60,000 poisoning cases annually worldwide [85]. In order to guarantee consumer safety and protect the aquaculture industry from financial damages, sensitive and effective monitoring tools for contaminated seafood are required. Many countries have established regulatory guidelines and set maximum allowable concentrations for seafood samples. However, marine toxins exhibit a wide range of chemical structures, molecular weights, and physicochemical properties, making not only routine identification of known toxins difficult, but particularly complicating the structural determination of unknown toxins and their metabolites.

Several classes of marine toxins exist with a large variation in molecular structure. Some major groups, based on their toxic effects, are the paralytic shellfish poisons (PSPs), including the well-known saxitoxin and its derivatives [86], diarrhetic shellfish poisons (DSPs), such as the polyethers okadaic acid and the dinophysistoxins [87], amnesic shellfish poisons (ASPs), with domoic acid [88] as the main culprit of toxicity in this class, and neurotoxic shellfish poisons (NSPs), including the brevetoxins [89]. There continues to be much progress in the routine analysis of these poisons as well as the discovery of new toxins. The following work consists of a study on a relatively new class of marine toxins, the spirolides.

The spirolides are bioactive macrocyclic imines, initially discovered through routine DSP monitoring of lipophilic shellfish extracts from aquaculture sites along the

[†] Reproduced (in part) from: Sleno L, Windust AJ, Volmer DA. *Anal. Bioanal. Chem.* 2004; **378**: 969 and Sleno L, Chalmers MJ, Volmer DA. *Anal. Bioanal. Chem.* 2004; **378**: 977. With kind permission of Springer Science and Business Media.

southeastern coast of Nova Scotia, Canada [90, 91]. Since the early 1990's, there has been an annual recurrence of spirolides in this region in the period from May to July [92]. They have also been detected from sites in the United States [93], Denmark [94] and off the Scottish east coast [95]. These compounds were found to be toxic in the mouse bioassay by intraperitoneal (IP) injection of both crude lipophilic extracts from shellfish and purified compounds. Their mode of action is seen by rapid death following neurological symptoms, including convulsions. Toxicity studies in laboratory mice gave an LD_{50} of 40 μg/kg and 1 mg/kg for IP and oral dosing, respectively [96]. Some evidence indicates that the spirolides are muscarinic acetylcholine receptor antagonists [96] and weak L-type transmembrane calcium channel activators [90] in mammalian systems. Human toxicity is still unknown. Vague symptoms, however, have been documented, including gastric distress and tachycardia, following shellfish consumption from Nova Scotian sites in the period of late spring and early summer when the spirolides have been detected [96].

The spirolides have been found to be natural products of the dinoflagellate *Alexandrium ostenfeldii* [92, 97, 98], and several cultures of this species have been analyzed with important variations in toxin profiles from different regions [99]. Several spirolides have been isolated and analyzed by nuclear magnetic resonance (NMR) spectroscopy [90, 100] and characterized as polyketides with cyclic imine and spiro-linked tricyclic ether moieties. Compounds isolated from Nova Scotian sites (Figure 2.1(a)) include spirolide A-D and 13-desmethyl derivatives of spirolides C and D. Ship Harbour and Graves Shoal represent two major aquaculture sites in Nova Scotia and previous profiling studies have used cultures from these two sites [90, 92, 97, 98, 100, 101]. The present work focuses on a Ship Harbour isolate of *A. ostenfeldii*, AOSH1 [97].

There are notable structural similarities between the spirolides and other marine toxins, namely the pinnatoxins [102] and gymnodimines [103], including the cyclic imine group [101] (see Figure 2.1(b)). Interestingly, pinnatoxins have been attributed to major toxic outbreaks in China and Japan [102, 104], yet gymnodimine has very low oral toxicity [105]. Two shellfish metabolites of spirolides A and B have been observed, namely spirolides E and F. These compounds are hydrolysis products yielding an acyclic keto-amine group. These transformation products are also inactive in the mouse bioassay,

deducing the cyclic imine as the pharmacophore for toxicity [101]. Spirolides E and F can also be formed by acid-catalyzed hydrolysis of spirolides A and B, but the C/D class of these compounds, with an extra methyl substituent on the cyclic imine, is not altered under the same conditions. This pathway has been proposed as a detoxification mechanism, since preliminary results show that the A/B class may be less orally toxic than the C/D class [100]. Therefore, it remains essential to identify structural differences in related compounds, possibly causing altered toxicological effect. Some initial investigations on the metabolism of these toxins will be presented in this chapter.

a)

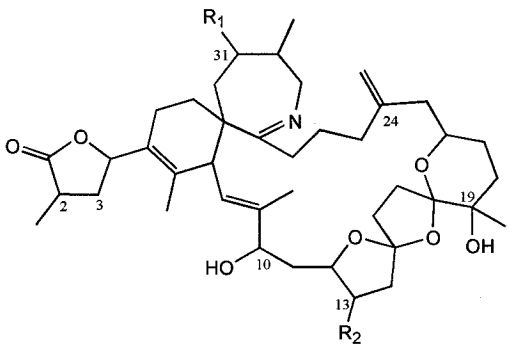

Spirolide	R_1	R_2	$\Delta^{2,3}$	MH^+
A	H	CH_3	√	692.5
B	H	CH_3		694.5
C	CH_3	CH_3	√	706.5
D	CH_3	CH_3		708.5
desmethyl-C	CH_3	H	√	692.5
desmethyl-D	CH_3	H		694.5

b)

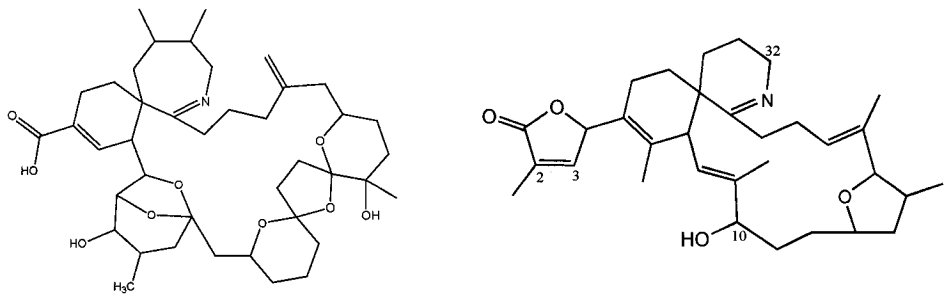

Figure 2.1 a) Structures of known spirolides found in *Alexandrium ostenfeldii.* b) Structures of structurally-related marine toxins, pinnatoxin A (left) and gymnodimine (right).

The spirolides have been characterized using several techniques, mainly NMR and mass spectrometry [90, 100, 101, 106]. A major drawback of NMR is that large amounts of purified material are necessary for structure elucidation of unknown compounds. Most previous analytical techniques for the spirolides have employed liquid chromatography/mass spectrometry [92, 97, 98, 100]. These methods have been used in the monitoring of known spirolides, as well as in the identification of some unknown spirolides by using specific abundant product ions in MS/MS spectra [100]. Mass

spectrometry is also an essential analytical tool for the structural elucidation of minor compounds and has been successfully used in this manner [107, 108]. Triple quadrupole mass spectrometers are rugged instruments giving reliable MS/MS data [109, 110], and are often used for the detection of unknown compounds. The arrival of electrospray quadrupole ion trap instruments [111] afforded the ability for MS^n scans and these experiments have been shown to be very helpful in the elucidation of fragmentation schemes [112]. A new design of hybrid quadrupole-linear ion trap (QqLIT) yields a high sensitivity tandem mass spectrometer with triple quadrupole-like MS/MS spectra with an extra stage of tandem mass spectrometry possible in the LIT [55]. Also, important information can be gained by high-resolution mass spectrometry, from which elemental formulae can be deduced [53], providing evidence to support proposed fragmentation pathways. FT-ICR instruments have recently become very popular for this application, due to their high sensitivity and excellent resolution and mass accuracy [53]. A collection of these techniques should prove very useful for the elucidation of fragmentation mechanisms for the spirolides and consequently, the characterization of unknowns.

Understanding the fragmentation mechanisms of the spirolides is crucial for the characterization of unknown analogs by mass spectrometry. The aim of the present study was to carry out a thorough analysis of collision-induced dissociation (CID) reactions of the spirolides, concentrating on the major component present in the crude phytoplankton extract. The major component was verified as 13-desmethyl spirolide C by LC/MS analysis. Subsequently, CID product ions were identified using triple quadrupole and quadrupole-linear ion trap instruments. Finally, FT-ICR data confirmed the proposed fragments with exact masses. A fragmentation scheme is proposed for the formation of all major CID product ions from 13-desmethyl spirolide C. Several other components present in the extract were analyzed in a similar manner. Mass-triggered semi-preparative fraction collection allowed several fractions to be enriched with different spirolide components. These isolated fractions were analyzed using triple quadrupole mass spectrometry, resulting in product ion spectra for all components present in the original extract. Finally, FT-ICR mass spectrometry was utilized for accurate mass measurements. This combination of advanced mass spectrometry techniques yielded important structural information for unknown spirolides and related compounds.

Experimental

Chemicals

Acetonitrile, methanol, hexane (Caledon, Georgetown, ON, Canada) and Milli-Q organic free water (Millipore, Bedford, MA, USA) were used as solvents. Ammonium formate, formic acid, trifluoroacetic acid, potassium chloride, glycerol, potassium phosphate, reduced β-nicotinamide adenine dinucleotide phosphate (β-NADPH), Folin and Ciocalteu's phenol reagent, angiotensin II, bombesin, mellitin, substance P and [Glu^1]-Fibrinopeptide B were purchased from Sigma-Aldrich (Mississauga, ON, Canada).

Culture and Sample Preparation

Alexandrium ostenfeldii clone AOSH1 [97] was grown in 10 x 1 liter volume batch cultures in 2.8 l Fernbach flasks for one month in L1 enriched seawater medium [113] attaining a final cell density of *ca.* 12 x 10^3 cells/ml. Culture temperature was 12°C and light was supplied by overhead fluorescent light banks providing an irradiance of 24 µmol photons/m^{2}sec. A 14h:10h (light:dark) photoperiod was employed throughout. The cells were harvested by gravity filtration on a 20 µm nylon mesh filter, rinsed with fresh seawater and frozen at -20°C prior to extraction. Next, the cells were sonicated in 100% methanol using a microtip at 45% maximum intensity (*ca.* 25 W) on a 50% pulse-duty mode. The sonicated suspension was then centrifuged at 6675g for 15 min at 5°C, followed by the filtration of the supernatant in a 0.45 µm centrifuge cartridge (Ultrafree-MC, Durapore membrane, Millipore) prior to LC/MS analysis.

The resulting extract was purified as follows: a total biomass of 62 g wet weight of cells was extracted by sonication with 275 ml of methanol, followed by cleanup with hexane for the removal of lipophilic interferences. The methanol extract was then evaporated to dryness on a rotary evaporator. The dried sample was subsequently partitioned against dichloromethane/water (1:1) and the dichloromethane extract was dried using a rotary evaporator. The dried spirolides were then reconstituted in 15 ml methanol and the entire solution was used for mass-triggered fraction collection.

In vitro microsomal incubations

Mouse liver microsomes were prepared in the following manner: homogenize fresh livers (8 portions, obtained through Dalhousie University's Animal Care department) in 2 volumes of 1.15% KCl, centrifuge at 9000 rpm for 10 min, transfer supernatant to ultracentrifuge tubes and spin at 40,000 rpm for 50 min at 4°C, resuspend resulting pellet in 0.1 M potassium phosphate buffer containing 20% glycerol (50% liver weight), homogenize and store at -80°C. Protein content was determined using the Lowry [120] method. Human liver microsomes were purchased from Sigma. Metabolism studies were conducted with 13-desmethyl spirolide C and gymnodimine at 10 μM with 1 mM β-NADPH, 1 mg/ml microsomal (human or mouse) protein in 50mM KH_2PO_4, pH 7.4 buffer. Incubations were done at 37°C, and were quenched after 1 hour with 1:1 acetonitrile, centrifuged at 10,000g and stored at -20°C.

High Performance Liquid Chromatography

The HPLC system employed was an Agilent 1100 (Palo Alto, CA, USA) binary pump. A Phenomenex ODS (30) 150 x 3.2 mm C18 reversed-phase column filled with 5 μm particles was used at a flow rate of 0.5 ml/min. Compounds were separated with the following mobile phases: A: water and B: 95% acetonitrile containing 2 mM ammonium formate and 50 mM formic acid each. The profile for gradient elution was as follows:

Time (min)	A (%)	B (%)
0.0	70	30
0.5	70	30
8.0	30	70
8.5	10	90
10.0	10	90
10.5	70	30
16.0	70	30

Mass-triggered Fraction Collection

A Waters (Milford, MA, USA) 600 pump and 2767 sample manager (fraction collector), controlled by the Micromass (Manchester, UK) MassLynx 3.5 software, were used for mass-triggered fraction collection of the phytoplankton extract. The extract was injected in individual 1 ml aliquots (diluted to 30% organic) and separated on a YMC

(Wilmington, NC, USA) Combiprep ODS-AM preparative HPLC column (50 x 20 mm filled with 5 μm particles) at 10 ml/min. The mobile phase used consisted of A: water and B: acetonitrile, each with 0.1% trifluoroacetic acid with a total run time of 20 minutes. The gradient consisted of an initial 10 minute isocratic step at 35% B, a linear increase to 75% B, followed by a further increase to 90% B in 1 min. An ACURATE (LC Packings, Amsterdam, The Netherlands) flow-splitter (1/1000 split ratio) after the preparative column was used to divert 10 μl/min portion (plus make-up flow of methanol to give 1 ml/min for MS detection) to the single quadrupole mass spectrometer (Micromass ZQ) for continuous signal monitoring of the masses of interest (*m/z* 536.5, 604.5, 606.5, 692.5, 694.5, 706.5, 708.5).

Mass spectrometry

Ion trap

Full-scan experiments in the range *m/z* 150–900 were carried out on an Agilent 1100 LC/MSD SL ion trap mass spectrometer in the positive ion mode. The instrument was operated at the following settings: capillary voltage, -3.3 kV; nebulizer, 60 psi; dry gas, 9 l/min; dry temperature 350 °C; trap target, 50,000.

Triple quadrupole

A MDS Sciex (Concord, ON, Canada) API 4000 triple quadrupole mass spectrometer was operated in the positive ion mode at a spray voltage of 5.5 kV, a declustering potential of 50 V and a source temperature of 450°C. Ultra-pure nitrogen was used as both curtain gas and collision gas. MS/MS of the MH^+ ion of 13-desmethyl spirolide C was performed with a CAD gas setting of 6 (arbitrary units) and a collision offset voltage of 60 V, with the exception of two unknown compounds, as specified in the Results and Discussion section.

Quadrupole-linear ion trap

A QTRAP instrument (MDS Sciex) was employed with a TurboIon spray source with the interface heater turned off and ionspray voltage of 5 kV. The following parameters were used for MS^3 experiments: curtain gas of 20 (arbitrary units), nebuliser

gas (GS1) and turbo gas (GS2) set at 20 psi, declustering potential (DP) of 80 V, a collision-offset voltage of 50 V, a CAD gas setting at high and excitation energy in the linear ion trap of 200 mV for a duration of 100 msec per scan. The resulting spectra were averaged for 5 minutes at a direct infusion rate of 10 μl/min.

Fourier transform-ion cyclotron resonance

FT-ICR experiments were performed on a homebuilt 9.4 Tesla Q-FT-ICR instrument at the National High Magnetic Field Laboratory in Tallahassee, FL. Sample and calibrant ions were introduced at a flow rate of 400 nl/min from separate ESI emitters of a dual ESI source. Ions were accumulated within a linear octopole. Mass selected calibration and sample ions were individually accumulated for 5 and 1 seconds, respectively. All ions were then transferred through an octopole ion guide to the ICR cell. Hanning apodization and one zero-fill were applied to all data prior to fast Fourier transformation and magnitude calculation [114]. Frequency spectra were calibrated [115, 116] internally from the measured ICR frequencies of the calibration mixture ions in the ESI tuning mix (G2431A, Agilent) (*m/z* 622.02895, 922.00979 and 1521.97146 respectively). Each spectrum represents the sum of 50 time-domain transients (2 Mb data).

In IRMPD FT-ICR-MS, the mass-selected precursor ion was first accumulated and then transferred to the ICR cell. Stored-waveform inverse Fourier transform (SWIFT) [117, 118] ion ejection was applied to further isolate the precursor ion under investigation. Product ion data were internally calibrated by tailoring the SWIFT waveform to isolate the precursor ion of interest and the [Glu^1]-Fibrinopeptide $(M+2H)^{2+}$ ion (*m/z* 785.8). Internal calibration data was performed based upon the measured frequencies of the [Glu^1]-Fibrinopeptide product ions at *m/z* 175.1195, 333.1886 and 480.2571. IRMPD was performed with a 40 W CO_2 laser for 150 ms at 50% laser power. Spectra represent the sum of 50 scans (1 Mb data). Elemental formulae were calculated using MIDAS [119] analyzer software. For elemental formula assignments of product ions, the atom constraints for C, H, N and O were set to the number of atoms in the precursor ion.

Additional studies were performed on a commercial 9.4 T Qq-FT-ICR MS (IonSpec, Irvine, CA) with external calibration using a mix of the following four peptides: Angiotensin II (MH^+ 1046.5419, $(M+2H)^{2+}$ 523.7740), Bombesin (MH^+ 1619.8224, $(M+2H)^{2+}$ 810.4142), Melittin (MH^+ 2845.7615, $(M+2H)^{2+}$ 1423.3839, $(M+3H)^{3+}$ 949.2576, $(M+4H)^{4+}$ 712.1942), Substance P (MH^+ 1347.7354, $(M+2H)^{2+}$ 674.3708) followed by direct infusion of the purified fractions at 10 μl/min. Electrospray needle potential was set to 3.8 kV with cone voltage of 30 V and extractor of 5 V. Precursor ion selection used an arbitrary waveform generator (±0.5 Da). IRMPD (50 W CO_2 laser, 40-60% laser power) was performed for MS/MS data on unknown components from the algal extract (*m/z* 622, 536, 598, 604). Elemental formulae were deduced using the MIDAS software.

Results and Discussion

A novel approach using a combination of mass spectrometric methods is described for the detailed study of the gas-phase dissociation reactions of 13-desmethyl spirolide C, with subsequent structural studies on other components in a phytoplankton extract. Separation of these components was achieved by high performance liquid chromatography. The results are divided into the following sections: an initial survey of the components in the analyzed extract; an in-depth look at the product ions resulting from collision-induced dissociation of 13-desmethyl spirolide C; a purification step by mass spectrometry-based fraction collection, yielding several fractions that were subsequently analyzed; and lastly, a collection of FT-ICR data for the accurate mass measurements of the precursor and product ions generated by IRMPD. The mechanisms of dissociation for the main component of the extract are discussed in detail, followed by comparison with other spirolide compounds.

LC/MS Analysis of Phytoplankton Extract

In these experiments, a methanolic extract of *Alexandrium ostenfeldii* cells was analyzed by LC/MS. The crude extract was initially subjected to a full scan analysis on an ion trap. The separation of spirolide components was performed within a ten minute HPLC run with good peak shape and resolution of isobaric and isomeric species. The high sensitivity full scan experiment afforded by this instrument allowed very minor components to be detected in the complex sample, since ion traps are inherently more sensitive than quadrupole mass analyzers [121]. Moreover, the differences in sensitivity between full-scan and selected-ion monitoring in an ion trap are much less pronounced than those in a quadrupole instrument. The reason for this lies in the fact that decreasing the acquisition range shortens only one part of the total microscan and, consequently, merely a slight reduction in scan time is seen (see Background).

Subsequently, SIM experiments on the crude extract were conducted on a QqQ instrument. Figure 2.2 represents a selected-ion chromatogram from QqQ analysis for the detected species from the IT experiment. An advantage is seen in the SIM scan mode of quadrupole versus ion trap instruments, since the duty cycle [=(ion detection time/total

scan time) x 100%] is close to 100%. Conversely, in an ion trap, the duty cycle is decreased since the total scan time has a significant contribution from the ion injection and isolation time [122].

Several peaks for the known spirolides were observed in the crude extract, including spirolides C and D, and their 13-desmethyl analogs. Also, two previously reported peaks [98] corresponding to spirolide isomers C3 and D3 were detected, as well as a minor unknown peak labelled 706.5(c) in Figure 2.2. Moreover, two peaks representing a new, slightly more polar compound with the same molecular weight as 13-desmethyl spirolide D (*m/z* 694.5) and another at *m/z* 708.5 with a similar increase in polarity from its isobaric counterpart were seen in the extract. Finally, several unexpected masses, ranging from *m/z* values 536 to 622, had significant signal intensities (Figure 2.2). Note that there are significant M+2 ^{13}C isotopic contributions for some of these compounds, seen at *m/z* 694.5 and *m/z* 708.5. For quantitation purposes, it was assumed that the response factor for all spirolides was constant. This was thought to be a valid assumption since these toxins have one predominantly basic site with a hydrophobic backbone, therefore small changes to the molecule should not affect the ionization efficiency significantly.

MS-triggered Fraction Collection

The purification of the crude extract allowed for the enrichment of some spirolides in different fractions and provided an opportunity to perform extensive MS/MS experiments on very minor compounds. Previously, MS/MS experiments on the crude extract resulted in significant product ion signal for only the major compounds present, namely 13-desmethyl spirolides C and D as well as spirolides C and C3. All other ions exhibited unsatisfactory CID spectra without prior purification. Figure 2.3 illustrates the collection of twelve fractions and the relative contributions of each species identified in the extract. The quantitation of each component used a standard curve of 13-desmethyl spirolide C with gymnodimine as an internal standard (IS). The IS showed important structural similarity with the spirolide toxins and was assumed to have a similar response factor with electrospray MS detection. A representative chromatogram of 13-desmethyl spirolide C and gymnodimine at equal amounts (5 ng/ml), as well as the structure of the

internal standard, are shown in Figure 2.4a. The calibration curve and relative response factors for the analyte and IS are represented in Figure 2.4b. This standard curve was used for the quantitation of all components identified in the extract.

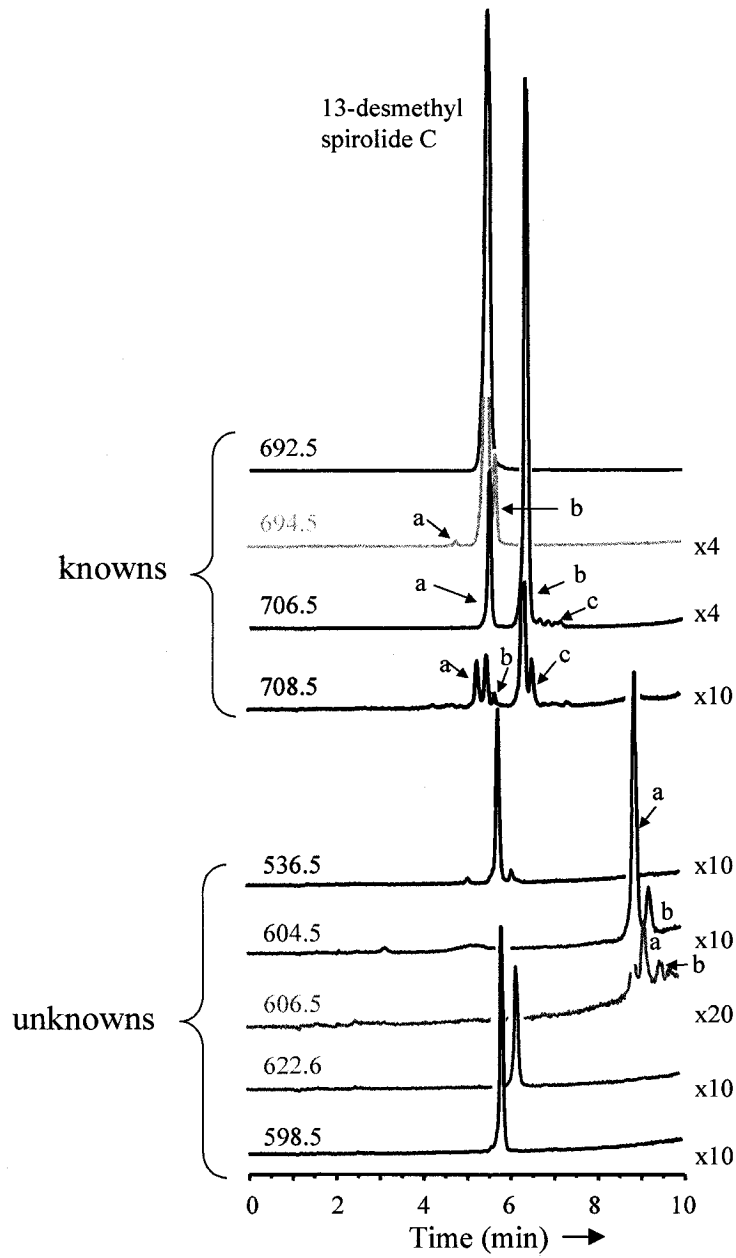

Figure 2.2 SIM traces of MH^+ ions of various known and unknown spirolide species in a crude *Alexandrium ostenfeldii* extract. Multiple peaks at the same *m/z* values are distinguished by lower case letters (a, b, c). Note that some peaks represent M+2 ^{13}C isotopic contributions and thus are not labelled.

This fractionation was invaluable especially for FT-ICR results, as will be described later, since no prior chromatography was performed in these experiments. Additionally, most of the 13-desmethyl spirolide C was collected and pre-concentrated in fraction 3, resulting in >96% purity. Hence, this sample is expected to be quite useful in subsequent studies, including metabolic profiling and as a standard for quantitation.

a

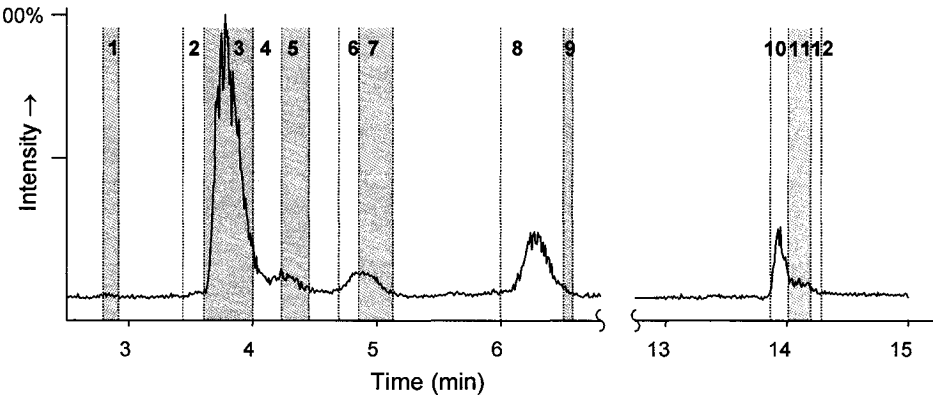

b

	% Composition												
MH+	Fraction 1	Fraction 2	Fraction 3	Fraction 4	Fraction 5	Fraction 6	Fraction 7	Fraction 8	Fraction 9	Fraction 10	Fraction 11	Fraction 12	Extract *
692.5	75	96.6	96.4	92.2	87.3	44.7	30.3	0.3	1.2	0.8	1.2	2.5	80.3 (207)
694.5 (a)	23.3	0.1		0.1	0.1								0.1 (0.32)
694.5 (b)			0.7	3.6	6.4	7.7	3.4						1.5 (4.0)
706.5 (a)	1.2	2.1	2.5	3.6	3.9	1.9	1	0.4	0.6				2.3 (5.9)
706.5 (b)					0.1	0.2	0.5	59.3	63.1	4.9	0.1	0.1	9.3 (24)
706.5 (c)						0.1	0.3	34.5	5.9	0.3			0.2(0.40)
708.5 (a)	0.5	1.1	0.4	0.4	0.1	0.2	0.2	0.1					1(2.6)
708.5 (b)				0.1	0.3	0.5	0.2						<0.1
708.5 (c)								0.2	26.2				0.2 (0.52)
536.5					0.3	18.3	30.6	0.2					1.3(3.3)
598.5					1.6	26.4	33.5	0.2					1.5 (4.0)
604.5 (a)										80.2	78.6	64.7	0.6 (1.5)
604.5 (b)										3.3	3.2	7.5	1.5 (3.8)
606.5 (a)										10.4	16.2	22.1	0.1 (0.35)
606.5 (b)											0.6	3.1	0.1 (0.25)
622.6								4.9	2.9	0.2			<0.1

* concentrations are shown in paratheses (μg/ml)

Figure 2.3 a) Representative full-scan chromatogram during LC-preparative mass-triggered fraction collection. b) Percent composition of each spirolide species in the fractions collected and in the phytoplankton extract.

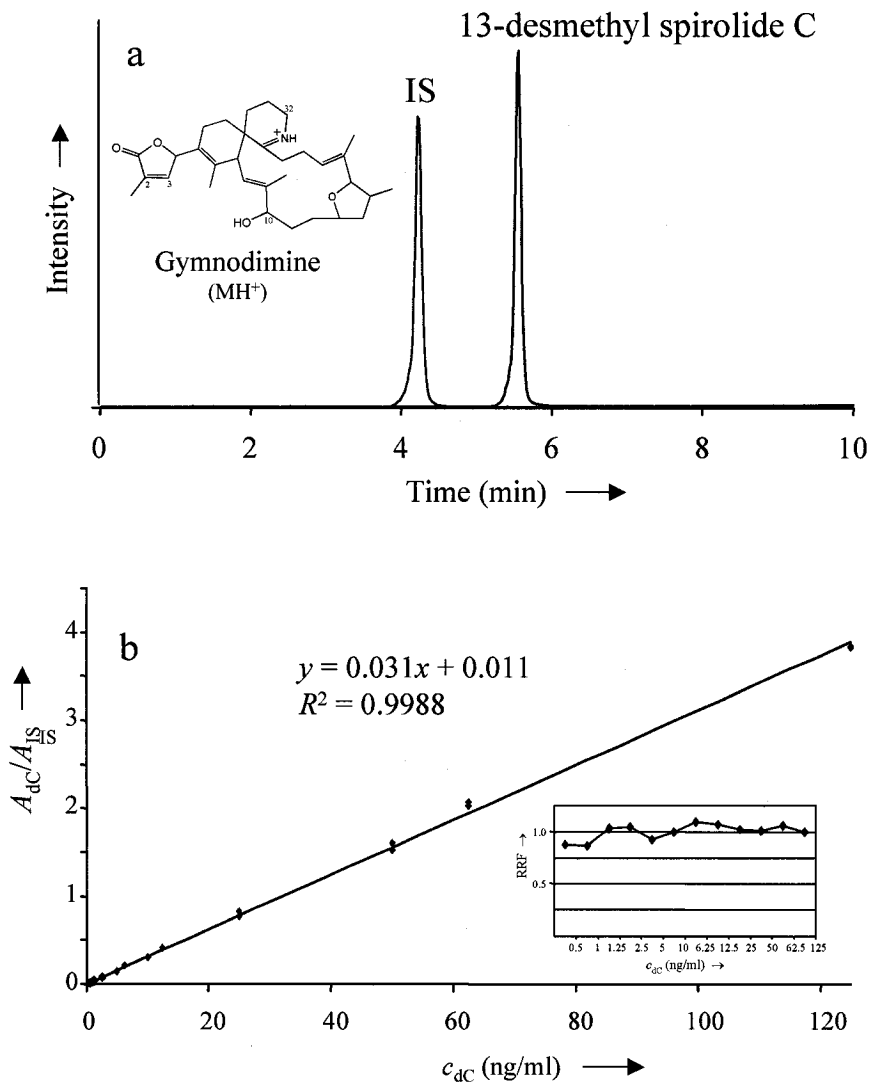

Figure 2.4 LC/MS quantitative analysis of spirolide fractions using gymnodimine as an internal standard. Chromatogram of 5 ng/ml each of 13-desmethyl C and gymnodimine (a) and calibration curve for 13-desmethyl C and relative response factor (RRF) for 13-desmethyl C and the IS (A_{dC}/A_{IS}=peak area ratio (analyte/internal standard), C_{dC}= concentration of 13-desmethyl C) (b).

Collision-induced dissociation

Tandem mass spectrometry was used for the identification of important product ions of the spirolide toxins. Collisional activation was optimized on the triple quadrupole instrument for the nearly complete fragmentation of protonated 13-desmethyl spirolide C (Figure 2.5). Multiple water losses, characteristic of several polyether compounds [123-126], are observed, as well as a cluster of ions in the region of *m/z* 444, also related by

several water losses. The base fragment, at *m/z* 164, is represented as a cyclic imine with stabilizing conjugation (Figure 2.6) and has previously been identified as a characteristic fragment for the C/D class of spirolides, with a methyl substituent at C(31) [100].

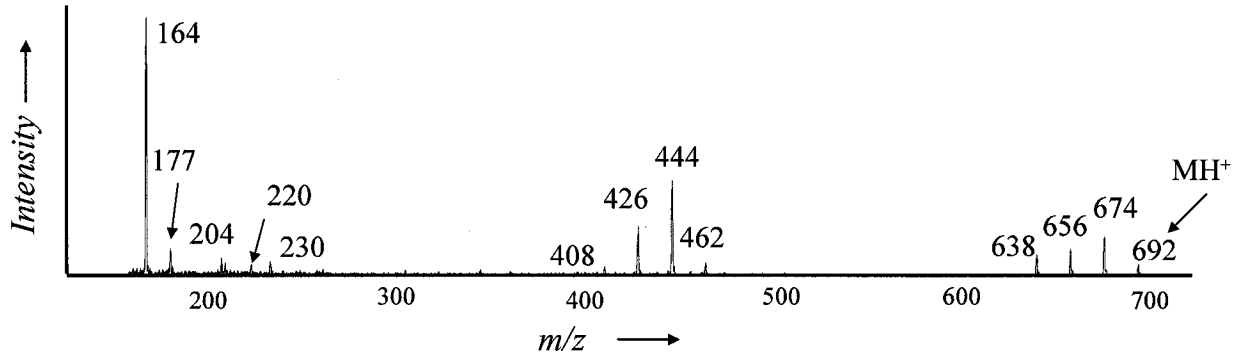

Figure 2.5 CID spectra of protonated 13-desmethyl spirolide C on the triple quadrupole instrument

A subsequent set of experiments was performed on a quadrupole-linear ion trap instrument to aid in the elucidation of fragmentation mechanisms. The protonated molecule was first activated in a quadrupole collision cell (q_2) prior to isolation of an important intermediate in order to deduce the pathways forming the low mass product ions. Conditions for activation in the collision cell (q_2) were optimized for *m/z* 444 signal intensity and this ion was then isolated in the trap and further fragmented to determine its secondary products. The ions at *m/z* 164, 177, 204, 206 and 230 were confirmed as being formed from this precursor ion, thus the mechanism for the formation of these products have *m/z* 444 as an intermediate in the proposed fragmentation scheme (Figure 2.6).

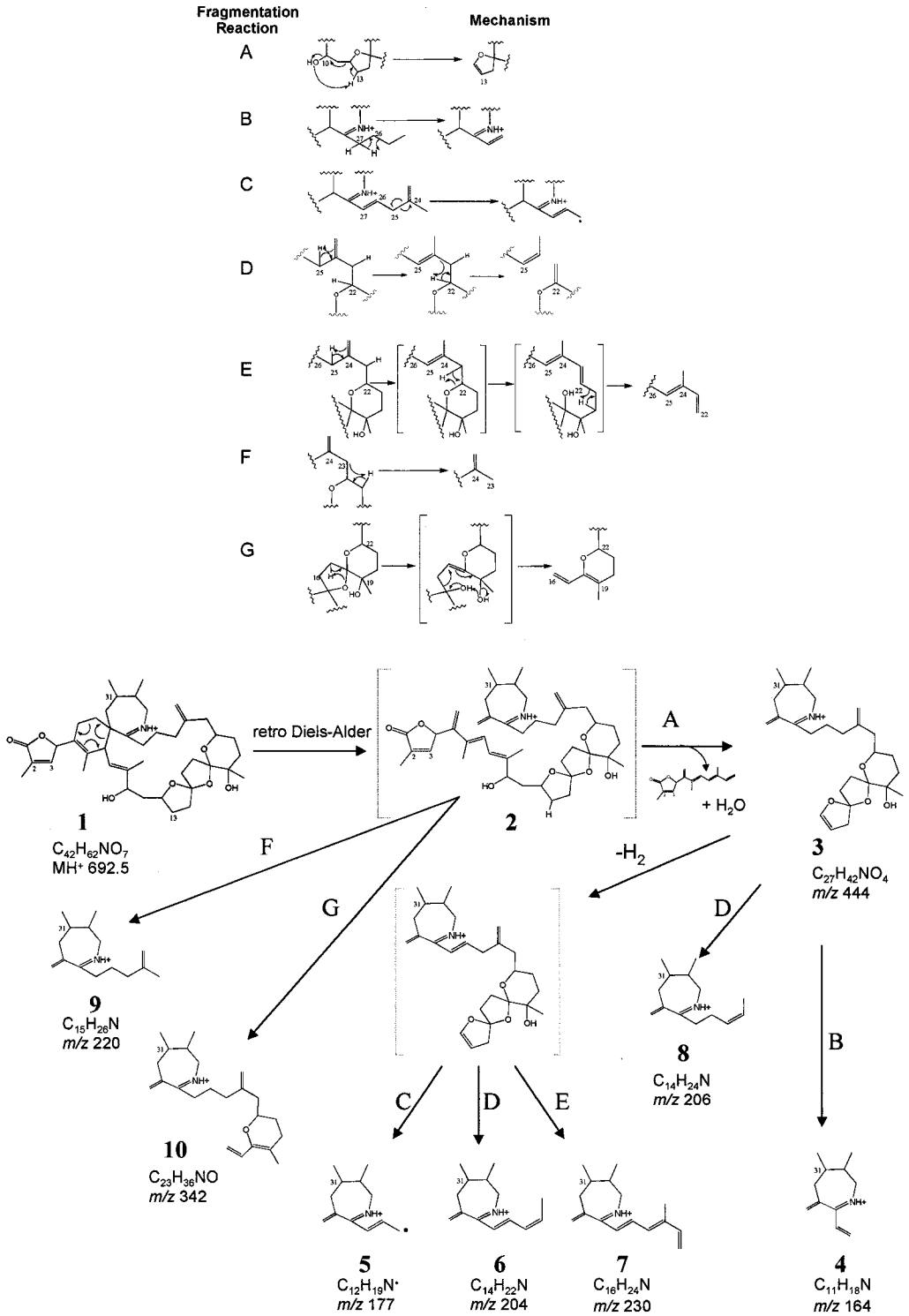

Figure 2.6 Proposed fragmentation scheme for 13-desmethyl spirolide C. Mechanistic details of each fragmentation are shown above. The overview of dissociation pathways (**A-G**) with final product ion structures (**1-10**).

All known and unknown compounds in the phytoplankton extract were analyzed by collision-induced dissociation in the triple quadrupole instrument. Figure 2.7 shows the comparison of CID spectra for MH^+ ions at *m/z* 694.5 and *m/z* 708.5. Similar conditions were used for each species, with the exception of a slightly lower collision energy (30 V) for *m/z* 536.5. This ion is apparently much less stable under CID conditions than the other components. Furthermore, the species at *m/z* 622.5 required a setting of 70 V for the formation of structurally diagnostic fragment ions. Excellent product ion spectra were produced for each of the detected species, afforded by the enrichment of certain compounds in the separate fractions. Thus, the mass-triggered fractionation was invaluable at removing interfering species for the MS characterization of several minor compounds present in the sample. For example, *m/z* 706.5 (c) is a very minor component of the crude extract, however, in fraction #8 (Figure 2.3), we see selective enrichment causing it to become the second most abundant species. The CID spectrum for this ion gives very similar product ions to the other two isomers present at this *m/z* value.

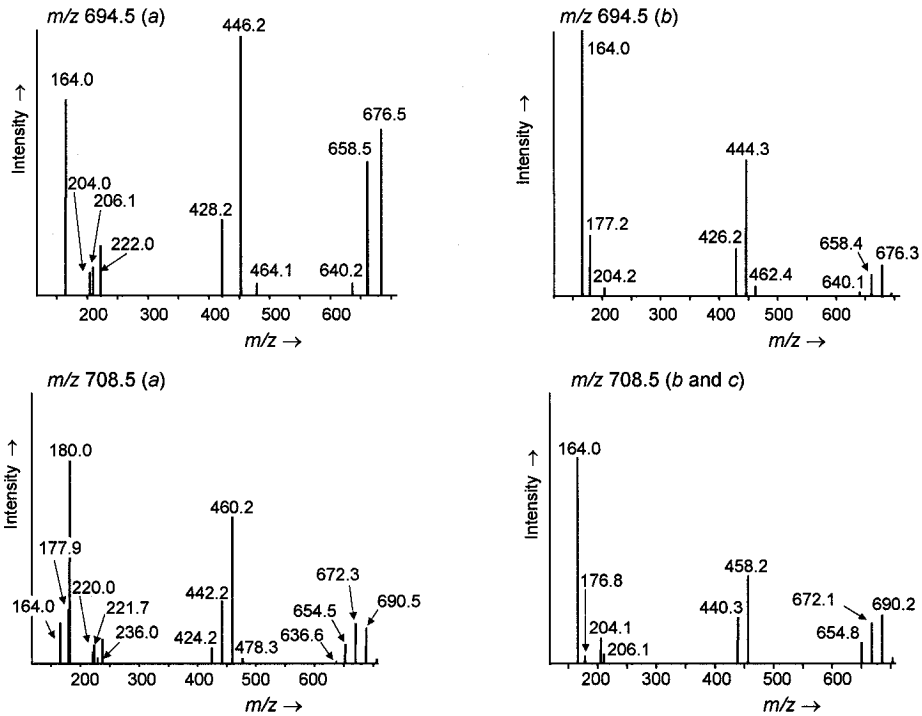

Figure 2.7 MS/MS spectra of various spirolide species in collected fractions (refer to Figure 2.2 for assignment of the species)

Interestingly, some dissociation pathways common to the known spirolides were detected for the unknown compounds, and as a consequence revealed their probable biogenetic link to this toxin family. For instance, similar water losses were observed for the collisional activation of these unknowns, as for the known spirolides. Also, *m/z* 598.5 exhibits important fragment ions in the CID spectra at *m/z* 164, 177 and 204 similar to all previously characterized spirolides present in this extract. Additionally, some common neutral losses were observed for the known and unknown compounds. For example, the product ion present in the CID spectra of both *m/z* 604.5 and 606.5 at *m/z* 356, most likely represents the same fragmentation pathway as for the formation of the *m/z* 444 ion from 13-desmethyl spirolides C (*m/z* 692.5) and D (*m/z* 694.5), respectively.

FT-ICR-MS

FT-ICR experiments provided accurate mass data, from which the elemental formulae of precursor and product ions were inferred. The MH^+ ion of 13-desmethyl spirolide C was determined to be *m/z* 692.45192, thus confirming the formula of $C_{42}H_{62}NO_7$ (MH^+, theoretical mass 692.45208) with an excellent accuracy of –0.2 ppm (Δm= 0.00016 amu). Figure 2.8 shows the MH^+ region in the FT-ICR spectrum revealing excellent peak shape with a resolving power of ~200,000.

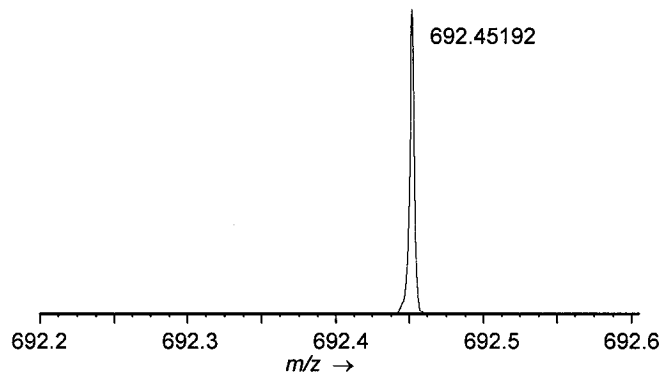

Figure 2.8 FT-ICR mass spectrum of the MH^+ region of 13-desmethyl spirolide C

IRMPD experiments were then performed for activation of the protonated molecule at *m/z* 692.5. Table 2.1 summarizes the accurate mass measurements and elemental formulae for those fragment ions also observed in the triple quadrupole instrument. Our experiments revealed that when the same product ions are formed in both CID and IRMPD, elemental formulae deduced from the FT-ICR data can help conclude which bonds are broken following ion activation. The formation of these products is explained in the proposed fragmentation scheme (Figure 2.6). The mechanisms for all the QqQ product ions, with the exception of *m/z* 462, are shown. This ion was expected to give an elemental formula of *m/z* 444 + H_2O to yield the first ion of the fragment cluster. However, IRMPD data revealed an ion at *m/z* 462.24679, resulting in an elemental formula of $C_{21}H_{32}N_7O_5$ (theoretical MH^+ *m/z* 462.245944, Δm=1.8 ppm). This corresponds to the Y_4-H_2O peptide fragment ion from the Glu-fibrinopeptide internal mass calibrant.

Table 2.1 Accurate mass IRMPD data of *m/z* 692.5 ion in crude extract

Measured Mass	Elemental Formula	Calculated Mass	Δ (ppm)	% Intensity	Resolving power
164.14335	$C_{11}H_{18}N$	164.143376	-0.2	100	89993
177.15117	$C_{12}H_{19}N^{\bullet}$	177.151201	-0.2	6	83385
204.17466	$C_{14}H_{22}N$	204.174676	-0.1	31	72348
206.19031	$C_{14}H_{24}N$	206.190326	-0.1	51	71641
220.20598	$C_{15}H_{26}N$	220.205976	0.0	5	67081
230.19034	$C_{16}H_{24}N$	230.190326	0.1	47	64171
342.27918	$C_{23}H_{36}NO$	342.279141	0.1	1	43157
408.28974	$C_{27}H_{38}NO_2$	408.289706	0.1	11	36180
426.30016	$C_{27}H_{40}NO_3$	426.300271	-0.3	12	34651
444.31078	$C_{27}H_{42}NO_4$	444.310835	-0.1	13	33247
638.42051	$C_{42}H_{56}NO_4$	638.420386	0.2	16	23138
656.43118	$C_{42}H_{58}NO_5$	656.43095	0.3	25	22715
674.44185	$C_{42}H_{60}NO_6$	674.441515	0.5	24	21902

Fortunately, chromatography was not necessary prior to MS detection of 13-desmethyl spirolide C in the present study. This clearly illustrates the ability of the FT-ICR to produce excellent results for analytes in complex matrices. Direct infusion of the crude extract was possible since there was only one species present at *m/z* 692.5. Isomeric

species would obviously be isolated together, and thus product ions of these compounds would interfere with each other. As a result, no distinction would be possible, in this case, unless prior chromatography or purification steps were completed. This scenario is observed with other spirolide species and initial fractionation of the extract was necessary to distinguish their IRMPD product ion spectra.

Fragmentation Pathways of 13-desmethyl Spirolide C

Several characteristic fragment ions for 13-desmethyl spirolide C were produced by collision-induced dissociation. The structure elucidation of new derivatives used the proposed fragmentation scheme, outlined in Figure 2.6, as a model for this toxin class. All collision-induced reactions in this molecule have been proposed as charge-remote fragmentations with the charge localized on the imine moiety [127, 128]. A structural requirement for these remote-site fragmentations is a stable site of charge localized in the molecule, and thus no significant intervention of the charge. With a stable ionized group, charge-mediated cleavages would not be possible and alternate cleavages involving other molecular orbitals (uncharged) predominate. It has been shown that charge-remote fragmentations have direct mechanistic analogies to thermal decompositions of neutrals [129, 130] and consequently, generate structurally informative ions, since bonds are cleaved via simple rearrangements and homolytic bond dissociations governed by classical thermolytic-like chemistry.

In Figure 2.6, a proposed fragmentation scheme is presented for the formation of collision-induced dissociation product ions of protonated 13-desmethyl spirolide C (**1**). Initially, the 6-membered monounsaturated ring undergoes an intramolecular retro-Diels-Alder (RDA) reaction. Since the diene and olefin parts of the protonated molecule are linked by more than two bonds, the RDA cleavage of the cyclohexene ring does not lead directly to fragmentation and an isomerized ion is formed instead. The latter may further decompose by a simple bond dissociation or rearrangement, but the overall fragmentation may be activated by the RDA cleavage [131]. The product ions produced all contain the dienophilic end of the molecule with the cyclic imine remaining intact. The predominant fragmentation pathway for this intermediate, **2**, is a 6-centered concerted loss of a water molecule and a highly conjugated neutral yielding the fragment **3** at *m/z* 444. This

mechanism is enthalpically favored, since the transition state geometry includes a stable 6-membered ring. The fate of this fragment is five-fold. There can be subsequent loss of one or two water molecules, leading to *m/z* 426 and 408, as often observed for polyether compounds [123-126]. It is important to mention that only two H_2O losses are seen from this intermediate as opposed to three H_2O-losses for the MH^+ ion, since there has been one water molecule lost in the fragmentation reaction. The base fragment, numbered **4** in Figure 2.6, contains a conjugated system and is formed by a four-centered reaction, common in charge-remote fragmentations [127, 128]. This reaction is shown in mechanism B. In the proposed scheme, an initial loss of a hydrogen molecule is followed by either a homolytic cleavage forming a stabilized radical ion **5**, or by the cleavage of C(23)-C(24) and C(21)-C(22) (mechanisms D and E) for **6** and **7**, respectively. Under the present conditions, the fragment at *m/z* 177, product **5**, is the only odd electron species seen in the CID spectra. Homolytic cleavages are normally enthalpically disfavoured with the exception of the case of conjugated products with the radical being allylic and thus distonic [129, 130]. The common theme for the reactions forming these second-generation fragments is a product stabilized by conjugation. The fragment **8** is formed by the same mechanism as the product ion **6**, without the preceding loss of H_2. Another pathway is the cleavage of the C(22)-C(23) bond generating **9** (mechanism F).

Additional product ions are predicted as direct products of the retro-Diels-Alder intermediate. Mechanism G (forming **10**) consists of two steps; initially the five-membered cyclic ether is opened through a four-centered reaction, followed by a similar reaction to mechanism A occuring with the concerted loss of a water molecule and a stabilized neutral.

There are significant similarities in the fragmentations patterns of 13-desmethyl spirolide C and the structurally related pinnatoxins [132]. They exhibit common fragments for their regions of identical molecular structure. These results could clearly be applicable to this class of toxins, as well as other related polyethers containing the cyclic imine moiety. Once these dissociation reactions have been extensively studied, it becomes easier to explain fragmentation pathways of related compounds. An important application is the elucidation of newly found compounds and unknown structures, such as metabolites or biological precursors.

Structural Elucidation of Unknown Spirolides

FT-ICR experiments using the crude *A. ostenfeldii* extract yielded accurate mass data for all MH^+ ions present in the sample as illustrated in Table 2.2. Subsequently, individual fractions were analyzed by infrared multiphoton dissociation to generate product ion spectra with accurate masses for the fragment ions. Tables 2.2a and 2.2b summarize all elemental formula deduced from FT-ICR experiments. The dissociation mechanisms of 13-desmethyl spirolide C were extensively studied using CID and IRMPD (see previous section). The product ions of previously characterized spirolides C & D gave expected IRMPD results for their molecular structures. Unfortunately, the species at *m/z* 694.5 could not be analyzed by IRMPD, since there was an interference by the M+2 isotopic contribution of the major component in the extract, 13-desmethyl spirolide C. 13-desmethyl spirolide D gave an accurate mass for the MH^+ ion of 694.46783, confirming its elemental formula of $C_{42}H_{64}NO_7$. The minor compound present in the extract at *m/z* 694.5 was found to have an elemental formula of $C_{41}H_{60}NO_8$ (MH^+ 694.43128, Δm=-0.1 ppm). Figure 2.9 illustrates the region of these protonated ions in the full scan FT-ICR spectrum. Another peak occurs at this *m/z*, consisting of the $^{13}C_2$ isotope of 13-desmethyl spirolide C. It is also consistent that the unknown component elutes earlier in the chromatogram, and thus is more polar than 13-desmethyl spirolide D. We were able to propose some important fragment ion structures from the CID spectrum of this unknown using the fragmentation scheme for 13-desmethyl spirolide C. The base peak in the CID spectra at *m/z* 164 demonstrates that the structure is unaltered on the imine portion of the molecule. A mass shift for the important product ion at *m/z* 444 for 13-desmethyl spirolide D to *m/z* 446 in this case allows the prediction that the methyl group on C(19) is absent in this new structure and a hydroxyl group is added on the molecule. Importantly, a spirolide species found in a Danish phytoplankton sample was previously characterized as 13,19-didesmethyl spirolide C [94], therefore the removal of this methyl group has been reported for this toxin class. This added hydroxyl group causes an additional fragmentation pathway forming the ion at *m/z* 206 by a 6-centered water loss reaction. Finally, a double bond is present on the lactone moiety as is common in most of the spirolides in this extract. Structures are proposed for some important fragment ions, leading to the characterization of this unknown, in Figure 2.10.

Table 2.2a The protonated molecules, elemental formulae and the fragment ion masses of the spirolide compounds at known *m/z* values (bold-faced values represent base peaks in CID spectra).

Spirolide	MH^+	structure	water losses	Fragments							
desmethyl-C	692.5 $C_{42}H_{62}NO_7$	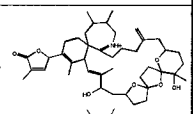	674*/656/638 $C_{42}H_{60}NO_6^+$	444*/426/408 $C_{27}H_{42}NO_4^+$	342 $C_{23}H_{36}NO$	230 $C_{16}H_{24}N$	220 $C_{15}H_{26}N$	206 $C_{14}H_{24}N$	204 $C_{14}H_{22}N$	177 $C_{12}H_{19}N\cdot$	**164** $C_{11}H_{18}N$
?	694.5 (a) $C_{41}H_{60}NO_8$	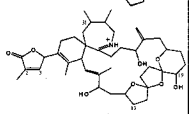	676/658 $C_{41}H_{58}NO_7^+$	446 $C_{26}H_{40}NO_5$		222 $C_{14}H_{24}NO$		206 $C_{14}H_{24}N$	204 $C_{14}H_{22}N$		**164** $C_{11}H_{18}N$
desmethyl-D	694.5 (b) $C_{42}H_{64}NO_7$	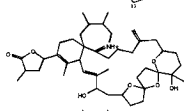	676/658/640 $C_{42}H_{62}NO_6^+$	444/426 $C_{27}H_{42}NO_4^+$		230 $C_{16}H_{24}N$			204 $C_{14}H_{22}N$	177 $C_{12}H_{19}N\cdot$	**164** $C_{11}H_{18}N$
C	706.5 (a) $C_{43}H_{64}NO_7$	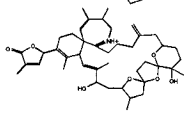	688*/670/652 $C_{43}H_{62}NO_6^+$	458*/440 $C_{28}H_{44}NO_4^+$					204 $C_{14}H_{22}N$	177 $C_{12}H_{19}N\cdot$	**164** $C_{11}H_{18}N$
C3[a]	706.5 (b) $C_{43}H_{64}NO_7$	unknown	688*/670/652 $C_{43}H_{62}NO_6^+$	458*/440/422 $C_{28}H_{44}NO_4^+$		230 $C_{16}H_{24}N$	220 $C_{15}H_{26}N$	206 $C_{14}H_{24}N$	204 $C_{14}H_{22}N$	177 $C_{12}H_{19}N\cdot$	**164** $C_{11}H_{18}N$
?	706.5 (c) $C_{43}H_{64}NO_7$	unknown	688/670	458/440/422			220	206	204	177	**164**
?	708.5 (a) $C_{42}H_{62}NO_8$	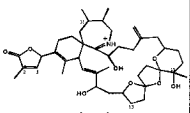	690*/672/654 $C_{42}H_{60}NO_7^+$	460*/442/424 $C_{27}H_{42}NO_5^+$	236	222 $C_{14}H_{24}NO$	220 $C_{14}H_{22}NO$		**180** $C_{11}H_{18}NO$	178 $C_{11}H_{16}NO$	164 $C_{11}H_{18}N$
D	708.5 (b) $C_{43}H_{66}NO_7$	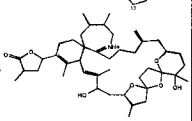	690*/672/654 $C_{43}H_{64}NO_6^+$	458/440		230 $C_{16}H_{24}N$		206	204 $C_{14}H_{22}N$	177	**164** $C_{11}H_{18}N$
D3[a]	708.5 (c) $C_{43}H_{66}NO_7$	unknown	690*/672/654 $C_{43}H_{64}NO_6^+$	458*/440 $C_{28}H_{44}NO_4^+$		230		206	204 $C_{14}H_{22}N$	177	**164** $C_{11}H_{18}N$

Note: Elemental formulae shown for product ions of *m/z* 694.5(a,b) are only proposed since no IRMPD data was obtained for these ions.

Table 2.2b The protonated molecules, elemental formulae and the fragment ion masses of the unknown spirolide-related compounds (bold-faced *m/z* values represent base peaks in CID spectra).

$[M+H]^+$	water losses	Fragments														
536.5 $C_{34}H_{50}NO_4$	518/500 $C_{34}H_{48}NO_3^{\bullet}$			260 $C_{17}H_{26}NO$					197				158	150	133	**122**
598.5 $C_{36}H_{56}NO_6$	580/562 $C_{36}H_{54}NO_5^{\bullet}$	348 $C_{21}H_{34}NO_3$	292 $C_{18}H_{30}NO_2$				204		197	177	**164** $C_{11}H_{18}N$		159	145		
604.5 (a) $C_{38}H_{54}NO_5$	586/568 $C_{38}H_{52}NO_4^{\bullet}$	**356**/338 $C_{23}H_{34}NO_2^{\bullet}$						218			176		159	148	135	
604.5 (b) $C_{38}H_{54}NO_5$	586/568	**356**						218			176		159	148	135	
606.5 (a) $C_{38}H_{56}NO_5$	588/570/552	**356**/328						218			176		157	148	135	
606.5 (b) $C_{38}H_{56}NO_5$		**356**						218			176		157	148	135	
622.6 $C_{39}H_{60}NO_5$	604 $C_{39}H_{58}NO_4$	402/384 $C_{25}H_{40}NO_3$	272 $C_{19}H_{30}N$	246 $C_{17}H_{28}N$	244 $C_{17}H_{26}N$	230 $C_{16}H_{24}N$	204 $C_{14}H_{22}N$		**191**		176		163	148	133	

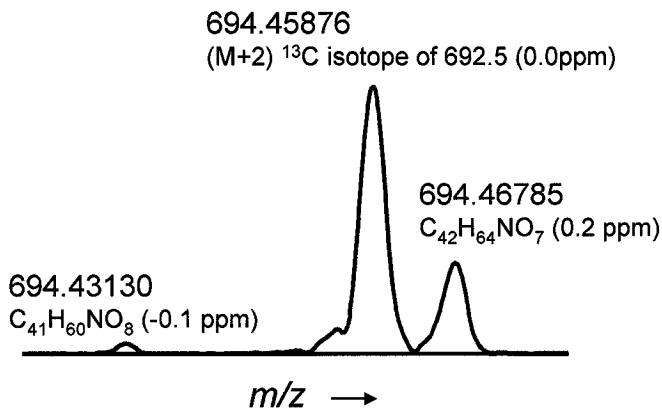

Figure 2.9 Enlarged 694.5^+ region of the FT-ICR-MS spectrum of the crude spirolide extract

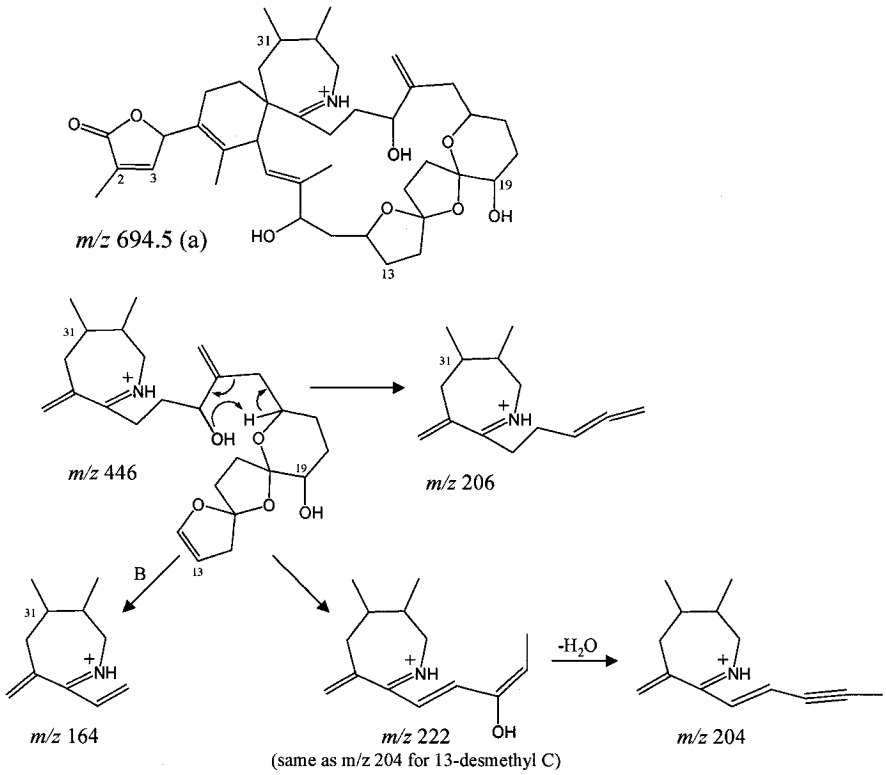

Figure 2.10 Proposed structures for important fragment ions and the MH^+ ion for component labelled 694.5(a)

Additionally, for the species labelled 706.5(a) and 706.5(b) in Figure 2.2, spirolides C and C3, respectively, it is apparent from the FT-ICR data for the MH^+ ions that these two compounds are isomers. The CID spectra of both are very similar, as is that of the unknown 706.5 (c) peak. Structure elucidation for these compounds would require NMR since the same CID ions are common to all of these species.

Another interesting observation was made for the three chromatographic peaks at *m/z* 708.5, other than those due to isotopic contributions from *m/z* 706.5 species. Note that three different species were detected at *m/z* 708.5 by FT-ICR-MS (Figure 2.11). The first of these species (t_r=5.0 min (Figure 2.2)) had not been examined previously. The accurate mass of this unknown yielded an elemental formula different from the latter two peaks. Again, we see an increase in polarity, consistent with the elemental formula of $C_{42}H_{62}NO_8$ (MH^+ 708.44707, 0.1 ppm). Figure 2.12 illustrates the proposed structure for this unknown compound. Structural elucidation was readily achieved here, since IRMPD experiments were possible for both peaks 1 and 3 (D3 isomer). Fractions 2 and 9 were

both analysed by IRMPD-MS and compared for accurate masses of product ions of 708.5 (a) and (c), respectively. The base peak (*m/z* 180) in the CID spectrum of 708.5 (a) was identified as $C_{11}H_{18}NO$, and its formation is explained by the same mechanism producing *m/z* 164 from 13-desmethyl spirolide C. Also, an important ion, analogous to the *m/z* 444 from the 13-desmethyl spirolide C product ion spectra, was detected at *m/z* 460 (Figure 2.12). It must, however, be kept in mind that absolute confirmation of these unknown compounds is difficult by mass spectrometry and the proposed structures shown here would benefit from NMR characterization if enough material was available.

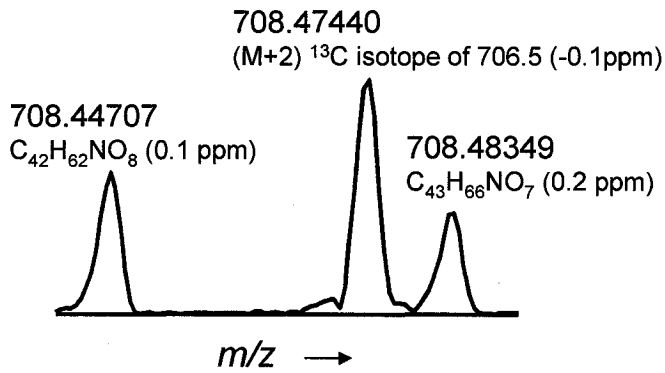

Figure 2.11 Enlarged 708.5^+ region of the FT-ICR-MS spectrum of the crude spirolide extract

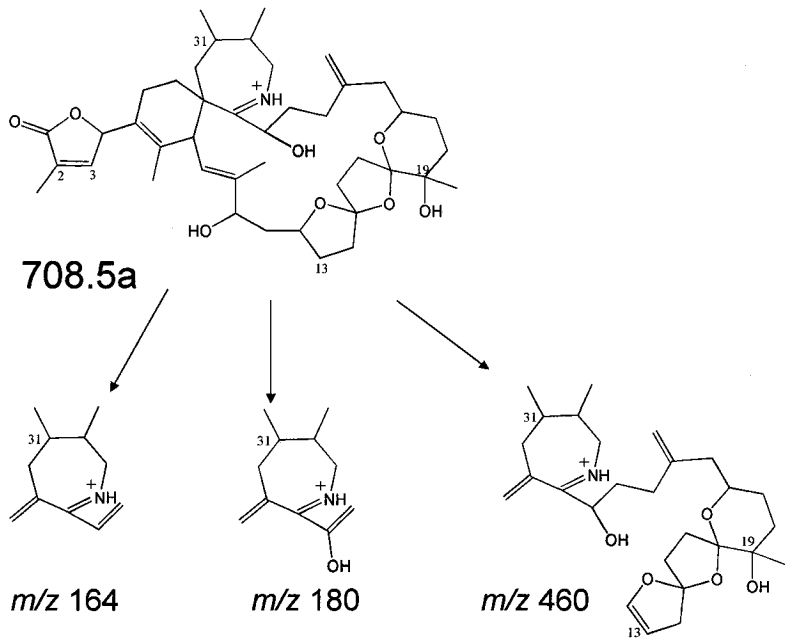

Figure 2.12 Proposed structures for important fragment ions and MH^+ for component labelled 708.5(a)

Other unknown compounds were detected in the analysis of the phytoplankton extract and their characterization by mass spectrometry provided evidence for their structural similarities to the previously identified spirolides. From MS/MS data of these unknowns, namely ions present at *m/z* 536, 598, 622, 604 and 606, several common fragmentation pathways were assumed between these species and the spirolide toxins. Accurate mass data from FT-ICR experiments gave elemental formulae for the protonated molecules of each of these unknowns, shown in Table 2.2b. Moreover, IRMPD data allowed elemental formulae for several of these fragment ions to be deduced and these are shown in Table 2.2b. We see that, for example, *m/z* 356 (product of *m/z* 604 and 606), represents $C_{23}H_{34}NO_2^+$, which corresponds to the same neutral loss for the formation of the ion at *m/z* 444 for 13-desmethyl spirolide C. Additionally, *m/z* 598 gave a strong product ion signal at *m/z* 164, which was confirmed to have the same elemental formula as the *m/z* 164 for the C/D class of the spirolides. Also, the unknown species at *m/z* 622 exhibits several similar product ions as seen with the spirolides (Table 2.2). These compounds therefore have some relationship to the spirolides, however, their molecular structures, their toxicity and biogenetic link to these toxins still remain unknown.

In vitro metabolism of spirolide toxins

Based on some earlier investigations into the metabolism of the spirolide toxins [101], it was found that an important detoxification route exists through the hydrolysis of the cyclic imine portion of the molecule (Figure 2.13). This reaction occurs in shellfish and under certain acidic conditions, however, it seems to take place only for classes A and B of the toxins. This suggests that the methyl group at C(31), present in the case of spirolides C and D, is involved in the increased toxicity of some of the spirolides. Spirolides E and F were found in shellfish isolations of these toxins and represent the hydrolysis products of spirolides A and B, respectively.

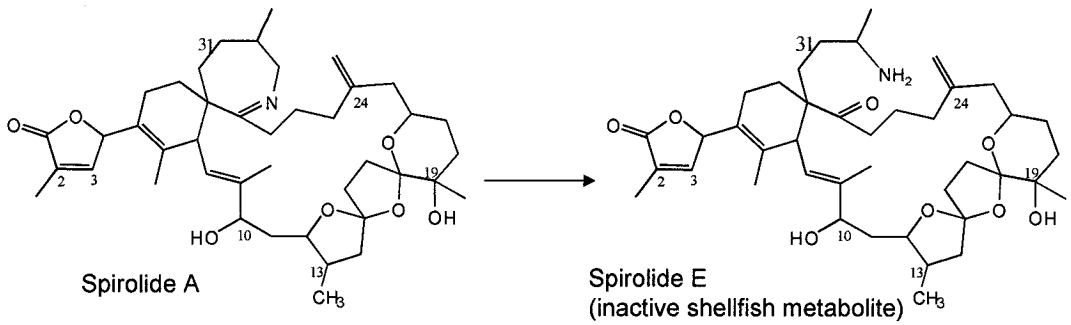

Figure 2.13 Detoxification of spirolide A through hydrolysis of the imine group, forming spirolide E. This reaction is also seen in the case of spirolide B, forming its hydrolysis product, spirolide F.

The metabolism of these toxins was further investigated here using the purified 13-desmethyl spirolide C from the fractionation of the crude extract in *in vitro* incubations of human and mouse liver microsomal preparations. Several metabolites were found for 13-desmethyl spirolide C, however no hydrolysis product was detected. Figure 2.14 shows the extracted ion chromatograms for the detected metabolites from human liver microsomal incubations. The most abundant ions in this metabolism study represent mono-hydroxylation products (*m/z* 708.5). Metabolites seen at *m/z* 706.5 are presumably formed via hydroxylation and dehydrogenation reactions. Mouse liver microsomes yielded a very similar metabolic profile for 13-desmethyl spirolide C. Also, all detected metabolites exhibited a base peak at *m/z* 164 in their MS/MS spectra. This is further evidence that none of the detected metabolites were altered in their cyclic imine portion of the molecule. This also most likely indicates that metabolism of this compound in humans does not cause detoxification, since the toxicophore is unaltered, and therefore human toxicity could be a problem. Ideally, if spirolide A or another analog without a methyl group at position 31, was available in a purified form, a comparison of the metabolic profiles of these two compounds could yield quite interesting results. Unfortunately, though, no such standard was available. Gymnodimine, the internal standard used in the quantitative analysis of the spirolides, has a similar structure to the spirolides. Some differences include a 6-membered cyclic imine instead of the 7-membered ring and no methyl group being present on the ring. This compound was

therefore tested to see whether a hydrolyzed product could be detected following human liver microsomal incubations. These experiments resulted in hydroxylated metabolites being detected and no hydrolysis product formed. This represents preliminary data and further work would be needed in order to fully understand the importance of the C(31) methyl group in both shellfish and human metabolism of the spirolide toxins.

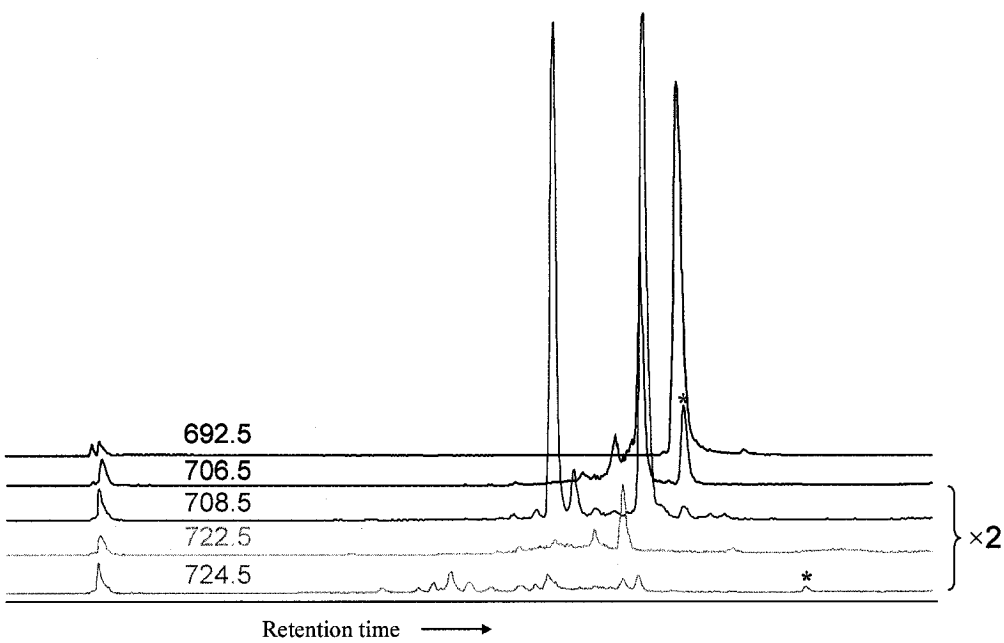

Figure 2.14 Extracted ion chromatograms for 13-desmethyl spirolide C and detected metabolites from human liver microsomal incubations. Peaks denoted with * were also in control samples (no NADPH). Peak at *m/z* 706.5 co-eluting with 13-desmethyl spirolide C was present in standard solution (97% Des-C) used in these incubations.

Conclusions

Dissociation reactions of 13-desmethyl spirolide C, the major component in a crude phytoplankton extract, have been extensively studied. Triple quadrupole MS/MS spectra provided a good overview of the main dissociation products. Quadrupole-linear ion trap data added information by confirming second generation fragment ions. Subsequent high-resolution FT-ICR experiments allowed accurate masses for MH^+ and product ions, formed via infrared multiphoton dissociation, to be determined. The main dissociation pathway represents a favorable retro-Diels-Alder reaction followed by the loss of a highly conjugated neutral and H_2O, and subsequent formation of a stable product ion with the cyclic imine remaining intact. Several other fragmentation pathways have also been highlighted. All of these mechanisms represent charge-remote fragmentations, commonly seen with molecules containing one fixed charge site [127, 128] and similar fragmentation patterns have been observed with the pinnatoxins [132]. The information gained from this detailed study of the mass spectrometric fragmentation behavior of 13-desmethyl spirolide C was used to further characterize unknown spirolides and related compounds present in the phytoplankton extract. The systematic study of the main component proved crucial for elucidating the structures or confirming structural features for the previously unidentified species.

The analysis of the phytoplankton extract by LC/MS allowed for the detection of several previously characterized spirolides as well as some new unexpected compounds. Purification of the crude extract into several fractions permitted the enrichment of different species, the analysis of which resulted in high quality CID spectra for all known and unknown spirolides. The product ion spectra for all of the identified components in the crude extract have been described, exhibiting common product ions and neutral losses between known and unknown structures. The consistency in the different spectra of the unknown components with the spirolides further substantiated their biogenetic link to the previously characterized toxins. Overall, several interesting observations have been detailed with the addition of accurate mass data using the crude extract and purified fractions. Importantly, this report represents the first FT-ICR data for any of the spirolide toxins. FT-ICR experiments were very useful for the confirmation of elemental formulae

of both known and unknown spirolides. The collection of advanced mass spectrometric techniques used in the investigation of spirolide toxins aided in the elucidation of fragmentation mechanisms of a known compound and was involved in the structural elucidation of unknown spirolides and related compounds.

Future Work

Additional mass spectrometric studies with the individual purified fractions of spirolides could shed further light on the structures of the unknowns present in the extract. One such study would be to conduct MS^n experiments in order to further characterize these species. If more material was available and extensive purification protocols were used in order to separate the components of the extract, NMR studies would allow us the fully characterize these unknowns.

Furthermore, the assumption that compounds with important structural similarities exhibit near equal response factors by ESI-MS should be studied. In our experiments, only one pure, quantified standard was available for the analysis of all spirolide analogs. These types of assumptions are generally seen for electrospray assays. This theory could be studied, however, if the compounds would be derivatized to exhibit fluorescent properties. Response factors in ESI-MS and fluorescence could then be compared, since each derivatized compound would have almost identical fluorescence response. A small subset of compounds could, in theory, be used as a model. For example, compounds with a common backbone with only slight structural changes, such as methyl or hydroxyl additions or displacements, could be employed. It would be important to investigate these assumptions, since at the present time, spirolide analogs and unknowns are defined as "major" and "minor" components based on their response factors by ESI-MS. These experiments, however, should make these quantitative statements more convincing. This study would also have general relevance for pharmaceutical laboratories, in the case of quantifying unknown metabolism products or in impurity profiling of drug formulations, as required by regulatory agencies. Another strategy for this type of study would be to use a "universal detector", where response factors are not affected by changes in molecular structure. For example, an evaporative

light scattering detector (ELSD) should give similar response factors for molecules of the same molecular weight. One such study is currently being conducted in our group to help better understand response factors in electrospray and ELSD assays.

As a result of the fractionation experiment, 13-desmethyl spirolide C was purified to >96% in one fraction. This fraction was used in some preliminary studies to investigate the metabolism of these toxins in different species. Ideally, if spirolide A or another analog which would not have a methyl group at position 31, was available in a purified form, a comparison of the metabolic profiles of these two compounds could be performed. It has been proposed that this methyl group is somehow responsible for the increased toxicity of some of the spirolides. When this group is removed, the spirolides undergo facile acid-catalyzed imine hydrolysis, which is also seen as a pathway in shellfish metabolism. Once the imine group is hydrolyzed, the keto-amine product does not exhibit any toxicity. A direct comparison of *in vitro* human and mouse metabolism of these two compounds could possibly help further understand this phenomenon. Also, the metabolic profiling of spirolide transformation products formed in these incubations could help discover some chemical regions susceptible to oxidative metabolism in these toxins.

CHAPTER III- Paralytic Shellfish Poisons

A. Gas-phase Dissociation Reactions of Protonated Saxitoxin and Neosaxitoxin[†]

Introduction

Paralytic shellfish poisons (PSPs) are a group of over 20 neurotoxins produced by several strains of marine dinoflagellates, mostly from the genus *Alexandrium* [133]. Shellfish grazing on these algae cause bioaccumulation of these toxins and the subsequent occurrence of PSPs in shellfish is of great concern, owing to the highly toxic properties that these compounds exhibit in humans [134]. Studies have shown that PSP toxins selectively block Na^+ channels on excitable membranes, thereby blocking the propagation of nerve and skeletal muscle action potentials [135-137] leading to characteristic neurological symptoms [138]. Nausea, vomiting and diarrhea are also sometimes observed [139]. Occasionally, respiratory paralyses occur with fatal consequences [140].

The chemical structures of PSPs are based on a tetrahydropurine skeleton to which a 5-membered ring is fused. They contain a unique hydrated ketone stabilized by two electron-withdrawing guanidinium moieties. Figure 3.1 illustrates the structures of two highly toxic carbamate PSPs, saxitoxin and neosatoxin. The wide variety of known PSP analogs originates from transformations at N(1) (hydroxyl addition [141]), C(11) (hydroxysulfate addition [142]) and N(21) (sulfonate addition [86]). The large number and the highly toxic nature of some of the PSP analogs require effective monitoring tools to detect their presence in contaminated seafood for consumer protection. Many countries have set maximum allowable concentrations for seafood samples; for instance, the European Union established a maximum amount of 80 μg per 100 g of edible flesh for molluscs [143].

The most widely used monitoring tool for PSP toxins is the mouse bioassay [144]. It is flawed, however, with respect to its narrow dynamic range and its inherent variability that can exceed ±20% [145]. There is also no structural differentiation possible with this assay and further confirmatory evidence is always needed. More importantly,

---

[†] Reprinted by permission of Elsevier from: Sleno L, Volmer DA, Kovacevic B, Maksic ZB. *J. Am. Soc. Mass Spectrom.* 2004; **15**: 462, by the American Society for Mass Spectrometry.

because of ethical considerations, animal-based methods are undesirable. Consequently, alternative methodologies based on physicochemical properties are preferred for the detection of PSPs.

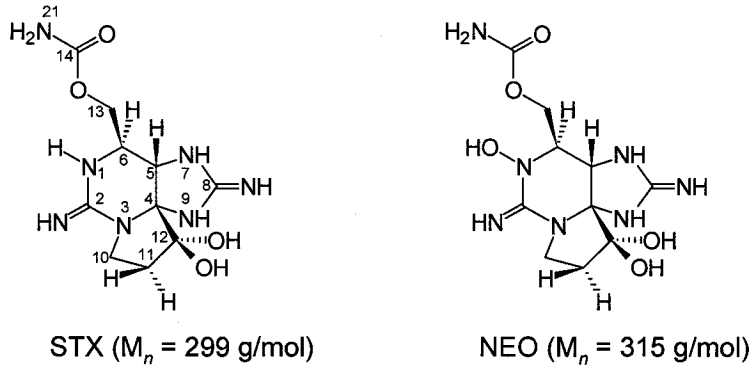

Figure 3.1 Chemical structures and nominal molecular weights of saxitoxin (STX) and 1-*N*-hydroxysaxitoxin (neosaxitoxin, NEO).

To date, the majority of instrumental analytical methods for monitoring PSP toxins have employed liquid chromatography (LC) or capillary electrophoresis (CE) with various detectors. It should be briefly mentioned that PSPs are not easily analyzed by regular reversed-phase chromatography because of the high polarity of these molecules. Approaches such as ion-pairing or hydrophilic interaction LC, however, have overcome many of the problems associated with PSP separations. Several reviews summarize many PSP chromatographic [133, 145-147] and CE [148] assays.

The disadvantage of all non-specific CE or LC techniques is that subsequent confirmation is needed to ensure that the method does not yield any false responses. While enzyme immunoassay methods have been reported as screening tools for PSPs [149], only mass spectral analysis with a sufficient number of structurally significant product ions can provide unequivocal proof of the compound's presence in a sample [150]. Depending on the compound's structure, diagnostic product ions can be generated by classical electron ionization mass spectrometry or, for soft ionization techniques, by tandem mass spectrometry.

Unfortunately, EI mass spectrometry cannot be implemented for PSPs because of their extremely high polarities. A number of authors, however, have reported mass spectrometric assays based on soft ionization techniques, such as fast-atom bombardment

(FAB) since the 1980s, with more sensitive and selective LC/MS methodologies dominating the field since the early 1990s. FAB studies have generated intact protonated molecules and adduct ions for saxitoxin (STX) with some fragmentation from the carbamoyl moiety [151]. White *et al.* [152] described mass spectra with intact protonated molecules for 12 PSP toxins using FAB. The authors were also able to generate a series of diagnostic fragment ions in the mass range *m/z* 200-270 using mass-analyzed ion kinetic energy scans (MIKES) from the MH^+ ions. An improved continuous flow FAB method for saxitoxin was also reported with a detection limit of 200 pg [153].

In recent years, electrospray ionization has been the technique of choice for mass spectrometric determinations of PSPs [145-147, 154-157], although a recent paper demonstrated successful analysis of PSP analogs via sonic spray ionization (SSI) [158]. Furthermore, Andrinolo and coworkers [159] showed APCI analysis of STX at low cone voltages with some fragment ions visible in the spectrum. Wils and Hulst [160] made an interesting observation during thermospray LC/MS of STX. Using buffer ionization, the authors were able to generate MH^+ ions only when spraying acidic solutions (pH = 2) with additional abundant fragment ions present. No intact MH^+ ions were observed from regular ammonium acetate buffered solutions. Unfortunately, the reported APCI fragment ions [159] and the thermospray fragment ions [160] do not seem to match to any significant degree, and thus did not allow identification of potential thermal degradations during the ionization of PSPs.

The pioneering PSP research in the area of electrospray ionization analysis has been conducted in the groups of Thibault [157, 161-163] and Quilliam [145-147, 154, 164]. In their studies, the authors used CE and LC separations prior to pneumatically-assisted ESI. Detection limits as low as 30 pg were obtained for positive ions of several saxitoxin analogs [164]. Since then, many other groups have established LC/ESI assays for PSPs with equally good sensitivities, mainly utilizing single or triple quadrupole mass spectrometers, although some authors have successfully established ESI methods on ion trap [165], time-of-flight [166] and quadrupole-time-of-flight instruments [155].

Unfortunately, only a very limited number of tandem mass spectrometry analyses of PSP toxins have been described previously. No detailed information on the dissociation pathways of protonated PSP molecules in the gas-phase appears to be

available in the literature. A few authors have reported neutral loss and ring cleavage reactions from the protonated toxin molecules. For example, Pleasance and coworkers [161] not only obtained product ions from the carbamoyl side chain for STX and NEO after electrospray ionization and collision-induced dissociation of the MH^+ ions in a triple quadrupole instrument but also several product ions from the cyclic portions of the molecules. The authors presumed that these additional ions were due to cleavage reactions at various charge sites in the molecules, the mechanisms of which were not described. Buzy and coworkers [162] used electrospray MS/MS on a triple quadrupole instrument and described abundant dissociations during CID analysis from protonated decarbamoyl-saxitoxin (dcSTX), decarbamoyl-neosaxitoxin (dcNEO) and several other PSP analogs. A few ion trap tandem mass spectra were shown by Reyero *et al.* [166] for dcSTX and NEO but only one non-specific H_2O loss was observed in their analyses. Andrinolo *et al.* [159] reported an unexpected in-source CID spectrum for STX at high cone voltages. The authors interpreted the solitary product ion at *m/z* 74 as a protonated guanidine fragment of STX.

The goal of this study was to investigate the behavior of PSPs after collisional activation in the gas-phase, with a detailed mechanistic look at the dissociation of the protonated molecules and the identification of fragmentation pathways. A variety of MS/MS techniques were used throughout the study including collisional activation in triple quadrupole and ion trap instruments, as well as Fourier transform-ion cyclotron resonance infrared multiphoton dissociation. These small molecules exhibit a surprisingly large variety of competing low energy dissociation pathways. The resulting product ion mass spectra exhibit an unusually rich variety of different ion species. The insight gained from this investigation is expected to be extremely valuable in the characterization of other PSP analogs as well as in the identification of yet unknown toxins. In the present work, two different PSPs were chosen as representative test compounds, saxitoxin (MH^+ at *m/z* 300) and neosaxitoxin (MH^+ at *m/z* 316). These two molecules only differ in their substituent at N(1), with STX carrying hydrogen and NEO having a hydroxyl group at this position (Figure 3.1). As will be discussed, the subtle substitution difference causes several significant variations in the appearance of the product ion spectra of the protonated molecules.

Experimental

Chemicals

Reference standard solutions of saxitoxin (65 μmol/l in 0.003 *M* HCl) and neosaxitoxin (65 μmol/l in 0.003 *M* HCl) were obtained through IMB's Certified Reference Materials Program (Halifax, NS, Canada) and were diluted 40-fold in 50:50 (v/v) methanol/water (+ 0.1% formic acid) prior to infusion into the mass spectrometers. Formic acid, N_{α}-acetyl-Arg, Lys-Leu, Phe-Gly-Gly-Phe and [Glu^1]-Fribrinopeptide were purchased from Sigma-Aldrich. Methanol and Milli-Q organic free water were used as solvents.

Triple Quadrupole and Ion trap Mass Spectrometry

Electrospray MS/MS and MS^n data were acquired on MDS Sciex (Concord, ON, Canada) API 4000 triple quadrupole and Agilent (San José, CA, USA) 1100 LC/MSD SL ion trap (IT) mass spectrometers in the positive ion mode. The sample solutions were introduced into the mass spectrometers via a Harvard (Holliston, MA) syringe pump at 5 μl/min. The API 4000's orthogonal Turbo-V source was operated at a spray voltage of 5 kV and a declustering potential of 60 V. The heat injectors were set to 450 °C. N_2 was used as the collision gas (CAD gas setting at 6) at a collision-offset voltage of 35 V. In MS/MS mode, Q1 and Q3 were set to unit resolution. The ion trap instrument was operated at the following settings: capillary voltage, -4.5 kV; nebulizer, 45 psi; dry gas, 7 l/min; dry temperature, 325 °C; trap target, 50,000; max. scan time, 5 msec. The fragmentation voltage was set to between 1–5 V; it was also ramped during the CID experiments from 50 to 150% (SmartFrag). An isolation width of 2 u was used in all MS^n experiments.

FT-ICR-MS

Accurate mass measurements were performed at the National High Magnetic Field Laboratory (Tallahassee, FL, USA) with a home-built 9.4 Tesla FT-ICR instrument [167]. Sample and calibration solutions were introduced at 400 nl/min from separate sprayers of a dual ESI source. Ions were transferred through a Chait-style atmosphere-to-

vacuum interface [168] and accumulated within a linear octopole, modified for improved ion ejection along the z-axis [169]. Mass-selected calibration and sample ions were individually accumulated for 5 and 1 sec, respectively. All ions were then transferred through an octopole ion guide to the ICR cell. Hanning apodization and one zero-fill were applied to all data prior to the fast Fourier transform and magnitude calculation [114]. Frequency spectra were calibrated internally [115, 116] from the measured ICR frequencies of the calibration mixture ions at *m/z* 217.12952 (N_α-acetyl-Arg), *m/z* 260.19687 (Lys-Leu) and *m/z* 427.19760 (Phe-Gly-Gly-Phe). The spectrum was the sum of 50 time-domain transients (2 Mb data). In infrared multiphoton dissociation experiments, product ion data were internally calibrated by tailoring the stored-waveform inverse Fourier transform (SWIFT) [117, 118] waveform to isolate precursor (STX, *m/z* 300; NEO, *m/z* 316) and Glu-Fib $[M+2H]^{2+}$ (*m/z* 785.8) ions, followed by irradiation with a 40 W CO_2 (10.6 μm wavelength) laser (Synrad E48-2-115, Bothell, WA, USA) for 150 ms at 90% laser power. Glu-Fib product ions at *m/z* 175.11893 (y_1), 246.15607 (y_2), and 333.18807 (y_3) were used for internal calibration. The generated product ions were then subjected to chirp excitation and direct-mode broadband detection. Spectra represent the sum of 50 scans (2 Mb data). For elemental formula assignments of product ions in IRMPD, the atom constraints for C, H, N and O were set to the respective number of atoms in the precursor ion molecules ($C_{10}H_{18}N_7O_4$ for STX and $C_{10}H_{18}N_7O_5$ for NEO, respectively).

Computational Calculations of Absolute Proton Affinities

Computational studies were conducted by collaborators (B. Kovačević and Z.B. Maksić) from the Quantum Chemistry group at the Rudjer Bošković Institute in Zagreb, Croatia. The theoretical framework [170-172] for calculating the absolute proton affinity (APA) in the gas-phase is given by:

$$APA(B_\alpha) = (\Delta E_{el})_\alpha + (\Delta E_{vib})_\alpha + (5/2)RT \quad (3.1)$$

$$(\Delta E_{el})_\alpha = E(B) - E(B_\alpha H)^+ \quad (3.2)$$

$$(\Delta E_{vib})_\alpha = E_{vib}(B) - E_{vib}(B_\alpha H)^+ \quad (3.3)$$

The base and its conjugate acid are denoted by B and BH^+, respectively, whereas α indicates the site of proton attack. Equations (3.2) and (3.3) describe the electronic $(\Delta E_{el})_\alpha$ and vibrational $(\Delta E_{vib})_\alpha$ energy contributions to the proton affinity, respectively. The former includes the nuclear repulsion term. The latter (E_{vib}) involves the zero point vibrational energy at 0K and the temperature correction to 298K. The (5/2)RT contribution recovers the translational energy of the proton and the $\Delta(PV)$ term. The search of the Born-Oppenheimer energy hypersurfaces was performed with an efficient DFT (density functional theory) - B3LYP computational scheme [173] employing the 6-31G* basis set. The minima on the hypersurface, which correspond to equilibrium spatial structures, were verified by vibrational analyses at the same level. The resulting geometries were used in the final single point calculations utilizing the 6-311+G** basis set, which is flexible enough to describe the nitrogen lone pair [174]. The full notation for the applied theoretical method is B3LYP/6-311+G**//B3LYP/6-31G* + E_{vib}(B3LYP/6-31G*), which will be abbreviated as B3LYP. All computations were carried out using the GAUSSIAN 98 program package [175].

Results and Discussion

This study describes the dissociation behavior of electrosprayed PSP toxins in the gas-phase, after ion activation of the protonated molecules (MH^+). From a mass spectrometric standpoint, PSP analogs are very intriguing as they contain a large number of different functional groups within a rather small skeletal structure. They also exhibit multiple charge sites [176, 177] owing to the two guanidinium groups per molecule, and the possibility for extensive resonance stabilization of fragment ions after dissociation, thus making a wide variety of competing low energy dissociation pathways possible. As will be shown, the resulting product ion mass spectra of PSPs exhibit an unusually rich variety and abundance of different ion species.

Saxitoxin (STX) and 1-*N*-hydroxy-saxitoxin (Neosaxitoxin, NEO) (Figure 3.1) were chosen as representative PSP model compounds because of their uncommon solution-phase basicity variations among the guanidinium moieties (the indices L and R are used in the following text to distinguish between the left-hand [pyrimidine ring] and the right-hand [imidazoline ring] moiety). Both compounds are virtually identical in their skeletal structure including the fused 5-ring at N(3)/C(4) and the carbamoyl group at C(6) (Scheme 1). According to studies on the aqueous dissociation constants (pK_a), the subtle substitution difference at N(1) of the pyrimidine guanidinium group, however, results in a significant change of pK_a. While the guanidinium group in the imidazoline ring of NEO was reported to have a pK_a value similar to that of STX (pK_a(R) = 8.24 *vs.* 8.65 [86, 175]), the additional –OH group of NEO at N(1) seems to significantly diminish the basicity of the imino nitrogen at C(2) of the pyrimidine moiety in aqueous solutions. This can clearly be seen from a sharp drop in the pK_a(L) values from 11.28 for STX to 6.75 for NEO [175, 176]. Shimizu [86] pointed out that pK_a values for the imidazoline guanidinium groups of PSPs are significantly lower than usually observed for guanidinium compounds. Presumably this is a result of insufficient participation of N(7) in the guanidinium resonance, caused most likely by stereochemical strain of the 5-ring. It was of interest to see if similar basicity differences could be observed in the gas-phase, as well as if and how they may affect the dissociation behavior of the protonated

molecules with respect to the site of charge retention and the availability of competing low energy dissociation pathways.

The main features of the CID spectra of STX and NEO in a triple quadrupole (QqQ) instrument are summarized along with a subsequent comprehensive mapping of the precursor ion/product ion relationships by ion trap (IT) MS^n analysis, to give proposed dissociation schemes. Subsequently, elemental formulae assignments were made to the tentatively identified ion structures from accurate mass measurements obtained by IRMPD FT-ICR mass spectrometry. A detailed discussion of the proton affinities of the PSPs and an in-depth description of the dissociation pathways and mechanisms are presented herein.

Collisional Activation of Protonated PSPs

Collisional activation of the protonated molecules was initially performed in a triple quadrupole instrument. The product ion spectra of saxitoxin and neosaxitoxin after collisional activation of the MH^+ ions are shown in Figure 3.2(a,b). As can be clearly observed, the two compounds exhibited an unusually large number of different product ions of significant abundance in the entire mass range investigated. When comparing the STX and NEO product ion spectra (Fig. 3.2(a,b)), similarities between product ions of the two compounds can be readily noticed, indicating parallel dissociation mechanisms. A closer inspection, however, revealed several ion species formed by STX and NEO that were not the result of a simple 16 u mass shift due to the additional hydroxyl group of NEO at N-1. The fragmentation pathways and the mechanistic details are described later in the chapter.

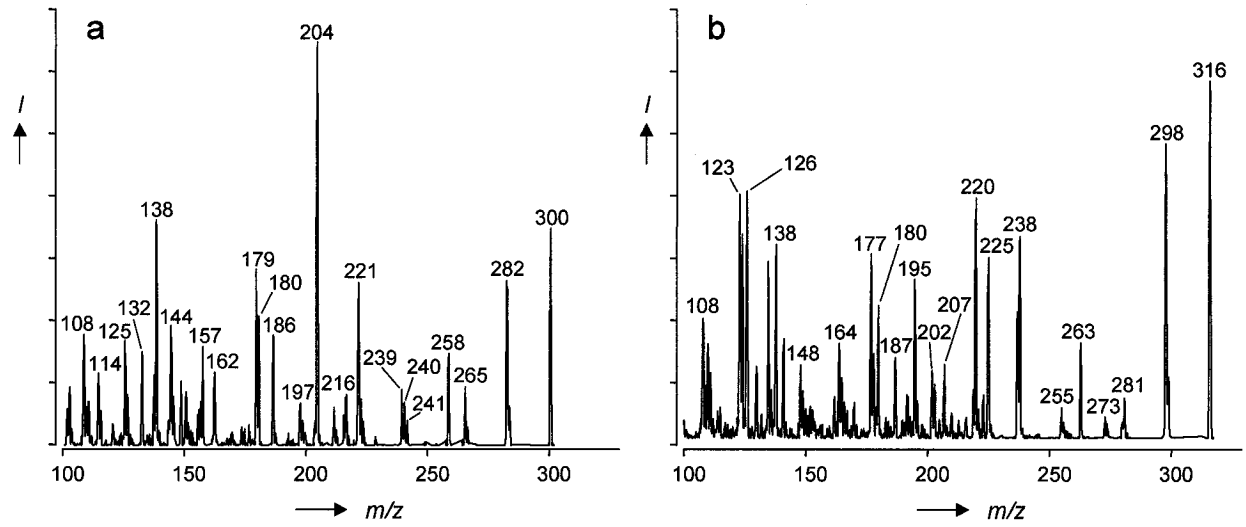

Figure 3.2 Triple quadrupole CID spectra of STX (a) and NEO (b) after collisional activation of the MH^+ ions (*m/z* 300 and 316, respectively)

This study only focused on the mass range between *m/z* 137 and *m/z* 300/316 (MH^+, STX/NEO), because of the large number of abundant product ions in this region. Nonetheless, the chosen *m/z* range covers up to six generations of consecutive reaction species. The elucidation of dissociation pathways is difficult based on the QqQ data alone, as there is limited information on genealogical dissociation links. Consecutive dissociation reactions likely occur in the rich QqQ CID spectra of STX and NEO because extensive resonance stabilization of the STX and NEO product ions is possible. An additional complication in assigning unambiguous product ion structures and fragmentation pathways arose from the two possible protonation sites that both STX and NEO exhibit. While the solution-phase basicities (pK_a's) could be used to assign the most basic site for proton attachment (and thus a starting precursor ion structure for the elucidation of the fragmentation mechanisms), a computational calculation of the gas-phase proton affinities for STX and NEO was chosen to investigate potential differences between solution and gas-phase behavior.

Genealogical maps of the linked precursor ion/product ion relationships were constructed from comprehensive ion trap (IT) MS^n mapping experiments for many of the ion species observed in the QqQ CID experiments. As demonstrated by Strife *et al.* [112], ion trap MS^n data can be added to QqQ CID spectra to give linked information for the CID ions. An illustrative example for the type of information gained through these

analyses is seen in Figure 3.3. Here, direct products from a third generation fragment ion (*m/z* 265) are represented in a MS^4 spectrum. A collection of ion trap data is shown in the resulting maps summarized in Tables 3.1 and 3.2 for many of the ions from Figure 3.2(a,b). By combining the CID data from QqQ and IT experiments, tentative linked dissociation schemes were generated for STX and NEO, as illustrated in Figures 3.4 and 3.5. Most of the observed consecutive fragmentation reactions can be rationalized through multiple neutral losses of H_2O, NH_3, CO, CO_2, CH_2O and different isocyanate, ketenimine and diimine species. Prior to explaining the exact dissociation mechanisms, it was necessary to confirm the identity of the product ions by accurate mass measurements.

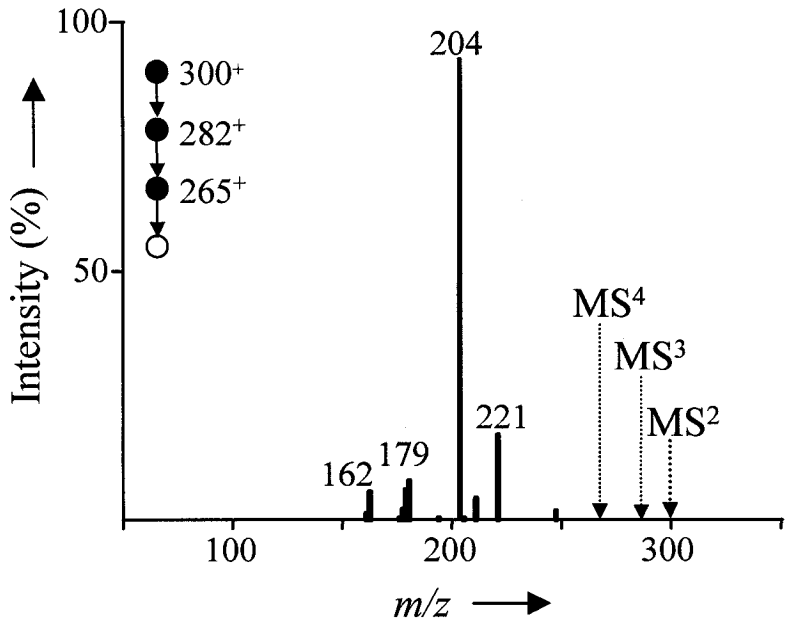

Figure 3.3 Ion trap product ion spectrum (MS^4) of the 3rd generation precursor ion at *m/z* 265, from the MH^+ ion of STX (*m/z* 300).

Table 3.1 The relationships between several *n*th order precursor and product ions of STX (MH^+, *m/z* 300) from ion trap MS^n experiments.[a]

$$MH^+ \xrightarrow{MS^2} P_1^+ + N_1 \xrightarrow{MS^3} P_2^+ + N_2 \xrightarrow{MS^4} P_3^+ + N_3$$

MS^n where n=	2	3	3	4	3	4	3	3	3	4	3	4	4	QqQ (35V)
MH^+	300	300	300	300	300	300	300	300	300	300	300	300	300	300
P_1^+		282	266	282	258	258	240	239	221	282	204	282	258	
P_2^+				265		241				221		204	198	
Products	283													
	282													282
	266													
		265												265
		264												
														258
					241									
		240			240									
	239				239									239
								223						
							222	222						222
	221	**221**		221			221	221						221
	216													216
					215									
			205											
	204	**204**	204	**204**				204	**204**	**204**				**204**
		203		203										
					198	198	198							
					197		197	197						197
											194	194		
												187		
	186				186							186		186
		180			180	**180**	180	180						180
	179	179		179			**179**	**179**	179	179			**179**	179
			177											
			163											
		162		162			162			162	162	162		162
		161									161	161		
	157													157
						155								
							153			153				
			150	150			150				150	**150**		150
				148							**148**	**148**		148
		145												145
	144				**144**									144
		138					138							138
				137	137	137	137						137	137
	132													132
					126									126
							125							125
							114			114				114
													109	
														108

[a]Only ions with >10% relative abundance are listed. Ions highlighted in bold-face exhibited relative abundances >95%.

Table 3.2 The relationships between several *n*th order precursor and product ions of NEO (MH^+, *m/z* 316) from ion trap MS^n experiments.[a]

$$MH^+ \xrightarrow{MS^2} P_1^+ + N_1 \xrightarrow{MS^3} P_2^+ + N_2 \xrightarrow{MS^4} P_3^+ + N_3$$

MS^n where n=	2	3	4	4	3	3	4	3	4	QqQ (35V)
MH^+	316	316	316	316	316	316	316	316	316	316
P_1^+		298	298	298	263	238	298	220	298	
P_2^+			281	263			237		220	
Products	**298**									**298**
		281								
		263	263							263
										238
	237	**237**								237
										225
						223				223
	220	**220**		**220**	**220**	**220**	**220**			**220**
						219	219			219
						210				
						209				
			207	207		207				207
							205		205	
		203	203					203	**203**	203
			202							202
										196
						195	195			195
								192	192	192
	187									187
		180								180
			179							
		178				178	**178**	178	178	178
	177	**177**				177	177		177	177
						170				170
							167			
		166				166	166	166		166
			165			165				165
		164	164					**164**	**164**	164
		162					162			162
			154							
		153					153			153
		152								152
			151							151
			150			150				150
										149
										148
							141			141
	138	138								**138**
			136							136
		135	135				135			135
							130			130
										126
						124	124			124
						123	123		123	123
			122							
							114			
										111
										110
										108

[a]Only ions with >10% relative abundance are listed. Ions highlighted in bold-face exhibited relative abundances >95%.

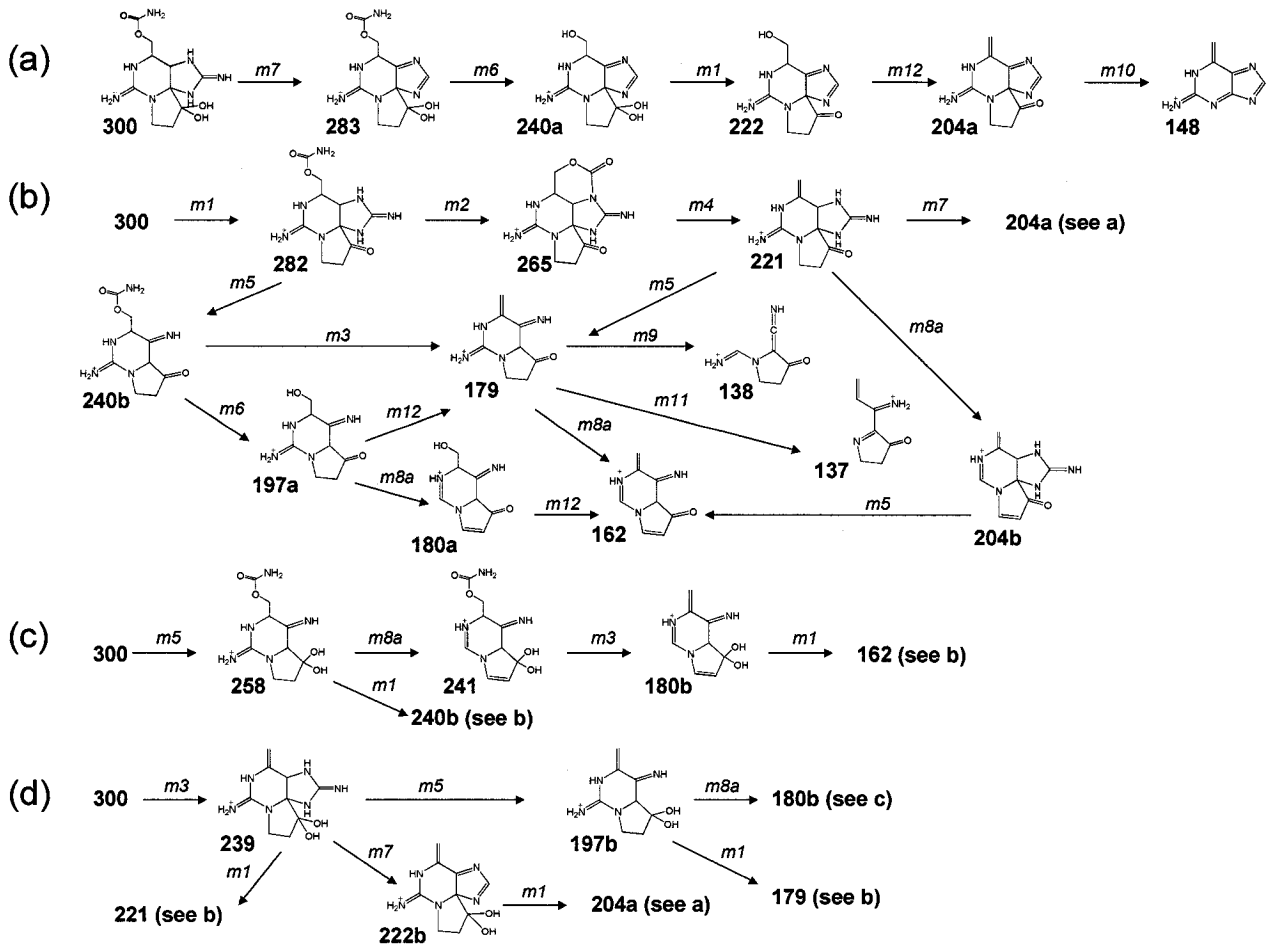

Figure 3.4 Proposed principal dissociation reactions of the MH^+ ion of STX (*m/z* 300). (Parallel reactions are described by pathways a-d. The reaction mechanisms ***m1-m18*** are summarized in Figure 3.7)

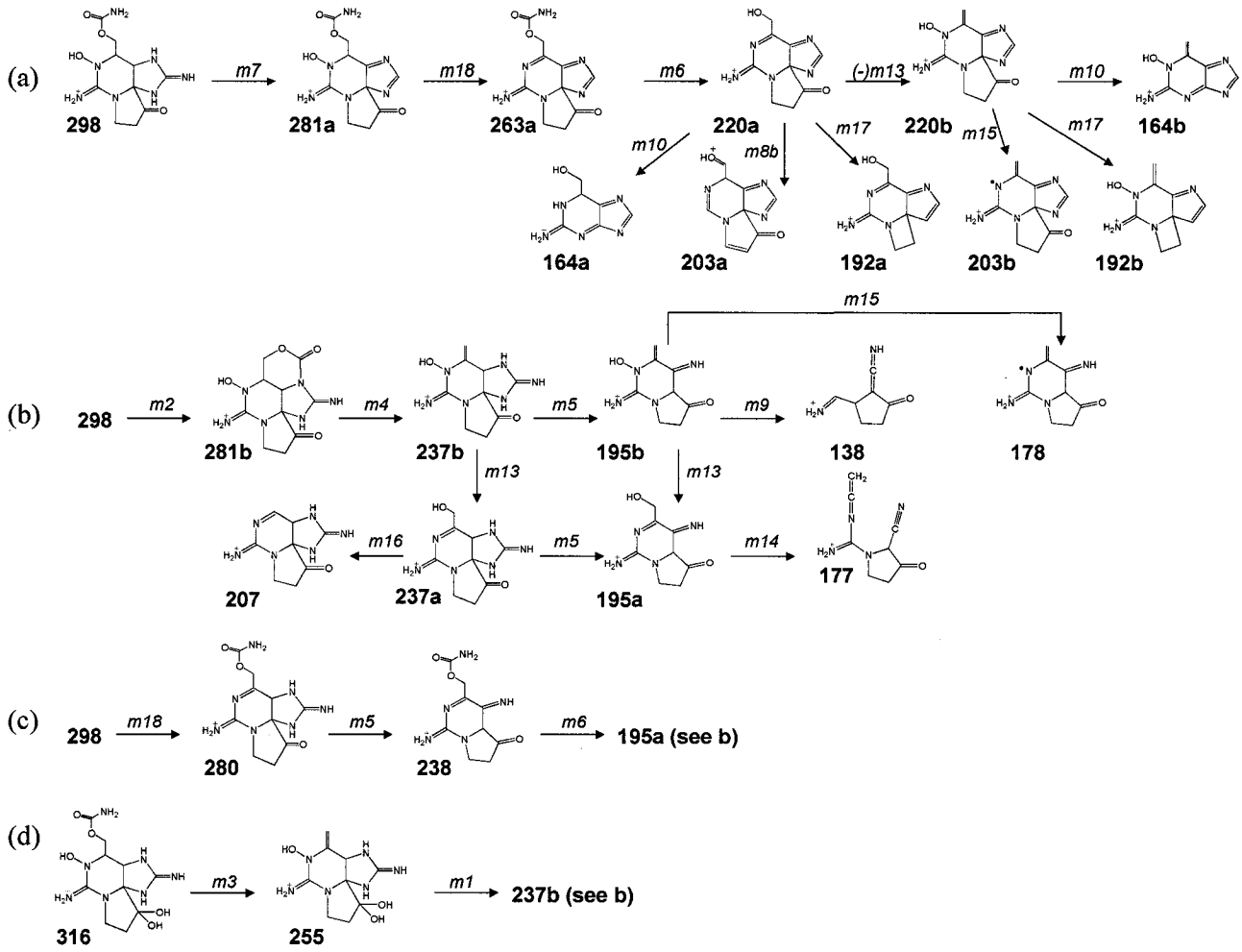

Figure 3.5 Proposed principal dissociation reactions of the MH^+ ion of NEO (*m/z* 316). (Parallel reactions of the MH^+ and $[MH–H_2O]^+$ ions are described by pathways a-d. The reaction mechanisms ***m1-m18*** are summarized in Figure 3.7)

Elemental Formula Assignment from Accurate Mass Measurements

In a series of accurate mass measurement experiments, elemental formula assignments were made for product ions observed in the QqQ CID spectra, to confirm the identity of the dissociation products. Infrared multiphoton dissociation analyses of the isolated protonated molecules of STX and NEO were carried out in the FT-ICR cell. Most of the product ions of the QqQ CID analyses (Figure 3.2) also appeared in the IRMPD spectra. Recently, Xie and Lebrilla [79] made a similar observation when comparing IRMPD and CID methods for alkali metal-coordinated oligosaccharides.

Accurate mass measurements with errors between –0.9 and +0.5 ppm were achieved for all of the STX and NEO product ions using internal mass calibration, as illustrated in Tables 3.3 and 3.4 (note: only ions observed in both QqQ and FT-ICR instruments are shown). As a result, only one possible elemental formula match for each fragment ion was obtained, thus establishing excellent confidence in the IRMPD FT-ICR MS technique and in the identities of the proposed structures in Figures 3.4 and 3.5. Figure 3.6 illustrates a partial IRMPD FT-ICR spectrum of STX, exhibiting excellent peak shapes with resolving powers between 105,000 (*m/z* 283) and 215,000 (*m/z* 137). Similarly, for NEO, resolving powers in IRMPD spectra ranged from 100,000 (*m/z* 298) to 217,000 (*m/z* 138).

Table 3.3 The nominal, measured and theoretical masses, mass measurement error (ppm), product ion identity and ion intensity for product ions observed in the IRMPD FT-ICR-MS experiments on STX.[a]

Nominal	Measured	Calculated	ppm[b]	Formula	Intensity %
300[c]	300.14148	300.14143	+0.0	$C_{10}H_{18}N_7O_4^+$	
283	283.11493	283.11493	+0.0	$C_{10}H_{15}N_6O_4^+$	12
282	282.13093	282.13091	+0.1	$C_{10}H_{16}N_7O_3^+$	95
265	265.10441	265.10436	+0.2	$C_{10}H_{13}N_6O_3^+$	8
258	258.11969	258.11968	+0.0	$C_9H_{16}N_5O_4^+$	4
241	241.09314	241.09313	+0.0	$C_9H_{13}N_4O_4^+$	8
240	240.10912	240.10911	+0.0	$C_9H_{14}N_5O_3^+$	8
239	239.12504	239.12510	–0.3	$C_9H_{15}N_6O_2^+$	8
222	222.09850	222.09855	–0.2	$C_9H_{12}N_5O_2^+$	8
221	221.11454	221.11453	+0.0	$C_9H_{13}N_6O^+$	50
204	204.08797	204.08799	–0.3	$C_9H_{10}N_5O^+$	100
197	197.10334	197.10330	+0.2	$C_8H_{13}N_4O_2^+$	5
180	180.07674	180.07675	–0.1	$C_8H_{10}N_3O_2^+$	8
179	179.09273	179.09274	+0.0	$C_8H_{11}N_4O^+$	25
162	162.06622	162.06619	+0.2	$C_8H_8N_3O^+$	5
137	137.07101	137.07094	+0.5	$C_7H_9N_2O^+$	2

[a]Only those ions that were also observed in the triple quadrupole CID spectra are listed here.
[b]Internally calibrated IRMPD spectra
[c]Obtained from a separate internally calibrated FT-ICR full-scan experiment (see Experimental).

Table 3.4 The nominal, measured and theoretical masses, mass measurement error (ppm), product ion identity, and ion intensity for product ions observed in the IRMPD FT-ICR-MS experiments on NEO.[a]

Nominal	Measured	Calculated	ppm[b]	Formula	Intensity %
316[c]	316.13639	316.13639	+0.0	$C_{10}H_{18}N_7O_5^+$	
298	298.12573	298.12583	–0.2	$C_{10}H_{16}N_7O_4^+$	100
281	281.09919	281.09928	–0.3	$C_{10}H_{13}N_6O_4^+$	30
280	280.11501	280.11526	–0.9	$C_{10}H_{14}N_7O_3^+$	1
263	263.08866	263.08872	–0.2	$C_{10}H_{11}N_6O_3^+$	12
255	255.11987	255.12002	–0.5	$C_9H_{15}N_6O_3^+$	1
238	238.09342	238.09347	–0.2	$C_9H_{12}N_5O_3^+$	3
237	237.10942	237.10945	–0.1	$C_9H_{13}N_6O_2^+$	20
225	225.10941	225.10945	–0.2	$C_8H_{13}N_6O_2^+$	3
220	220.08285	220.08290	–0.2	$C_9H_{10}N_5O_2^+$	25
207	207.09885	207.09888	–0.2	$C_8H_{11}N_6O^+$	10
203	203.05629	203.05635	–0.3	$C_9H_7N_4O_2^+$	3
203	203.08013	203.08016	–0.2	$C_9H_9N_5O^{+\bullet}$	2
195	195.08762	195.08765	–0.2	$C_8H_{11}N_4O_2^+$	7
192	192.08791	192.08799	–0.4	$C_8H_{10}N_5O^+$	3
178	178.08489	178.08491	–0.1	$C_8H_{10}N_4O^{+\bullet}$	10
177	177.07707	177.07709	–0.1	$C_8H_9N_4O^+$	50
138	138.06619	138.06619	+0.0	$C_6H_8N_3O^+$	6

[a]Only those ions that were also observed in the triple quadrupole CID spectra are listed here.
[b]Internally calibrated IRMPD spectra
[c]Obtained from a separate internally calibrated FT-ICR full-scan experiment (see Experimental).

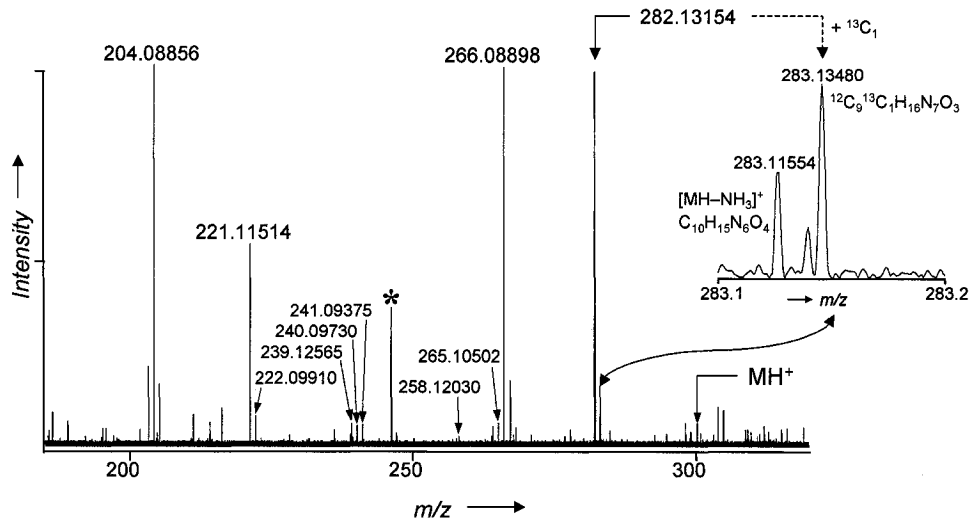

Figure 3.6 IRMPD/FT-ICR product ion spectrum of the MH^+ ion of STX and accurate masses for several important STX ions. The region around the $[M+H^+–NH_3]^+$ ion is enlarged (* denotes Glu-Fib product ions)

Proton Affinities of STX and NEO

STX and NEO exhibit two interesting structural features: (***a***) two guanidinium sites for potential proton attachment per molecule; and (***b***) an opposite order of aqueous basicities of these two groups in NEO as compared to STX. For the elucidation of the dissociation pathways, it was important to find out if this trend was the same in the gas-phase. The influence of the –OH group at N(1) on basicity and the site of proton attack on the STX and NEO molecules was investigated by first examining the proton affinities of two simple model compounds, *N,N'*-trimethylguanidine, **1**, and its hydroxyl derivative, **2** (Figure 3.7 and Table 3.5). When the B3LYP model (see Experimental) was applied to both molecules, the most susceptible position for proton attack was determined to be the imino nitrogen. Interestingly, the difference of *PA*(**1**) and *PA*(**2**) was very small, only 0.4 kcal/mol, indicating that the –OH group only slightly diminishes the proton affinity of **2** in comparison to **1**. Since the target compounds STX and NEO both possess carbamoyl groups at C(6) (Figure 3.1), which can readily undergo intra-molecular hydrogen bonding, additional comparative calculations were carried out for two hypothetical molecules, **3** and **4**, in which the carbamoyl groups were replaced with $–CH_3$ to rule out intra-molecular hydrogen bonding effects (Figure 3.7). It is important to emphasize that **3** and **4** represent the most stable forms of several possible tautomers. A significant feature is that the five-membered imidazoline ring has the imino nitrogen within the ring (*endo*),

whereas the amino group is attached in *exo* position to the ring. Protonation of **3** on either guanidinium moiety of the molecule ($\mathbf{3_L}$, $\mathbf{3_R}$) showed that $PA(\mathbf{3_L})$ (= 254.3 kcal/mol) was significantly higher than $PA(\mathbf{3_R})$ (= 242.5 kcal/mol), by *ca.* 12 kcal/mol. In both cases, the calculations revealed that the proton attack occurred at the imino nitrogen. This was not surprising as imino nitrogen atoms are generally more basic than amino nitrogen atoms, as was observed in previous studies of guanidino derivatives [170-172]. The proton affinities calculated for the two protonated species of **4** were similar; $PA(\mathbf{4_L})$ = 253.8 and $PA(\mathbf{4_R})$ = 240.6 kcal/mol, indicating that the *PA*s were reduced by 0.5 and 1.9 kcal/mol, respectively, relative to the corresponding values of **3**. The difference in stability between the protonated species $\mathbf{4H^+L}$ and $\mathbf{4H^+R}$ was 13.2 kcal/mol (Table 3.5).

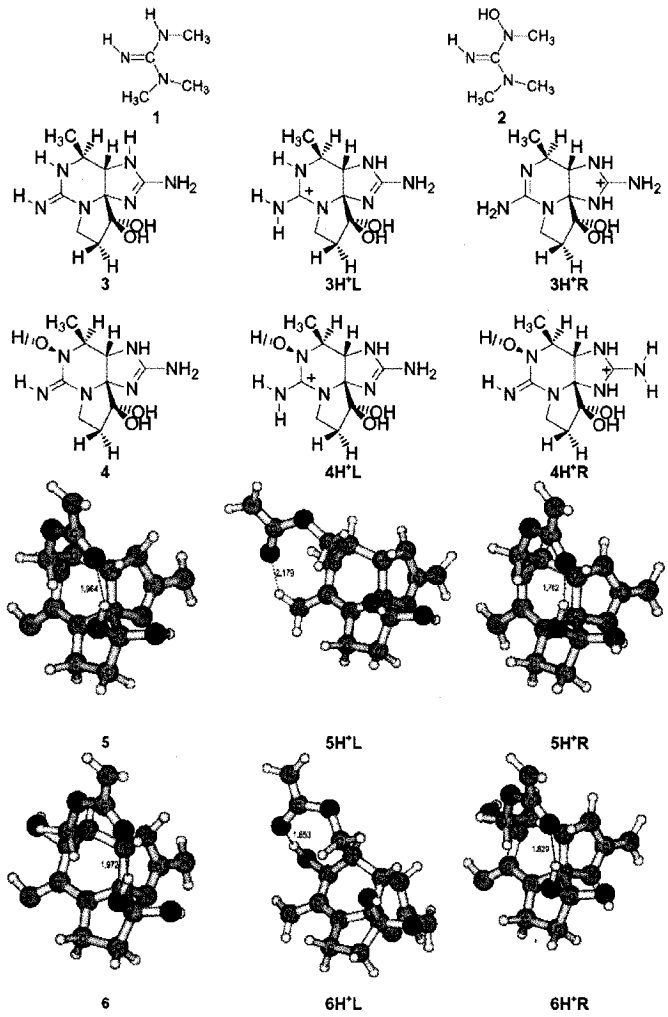

Figure 3.7 Structures of the investigated protonated guanidinium species for proton affinity calculations (hydrogen bond distances [Å] are given for **5** and **6**).

Table 3.5 The calculated proton affinities (*PA*) of the various investigated guanidinium species.

Species (Figure 3.6)	*PA* [kcal/mol]
1	245.3
2	244.9
$\mathbf{3_L}$	254.3
$\mathbf{3_R}$	242.5
$\mathbf{4_L}$	253.8
$\mathbf{4_R}$	240.6
$\mathbf{5_L}$	257.7
$\mathbf{5_R}$	250.2
$\mathbf{6_L}$	254.0
$\mathbf{6_R}$	244.4

In a similar manner, the structures of STX (**5**) and NEO (**6**) were investigated. The most stable structures of STX and NEO are shown in Figure 3.6, with the intra-molecular hydrogen bonding indicated by dashed lines. The proton affinities $PA(\mathbf{5_L})$ and $PA(\mathbf{5_R})$ for STX were 257.7 and 250.2 kcal/mol, respectively, indicating that the pyrimidine imino nitrogen is more basic in the gas-phase than the imidazoline imino nitrogen, similar to the behavior of **3**. The difference of $PA(\mathbf{5_L})$ and $PA(\mathbf{5_R})$ was 7.5 kcal/mol, following the same basicity order as the pK_a values in aqueous solution (p$K_a(\mathbf{5_L})$ = 11.5 and p$K_a(\mathbf{5_R})$ = 8.2). Protonation of NEO (**6**) in the gas-phase gave similar results as compared to STX (**5**). The behavior, however, represented a reversal from the trend in the aqueous phase. The proton affinity $PA(\mathbf{6_L})$ = 254.0 kcal/mol was higher than $PA(\mathbf{6_R})$ = 244.4 kcal/mol, with a ΔPA of 9.6 kcal/mol, in contrast to the observed pK_a values in water (p$K_a(\mathbf{6_L})$ = 6.5, p$K_a(\mathbf{6_R})$ = 8.3). The important conclusion from these calculations is that the MH^+ precursor ion is predominantly protonated at the left guanidinium moiety for both STX and NEO in the gas phase.

Dissociation Pathways and Mechanisms

The QqQ CID spectra (Figure 3.2) of STX and NEO were characterized by multiple consecutive losses of small neutrals from their protonated molecules. The general fragmentation schemes in Figures 3.4 and 3.5 are based on protonation at the left guanidinium moiety. The corresponding fragmentation mechanisms for the observed reactions of STX and NEO comprised a combination of charge-remote and charge-mediated fragmentations, as summarized in Figure 3.8. For the dissociation mechanisms, ***m1*** to ***m18***, refer to Figures 3.4, 3.5 and 3.8.

There are a number of possible fragmentation possibilities for the MH^+ ions of STX and NEO. For example, after initial loss of H_2O from the ketone hydrate at C(12) (***m1***), the resulting ions at *m/z* 282 (STX) and 298 (NEO) readily undergo secondary neutral loss reactions of various small neutrals; NH_3 (***m2***, ***m7***), (CO_2 + NH_3) through a 6-centered concerted loss from the carbamoyl moiety (***m3***), or HN=C=NH after opening of the imidazoline ring (***m5***). Third generation dissociation products are formed by expulsion of CO_2 after ring opening (***m4***) of the cyclic amide (formed via ***m2***), isocyanate cleavage NH=C=O (***m6***), or expulsion of other neutrals via ***m1-m3***, ***m5***, ***m7***, ***m9***, ***m11*** or ***m12***. The mechanisms of these reactions are detailed in Figure 3.8. Consecutive fragmentations reached up to six generations in the investigated *m/z* range (Figures 3.4 and 3.5). Also, several of these reactions occurred in parallel from the MH^+ and subsequent product ions, as competing low energy CID reactions.

The following discussion focuses on two important aspects of the fragmentation pattern: (***a***) differences between STX and NEO due to their dissimilar substitution pattern at N(1); and (***b***) differences originating from the ion activation techniques used in this study:

(a) Differences between STX and NEO: There are several unique mechanisms in the dissociation pathways that either STX or NEO could or could not undergo because of the influence of the specific substitution at N(1). STX, for example, exhibited a specific cleavage of NH_3 from *m/z* 258 (which originated via ***m5***) after going through a tautomeric transition state (***m8a***). The subsequent concerted loss of 61 u (CO_2 + NH_3, ***m3***) was specific to STX and was not observed for any later-generation NEO product ions. NEO showed a comparable reaction, originating from *m/z* 220 (*220a*): after transfer

of 2 hydrogens to give the tautomeric amino form at N(1), NH_3 was cleaved off at C(2) (***m8b***). In addition, NEO exhibited several further reactions involving the hydroxyl group at N(1) as one of the reaction centers, described by mechanisms ***m13***, ***m15*** and ***m18***.

Additionally, an interesting change from even-electron to odd-electron ions was observed for two later-generation product ions in the CID spectra of NEO. The ions at *m/z* 220 (*220b*, Figure 3.5) and *m/z* 195 (*195b*) cleaved off hydroxyl radicals from N(1) (***m15***) to give *m/z* 203 (*203b*) and *m/z* 178, as confirmed by their accurate masses in IRMPD (Table 3.4). The corresponding ions in the STX spectrum at *m/z* 204 (*204a*) and *m/z* 179 (Figure 3.4) therefore did not exhibit comparable radical ·OH losses, as STX does not have a hydroxyl group at N(1). Interestingly, the NEO species *237b* and *195b* can further rearrange to *237*a or *195a* via hydroxyl transfer from N(1) to C(13) (***m13***; Figures 3.5b and 3.8b). These rearrangements were followed by loss of either CH_2O (***m16***) or water (***m14***) to yield *m/z* 207 and 177, respectively. There was one further reaction unique to NEO that resulted from consecutive fragmentation following a NEO-specific cleavage; the formation of *m/z* 192 (*192b*) via expulsion of CO (***m17***) from *m/z* 220 (*220b*).

(b) Differences between the ion activation techniques: There were a few noteworthy differences between the CID and IRMPD spectra. For example, while all MS/MS techniques formed abundant first generation $[MH–H_2O]^+$ ions (STX: *m/z* 282; NEO: *m/z* 298), the product ion at *m/z* 283 in the spectrum of STX (loss of NH_3 from the MH^+ ion; see expanded region of Figure 3.6) was observed with a significant abundance only in the IRMPD and IT MS^2 spectra. QqQ CID formed this ion only to a very small amount or it may be a short-lived unstable intermediate under these conditions. Furthermore, the two-fold loss of NH_3 from the MH^+ ion of STX yielded one of the most abundant ions in the IRMPD spectrum (*m/z* 266; Figure 3.6) and it was also a major ion in the IT MS^2 spectrum of *m/z* 300 (Table 3.1). It was not, however, observed in the QqQ CID spectrum (Figure 3.2a). It appears that the ion activation by IRMPD and IT CID favored the initial losses of NH_3 in comparison to the triple quadrupole instrument. Consequently, the STX ion species at *m/z* 205 in IRMPD and MS^n spectra due to a 61 u loss from *m/z* 266 (concerted CO_2/NH_3 cleavage, ***m3***) was naturally absent in the QqQ CID spectra, while it

formed the base peak in the IT MS^3 spectrum ($300^+ \rightarrow 266^+ \rightarrow 205^+$). A similar behavior was obtained for NEO only in IRMPD.

Another interesting observation was made for the intense product ions at *m/z* 148 (STX) and *m/z* 164 (NEO) in the QqQ CID spectra (Figures 3.2, 3.4 and 3.5). Both products were confirmed as being formed from *m/z* 204 (STX) and *m/z* 220 (NEO), respectively, from IT MS^3 (STX: $300^+ \rightarrow 204^+ \rightarrow 148^+$; NEO: $316^+ \rightarrow 220^+ \rightarrow 164^+$) and IT MS^4 (STX: $300^+ \rightarrow 282^+ \rightarrow 204^+ \rightarrow 148^+$; NEO: $316^+ \rightarrow 298^+ \rightarrow 220^+ \rightarrow 164^+$) experiments (Tables 3.1 and 3.2). As neither ion was observed in the IRMPD analyses, their identities could not be confirmed by their accurate masses. The loss of 56 u from *m/z* 204 and 220 and the fact that they form the base peaks in the corresponding IT MS^3 and MS^4 spectra suggest that they originate from loss of cyclopropanone (C_3H_4O, ***m10***), as proposed in Figures 3.4, 3.5 and 3.8.

In general, the relative ion abundances in the QqQ CID and IRMPD spectra correlated very well for most product ions, including *m/z* 282, 221, 204, 180 and 179, but differed significantly for a few others such as m/z 283 and 266. Another poor correlation between IRMPD and CID was observed for the product ion at *m/z* 138, which represented a major ion in the QqQ spectra of both STX and NEO. This ion was formed by loss of a ketenimine from *m/z* 179 (STX) and *m/z* 195 (195b) via ***m9***. IRMPD of NEO's MH^+ ion, however, generated *m/z* 138 only to a small extent (Table 3.4); it was not observed at all in the IRMPD spectrum of STX.

a

Fragmentation Pathway	Loss	Mechanism
m1	H_2O	
m2	NH_3	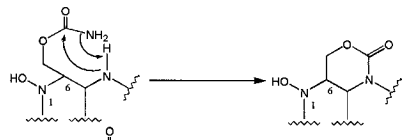
m3	CO_2, NH_3	
m4	CO_2	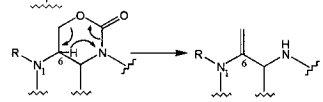
m5	HN=C=NH	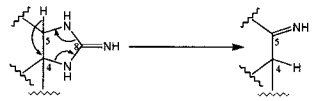
m6	O=C=NH	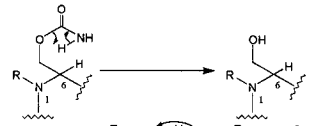
m7	NH_3	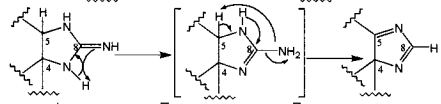
m8a	NH_3	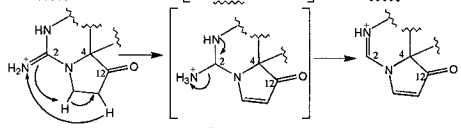
m8b	NH_3	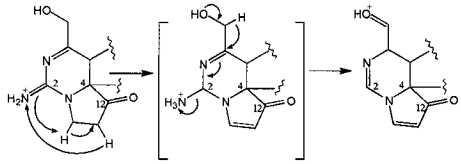

Figure 3.8a) Proposed principal dissociation mechanisms for STX and NEO (the numbering scheme ***m1*** to ***m8*** refer to reactions in Figures 3.3 and 3.4).

b

Fragmentation Pathway	Loss	Mechanism
m9	$H_2C{=}C{=}NR$ (R=H/OH)	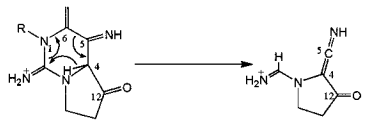
m10	C_3H_4O	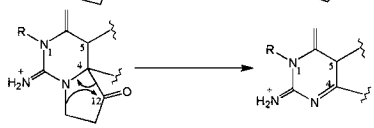
m11	$NH{=}C{=}NR$ (R=H/OH)	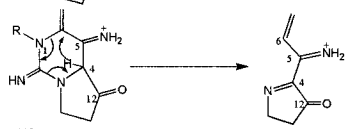
m12	H_2O	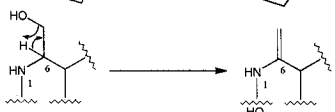
m13	rearrangement	
m14	H_2O	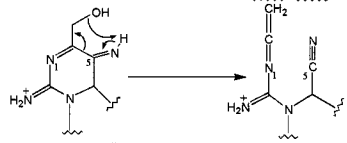
m15	$OH^{\bullet}$	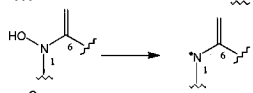
m16	CH_2O	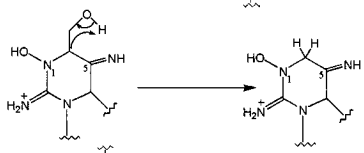
m17	CO	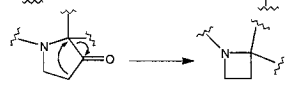
m18	H_2O	

Figure 3.8b) Proposed principal dissociation mechanisms for STX and NEO (the numbering scheme ***m9*** to ***m18*** refer to reactions in Figures 3.3 and 3.4).

Conclusions

The gas-phase dissociation pathways of two paralytic shellfish poisons (PSPs), saxitoxin and neosaxitoxin, were investigated. Structural studies on these poisons are important for both analytical characterization of the highly toxic PSPs and for identification of yet unknown toxins. The product ion mass spectra of the PSPs exhibited an unusually rich abundance of species due to the large number of functional groups within their small skeletal structures. A comprehensive approach to structural elucidation was successfully carried out, using triple quadrupole product ion spectra as templates, followed by linked ion trap MS^n data. Subsequent high-resolution FT-ICR analyses provided the accurate mass data and elemental formulae for confirming the identity of the product ions.

The actual dissociation mechanisms of the PSPs were proposed after calculations of proton affinities revealed that protonation mainly took place at the pyrimidine guanidinium moieties for both STX and NEO. Most of the parallel and consecutive dissociation reactions could then be rationalized through multiple neutral losses of H_2O, NH_3, CO, CO_2, CH_2O and different isocyanate, ketenimine and diimine species. The high degree of similarity between many of the pathways of STX and NEO will undoubtedly help characterize the chemical structures of other PSPs. For example, the related gonyautoxins are expected to show similar fragmentation patterns. Furthermore, some of the described product ions could be used for screening assays or rapid discovery of new analogs and biotransformation products.

B. Assigning product ions from complex MS/MS spectra: The importance of mass uncertainty and resolving power[†]

Introduction

Mass spectrometry-based structural identification of drugs and their metabolites frequently employ combinations of collision-induced dissociation analyses on triple quadrupole and ion trap mass analyzers. These methods often provide adequate information for determining the sites of modification for structural analogs [19, 178-181]. In those cases, however, in which the variety of fragment ions is limited or the spectra do not allow unambiguous structure assignments, tentatively identified structures are often further examined by high-resolution mass spectrometry, from which elemental compositions can be obtained. In these experiments, it is required to measure the mass-to-charge ratios with the smallest mass uncertainties possible, in particular if the methodologies are part of routine structure identification protocols. Ideally, automated analytical routines with sufficient resolution and mass accuracy would yield a single empirical formula. In most structural elucidation studies, QqTOF and, increasingly, FT-ICR mass spectrometers enable exact mass measurements of protonated molecules as well as of their MS/MS product ions [182-187]. Sometimes low-resolution mass spectrometers can be used, when additional information about the atomic composition is available. For example, Fiehn and coworkers [188] recently used gas chromatography/low-resolution quadrupole mass spectrometry to determine elemental formulae of unknown plant metabolites. The authors limited the range of possible formulae by combining the measured masses with isotope ratios.

The number of possible empirical formulae calculated from the data decreases rapidly with increasing mass accuracy. In the absence of a unique empirical formula, analysis can be highly ambiguous. TOF instruments are often described as having the capability of allowing accurate mass measurements of small molecules with uncertainties of less than 10 ppm in full scan mode. Several published reports on mass uncertainties for TOF and QqTOF instruments claim mass accuracies very close to those seen with FT-ICR systems [183, 189-191]. Such accuracy requires mass precision and accuracy within

[†] Reprinted by permission of Elsevier from: Sleno L, Volmer DA, Marshall AG. *J. Am. Soc. Mass Spectrom.* 2005; **16**: 183, by the American Society for Mass Spectrometry.

as little as 1% of the TOF mass spectral peak full width at half-maximum peak height. Thus, accurate *m/z* measurements are possible *only* if the mass analyzer can resolve adjacent peaks. This can be extremely difficult in the case of very complex samples; *e.g.*, those encountered by researchers in the petroleum industry [192] and by environmental scientists dealing with humic and fulvic acids [193], as well as any sample for which large background signals obscure the measured ion of interest.

Other examples of such "cluttered" mass spectra are CID spectra of molecules having a large number of functional groups and extensive resonance stabilization of a wide variety of ions formed in competing fragmentation pathways. The CID spectra of the protonated molecules of saxitoxin and neosaxitoxin (Figure 3.1) exhibit an unusual variety of fragments and also show numerous isobaric ions as well as interfering M+1 contributions from $^{13}C^{12}C_{c-1}$ species. The FT-ICR instrument employed for exact mass measurements was able to resolve all of those species and no false *m/z* assignments from overlapping peaks with resulting mass centroid shifts were observed. The unique complexity of those spectra introduced an interesting example for an instrumental comparison between high-resolution FT-ICR and medium-resolution QqTOF mass spectrometry. Several such comparisons have recently been published for MS/MS spectra [194-196]. For example, Thompson *et al.* compared [194] mass accuracies for fluconazole fragment ions based on external calibration SORI-CID with a 4.7 T FT-ICR and a one-point lock-mass corrected CID external calibration curve for a QqTOF instrument. The mass uncertainties were on average ±0.7 ppm for FT-ICR and ±2.9 ppm for QqTOF experiments. Except for one peak in the QqTOF MS/MS spectrum, the peaks for the 13 fragment ions in the MS/MS spectra were not distorted and the experimentally observed QqTOF resolution of 3,200 FWHM (full-width at half maximum; $m/\Delta m$, in which Δm = FWHM) was sufficient to resolve all peaks. Also, Hau and coworkers demonstrated [195] an excellent comparison of QqTOF and FT-ICR MS/MS spectra for a group of eight low-molecular weight aza-heterocycles. The authors recalibrated the externally calibrated MS/MS spectra by merging the individual analyte spectra with the MS/MS spectrum of a reference compound acquired under the same conditions. As a result, they obtained an average mass uncertainty of approximately 30 ppm with the QqTOF for 51 fragment ions, whereas the FT-ICR error was always less than 1.5 ppm.

More important, true elemental composition as the "first hit" was established for only about 70% of all fragment ions with the QqTOF, whereas FT-ICR revealed the correct formula with a 100% hit rate. Finally, the precision of any mass measurement is related to the peak shape, the signal-to-noise ratio, and the square root of the number of data points per peak width for a *single* measurement [197].

The aim of this study was to investigate particularly complex CID spectra, for which accurate mass assignments are much more difficult because of isobaric interferences and thus, potentially, overlapping peaks and shifts in the centroid masses. Except for isomeric ions, isobaric signals will always lead to inhomogeneous peak broadening in the spectra due to the different mass defects of the elements, if the mass spectrometer has insufficiently high resolving power. The question then arises, whether or not the resolving power of QqTOF is sufficient or FT-ICR is required for unambiguous identifications. A comparison of different calibration techniques for MS/MS was performed using QqTOF and FT-ICR instruments. Also, regions of spectral interferences in the MS/MS spectra and the influence of resolving power were studied. Finally, the ability to fully automate the assignment of elemental compositions to MS/MS fragment ions in both instruments was assessed.

Experimental

Chemicals

Glutathione (γ-Glu-Cys-Gly) was purchased from Sigma-Aldrich. Please refer to Part A of this chapter for other chemicals used in this study.

Quadrupole-Time-of-Flight MS/MS

Q_1q_2TOF experiments were performed with a MDS Sciex QSTAR Pulsar *i* mass spectrometer. The instrument was operated under the following conditions: spray voltage, 5 kV; declustering potentials, DP1 30 V, DP2 40 V; collision gas, N_2 (collision gas pressure, 6 [arbitrary units]). Internal mass calibration for MS/MS was performed with glutathione product ions. Two different procedures were compared. Initially, the Q_1 resolution was modified to allow transfer of MH^+ ions of both PSP and glutathione into q_2 (*m/z* 300-308 or 308-316), for concurrent activation of all ions in that mass range. Because of the different activation energies required for equivalent dissociation yields for *m/z* 300/316 (STX/NEO) and 308 (glutathione), simultaneous activation was not possible with the chosen mass calibrant. Instead, the MH^+ ions were dissociated sequentially (30 s PSP at 27 eV and then 30 s glutathione at 15 eV, with all other experimental parameters identical), but the data acquisition was never stopped during this process. The acquisition sequence is illustrated in Figure 3.9a. This procedure closely resembled true internal mass calibration. A second method involved mono-isotopic selection and rapid 'back-and-forth' switching between *m/z* 300/316 and 308 in Q_1, followed by CID in q_2. During these scans, the PSP MH^+ ions were activated at 27eV activation energy for 4 s, followed by activation of glutathione MH^+ ion for 2 s at 15eV (Figure 3.9b). In other words, the MS/MS scans were acquired in repeating cycles, for the analyte first and then the calibrant. The scans were continuously acquired into one data file, allowing internal mass re-calibration of the data. For both calibration routines, a three-point internal calibration based on three glutathione fragment masses (*m/z* 76.02209, 162.02194, and 308.09108) was performed. From the same data without the 3-point calibration correction, external calibration data was used for a separate comparison.

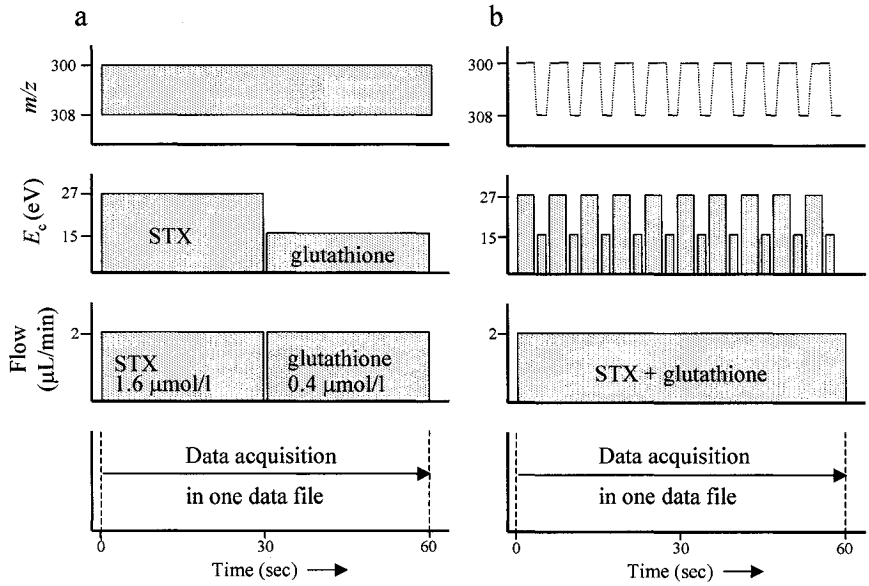

Figure 3.9 Two different mass calibration protocols used in QqTOF experiments (shown for STX). (a) Simultaneous activation of the *m/z* range 300-308 with sequential infusion of STX and glutathione; (b) Alternating monoisotopic activation of *m/z* 300 (STX) and *m/z* 308 (glutathione) while continuously infusing PSP + glutathione.

Fourier Transform-Ion Cyclotron Resonance MS/MS

FT-ICR measurements with internal calibration were performed with a 9.4 Tesla FT-ICR instrument as described in Part A of this chapter. Experiments with external calibration (see Chapter II for calibrant ions (4 peptide mix)) were conducted on a commercial 7 Tesla FT-ICR mass spectrometer (Ionspec, Lake Forest, CA, USA). The sample solutions (1.6 µmol/l) were introduced at 2 µl/min into the electrospray source (needle potential, 3.8 kV). The cone voltage was set to 30 V and the extractor to 5 V. A hexapole collection period of 1000 ms was used with an offset voltage of 1 V. IRMPD was conducted with a 25 W CO_2 laser. For STX, either a 50% laser power setting with a 1400 ms pulse or 100% for 500 ms pulse duration was used (see Tables 3.8a and 3.8b for details). The precursor selection was achieved with an arbitrary waveform generator (±1.5 Da window). For NEO, the laser power was set to 80% or 100% for 500 ms pulse duration. The precursor at *m/z* 316 was initially isolated with an arbitrary waveform generator at ±4 Da, followed by an ion isolation pulse was applied to narrow the window to ±0.184 Da to remove an isobaric interference in the spectrum at *m/z* 316.

Results and Discussion

This study illustrates the importance of concurrent high mass spectral resolution and accurate mass assignment capability for determining elemental compositions from complex product ion spectra of PSP toxins. While medium-resolution tandem mass spectrometers, such as QqTOF instruments, can generate excellent mass accuracies (<10 ppm in MS/MS experiments) with resolving powers up to 10,000 (FWHM), the situation becomes more difficult when these instruments are applied to dense MS/MS spectra, in which interferences lead to numerous overlapping signals. Such interferences may originate from: (***a***) multiple isobaric species formed through competitive fragmentation reactions after ion activation of MH^+ ions; (***b***) overlap of analyte and internal calibrant product ion signals; or (***c***) M+1 contributions, when both the MH^+ precursor as well as its $^{13}C^{12}C_{c-1}$ isotopomer are simultaneously activated in MS/MS experiments. The latter situation can occur when an analyte and a mass calibrant of similar molecular weight are simultaneously activated in the collision or trapping cell to obtain a composite product ion spectrum for internal calibration purposes. To a lesser extent, M+1 interferences can be expected when the precursor ion selection in Q_1 of a QqTOF instrument is not narrow enough to completely isolate the $^{12}C_c$ species of the precursor ion from its $^{13}C^{12}C_{c-1}$ isotopomer.

An instrumental comparison between high-resolution FT-ICR and medium-resolution QqTOF mass spectrometry was conducted using STX and NEO (Figure 3.1) as test molecules. Not surprisingly, the QqTOF spectra appear quite similar to the triple quadrupole MS/MS spectra reported before, as the collision conditions in q_2 were almost the same. There are also similarities between the fragment ions of STX and NEO, indicating parallel dissociation mechanisms (refer to Part A). Table 3.6 summarizes most of the chemical structures of the observed STX and NEO product ions employed for this comparison.

Table 3.6 The chemical structures of selected product ions of STX (R=H) and NEO (R=OH) for mass accuracy comparison

Ion	Structure	Ion	Structure	Ion	Structure
298 282	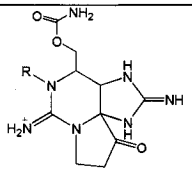	240	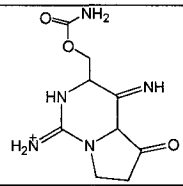	195 179	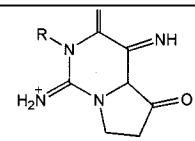
283	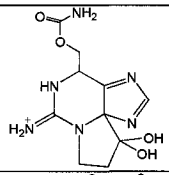	238	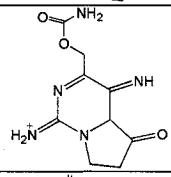	192	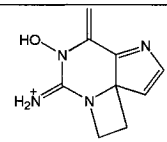
281 265	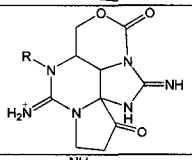	237 221	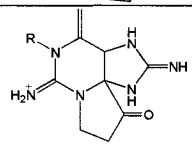	180	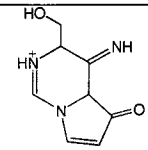
280	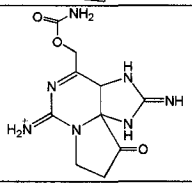	225	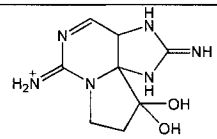	178	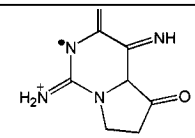
266	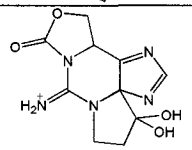	222	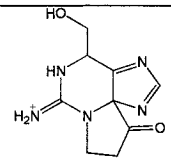	177	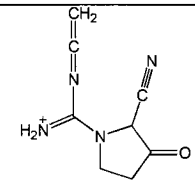
263	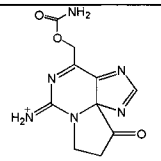	220 204	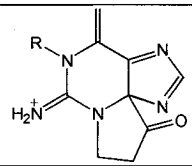	164 148	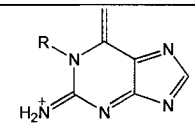
258	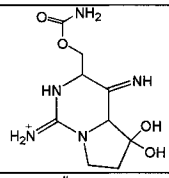	207	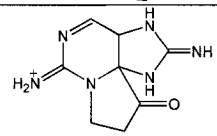	162	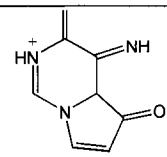
255 239	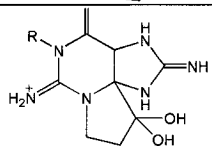	203	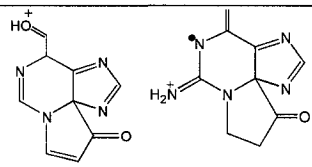	138	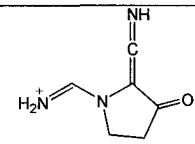
241	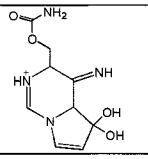	197	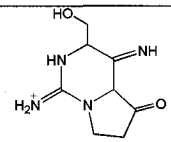	137	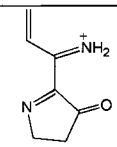

General considerations for mass accuracy comparison

The experimental resolving powers shown are expressed as full width at half maximum values, $m/\Delta m$ (FWHM). The theoretical resolving powers needed to distinguish between two isobaric interferences are calculated simply from the difference between the masses of the two species, $m/\Delta m_{\delta}$. The accurate mass numbers discussed for the QqTOF measurements are peak centroid data, whereas the FT-ICR numbers are the maximum of a best-fit parabola drawn through the three highest-magnitude data points.

The QqTOF experiments yielded low energy collision-induced dissociation spectra for STX and NEO. All spectra were then compared with results from experiments with a 9.4 Tesla FT-ICR instrument. The FT-ICR MS/MS experiments employed infrared multiphoton dissociation for generating the product ions. As IRMPD is rather non-selective, all trapped ions are excited simultaneously. The resulting IRMPD spectra of the PSP toxins exhibit strong similarity to QqTOF CID spectra, allowing for numerous direct comparisons.

Comparison of QqTOF and FT-ICR

QqTOF experiments were initially conducted with semi-internal calibration. The originally plan was to implement a true internal calibration procedure similar to the FT-ICR experiments, by activating the PSP toxin and the internal standard at the same time in q_2, giving CID spectra with *in situ* reference ions. This proved to be difficult, however, because the optimum collision energies for the PSPs and glutathione were quite different. To circumvent this problem, we sequentially infused the analyte and the calibrant solutions and adjusted the collision energy in between, without stopping data acquisition. This procedure was very close to internal mass calibration because all experimental parameters (except the collision energy) were identical and the resulting spectra contained product ions of the analyte and the calibrant (Figure 3.9). More importantly, the CID spectra exhibited all of the important characteristic features, in particular the excitation of multiple species in q_2 (the isolation window of Q_1 was widened to allow passage of MH^+ ions of PSP and glutathione [STX, range, $300 < m/z < 308$; NEO, $308 < m/z < 316$]). All spectra were then compared with results from IRMPD FT-ICR experiments, for which true internal calibration was implemented by the use of alternated

dual electrospray of PSP and calibrant ions ([Glu^1]-fibrinopeptide) into an external octopole trap, followed by injection into the ICR cell for additional SWIFT isolation prior to IRMPD (see Experimental).

The resulting mass accuracies and resolving powers from QqTOF and FT-ICR measurements are summarized in Tables 3.7a and 3.7b (note that the QqTOF results from these experiments are listed in the QqTOF (1) column). For FT-ICR experiments, accurate masses with measurement uncertainties <1 ppm were achieved for all product ions, allowing unambiguous assignment of only one possible elemental formula to each fragment ion. Many of the same product ions were also observed with excellent mass accuracy in the QqTOF spectra, often with measurement uncertainties <5 ppm. A significant number of the QqTOF MS/MS product ions, however, exhibited unusually large deviations from the expected *m/z* values, with some measurement errors higher than 100 ppm. A closer look at those peaks and a direct comparison with the corresponding FT-ICR results revealed overlapping peaks from multiple isobaric interferences as the source of the mass errors.

The interferences in the QqTOF spectra can be grouped into the three categories: multiple isobaric species formed via different fragmentation pathways, ^{13}C-containing (M+1) species, and isobaric analyte/calibrant product ions. Two product ions from the calibrant at *m/z* 162 and 179 came close to STX product ions (Table 3.7). In theory, a resolving power of only $m/\Delta m_{\delta} \approx 3{,}500$ is required to separate them and the QqTOF instrument should be able to easily resolve the isobaric species. However, only the *m/z* 179 ions were identified by QqTOF, whereas the *m/z* 162 peak exhibited a surprisingly large measurement uncertainty (Table 3.7a). A possible explanation is the presence of a third interfering species at *m/z* 162 (expected elemental formula $C_7H_8N_5^+$), whose analog was observed in the NEO spectrum (*m/z* 178, $C_7H_8N_5O^+$). Unfortunately, we could not confirm the identity of the $C_7H_8N_5^+$ ion from the FT-ICR spectrum. The most interesting interferences and the theoretical resolving power needed to separate the isobars are summarized in Table 3.8.

Table 3.7a The measured and theoretical masses, mass measurement errors (ppm), elemental formulae, and resolving powers for product ions observed in the internal calibration QqTOF CID and IRMPD FT-ICR experiments for STX.

Calculated mass	Elemental formula	FT-ICR (9.4T) (m/Δm)	Error (ppm)	QqTOF (1) (m/Δm)	Error (ppm)	QqTOF (2) (m/Δm)	Error (ppm)
283.11493	$C_{10}H_{15}N_6O_4^+$	283.11493 (104,000)	0.0	283.1241[a] (6,000)	32	283.1179 (9,900)	11
282.13091	$C_{10}H_{16}N_7O_3^+$	282.13093 (105,000)	0.1	282.1308 (9,000)	-0.4	282.1306 (9,000)	-1.1
266.08838	$C_{10}H_{12}N_5O_4^+$	266.08837 (111,000)	0.0	266.0948[a] (5,800)	24.0	266.0908	9.1
265.10437	$C_{10}H_{13}N_6O_3^+$	265.10441 (111,000)	0.2	265.1045 (8,700)	0.5	265.1036 (9,600)	-2.9
258.11968	$C_9H_{16}N_5O_4^+$	258.11969 (114,000)	0.0	258.1203 (9,500)	2.4	258.1208 (9,500)	4.3
241.09313	$C_9H_{13}N_4O_4^+$	241.09314 (123,000)	0.0	241.0987[a] (6,900)	23	241.0945 (6,900)	5.7
240.10911	$C_9H_{14}N_5O_3^+$	240.10912 (123,000)	0.0	240.1107[a] (9,200)	6.6	240.1090 (10,300)	-0.5
239.12510	$C_9H_{15}N_6O_2^+$	239.12504 (124,000)	-0.3	239.1250 (8,200)	-0.4	239.1253 (9,200)	0.8
222.09855	$C_9H_{12}N_5O_2^+$	222.09850 (133,000)	-0.2	222.1025[a] (6,100)	18	222.1000 (8,800)	6.5
221.11454	$C_9H_{13}N_6O^+$	221.11454 (134,000)	0.0	221.1147 (8,800)	0.7	221.1151 (9,900)	2.6
204.08799	$C_9H_{10}N_5O^+$	204.08797 (145,000)	-0.1	204.0882 (8,500)	1.0	204.0884 (8,500)	2.0
197.10330	$C_8H_{13}N_4O_2^+$	197.10334 (150,000)	0.2	197.1027 (8,300)	-3.1	197.1044 (9,400)	5.6
180.07675	$C_8H_{10}N_3O_2^+$	180.07674 (131,000)	-0.1	180.0846[a] (7,200)	44	180.0833[a] (7,200)	36
179.09274	$C_8H_{11}N_4O^+$	179.09273 (165,000)	0.0	179.0930 (7,100)	1.5	179.0932 (7,900)	2.6
162.06619	$C_8H_8N_3O^+$	162.06622 (182,000)	0.2	162.0690[b] (5,700)	17	162.0702[b] (6,200)	25
137.08217	$C_6H_9N_4^+$	137.08222 (216,000)	0.3	137.0796[b] (6,200)	-19	137.0785[b] (5,700)	-27
137.07094	$C_7H_9N_2O^+$	137.07101 (216,000)	0.5	137.0796[b] (6,200)	63	137.0785[b] (5,700)	55

The QqTOF (1) lists the experiments with semi-internal calibration (low-resolution in Q_1). QqTOF (2) summarizes the measurements for rapid 'back and forth' switching between MH^+ and glutathione and monoisotopic activation.

[a]M+1 interference, [b]Overlapping fragment ion species

Table 3.7b The measured and theoretical masses, mass measurement errors (ppm), elemental formulae, and resolving powers for product ions observed in the internal calibration QqTOF CID and IRMPD FT-ICR experiments for NEO.

Calculated mass	Elemental formula	FT-ICR (9.4 T) (m/Δm)	Error (ppm)	QqTOF (1) (m/Δm)	Error (ppm)	QqTOF (2) (m/Δm)	Error (ppm)
298.12583	$C_{10}H_{16}N_7O_4^+$	298.12573 (99,000)	-0.3	298.1257 (8,400)	-0.4	298.1242 (9,200)	-5.5
281.09928	$C_{10}H_{13}N_6O_4^+$	281.09920 (105,000)	-0.3	281.0986[a] (8,100)	-2	281.0995 (12,800)	0.8
280.11526	$C_{10}H_{14}N_7O_3^+$	280.11502 (105,000)	-0.9	280.1157 (8,100)	1.6	280.1161 (14,900)	3.0
263.08872	$C_{10}H_{11}N_6O_3^+$	263.08866 (112,000)	-0.2	263.0884 (9,600)	-1.2	263.0876 (8,700)	-6.1
255.12002	$C_9H_{15}N_6O_3^+$	255.11987 (116,000)	-0.6	255.1189 (9,500)	-4.4	255.1189 (8,700)	-4.4
238.09347	$C_9H_{12}N_5O_3^+$	238.09342 (124,000)	-0.2	238.1159[a,b] (8,300)	94	238.1165[b] (10,000)	97
238.11728	$C_9H_{14}N_6O_2^{+\bullet}$	238.11710 (124,000)	-0.7	238.1159[a,b] (8,300)	-5.8	238.1165[b] (10,000)	-3.3
237.10945	$C_9H_{13}N_6O_2^+$	237.10942 (125,000)	-0.1	237.1092 (8,200)	-1.1	237.1092 (10,100)	-1.1
225.10945	$C_8H_{13}N_6O_2^+$	225.10941 (131,000)	-0.2	225.1089 (8,000)	-2.4	225.1096 (8,900)	0.7
220.10671	$C_9H_{12}N_6O^{+\bullet}$	220.10667 (134,000)	-0.2	220.0974[a] (4,600)	-42	220.0967[b] (4,600)	-46
220.08290	$C_9H_{10}N_5O_2^+$	220.08285 (134,000)	-0.2	220.0974[a] (4,600)	66	220.0967[b] (4,600)	63
207.09889	$C_8H_{11}N_6O^+$	207.09888 (143,000)	0.0	207.0993 (8,500)	2.0	207.0989 (8,500)	0.1
203.05635	$C_9H_7N_4O_2^+$	203.05629 (145,000)	-0.3	203.0793[b] (6,900)	113	203.0794[b] (6,900)	114
203.08016	$C_9H_9N_5O^{+\bullet}$	203.08013 (145,000)	-0.2	203.0793[b] (6,900)	-4.2	203.0794 (6,900)	-3.7
195.08765	$C_8H_{11}N_4O_2^+$	195.08762 (151,000)	-0.2	195.0860 (7,500)	-8.5	195.0865 (6,900)	-5.9
192.11180	$C_8H_{12}N_6^{+\bullet}$	192.11176 (123,000)	-0.2	192.1097[b] (6,200)	-11	192.1060[b] (5,700)	-30
192.08799	$C_8H_{10}N_5O^+$	192.08791 (153,000)	-0.4	192.0809[b] (8,200)	-36	192.0804[b] (8,000)	-40
178.06110	$C_8H_8N_3O_2^+$	178.06107 (166,000)	-0.2	178.0828[a,b] (5,900)	122	178.0815[b] (5,500)	115
178.07234	$C_7H_8N_5O^+$	178.07233 (166,000)	0.0	178.0828[a,b] (5,900)	59	178.0815[b] (5,500)	52
178.08491	$C_8H_{10}N_4O^{+\bullet}$	178.08489 (166,000)	-0.1	178.0828[a,b] (5,900)	-12	178.0815[b] (5,500)	-19
177.07709	$C_8H_9N_4O^+$	177.07708 (167,000)	0.0	177.0785 (7,100)	8.0	177.0779 (7,900)	2.3
138.06619	$C_6H_8N_3O^+$	138.06619 (214,000)	0.0	138.0663 (6,300)	0.8	138.0669 (7,000)	5.2

The QqTOF (1) lists the experiments with semi-internal calibration (low-resolution in Q_1). QqTOF (2) summarizes the measurements for rapid 'back and forth' switching between MH^+ and glutathione and monoisotopic activation.

[a]M+1 interference, [b]Overlapping fragment ion species

Table 3.8 The theoretical resolving power ($m/\Delta m_{\delta}$) required to separate several important interfered species in the MS/MS spectra of STX and NEO

Nominal mass	Calculated masses	Formulae	$m/\Delta m_{\delta}$ required
NEO			
281	281.09928	$C_{10}H_{13}N_6O_4^+$	14,529
	281.11862	$^{12}C_9{}^{13}C_1H_{14}N_7O_3^+$	
238	238.09347	$C_9H_{12}N_5O_3^+$	12,307
	238.11281	$^{12}C_8{}^{13}C_1H_{13}N_6O_2^+$	
	238.11728	$C_9H_{14}N_6O_2^{+\bullet}$	53,243
220	220.08920	$C_9H_{10}N_5O_2^+$	12,564
	220.10671	$C_9H_{12}N_6O^{+\bullet}$	
203	203.05635	$C_9H_7N_4O_2^+$	8,526
	203.08016	$C_9H_9N_5O^{+\bullet}$	
192	192.08799	$C_8H_{10}N_5O^+$	8,065
	192.11180	$C_8H_{12}N_6^{+\bullet}$	
178	178.06110	$C_8H_8N_3O_2^+$	15,836
	178.07234	$C_7H_8N_5O^+$	
	178.08044	$^{12}C_7{}^{13}C_1H_9N_4O^+$	21,975
	178.08491	$C_8H_{10}N_4O^{+\bullet}$	39,821
STX			
283	283.11493	$C_{10}H_{15}N_6O_4^+$	14,633
	283.13427	$^{12}C_9{}^{13}C_1H_{16}N_7O_3^+$	
241	241.09313	$C_9H_{13}N_4O_4^+$	12,461
	241.11247	$^{12}C_8{}^{13}C_1H_{14}N_5O_3^+$	
222	222.09855	$C_9H_{12}N_5O_2^+$	11,478
	222.11789	$^{12}C_8{}^{13}C_1H_{13}N_6O^+$	
180	180.07675	$C_8H_{10}N_3O_2^+$	9,308
	180.09609	$^{12}C_7{}^{13}C_1H_{11}N_4O^+$	
137	137.07094	$C_7H_9N_2O^+$	12,196
	137.08217	$C_6H_9N_4^+$	

The first group of potential interferences consists of multiple isobaric species formed from the MH^+ ion and through subsequent dissociations; for example, *m/z* 137 for STX and *m/z* 220, 203 and 192 for NEO. NEO exhibits more interfering isobaric products because most originate via a radical loss of the hydroxyl group at N(1). Theoretical resolving powers in the range $m/\Delta m_{\delta} = 8{,}000$ to 12,500 are necessary to separate the peak pairs, usually out of reach of the QqTOF instrument (Table 3.8) which provided resolutions in the range $m/\Delta m$ (FWHM) = 6,900 to 9,900. For example, resolution of the two isobaric fragment ion species at *m/z* 203 of NEO (Table 3.6) requires a theoretical resolving power of $m/\Delta m_{\delta} \approx 8{,}500$. Figure 3.10 illustrates this deficiency compared to the unambiguous results of the corresponding IRMPD FT-ICR experiments. In IRMPD MS/MS, $m/\Delta m$ (FWHM) ranged from 99,000 (*m/z* 298) to 216,000 (*m/z* 137) for STX and NEO. Similarly, the species at *m/z* 137 (STX) as well as *m/z* 220 and 192 could not be resolved into their doublets with the QqTOF instrument.

The relative contributions of two isobaric species in the TOF spectra can be estimated by mass-domain based signal deconvolution, as recently outlined by Meija and Caruso [198]. It was shown that the observed centroid mass is the weighted average of the isobar masses when the TOF peak width Δm is larger than the mass difference of the isobars, $\Delta m \geq |m_A - m_B|$:

$$m_{\max} \cong x_A m_A + x_B m_B ,$$

where $m_{\max}$ is the *m/z* value with maximum amplitude of the observed composite peak and x_A and x_B are the relative abundances of the ions of masses m_A and m_B. For the example discussed above (NEO, *m/z* 203; Figure 3.10), the mass difference between $C_9H_7N_4O_2^+$ (203.05635 u) and $C_9H_9N_5O^{+\bullet}$ (203.08016 u) is 24 mDa whereas the estimated peak width Δm is about 26 mDa. The above equation yields relative abundances of 4% for $C_9H_7N_4O_2^+$ and 96% for $C_9H_9N_5O^{+\bullet}$. Not surprisingly, the TOF mass measurement gave accurate results for $C_9H_9N_5O^{+\bullet}$ ion with an error of only -4.2 ppm. Conversely, the elemental formula fit for $C_9H_7N_4O_2^+$ was not very accurate (112 ppm) because the peak centroid maximum was shifted almost entirely away from this low abundant component. Of course, for convolved peaks for which both species contribute significantly, inaccurate results are obtained for both isobars. For example, the two

species contributing to the isobaric signal at *m/z* 220, $C_9H_{10}N_5O_2^+$ and $C_9H_{12}N_6O^{+\bullet}$, are 24 mDa apart. The TOF peak width for a non-interfered peak at *m/z* 220 was estimated to be 26 mDa, so the above equation could be applied. As a result, the relative contributions of x_A and x_B were 39% and 61%. Consequently, the elemental formula calculations did not yield a good fit for either species (-42 and 66 ppm, respectively), because the centroid mass was shifted to an intermediate value between the two peaks.

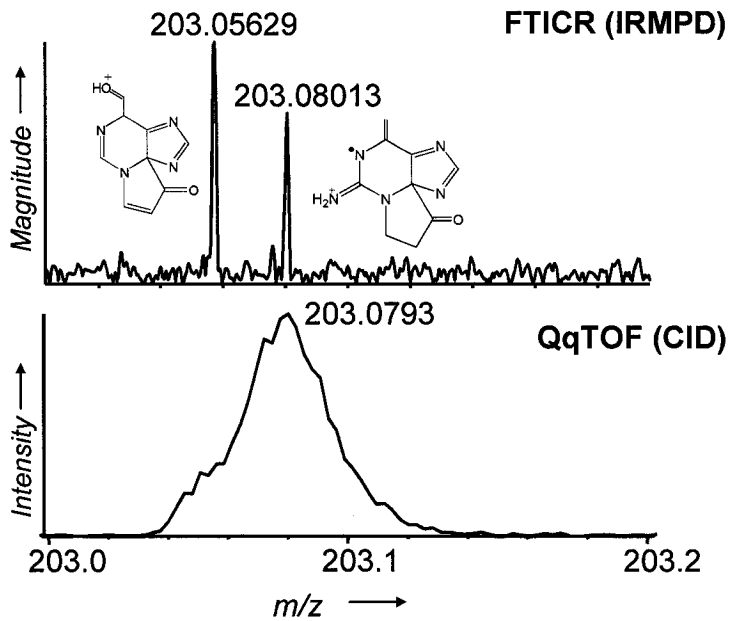

Figure 3.10 Two isobaric NEO product ions at *m/z* 203. IRMPD FT-ICR mass scale expansion of the isobaric region (top) and corresponding QqTOF spectrum (bottom).

Other overlapping peaks originate from M+1 contributions, due to co-collisional activation of the precursor's $^{13}C^{12}C_{c-1}$ ions. As a result, multiple potential interferences occur in segments of high peak density in the MS/MS spectra. These interferences are highlighted in Table 3.8. To separate all $^{12}C_c$ products from $^{13}C^{12}C_{c-1}$ species, even higher resolving power required, up to $m/\Delta m_{\delta} = 53{,}000$, well beyond the capability of QqTOF instruments. Incidentally, the two interfering species were always of the general formulae $C_cH_xN_yO_z$ and $^{13}C_1{}^{12}C_{c-1}H_{x+1}N_{y+1}O_{z-1}$; *i.e.*, Δm was always 19.4 mDa. The QqTOF experimental resolving power, however, was never high enough to resolve these two species, whereas the FT-ICR instrument was always well above the required theoretical resolving power, resulting in clearly separated isobars (Figure 3.11).

The M+1 interferences in the QqTOF spectra clearly result from a specific weakness of the applied semi-internal calibration routine, as the procedure activates unwanted $^{13}C^{12}C_{c-1}$ species at the same time. Although the isobaric fragment ion interferences obviously cannot be avoided, M+1 interferences would not occur with monoisotopic isolation and activation of the MH^+ ions, as with external calibration. In order to combine the advantages of internal calibration and monoisotopic activation and thus reduce or completely eliminate some of these M+1 interferences, the data acquisition protocol was altered in a new method.

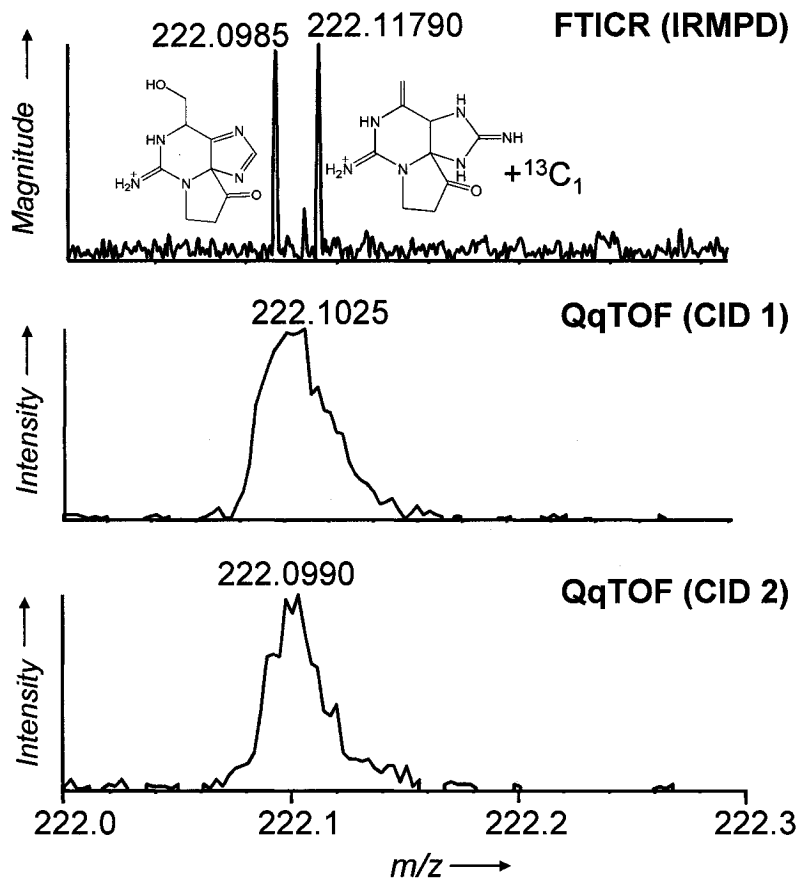

Figure 3.11 Isobaric $^{12}C_9$ and $^{13}C_1{}^{12}C_8$ species at *m/z* 222 in STX product ion spectra. Mass scale expansion of the isobaric IRMPD FT-ICR spectrum (top), QqTOF spectrum after co-activation of *m/z* 222 and calibrant ions (middle); and QqTOF spectrum after monoisotopic activation of *m/z* 222 ions (bottom).

The refined approach: monoisotopic activation cycles

For an improved acquisition technique, the QqTOF instrument software was modified to allow rapid "back and forth" switching between the MH^+ ion of the analyte and that of the mass calibrant (see Experimental). The results of the modified procedure are summarized in Tables 3.7a and 3.7b for comparison to the previous method. The M+1 interferences are clearly reduced significantly compared to the previous activation method. The improvement is particularly important for mass assignments in the STX spectra as more isotope interferences are seen compared to NEO. An example for the improved peak centroid is shown in Figure 3.11 for the STX fragment ion at *m/z* 222 ($C_9H_{12}N_5O_2^+$, calculated mass at *m/z* 222.0986). Note how the centroid mass shifts from *m/z* 222.1025 to 222.0990 by eliminating the mass shift-causing ^{13}C isotope of *m/z* 221. At the same time, the uncertainty of measurement improves from 18 ppm to 6.5 ppm. By comparison, the FT-ICR spectrum clearly shows two well-separated signals for the two species present (because they were produced by IRMPD, the relative abundances differ somewhat from the QqTOF CID MS/MS spectrum). Some products ions still exhibit small mass centroid shifts because the chosen resolution setting of Q_1 allowed a small number of $^{13}C^{12}C_{c-1}$ ions to pass through into q_2 before TOF analysis. These minor interferences then had an effect on low abundance fragments such as *m/z* 180 in the spectrum of STX. Although the $^{13}C^{12}C_{c-1}$ contribution from highly abundant *m/z* 179 was almost completely eliminated in the Q_1 isolation step, the very small residual signal still interfered with *m/z* 180 (Table 3.7a), with the result that the mass measurement error dropped only from 44 ppm to 36 ppm. Such "cross-talk" could be completely eliminated by increased Q_1 resolution, at the cost of signal reduction. Of course, the inherent isobaric interferences (*e.g. m/z* 238, 220, 203, 192, 178 and 137) from different characteristic fragment ion species are not eliminated by the modified procedure and represent the ultimate limitation for applying a QqTOF instrument to the analysis of PSP MS/MS spectra.

Interestingly, the observation of peaks yielding poor mass accuracy of the QqTOF system offers an unexpected but convenient way for detecting the presence of multiple species in a composite peak, many of which had previously escaped our attention when

investigating the triple quadrupole CID behavior of PSPs (Part A). Some of the more important examples are illustrated in the following section.

A few interesting observations in the QqTOF spectra of STX and NEO

A comprehensive dissociation scheme for STX and NEO, observed under low-energy CID conditions has been presented (Figures 3.4 and 3.5). Because the accurate mass measurements were only used for confirmation of tentatively identified product ions, some of the isobaric ions discussed remained undetected at the time and were therefore not structurally investigated. The mechanisms of formation are interesting enough, however, to report them here briefly as an extension to the previous study.

The most interesting observation is the formation of several radical ion species. NEO exhibits radical hydroxyl loss from N(1), which is, of course, not observed in the corresponding STX spectra. Examples in the NEO CID spectra are *m/z* 220 and 192, which are related ions (Figure 3.12a). As mentioned above, we discovered these new species because several peaks in the QqTOF spectra display unusually large mass measurement errors, pointing to multiple species under the peak. The elemental compositions are given in Tables 3.7 and 3.8. Because there were no products ions at *m/z* 219 and 191 in the MS/MS spectrum of NEO, M+1 interferences are ruled out. Instead, as confirmed by FT-ICR, the additional species are formed by loss of •OH and CO from *m/z* 237 via the *m/z* 220 and 209 intermediates (Figure 3.12a). A similar mechanism has been proposed for *m/z* 203 (see Part A). Another interesting NEO-specific fragment was observed at *m/z* 225, the proposed mechanism of which is illustrated in Figure 3.12b. This intriguing mechanism involves a concerted loss of three small neutral molecules involving the hydroxyl group at N(1) and the carbamate function at C(6).

The next example illustrates two interfering isobars at *m/z* 137 in the product ion spectrum of STX that were previously undetected. The first species is the result of a HN=C=NH loss from *m/z* 179 after opening of the imidazoline ring ($C_6H_9N_4^+$; Figure 3.13). For the second *m/z* 137 species, a structure is proposed in Figure 3.13 ($C_7H_9N_2O^+$), based on the FT-ICR data. The two signals are only 11.2 mDa apart in the QqTOF CID spectrum; thus, the signal deconvolution calculation spectra described above reveals a

contribution of 33% for $C_7H_9N_2O^+$ and 67% for $C_6H_9N_4^+$, correlating well with the observed mass uncertainties (Table 3.7).

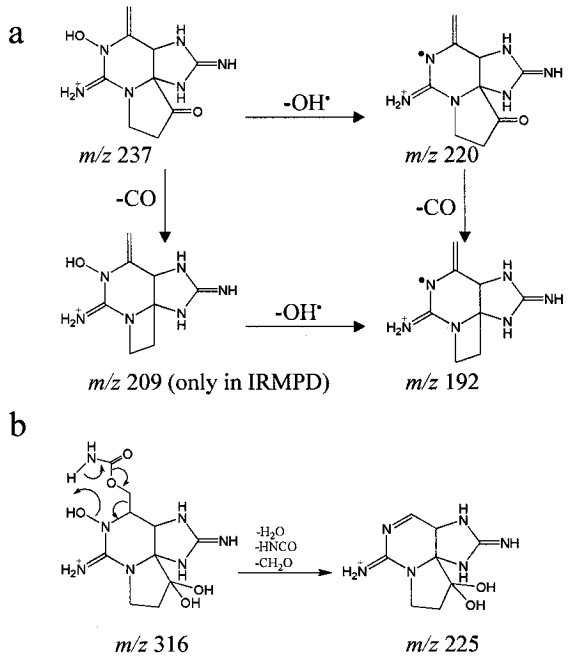

Figure 3.12 Proposed dissociation mechanisms for several interesting fragmentation reactions in the product ion spectra of NEO. (*a*) Formation of *m/z* 220 and 192 in the spectrum of NEO; (*b*) formation of *m/z* 225 from MH^+ of NEO.

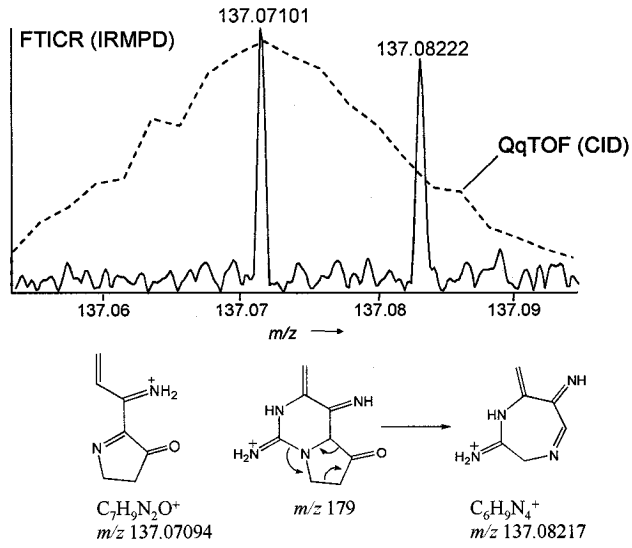

Figure 3.13 Two isobaric species differing by CO vs. N_2 (0.01123 Da) at *m/z* 137 in product ion spectra of STX. The measured masses are given for the IRMPD FT-ICR experiment. The spectrum obtained under QqTOF CID conditions is shown as a dashed line. The chemical structures of the two product ions as well as their calculated exact masses are illustrated below the spectrum.

Finally, the isobars at *m/z* 178 and 238 of NEO provide perfect examples for illustrating the need for FT-ICR over QqTOF in structural studies of the type described here (Figures 3.14 and 3.15). Initially, we suspected an M+1 interference from *m/z* 177 ($^{12}C_7{}^{13}C_1H_9N_4O^+$) to contribute to the $C_8H_{10}N_4O^+$ signal at *m/z* 178, thus shifting the mass centroid away from the true mass. The monoisotopic selection and activation of MH^+, however, did not improve the mass accuracy (Table 3.7b) for $C_8H_{10}N_4O_3{}^+$, pointing to a different or additional source of interference. A closer look at the FT-ICR spectrum revealed an interesting situation: the *m/z* 178 signal consists of four isobars within only 25 mmu ($C_8H_8N_3O_2{}^+$ and $C_7H_8N_5O^+$ plus the two mentioned species above; Figure 3.14); only one of them is an actual $^{13}C^{12}C_{c-1}$ interference, explaining the remaining interference after monoisotopic activation. In contrast, the limited resolving power of the QqTOF instrument yielded only one coalescent signal. A similar situation was encountered for *m/z* 238 (Figure 3.15), where three different NEO-derived species form the composite peak. Again, the similar mass accuracies for the two mass calibration procedures in Table 3.7b point to at least one additional interference other than M+1 contributing to the signal. Indeed, the FT-ICR analysis resolved four separate peaks at *m/z* 238 (Figure 3.15).

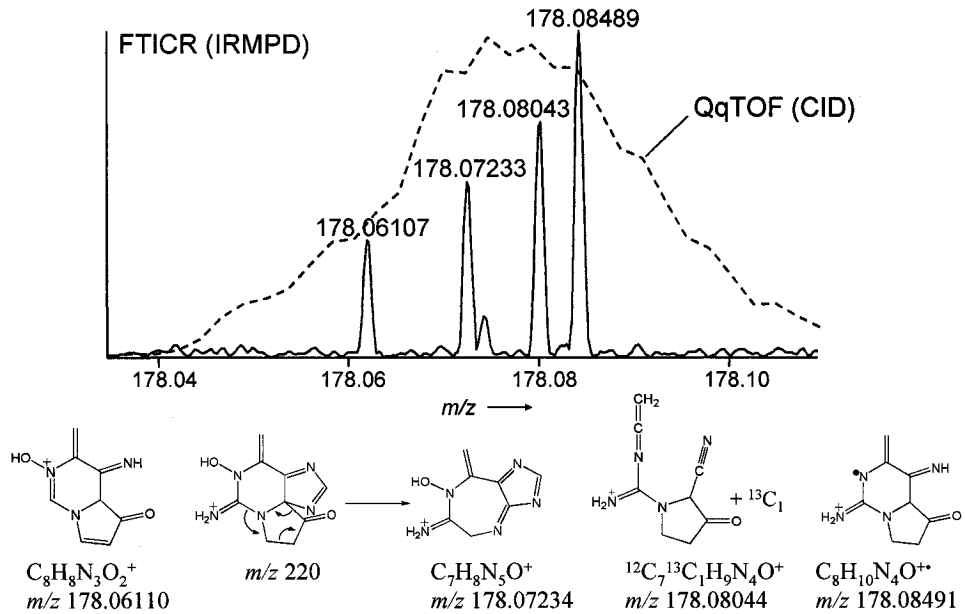

Figure 3.14 Four isobaric species at *m/z* 178 in the IRMPD product ion spectrum of NEO. The ion structures as well as their calculated exact masses are shown below the spectrum. For comparison, the QqTOF CID spectrum is given as a dashed line.

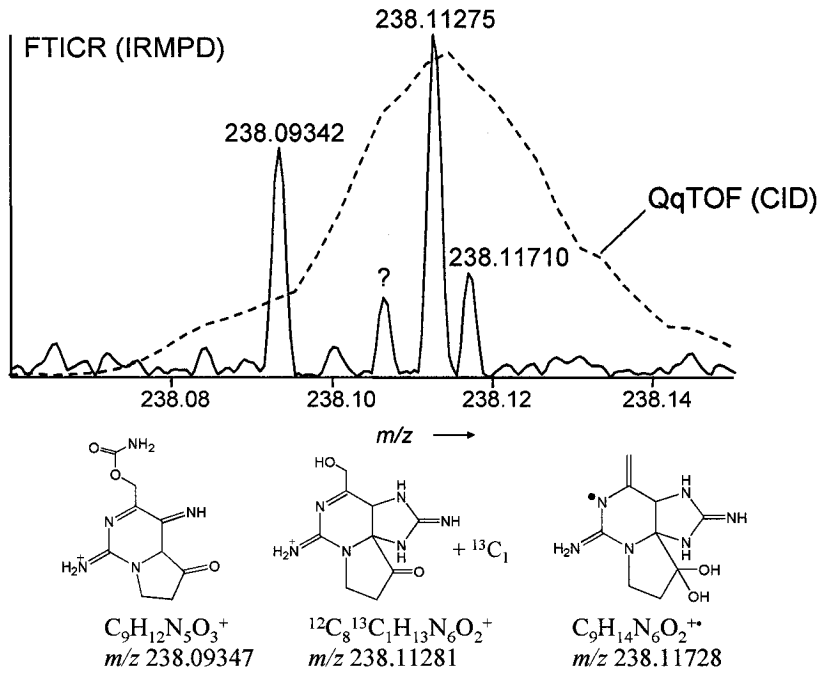

Figure 3.15 IRMPD spectrum of NEO near *m/z* 238 revealing four isobaric species. The structures of three of them as well as their calculated exact masses are given below the spectrum. The dashed line illustrates the QqTOF CID spectrum for comparison.

Prospects for automated formulae assignment

Here, the overall quality of the mass measurements for PSP product ions is expressed as a "first hit" rate, namely, the fraction of correct first-choice assignments of elemental compositions. For most small molecules with their usually simple CID spectra, the hit rate depends mainly on the error of the mass measurement alone, but not for these complex spectra. In these cases, both high mass accuracy and high resolving power must be available simultaneously. Not surprisingly, error-free assignments were possible only with FT-ICR, yielding a perfect 100% first hit rate. From the data in Table 3.7, the QqTOF first hit rate was only 56% and 65% for STX and NEO products, respectively, based on internal calibration with concurrent activation of the protonated molecules of PSPs and internal calibrant. The hit rate improves to 75% for STX with alternated data acquisition with monoisotopic activation, by largely eliminating the $^{13}C^{12}C_{c-1}$ interferences in the spectrum. The QqTOF first hit rate for NEO was calculated as 65% with both calibration methods, because the interferences in the NEO spectra originate

mostly from different fragmentation pathways. Interestingly, the QqTOF hit rate in these experiments approached almost 100% for both STX and NEO when only the non-interfered species were considered. That finding is important for routine QqTOF analyses, where less demanding analytical problems are more common, showing that automated formulae assignments are readily possible for pure samples in regular MS mode or for interference-free MS/MS spectra. Of course, since one never knows in advance whether potential interferences are present, only high mass resolution can give sample-independent reliable mass measurements.

Mass accuracies obtained with a commercial 7 Tesla FT-ICR instrument and QqTOF data were also compared using external calibration. Mass values were taken directly from the spectra, without any further processing and the results are summarized in Table 3.9. Naturally, the same isobaric interferences as discussed above occurred in the QqTOF spectra. The important point is under experimental conditions that many routine labs would choose, the mass measurement uncertainties of FT-ICR and QqTOF are quite similar, in the absence of peak overlap. The superior resolving power of the FT-ICR ($m/\Delta m$ (FWHM) between 60,000 to 150,000), however, is still seen in this comparison, in which interfering species are completely resolved, whereas accuracies still remain unacceptable with the QqTOF data.

The primary advantage of QqTOF over FT-ICR is higher sensitivity because TOF detectors approach single-ion detection limit, whereas FT-ICR detection typically requires of the order of 100 or more ions [199]. Thus, low-abundance MS/MS products are more easily detected by QqTOF than by FT-ICR. Furthermore, the experiment is usually simpler with a QqTOF instrument. The experiments done using the home-built 9.4 Tesla instrument were much less "routine" and required specialized considerations, as described in the Experimental section. It is almost certain, however, that the latest generation commercial FT-ICR instruments will allow more routine high-resolution tandem MS experiments.

Table 3.9 The measured masses, elemental formulae and mass uncertainties (ppm) for product ions observed in STX (a) and NEO (b) spectra from commercial 7 Tesla IRMPD FT-ICR and QqTOF CID instruments. Both systems were externally calibrated.

a)

Calculated mass	Elemental formula	FT-ICR (7 T)	Error (ppm)	QqTOF	Error (ppm)
300.14148	$C_{10}H_{18}N_7O_4^+$	300.14147	0.0	300.1411	-1.3
283.11493	$C_{10}H_{15}N_6O_4^+$	283.11536	1.5	283.1160	3.8
282.13091	$C_{10}H_{16}N_7O_3^+$	282.13129	1.3	282.1307	-0.8
266.08838	$C_{10}H_{12}N_5O_4^+$	266.08875	1.4	266.0886	0.8
265.10436	$C_{10}H_{13}N_6O_3^+$	265.10465	1.1	265.1040	-1.4
241.09313	$C_9H_{13}N_4O_4^+$	241.09345	1.3	241.0942	4.4
240.10912	$C_9H_{14}N_5O_3^+$	240.10954	1.8	240.1094	1.2
239.12510	$C_9H_{15}N_6O_2^+$	239.12550	1.7	239.1251	0.0
222.09855	$C_9H_{12}N_5O_2^+$	222.09883	1.3	222.0981	-2.0
221.11454	$C_9H_{13}N_6O^+$	221.11486	1.5	221.1145	-0.2
204.08799	$C_9H_{10}N_5O^+$	204.08829	1.5	204.0886	3.0
180.07675	$C_8H_{10}N_3O_2^+$	180.07712	2.0	180.0833	36.4
179.09274	$C_8H_{11}N_4O^+$	179.09302	1.6	179.0930	1.5
162.06619	$C_8H_8N_3O^+$	162.06644	1.6	162.0691	18.0
137.07094	$C_7H_9N_2O^+$	137.08241	1.7*	137.0801	66.8

*These numbers were obtained at 100% IRMPD laser setting. For all other experiments, a laser power setting of 50% was used.

b)

Calculated mass	Elemental formula	FT-ICR (7 T)	Error (ppm)	QqTOF	Error (ppm)
316.13639	$C_{10}H_{18}N_7O_5^+$	316.13656	0.5	316.1374	3.2
298.12583	$C_{10}H_{16}N_7O_4^+$	298.12596	0.4	298.1264	1.9
281.09928	$C_{10}H_{13}N_6O_4^+$	281.09954	0.9	281.1003	3.6
263.08872	$C_{10}H_{11}N_6O_3^+$	263.08888	0.6	263.0893	2.2
237.10945	$C_9H_{13}N_6O_2^+$	237.10964	0.8	237.1102	3.2
220.10671	$C_9H_{12}N_6O^{+\bullet}$	220.10691	0.9	220.0970	-44.1
220.08290	$C_9H_{10}N_5O_2^+$	220.08314	1.1	220.0970	64.1
207.09889	$C_8H_{11}N_6O^+$	207.09907	0.9*	207.0997	3.9
195.08765	$C_8H_{11}N_4O_2^+$	195.08799	1.7	195.0869	-3.9
178.08491	$C_8H_{10}N_4O^{+\bullet}$	178.08516	1.4*	178.0830	-10.7
177.07709	$C_8H_9N_4O^+$	177.07732	1.3	177.0797	14.8

*These numbers were obtained at 100% IRMPD laser setting. For all other experiments, a laser power setting of 80% was used.

Conclusions

The performance of two mass spectrometer designs, QqTOF and FT-ICR, has been compared for their ability to assign elemental formulae from very complex MS/MS spectra. The MS/MS spectra of two paralytic shellfish poisons were used for this comparison. The high peak density results in numerous spectral interferences in the QqTOF MS/MS spectra, mainly due to overlapping signals from isobaric fragment ion species and from M+1 interferences originating from the co-activated $^{13}C^{12}C_{c-1}$ MH^+ ions from PSPs. Accordingly, the QqTOF first hit rate for assigning true elemental composition was only 56% and 65% for STX and NEO product ions, respectively, whereas the FT-ICR experiments yielded first hits in 100% of all cases. The QqTOF hit rate improved to 75% for STX by using a modified data acquisition protocol, activating only monoisotopic precursor ions and thereby largely eliminating the $^{13}C^{12}C_{c-1}$ interferences. NEO proved to be more difficult because most interferences originate from unique fragment ions rather than $^{13}C^{12}C_{c-1}$ interferences. Moreover, the QqTOF hit rate was almost 100% when only non-interfering species were considered, showing that automated formulae assignments are readily possible for pure samples in full scan mode or for simple MS/MS spectra. Low energy CID spectra of synthetic pharmaceutical drugs and their metabolites are usually relatively uncomplicated, and automated high-throughput processing of QqTOF accurate mass data generated from these spectra would most likely give excellent hit rates in most cases.

Clearly, there are other factors that need to be included in a complete performance comparison of QqTOF and FT-ICR instruments. For example, practical issues such as the length of time required for obtaining statistically meaningful spectra, the practicality of hyphenation with fast chromatography or the suitability for applications in open access environments are important considerations. These are areas where QqTOF instruments have been scoring much higher than FT-ICR. The latest generation FT-ICR instruments, however, where MS/MS experiments can be conducted in the front end, either with a linear quadrupole ion trap or a Qq arrangement, coupled to an FT-ICR mass analyzer, allow increased compatibility with chromatographic runs [200]. Several researchers have investigated requirements for hyphenating high-resolution mass spectrometry with

modern separation techniques. For example, Grange and coworkers [201] have summarized the requirements for determining elemental compositions for compounds eluting from chromatographic columns. The current study, however, was mainly concerned with product ion spectra, which exhibit a variety of isobaric interferences. FT-ICR was required to obtain correct elemental compositions in these cases, since the required resolving power of >20,000 (FWHM) is currently out of reach for QqTOF instruments. For such spectra, both high resolving power and mass accuracy are required, as available from FT-ICR instruments.

Chapter IV- Dissociation Reactions of Protonated Anthracycline Antibiotics[†]

Introduction

Doxorubicin, a commonly prescribed treatment in several cancers, belongs to the family of anthracycline antibiotics [202]. Anthracyclines have been researched as cancer therapies for over 30 years and several structural analogs have been discovered through natural sources (e.g., *Streptomyces* bacteria) or synthesized, yielding different modes of action, potencies, targets and side effects [203]. The structure of these drugs includes a planar tetracyclic quinoid aglycone (anthracycline) with an aminoglycoside sugar (daunosamine) attached through an *O*-glycosidic bond (Figure 4.1). The therapeutic effect of this class of drugs is exhibited by stabilizing the complex between the topoisomerase IIα enzyme and DNA in the cell's nucleus [204]. Doxorubicin and daunorubicin have been used as antitumour antibiotics with potent activity against solid tumours and some leukemias. Several analogs have since been developed with the aim of improving the spectrum of activity or to lower toxicity, including epirubicin [205] and idarubicin [206].

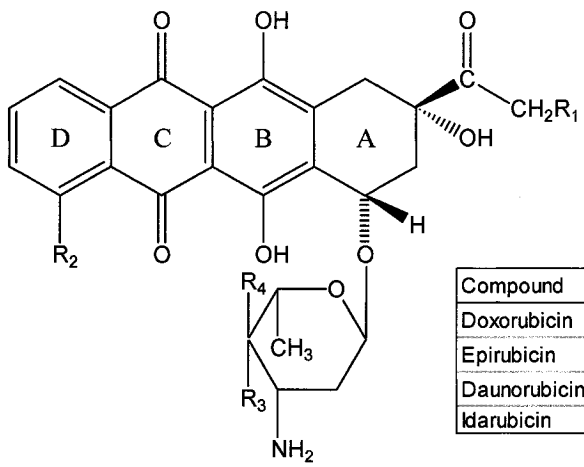

Compound	R_1	R_2	R_3	R_4
Doxorubicin	OH	OCH_3	OH	H
Epirubicin	OH	OCH_3	H	OH
Daunorubicin	H	OCH_3	OH	H
Idarubicin	H	H	OH	H

Figure 4.1 Structures of doxorubicin and three structurally-similar anthracycline drugs

[†] Reprinted in part from: Sleno L, Campagna-Slater V, Volmer DA. Dissociations reactions of protonated anthracycline antibiotics following electrospray ionization-tandem mass spectrometry. *Int. J. Mass Spectrom.* 2006, accepted for publication, with permission from Elsevier.

There have been many reports on the analysis of doxorubicin and related drugs by mass spectrometry. This technique has allowed the accurate quantitation of these drugs in biological matrices [207-209], as well as the analysis of drug-DNA complexes [210-212] and has also aided in the identification of numerous metabolites formed both *in vitro* and *in vivo* [213-216]. There have been numerous studies on the fragmentation of anthracyclines, using electron ionization [213, 214, 217-219], chemical ionization [219-221], field desorption [222, 223], fast atom bombardment [224, 225] and thermospray [219]. There has been no detailed investigation, however, using tandem mass spectrometry (MS/MS) with electrospray ionization. ESI has been applied to the analysis of anthracycline antibiotics previously, but mainly in quantitative applications. One previous report used in-source fragmentation for quantitation [207], while others implemented the higher selectivity technique of multiple-reaction monitoring for quantifying anthracyclines in urine [208] or doxorubicin and metabolites in rat plasma and tissue samples [209]. Some fragmentation studies have been reported for anthracyclines [219-221, 223-225], including some by FAB and CI-MS. Anthracyclines reveal an array of dissociation pathways by which they can form characteristic product ions. ESI, on the other hand, is a very soft method of ionization, yielding mostly protonated molecules. In this case, subsequent activation by tandem mass spectrometry can aid in the structural elucidation of analogous compounds such as metabolites or degradation products, and could also be useful for a more fundamental understanding of ion structure and stabilizing effects causing certain pathways to be favored under specific conditions.

ESI-MS/MS has a further advantage for this compound class since it has also been proven to be very useful for the analysis of anthracyclinones (aglycones) in positive ion mode, and therefore any analogs or metabolites of doxorubicin (or a related drug) can also be analyzed under similar conditions. In a previous study [224], the mass spectral characterization of several anthracyclines and corresponding aglycones was performed using fast atom bombardment. The aglycones were not ionizable in the positive ion mode, and therefore had to be characterized as negative ions. Also, no low mass fragments were monitored. Another problem with FAB spectra is that often there is a mix of molecular ions and protonated ions, causing the spectra to be potentially derived from

fragments of several precursors. Understanding all the fragmentation pathways for the anthracycline parent compound could also help in the elucidation of metabolites, even if the glycosidic bond has been cleaved. Main metabolic pathways for doxorubicin include the reduction of the keto group at C(13), cleavage of the glycosidic bond and conjugation with a glucuronide moiety [214]. Importantly, all these metabolites can be ionized with electrospray in positive ion mode. If a new anthracycline drug is assessed for metabolic pathways, ESI-MS/MS would be the method of choice for gaining important structural information, especially if there is a limited amount of sample.

This study describes the dissociative behavior of doxorubicin and three structurally similar compounds (epirubicin, daunorubicin, idarubicin). Epirubicin differs from doxorubicin only in the stereochemistry of a single hydroxyl group in the sugar moiety. Daunorubicin is structurally identical to doxorubicin, except the hydroxyl group at position C(14) on the A-ring side chain is removed (Figure 4.1). Idarubicin also has the same side chain as daunorubicin with an additional structural difference in the D-ring, caused by the removal of the methoxy group. Since all of these structures are extremely similar, we would also expect their mass spectrometric behavior to be quite comparable. Any differences we would observe in their fragmentation behavior should then be directly related to these small changes in the above-mentioned functional groups. In turn, more can be understood on their behavior when ionized in the gas phase. Certain pathways are seen to occur more readily in some structurally similar analogs vs. others. All major fragmentation reactions of these anthracyclines were studied in detail using tandem mass spectrometry and accurate mass data.

The usefulness of elucidating dissociation schemes for such molecules is exemplified in its application to metabolite identification. The study on the fragmentation of doxorubicin was further employed for the characterization of *in vitro* metabolites. These biotransformation products were analyzed using tandem mass spectrometry and accurate mass measurements with comparison to the fragmentation behavior of their parent compound.

Experimental

Chemicals

Doxorubicin hydrochloride, epirubicin hydrochloride, daunorubicin hydrochloride idarubicin hydrochloride, formic acid, potassium phosphate and human liver microsomes were purchased from Sigma. Methanol and Milli-Q organic-free water were used as solvents.

Mass Spectrometry

Collision-induced dissociation spectra were acquired in the positive ion mode on a MDS Sciex API 4000 triple quadrupole mass spectrometer with direct infusion of each anthracycline at a concentration of 10 μM in 50% methanol, 0.05% formic acid at a flow rate of 25 μl/min. The instrument was operated with a spray voltage of 5.5 kV, a declustering potential of 50 V, a source temperature of 100°C, a GS1 value of 50 and the curtain gas set at 10. Ultra-pure nitrogen was used as both curtain gas and collision gas. MRM transitions for important fragments (see Table 4.1) were monitored as the collision energy was ramped from 5-100 V (step size 0.5 V). The data for the fragment ion curves represent an average of five consecutive experiments.

MS^3 data were acquired on a MDS Sciex 4000 QTRAP (quadrupole-linear ion trap) system with the same doxorubicin stock solution (above) directly infused into the ion source at a flow rate of 25 μl/min. Source parameters were as follows: spray voltage 5.5 kV, declustering potential 40 V, source temperature 100°C, GS1 20 and curtain gas set at 10. Optimal CID conditions in q2 (see Table 4.2) were chosen to have maximal ion abundances for each ion chosen for secondary activation in the linear ion trap (LIT). Conditions in the LIT were: dynamic fill, excitation energy of 100 V and excitation time of 100 msec.

Accurate mass measurements were performed on an Agilent (Wilmington, DE, USA) LC/MSD TOF, equipped with an 1100 Agilent HPLC system, with a capillary voltage of 3 kV, source temperature at 350°C and fragmentor voltage of 125 V for MH^+ and 250 or 350 V for fragment ions. LC/MS was performed for these measurements with mobile phases: A; water, B; acetonitrile, both with 0.05% formic acid. Gradient elution

was as follows: 0.5 min isocratic at 15% B, followed by linear increase to 50% within a 15 minute run on a Zorbax SB-C18 rapid resolution 1.8 μm, 30 × 2.1 mm column at 0.1 ml/min. Internal mass calibration with *m/z* 121.050873 and 922.009827 (present in the Agilent ESI Tuning mix) delivered by the second sprayer of the dual electrospray source. Some measurements were conducted with loop injections of a standard solution of doxorubicin.

In vitro microsomal incubations and LC/MS Analysis

Mouse and human liver microsomes were incubated under the same conditions specified in Chapter 2, with 50 μM doxorubicin. Metabolism samples were analyzed by LC/MS on the API 4000 triple quadrupole MS in positive ion mode with the following source conditions: spray voltage 5 kV, declustering potential 50 V, curtain and nebuliser gas at 10 l/min, source temperature of 325°C. MS/MS experiments were conducted with a CAD gas setting of 6 and collision off set voltages of 20 V (doxorubicin) and 30 V (metabolites). Chromatographic separation was achieved using a Phenomenex Luna C18(2) 100 × 2 mm, 3μ column at 0.25 ml/min with same gradient as in ESI-TOF experiments above.

Results and Discussion

An extensive study of the fragmentation reactions of four anthracycline drugs (doxorubicin, epirubicin, daunorubicin, idarubicin) has been performed using tandem mass spectrometry following electrospray ionization. Several differences in the behavior of their protonated molecules following ion activation were seen, since certain fragmentation channels are more easily accessed in some of these analogs, presumably due to differences in stabilities or proton affinities of the product ions. The fragmentation of doxorubicin was initially studied in detail with tandem mass spectrometry, including MS/MS and MS^3 data. Accurate mass measurements also assisted in the elucidation of the dissociation reactions with corresponding ion structures for the product ions of doxorubicin. A fragmentation scheme is presented detailing the important dissociation pathways of protonated doxorubicin with a comparison to the other anthracycline drugs.

General fragmentation behavior of Doxorubicin and its analogs

Doxorubicin and its analogs exhibit similar fragmentation reactions following collision-induced dissociation. Table 4.1 lists the different fragment ions for doxorubicin and the corresponding *m/z* values for the analogous product ions of the other three molecules. The main pathways include the cleavage of the glycosidic bond with the charge either residing on the aglycone moiety or the sugar portion, cleavage of the side chain on the A-ring, and further small neutral losses, such as H_2O, NH_3 and CO. The CID spectra for each of the four analogs are shown in Figure 4.2. These spectra exhibit three main groups of ions; one due to the protonated molecule and some water loss ions, a cluster of ions due to the aglycone portion of the molecules with additional neutral losses and a third group in the low mass range for the ions of the daunosamine sugar. It is easily seen that several fragmentation pathways are lost for the aglycone portion due to changes in the precursor ion structure, as in the case of daunorubicin and idarubicin. The side chain hydroxyl group, which is missing in both of these molecules, must therefore be central in an important fragmentation reaction. Epirubicin also shows a more important water loss fragment from the protonated molecule, potentially due to the different orientation of the hydroxyl group in the sugar group (4′-epi daunosamine).

Table 4.1 Corresponding fragment ion masses for doxorubicin and its three analogs

MH^+	$-H_2O$	aglycone	CH_2OH (side chain)	-side chain	$-CH_3$ radical	sugar	sugar fragments
Dox/Epi (544)	526/508	415/397/379	361/346/333	321	306	148/130	113/95/86/72/69
Dau (528)	510/484	399/381/363	n/a				
Ida (498)	480/462	369/351/333		291	n/a		

Additional information for the elucidation of complex fragmentation pathways can be gained by using multiple stages of tandem mass spectrometry (e.g., in a conventional 3D ion trap [226] or in a quadrupole-linear ion trap [227]). Using a second stage of MS/MS in the linear ion trap of a QqLIT instrument provided important information for the assignment of dissociation reactions. The conditions in the second quadrupole (collision cell, q_2) were individually optimized for the formation of each product ion of doxorubicin seen in the triple quadrupole spectra. Several experiments were subsequently conducted with on-resonance CID in the LIT, producing fragment ions derived only from the isolated product ion initially formed in q_2. These results are summarized in Table 4.2. This data yields supplementary information on the fragmentation pathways of doxorubicin. For example, the MS^3 data shows that *m/z* 333 can be formed from *m/z* 361, a fragment involving the side chain of doxorubicin and epirubicin.

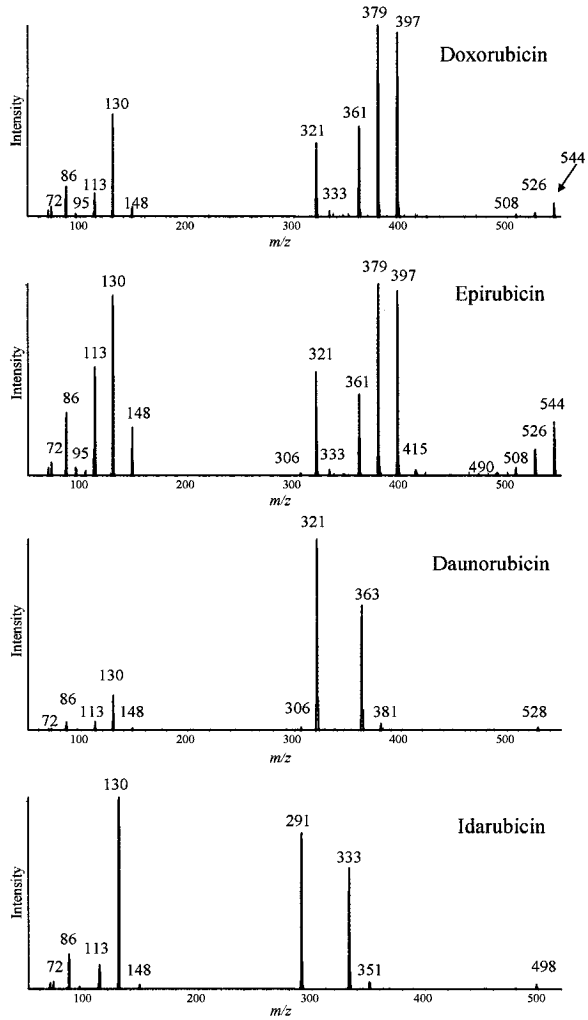

Figure 4.2 CID spectra of the four anthracycline drugs at a collision offset voltage of 25 V.

Table 4.2 Summary of MS^3 results for doxorubicin

m/z of precursor	CE (q2)	Ions detected
544	5	**526**, **508**, **490**, **415**, 398, **397**, **379**, **361**, **346**, **333**, **321**
526	12	**508**, **490**, 472, 423, 414, **397**, **379**, **361**, 351, 337, **321**
508	20	491, **490**, 473, 472, **397**, 396, 380, **379**, **361**, **346**, 337, **321**
415	10	**397**, **379**, **361**, **321**
397	15	**379**, **361**, 351, **346**, **333**, **321**
379	25	**361**, 351, **346**, **333**, **321**
361	37	**346**, **333**
346	57	--
333	42	331, 318, 315, 305, 303, 287, 275, 259, 145
321	37	**306**, 293, 277, 262
306	65	--
148	20	**130**
130	23	**113**, **95**, **86**, **72**, **69**
113	35	**95**, 85, **69**
95	50	67
86	50	--

Ions represented in the dissociation scheme for doxorubicin (Figure 4.3) are bolded in this table.

Accurate mass data were collected on an electrospray-time of flight (ESI-TOF) instrument. Very good accuracies were obtained for most product ions using internal calibration. This instrument did not allow precursor ion selection, therefore fragment ions were formed by increasing the voltage at the end of the capillary in the source (fragmentor voltage) [228]. These results are listed in Table 4.3, along with corresponding resolutions and relative intensities of the ions. The information gained from these experiments aided in the elucidation of the fragmentation scheme and the ion structures for all major ions formed from protonated doxorubicin (see Figure 4.3). Most of these results were produced using LC/MS, however, certain ions that did not have acceptable ion intensities showed better results during flow injection analysis.

Table 4.3 Accurate mass data for doxorubicin product ions

m/z (measured)	*m/z* (calculated)	Formula	mass accuracy (ppm)	% Intensity	Resolution
86.0612	86.0600	$C_4H_8NO^+$	13.5	*	3406
113.0609	113.0597	$C_6H_9O_2^+$	10.6	*	3723
130.0861	130.0863	$C_6H_{12}NO_2^+$	-1.2	8	4360
148.0969	148.0968	$C_6H_{14}NO_3^+$	5.3	*	4433
306.0545	306.0523	$C_{18}H_{10}O_5^{\bullet+}$	7.3	7	5958
321.0761	321.0758	$C_{19}H_{13}O_5^+$	1.1	100	6158
333.0759	333.0758	$C_{20}H_{13}O_5^+$	0.5	15	6754
346.0464	346.0472	$C_{20}H_{10}O_6^{\bullet+}$	-2.3	7	6191
361.0708	361.0707	$C_{21}H_{13}O_6^+$	0.4	51	6528
379.0820	379.0812	$C_{21}H_{15}O_7^+$	2.0	50	6712
397.0917	397.0918	$C_{21}H_{17}O_8^+$	-0.2	56	7005
415.1040	415.1024	$C_{21}H_{19}O_9^+$	4.0	*	6959
526.1700	526.1708	$C_{27}H_{28}NO_{10}^+$	-1.5	2	8070
544.1806	544.1813	$C_{27}H_{30}NO_{11}^+$	-1.4	17	7669

* Ions measured from loop injections of doxorubicin (see Experimental)

A fragmentation scheme (Figure 4.3) has been proposed using data generated from collision-induced dissociation experiments and accurate mass measurements. In the cases where the protonation site is not specified in the structures shown in the scheme, the *m/z* values have a (H^+) symbol next to them to remind the reader that the structure shown is not an ion unless it is protonated. It has been previously reported [221], however, that the initial site of protonation of anthracycline antibiotics occurs on the oxygen of the glycosidic bond, mainly due to the prominent fragmentation at that position, with the oxygen atom remaining on either the aglycone portion (e.g., *m/z* 415,

130) or the sugar moiety (e.g., *m/z* 397, 148). In both cases, the proton can remain attached to the aglycone or the sugar. For the ion at *m/z* 361, the charge is shown localized on the side chain, in order to rationalize its formation from *m/z* 379 (with protonation at the side chain). Proposed ion structures are given for all the major ions produced from the protonated doxorubicin molecule. The cleavage of the aglycone portion from the sugar can occur on either side of the oxygen of the glycosidic bond. Therefore, the resulting ions are *m/z* 415 or 397 for the charged aglycone portion or *m/z* 148 and *m/z* 130 for the protonated sugar. Further fragmentation of the aglycone ion consists of neutral losses of water (*m/z* 415→397→379→361), CO (*m/z* 361→333) or the side chain on the A-ring (*m/z* 379→321). Also, a stable radical ion is formed by the loss of a methyl radical from the methoxy group on the D-ring (*m/z* 361→346, *m/z* 321→306). The product ions at *m/z* 361, 346 and 333 are due to the presence of the hydroxyl group at R_1 (refer to Figure 4.1). A water molecule is lost from the side chain of the aglycone ion at *m/z* 379, and the resulting structure is shown in Figure 4.3 (*m/z* 361). This ion can further dissociate by loss of CO to form a stable tropylium-type ion at *m/z* 333. The detailed mechanism proposed for the formation of these two ions is illustrated in Figure 4.4.

In the case of the glycosidic bond cleavage occurring with retention of the charge on the sugar portion, *m/z* 148 and *m/z* 130 (oxonium ion) are formed by bond cleavage on either side of the glycosidic oxygen atom. These two ions are also related by a simple water loss reaction as well. Several fragmentation reactions are rationalized using the linear forms of the sugars, which are in equilibrium with the cyclic forms (Figure 4.3). Ammonia loss from *m/z* 130 yields an ion at *m/z* 113, which can subsequently lose a water molecule forming *m/z* 95. Additionally, the MS^3 results showed a product ion of *m/z* 95 at *m/z* 67, which is likely the product of a facile CO loss from the *m/z* 95 structure shown in the Figure 3. The ion at *m/z* 130 can also further dissociate into *m/z* 86 (loss of CH_3CHO, acetaldehyde) and *m/z* 72 (loss of CH_3CH_2CHO) as seen in the fragmentation scheme. The ion at *m/z* 69 is formed via a similar acetaldehyde loss from *m/z* 113.

All of the pathways discussed above were monitored for the four investigated anthracycline antibiotics under conditions of varying collision energy in the collision cell

of a triple quadrupole in order to see if certain pathways are preferred for the different structural analogs.

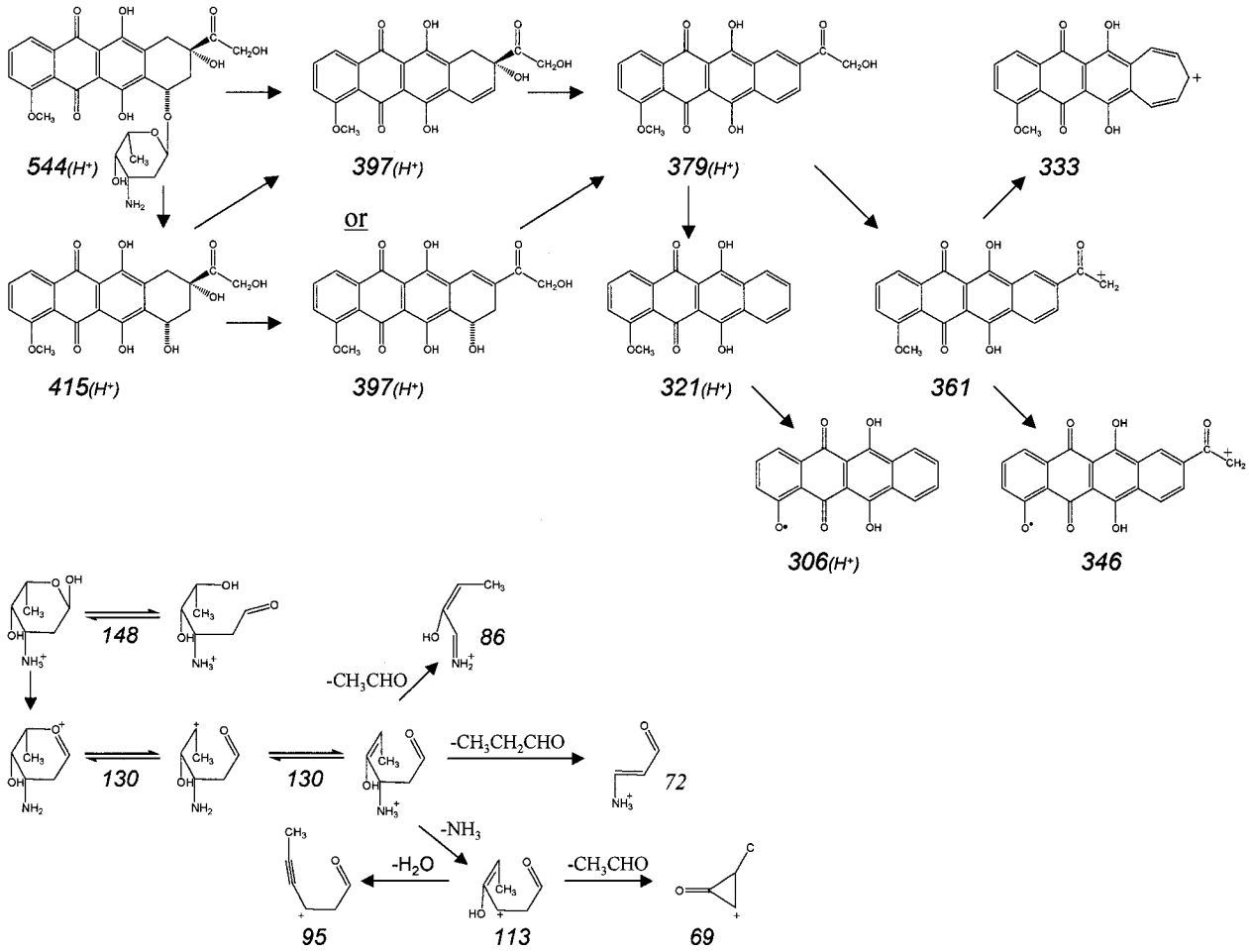

Figure 4.3 Proposed fragmentation scheme for doxorubicin. Note that a proton is added next to the mass of the ion for any structure where the protonation site is not specified. Some isomeric product ions are shown with two possible structures based on their different fragmentation pathways. Fragment ions for the sugar moiety are shown below those for the aglycone portion of doxorubicin.

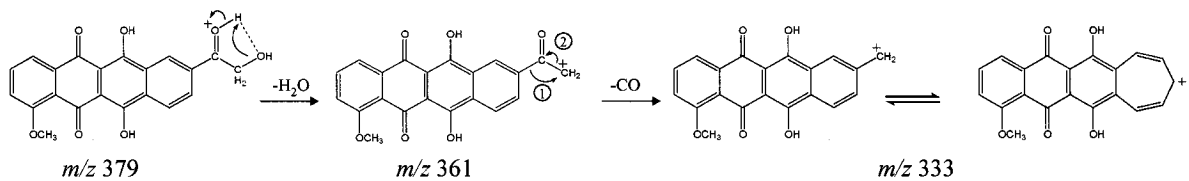

Figure 4.4 Proposed fragmentation scheme for the formation of ions at *m/z* 361 and 333 of doxorubicin.

Comparison of MS/MS of doxorubicin analogs

Figure 4.5 represents breakdown curves of the four investigated drugs for the important fragmentation pathways discussed above. The curves are divided into ions of the aglycone portion (with water loss from the protonated molecule as well, on the left of the figure) and ions of the amino sugar (on the right). The most obvious difference, of course, is observed when the side chain is altered, as for daunorubicin and idarubicin, and consequently, several dissociation reactions are absent. This causes the ions at *m/z* 321 and 291 to be more significant for daunorubicin and idarubicin, respectively. Daunorubicin can further dissociate by loss of a methyl radical producing *m/z* 306. Since idarubicin does not have the possibility for any neutral loss occurring due to the side chain of the A ring, nor is it able to lose the methyl radical from the D ring, it seems to exhibit no further fragmentation in comparison to the other three molecules at higher collision energies. There is, however, another pathway occurring above collision energies of 60 V with two main product ions at *m/z* 217 and 189. The structures of these ions can be easily rationalized from *m/z* 291. Figure 4.6 illustrates the appearance curves for these ions as well as our proposed mechanism for their formation. The keto group is the most likely position for the proton, which is initially removed by the OH group adjacent for a facile loss of H_2O. Then a double CO loss forms *m/z* 217, which can then cleave a further CO group for the final structure shown for *m/z* 189. These types of dissociations were not seen for the other anthracyclines under the energy regime monitored, since they had other reactions possible.

In Figure 4.5, epirubicin is shown to have a much larger relative abundance of the ion resulting from a single water loss from its protonated ion as compared to doxorubicin. This is assumed to be due to the different position of the hydroxyl group in the sugar, causing a more favorable orientation for water to be lost from that part of the molecule. Also, idarubicin has a much larger contribution of ions with the charge being retained on the sugar compared to the other anthracyclines. This is presumably due to the decrease in stability of the aglycone portion as a protonated product in comparison to the daunosamine sugar. The sole difference between the structures of daunorubicin and idarubicin is the presence of the methoxy group at R_2 (see Figure 4.1). The methoxy

group could therefore be very important in the stabilizing the charge site on the protonated aglycone ion.

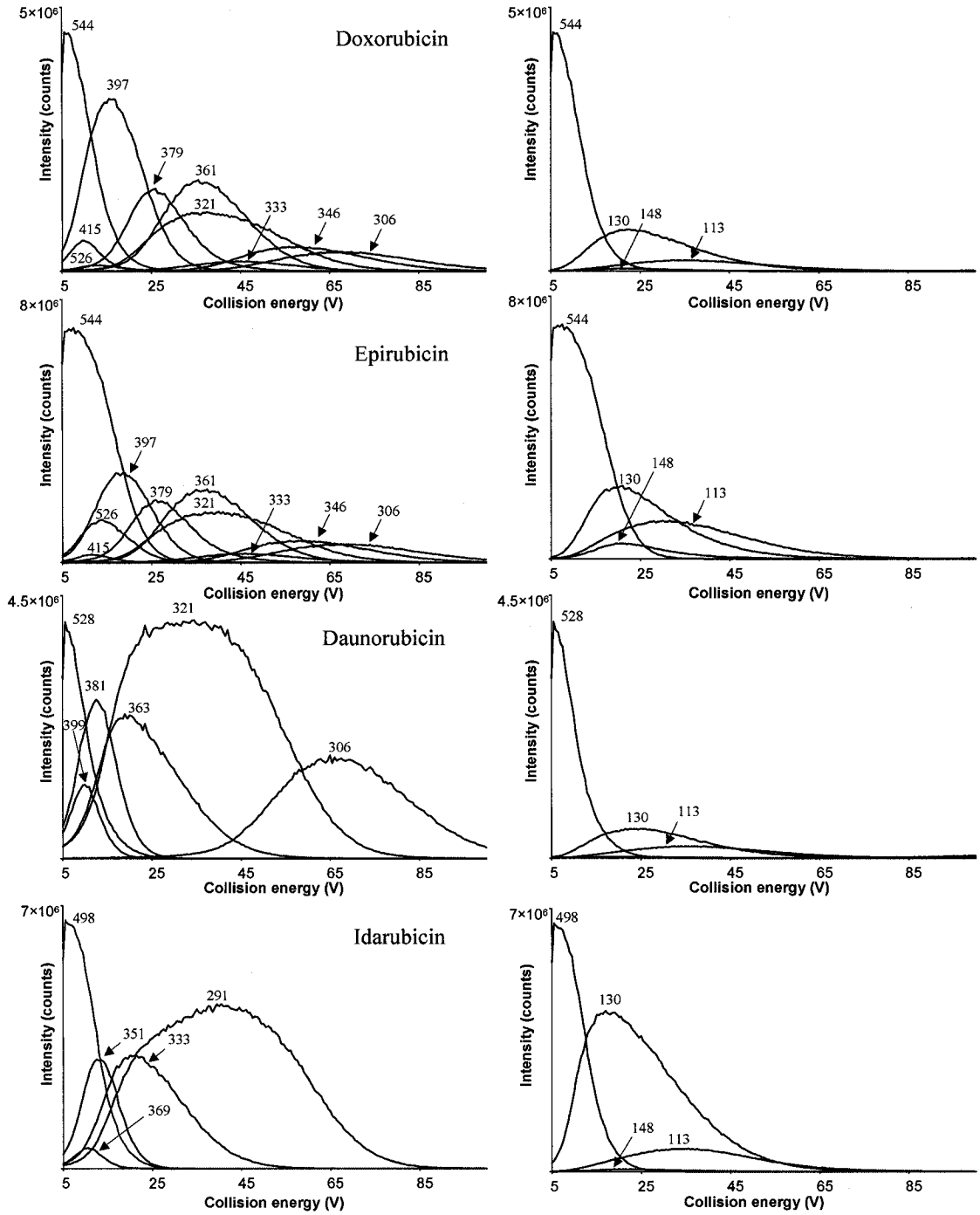

Figure 4.5 Breakdown curves showing differences between pathways of doxorubicin analogs.

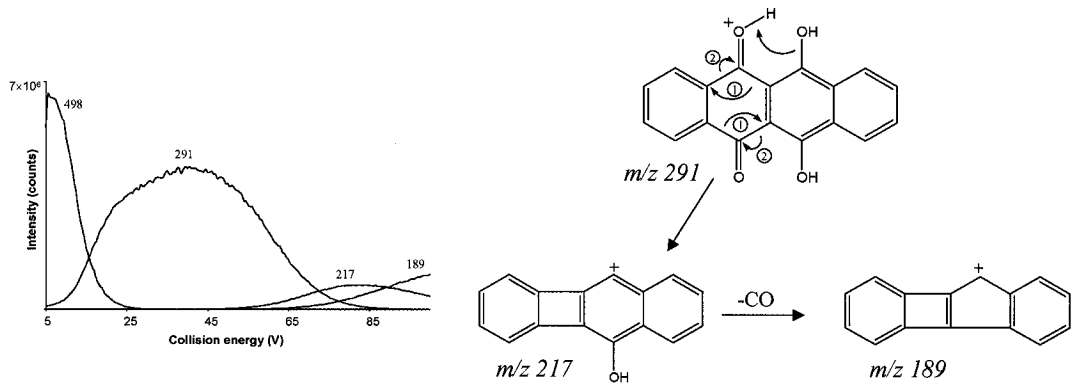

Figure 4.6 Specific dissociation reactions for idarubicin under investigated energy regime.

MS characterization of doxorubicin metabolites

In vitro incubations of doxorubicin were analyzed for the formation of metabolites. The MS/MS behavior of the formed metabolites was compared to that of doxorubicin using the fragmentation scheme of doxorubicin outlined above. Initially, a full scan analysis of control (no NADPH) and metabolism samples identified new chromatographic peaks due to doxorubicin metabolites. Representative chromatograms are shown in Figure 4.7 for mouse liver microsomal incubations. Human microsomes gave very similar results. Extracted ion chromatograms are shown for two major metabolites (at *m/z* 399 and 401). ESI-TOF analysis of these chromatographic peaks gave *m/z* 399.1080 and 401.1232 as accurate masses, yielding elemental formulae $C_{21}H_{19}O_8$ (1.4 ppm) and $C_{21}H_{21}O_8$ (0.3 ppm) for their protonated ions, respectively. As seen from these formulae, there has been enzymatic cleavage of the sugar moiety from doxorubicin. The spectra of these metabolites, along with accurate mass measurements for in-source fragments, allowed the elucidation of the metabolite structures shown in Figure 4.8. The protonated ions at *m/z* 399 and 401 show very similar fragmentation behavior. A proposed fragmentation scheme for these metabolites is illustrated in Figure 4.9. One major difference in the dissociation of these two ions is the presence of an important fragment at *m/z* 365 for the *m/z* 401 precursor. This ion occurs due to an extra water loss possible in this case. The two major metabolites formed were identified as deoxy-doxorubicin aglycone and deoxy-doxorubicinol aglycone. The daunosamine sugar has

been lost through reductive glycosidic cleavage and the carbonyl group on the A ring side chain has been reduced to a secondary alcohol for the metabolite at *m/z* 401. Tandem mass spectrometry and ESI-TOF accurate mass measurement represents a robust and facile strategy for metabolite identification when the fragmentation of the parent compound has been studied.

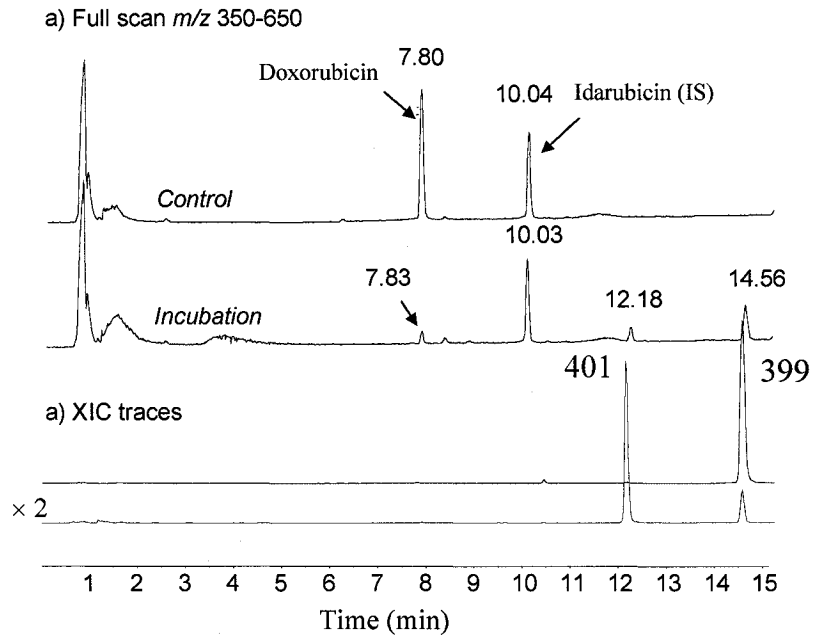

Figure 4.7 Representative chromatograms for mouse liver microsomal incubations with 50 μM doxorubicin (spiked with internal standard, idarubicin). Full scan analysis (*m/z* 350-650) shows two new peaks in sample incubated with NADPH cofactor versus control sample (above). Extracted ion traces (below) illustrate peaks for *m/z* 399 and *m/z* 401.

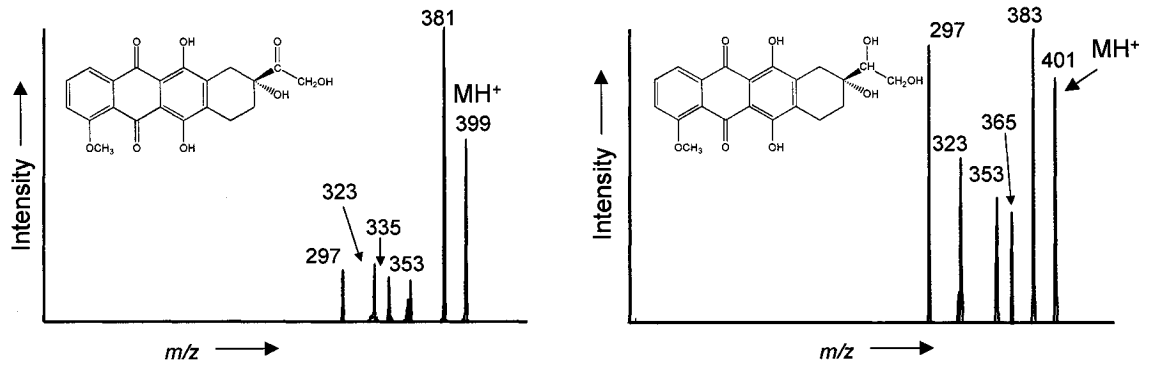

m/z (measured)	m/z (calculated)	Formula	mass accuracy (ppm)
282.0523	282.0523	$C_{16}H_{10}O_5^{+\bullet}$	0.1
297.0760	297.0758	$C_{17}H_{13}O_5^+$	0.8
323.0913	323.0914	$C_{19}H_{15}O_5^+$	-0.3
353.0977	353.1020	$C_{20}H_{17}O_6^+$	-12.1
381.0968	381.0969	$C_{21}H_{17}O_7^+$	-0.2
399.1079	399.1074	$C_{21}H_{19}O_8^+$	1.1

m/z (measured)	m/z (calculated)	Formula	mass accuracy (ppm)
282.0532	282.0523	$C_{16}H_{10}O_5^{+\bullet}$	3.3
297.0761	297.0758	$C_{17}H_{13}O_5^+$	1.2
323.0929	323.0914	$C_{19}H_{15}O_5^+$	4.6
353.1016	353.1020	$C_{20}H_{17}O_6^+$	-1.0
365.0994	365.0891	$C_{21}H_{17}O_6^+$	-7.0
383.1109	383.1125	$C_{21}H_{19}O_7^+$	-4.3
401.1228	401.1231	$C_{21}H_{21}O_8^+$	-0.7

Figure 4.8 Triple quadrupole CID spectra for doxorubicin metabolites (above) and accurate mass data from ESI-TOF analyses (below).

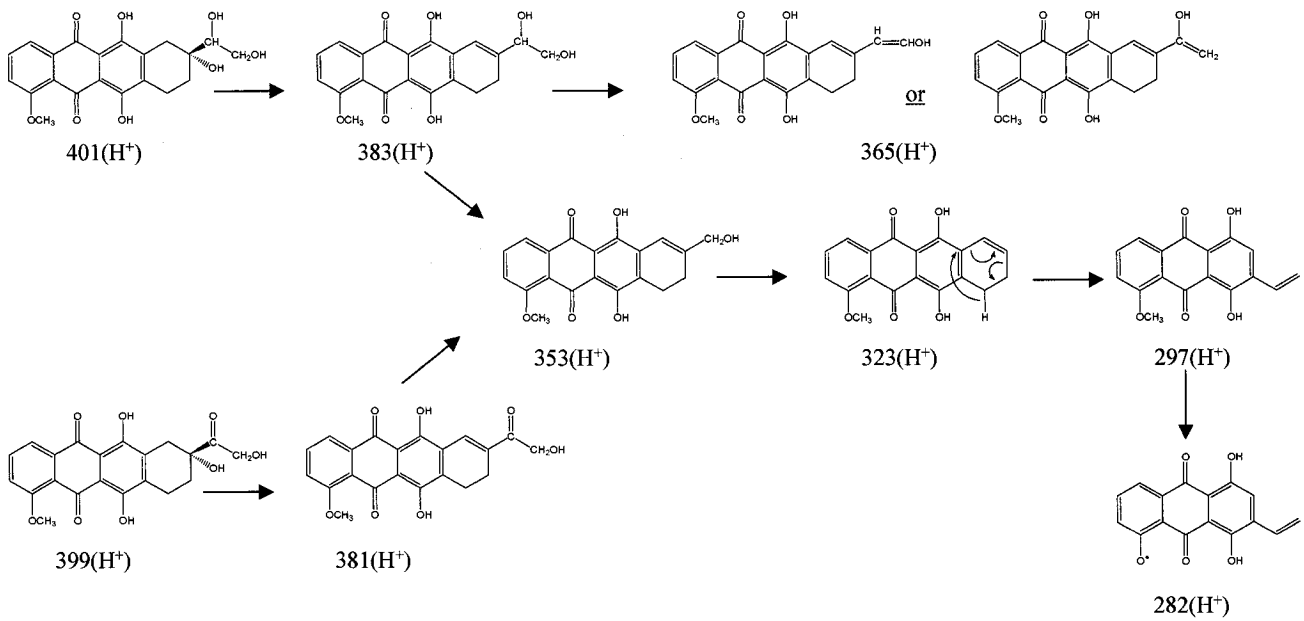

Figure 4.9 Proposed fragmentation scheme for doxorubicin metabolites

Conclusions

Doxorubicin and three of its structural analogs were studied by tandem mass spectrometry following electrospray ionization. MS/MS analysis led to several structurally informative product ions, and differences between these fragments were seen due to small alterations to the functional groups in these molecules. Doxorubicin was considered for the detailed study of its dissociation reactions by collision-induced dissociation, MS^3 experiments and accurate mass measurements. Subsequently, the important fragments for each of the four molecules were monitored at increasing collision energies in order to visualize the differences in stabilities of their product ions. This approach proved very useful for the understanding of fragmentation mechanisms in general and studying the varying stabilities of ion structures in the gas phase following ion activation under low energy CID conditions. Furthermore, a detailed investigation of the fragmentation of structural analogs can help shed light on the importance of certain functional groups in the stabilities of resulting product ions. These results can also be used to elucidate unknown structures of related compounds, as in the case of metabolism studies and the analysis of degradation products.

CHAPTER V- Quantitative Small Molecule MALDI[†,‡]

Introduction

Matrix-assisted laser desorption/ionization (MALDI) mass spectrometry is most often applied for qualitative measurements of biopolymers such as peptides and proteins. Recently, however, new instrumental developments, novel matrices and specialized MALDI sample preparation procedures have extended its application range. It has been demonstrated by several researchers that MALDI can be used for extremely rapid and quantitative analysis of small molecules as well as in imaging studies [229-231]. One important factor that supported the implementation of MALDI in various applications was the development of atmospheric pressure (AP) MALDI [232]. AP-MALDI sources are relatively inexpensive and can be easily mounted onto several commercial liquid chromatography/mass spectrometry instruments that are typically used for atmospheric pressure ionization (API) techniques, such as electrospray ionization or atmospheric pressure chemical ionization. MALDI has several advantages over these techniques. Most importantly, it can achieve a high sample throughput [230], making it attractive to analytical laboratories for increasing productivity and efficiency. Furthermore, in comparison to ESI, MALDI is not as susceptible to ion suppression from salts or buffers [31, 233, 234].

The use of MALDI in quantitative applications, however, is seriously complicated by the irreproducible analyte signals resulting from non-homogeneous co-crystallization of the analyte with the organic matrix used for desorption and ionization. Quantitative analysis of small molecules such as pharmaceutical drugs is even more difficult because of the strong signals for *m/z* <500 from MALDI matrix ions, which have been shown to appear at virtually every mass in the low *m/z* region [230]. Matrix-less desorption and ionization techniques (DIOS [235], *etc.*) would be the ideal solution, but the required

---

[†] From: Sleno L, Volmer DA. *Rapid Commun. Mass Spectrom.* 2005; **19**: 1928 and Sleno L, Volmer DA. Assessing the properties of internal standards for quantitative MALDI of small molecules. *Rapid Commun. Mass Spectrom.* 2006, accepted for publication, 2005 & 2006 © John Wiley & Sons Limited. Reproduced with permission.

[‡] Reproduced with permission from: Sleno L, Volmer DA. *Anal. Chem.* 2005; **77**: 1509. ©Copyright 2005 American Chemical Society.

substrates have so far failed to show their general applicability. Moreover, under regular MALDI sample preparation conditions, the interfering matrix ions are likely in much higher abundance than the analyte ions. Therefore, quantitation of compounds with low molecular weights, in full-scan or single-ion monitoring mode, is often very difficult. The isobaric interferences can be conveniently circumvented, however, if structure-specific precursor ion/product ion combinations for the analytes in a tandem mass spectrometer are used for quantitation [230]. In particular, the combination of MALDI with a triple quadrupole MS has shown great promise in drug analyses that are currently dominated by ESI methods. For the present work, there are two specific advantages of MALDI-QqQ that are important: first, the availability of dedicated QqQ scan modes (precursor ion and neutral loss scans), for selective class-specific screening of compound analogs. Second, the very high duty cycle of a QqQ instrument in the multiple reaction monitoring mode for a significant increase in sensitivity for quantitative measurements. These advantages are further enhanced by using a high frequency (kHz) laser [230, 236] for ion generation, instead of the more common N_2 lasers with repetition rates usually from 5 to 20 Hz. A kHz laser generates a semi-continuous ion beam, which is ideal for mass analysis in a beam-type instrument such as the triple quadrupole MS. Statistically meaningful results with several thousand laser shots per sample can be obtained in only a few seconds, the averaging of which dramatically improves the overall precision [230].

Furthermore, in MALDI analyses of small molecules, the type and concentration of the matrix compound is often also different from those used in peptide/protein analyses. α-Cyano-4-hydroxycinnamic acid (CHCA) has been shown to produce uniform crystallization and has been used successfully in numerous small molecule analyses [229, 237-239]. Moreover, it has been suggested that the optimum ratio of matrix-to-analyte for low molecular weight compounds is lower than for biopolymers [240]. At very low ratios, however, higher laser energies may be necessary, thus in-source fragmentation can become an important phenomenon in these cases. Also, sample spots are less evenly covered with matrix crystals and therefore the sample must be manually searched for so-called "sweet spots" of matrix/analyte co-crystals giving satisfactory signals [241]. Additionally, the use of an internal standard is crucial for any quantitative experiment.

One goal of this study is aimed at systematically investigating the suitability of different internal standards for analysis and quantitation of low molecular weight compounds (<500 Da) by MALDI mass spectrometry. An appropriate internal standard for MALDI must compensate for any crystallization irregularities but also for subsequent desorption and gas-phase effects. Crystallization irregularities result from sample segregation during the drying of the sample spots on the MALDI plate. The matrix/analyte mixture tends to partition during the slow crystallization process [242]; thus, it is very important that the solubilities of all components are ideally matched. Sample segregation is of particular concern when mixed solvents are used [243, 244], where one solvent component is more easily evaporated than another. Owens and coworkers have successfully demonstrated [243] the use of azeotrope mixtures for MALDI analysis of polymers, to avoid fractional precipitation of components during solvent evaporation. Other advanced sample preparation procedures for improved co-crystallization of matrix and analyte have been reported [245-248]. In reality, however, many scientists prefer the simplicity of the dried droplet technique.

In addition to the solvent solubility requirements, matching the analyte and the matrix in terms of their relative polarities is equally important for homogeneous incorporation of analytes in the final crystal structure of the matrix ("solid solution") [249]. Furthermore, it was interesting to see whether this structural similarity was important for all three mixture components; *viz.*, the analyte(s), the internal standard, and the matrix.

Naturally, an isotope-labeled standard is the ideal choice, as it chemically behaves almost exactly as its unlabeled counterpart. Such a standard guarantees identical crystallization and gas-phase behavior. The use of isotope standards, however, may not always be possible using linear MALDI-TOF instruments, because of the insufficient mass resolving power [250]. Although isotope standards are commercially available for many relevant small molecules, they are expensive and most often not offered for structural analogs of the analyte of interest, such as drug metabolites. Also, in certain multi-component assays, it is convenient to use a single internal standard for several compounds. Therefore, for general quantitative applications, it is very common to utilize structurally analogous compounds. The question then arises, how different can the

internal standard be from the analyte molecule, allowing quantitative measurements with a sufficient precision? Several interesting studies on the application of different internal standards for quantitative MALDI have been published [240, 241, 250-255]. No systematic study, however, on the comparison of internal standards for quantitative MALDI and correlation of the observed results with physicochemical differences between analyte and internal standard has been reported previously.

This chapter will involve some fundamental studies as well as some real applications of quantitative small molecule MALDI. First, some technical aspects pertaining to small molecule MALDI for quantitative purposes will be discussed for a group of four pharmaceutical drugs. In particular, the role of laser parameters on the ablation characteristics, and their impact on the analytical assays were systematically investigated. Different organic matrices were evaluated for automated high-throughput quantitative studies and precision of measurement. A series of pharmaceutical drugs were studied in terms of assay sensitivity and linearity of response.

Next, several small molecules with increasingly different structural features and physicochemical properties were investigated as internal standards. This allowed a set of rules to be defined for choosing appropriate internal standards for successful quantitative MALDI analyses. Three sets of compound classes were investigated, acylcarnitines, 4-quinolone antibiotics as well as a very diverse group of drug compounds.

Both screening and quantitative assays would benefit from high-throughput MALDI-triple quadrupole analyses. A comprehensive analytical study was carried out for the determination of spirolide toxins in phytoplankton samples. Only few studies have been reported for MALDI of toxins [256-261] and there appears to be no detailed study on the application of this technique for the characterization of non-peptide toxins. The reasons for the limited use of MALDI for toxins are based on the above-mentioned limitations: many non-peptide toxins have low molecular weights and there is significant potential for interferences with fluctuating ion signals from the MALDI matrix [229]. The quantitative analysis of 13-desmethyl spirolide C was compared and cross-correlated with results from ESI LC/MS/MS analyses. Precursor ion and neutral loss scans were also employed for screening the phytoplankton extract for spirolides.

Experimental

Chemicals

The following chemicals were obtained from Sigma-Aldrich: pipemedic acid, enoxacin, norfloxacin, ofloxacin, lomefloxacin, cinoxacin, oxolinic acid, nalidixic acid, flumequine, amprolium, nadolol, timolol, niflumic acid, enalapril maleate, ramipril, prazosin, sulfamethazine, vincamine, quinidine, hydroquinine, hydroquinine 4-methyl-2-quinolyl ether, α-cyano-4-hydroxycinnamic acid (CHCA), 2,5-dihydroxybenzoic acid (DHB), 3,5-dimethoxy-4-hydroxy cinnamic acid (sinapinic acid, SA), ammonium formate, formic acid, and trifluoroacetic acid (TFA). Ciprofloxacin was obtained as a 10 mg/ml I.V. dosing solution from Miles Canada Inc. (Etobicoke, ON, Canada). Sarafloxacin was a gift from Dr. Steve Cepa, Abbott Laboratories (Chicago, IL, USA), danofloxacin and desmethyldanofloxacin were from Pfizer Inc. (Groton, CT, USA) and enrofloxacin was provided by Bayer AG (Wuppertal, Germany). Acyl-L-carnitine standards were purchased from Dr. Herman J. ten Brink (VU Medical Center Metabolic Laboratory, Amsterdam, The Netherlands). Acetonitrile, methanol and Milli-Q organic-free water were used as solvents. Standard solutions of 13-desmethyl spirolide C (CRM-SPX1, 7.0 μg/ml) and gymnodimine (CRM-GYM, 5.0 μg/ml) in methanol with 0.05% TFA were obtained through IMB's Certified Reference Materials Program (Halifax, NS, Canada). The crude extract and fractions used as unknown samples in these experiments were prepared from *Alexandrium ostenfeldii* culture as described in Chapter 2.

Sample preparation

Standard solutions of each analyte and internal standard were prepared in 50% acetonitrile (ACN), combined with an equal volume of matrix solution (4 mg/ml CHCA in 50% ACN, 0.2% TFA). Each sample (1 μl) was spotted directly on a 10×10 stainless steel MALDI plate (Perseptive Biosystems, Framingham, MA, USA).

For spirolide analyses, calibration curves were analyzed at different matrix concentrations as well as for constant matrix-to-analyte ratios. For quantitative experiments in phytoplankton samples, a calibration curve for $C_{Des\text{-}C}$ = 0.01 to 1.75 μg/ml (C_{GYM} = 0.625 μg/ml) was used, with C_{CHCA} = 2.5 mg/ml and 75% methanol (with 0.1%

TFA). Phytoplankton samples (1-14) were prepared in the same manner with appropriate dilution factors. Five samples (samples 8, 11-14) were prepared by solid phase extraction by loading 500 µl diluted sample onto pre-conditioned cartridges (Oasis HLB 1cc, Waters, Bedford, MA, USA), followed by a washing step (1.5 ml 5% methanol) and elution with 1.5 ml of either 70% (sample 8) or 80% (samples 11-14) methanol. Samples 8 and 14 both consisted of crude extract samples with slightly different clean-up procedures and recoveries. Eluted samples were dried in a Speed-Vac (Thermo-Savant, Holbrook, NY, USA) and reconstituted in 50% methanol. Each calibration standard and sample (1 µl) were spotted in triplicate onto the MALDI plate and allowed to air dry prior to analysis. The calibration curve used for the electrospray quantitation included standards from 0.0005-0.15 µg/ml Des-C with 0.0625 µg/ml GYM. Unknown samples were prepared with an additional 1/10 dilution factor over those used for the MALDI experiments.

MALDI mass spectrometry

MALDI experiments were performed on a MDS Sciex API 3000 triple quadrupole mass spectrometer equipped with a prototype orthogonal MALDI source with a high repetition rate, frequency-tripled (355 nm) Nd:YAG laser (PowerChip NanoLaser, JDS Uniphase, San José, CA, USA) and a pulse rate of 1000 Hz. All measurements were carried out in the positive ion mode, with the MALDI plate located in the Q0 region at a pressure of ~8 mTorr. A laser power setting of 2.4-2.7 µJ/pulse was used for all measurements (unless otherwise stated).

MRM experiments for each analyte employed an appropriate internal standard, a nitrogen CAD gas setting of 6 (arbitrary units) and optimized collision offset voltages, as follows: quinidine and hydroquinine, 45 V (MRM 325→160, 327→160); danofloxacin and desmethyl-danofloxacin, 50 V (MRM 358→255, 344→255); ramipril and enalapril, 30 V (MRM 417→234, 377→234); nadolol and timolol, 25 V (MRM 310→254, 317→261).

Studies involving the investigations of different internal standards used a collision offset voltage of 30 V. The MRM transitions monitored were as follows:

Compound	Transition	Compound	Transition
Pipemedic acid	304 → 217	Oxolinic acid	262 → 216
Enoxacin	321 → 232	Nalidixic acid	233 → 187
Norfloxacin	320 → 233	Flumequine	262 → 202
Ofloxacin	362 → 261	Amprolium	316 → 288
Ciprofloxacin	332 → 245	Nadolol	310 → 254
Lomefloxacin	352 → 265	Niflumic acid	283 → 245
Desmethyldanofloxacin	344 → 283	Enalapril	377 → 234
Danofloxacin	358 → 283	Prazosin	383 → 341
Enrofloxacin	360 → 245	Sulfamethazine	279 → 124
Sarafloxacin	386 → 299	Vincamine	355 → 212
Cinoxacin	263 → 217	Quinidine	325 → 160

Standard curves were analyzed with slow vertical rastering of the MALDI plate (~0.06 cm/s, 3-4 sec/spot). Quantitative results were obtained by plotting peak area ratios (analyte/internal standard) vs. concentration of analyte. The following concentrations were measured for the quantitation of ciprofloxacin: 0, 0.025, 0.1, 0.25, 0.5, 1.0 μM on target with an internal standard concentration of 2.0 μM. For the quantitation of acylcarnitines, the concentrations analyzed were as follows: 0, 0.01, 0.025, 0.05, 0.075, 0.1, 0.25, 0.5, 1.0, 1.5 μM with a constant internal standard concentration of 1.0 μM. The MRM transitions monitored for the acylcarnitines corresponded to the fragmentation of each precursor ion to a common product ion at *m/z* 85. All acylcarnitines were investigated as internal standards in the quantitation of acetyl-carnitine and hexanoyl-carnitine. The deuterated derivative of hexanoyl-carnitine was not used for the acetyl-carnitine quantitation study since it caused a large background interference in the analyte's MRM transition and therefore was not suitable as an IS.

MRM transitions for 13-desmethyl spirolide C and gymnodimine used were *m/z* 692→164 and *m/z* 508→174, respectively, with a dwell time of 250 ms each. These experiments used a collision offset voltage of 60 V.

LC/MS analyses

LC/MS assays were performed on an Agilent 1100 binary pump coupled to a MDS Sciex API 4000 triple quadrupole instrument in positive ion mode. A Phenomenex (Torrance, CA, USA) Luna C18 100 × 2 mm, 3μ column with mobile phases; A, water and B, 95% acetonitrile, both containing 50 mM formic acid and 2 mM ammonium formate was used.

Purity tests for quinidine and two internal standards, hydroquinine and hydroquinine 4-methyl-2-quinolyl ether, were performed using a gradient elution of 10% to 60% B in 10 min followed by an increase to 90% in 1 minute and subsequent re-equilibration at the initial LC conditions, at a flow rate of 0.25 ml/min. The retention times for quinidine, hydroquinine and hydroquinine 4-methyl-2-quinolyl ether were 3.4, 4.4 and 9.0 minutes, respectively.

ESI/MS/MS quantitation of 13-desmethyl spirolide C was achieved within a 5 minute run (initial 0.5 min held at 30% B, followed by a linear increase to 70% B in 4.5 min), with a 5 min re-equilibration step. Source conditions were the same as specified for the spirolide LC/MS analyses in Chapter 2. MRM transitions monitored were *m/z* 692→164 for Des-C and *m/z* 508→174 for GYM, each with a dwell time of 500 ms and collision offset voltage at 60 V and a CAD gas setting of 12.

Light microscope images

Light microscope images were acquired using a Wild Photomakroskop M400 (Wild Leitz Canada, Willowdale, ON, Canada) equipped with a Nikon Coolpix 4500 digital camera (Nikon, Tokyo, Japan). Total spotted and ablated areas were determined from the digital images using ImageJ software (NIH, Bethesda, MD, USA). The average total sampled (ablated) area was determined from 80 spots measured before and after MALDI analysis.

Scanning electron microscope images

SEM images were obtained using a Hitachi S-3000N scanning electron microscope (Hitachi Science Systems, Hitachinaka, Japan). Various levels of magnification were used at 1.5 keV electron energy. Spots were analyzed at different

laser powers and frequencies for calculating % ablation in each laser trace across the spots from the corresponding SEM images. The ablated amount was calculated after converting the SEM images to binary images. ImageJ software was used for thresholding and counting the number and areas of the crystals on the spot surface.

log D, pK_a *calculations*

The PrologD and pKalc modules of the Pallas software (CompuDrug, Sedona, AZ, USA) were employed for the calculations of log *D* and pK_a values for compounds investigated in the quantitation of ciprofloxacin. The following parameters were used: pH 2.0 and ionic strength 0.01 M, corresponding to that of the solutions spotted on the MALDI plate (2 mg/ml CHCA, 0.1% TFA in 50% acetonitrile).

Quantitative MALDI of pharmaceutical drugs

Small molecule quantitation by mass spectrometry has mostly relied on LC/MS assays using electrospray and atmospheric pressure chemical ionization for ion generation. The triple quadrupole mass spectrometer represents the most rugged and routinely used instrument employed for these assays. A MALDI-QqQ instrument would therefore be the most appropriate for the MALDI quantitation of small molecules. Although the pulsed nature of the MALDI process does not seem an ideal match for a beam-type instrument such as the triple quadrupole, a high-frequency laser would generate the required (virtually) continuous ion beam. The quantitation of four different drug molecules was performed on a triple quadrupole instrument equipped with a MALDI source operating at 1 kHz pulse frequency. The quantitative assays measured ion currents from specific fragmentation pathways of the protonated molecules. A schematic representation of the MALDI-QqQ analysis is shown in Figure 5.1. The assay was run by slow vertical rastering down the MALDI plate, which produces a channel through each spot and integrating the resulting signal from the MRM transition.

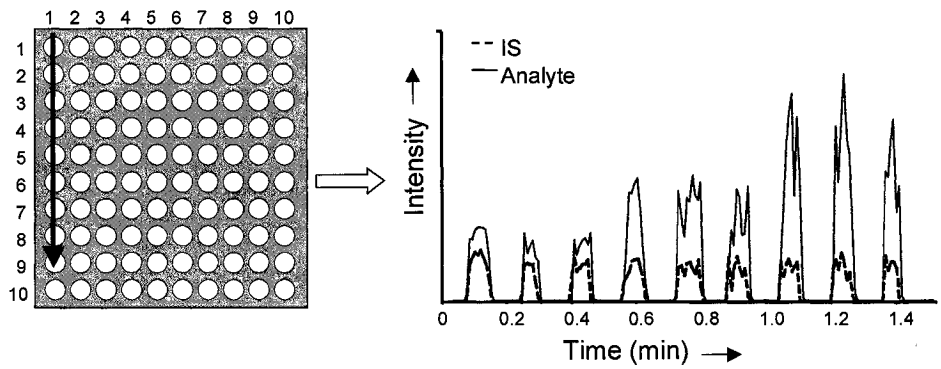

Figure 5.1 Schematic representation of quantitative MALDI-triple quadrupole assay. Slow vertical rastering down the sample plate yields ion currents for the chosen MRM transitions for the analyte and internal standard. Shown on the right are the ion currents for an analyte at three different concentrations (triplicate) with a constant concentration of internal standard.

Initially, some physical properties of the MALDI spots under different laser conditions were considered in order to optimize the settings for the quantitative assays. In general, MALDI suffers from problems of signal irreproducibility, which could originate

from several sources including crystallization behavior and laser properties, such as energy profile and firing repetition rate. Therefore, these conditions should be optimized and kept constant throughout the analyses. By performing experiments with different laser powers and pulse frequencies, we were able to estimate the ablated amounts and therefore characterize the laser conditions at which complete ablation occurs.

The results from these studies are shown in Figure 5.2. For quantitative purposes, the laser power was deliberately set to an energy level close to the plateau region of the ablation curve, to compensate for crystal irregularities and the non-flat top energy profile of the laser beam. This is illustrated in Figure 5.2a, where the amount of ablated material is plotted against the laser power. For this curve, the amount of consumed material was estimated from image analysis of the residual crystals in the ablated trench versus the crystal area in a non-irradiated area of the spot. An eventual plateau region occurs at 100% ablation for all measured values of 2.7 μJ and higher. There is also a qualitative difference in the profile of the ablated trace, that starts out as a Gaussian-type profile (due to the laser's power profile); however, when the laser power is above the threshold for complete ablation, the trace no longer shows differential ablation.

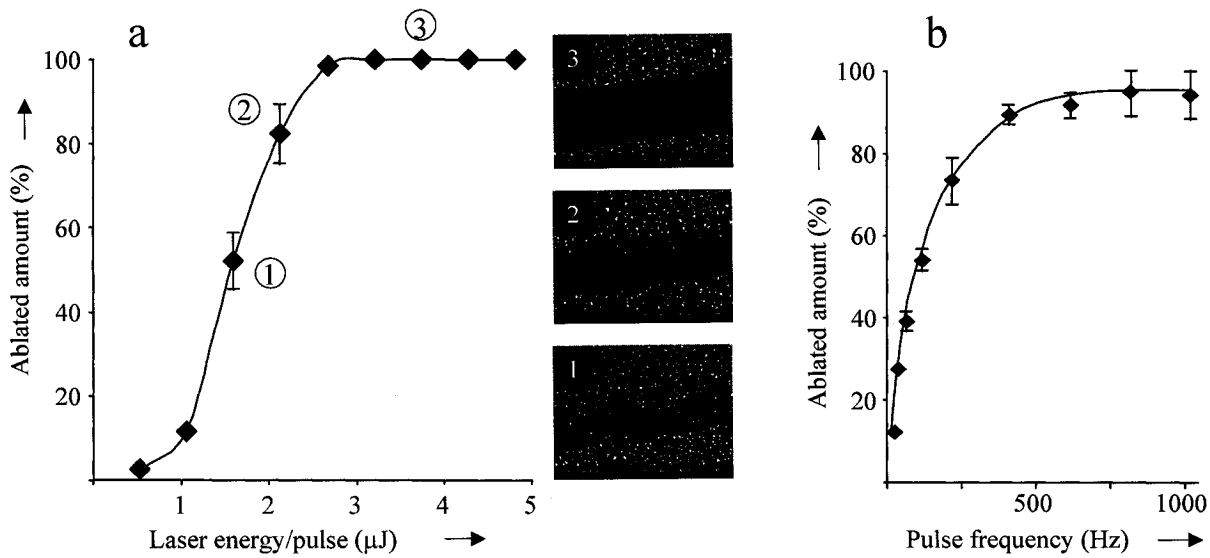

Figure 5.2 Effect of laser energy/pulse (a) and pulse frequency (b) on % ablation in MALDI traces. Laser energies from 0.53-5 μJ were compared for amount of material ablated using ImageJ analysis (see Experimental). An energy of 2.4 μJ was used for the assays at different laser frequencies. Preferential ablation occurs in the center of the laser's path at lower laser energies, however, at higher energies the trace is fully ablated throughout. Error bars represent standard deviation of the mean for each measurement (n=5). Note: where error bars are not seen, they are smaller than the data point symbols.

Similarly, the influence of the laser frequency on the amount ablated was studied, using a laser power of 2.4 μJ. The corresponding curve is shown in Figure 5.2b. Virtually complete ablation was achieved at frequency settings >400 Hz for the chosen rastering speed. For statistical reasons, in order to improve measurement precision, the laser was operated at a frequency of 1000 Hz to obtain the maximum number of spectra.

There is also a potential for precursor ion loss with increased laser power due to in-source fragmentation or losses during the desorption/ionization process. The protonated molecules of the four internal standard compounds employed in the quantitative assays were measured using selected-ion monitoring. Figure 5.3 represents the results for the signal intensities of the four compounds (each at 5 μM with the exception of timolol, which was present at 25 μM) monitored at discrete laser powers between 0.89 and 7.12 μJ over the course of a 40 sec acquisition time. A laser energy setting of 2.4 μJ lands in an optimal region for precursor ion sensitivity and was therefore ideal for quantitative experiments.

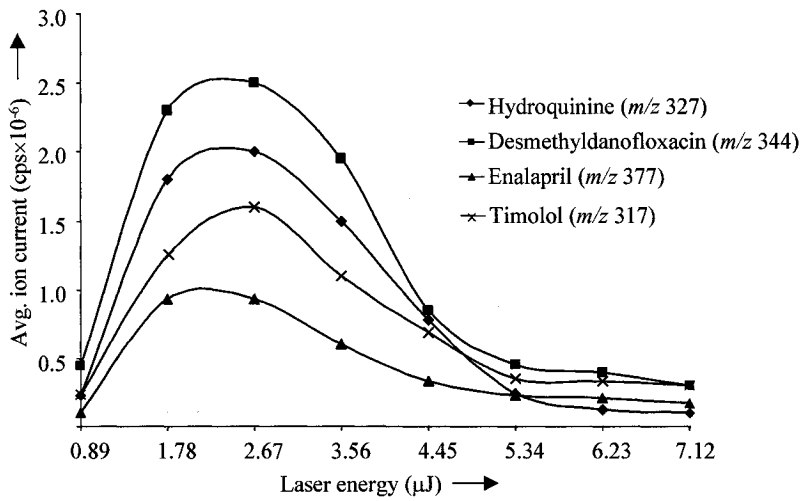

Figure 5.3 The effect of laser energy/pulse on precursor ion current (measured by single-ion monitoring) for four internal standards used in the quantitative assays.

With the optimized laser settings, an approximately 110 μm wide trench was drilled through the sample when the laser beam was moved over the spot. Figure 5.4(a,b) illustrates SEM images of a typical sample spot after laser irradiation. Note how the laser has ablated virtually the entire matrix and sample material on the irradiated area. The

laser fluence was sufficiently high across the channel to almost completely ablate the material, with no noticeable roll-off at the borders (Figure 5.2(c,d)). A light microscope image of a section of the ablated area from a sample spot is shown in Figure 5.2c, with a corresponding graph produced from ImageJ software analysis in Figure 5.2d. This imaging software enabled the ablated area to be visualized as a groove with a virtually flat bottom. The ablated area corresponded to 3.9 ± 0.5% of the total spot area per laser trace, as determined from image surface analysis of a large number of sample spots (n = 80). This matches the theoretically ablated area estimated as 3.9% by taking into account that the spot is limited by the round borders on the plate, and using a 110 µm channel width in the center of the spot. The non-ideal sample spot shapes, because of liquid spreading after pipette application of the sample or from surface contamination of the target surface, caused the variations in the ablated material.

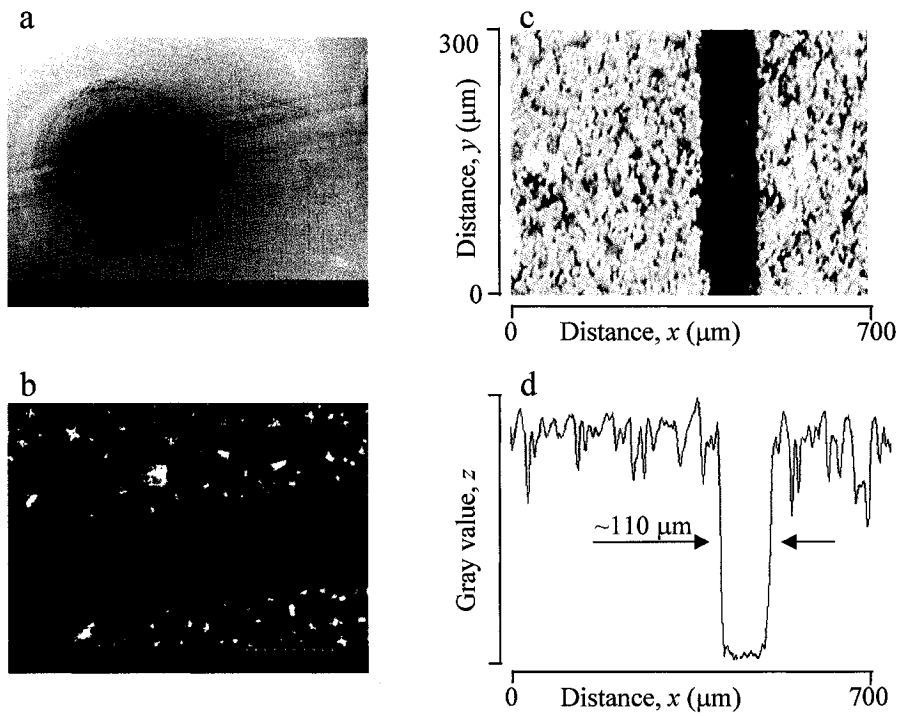

Figure 5.4 Scanning electron microscope and light microscope images of a MALDI sample spot on a stainless steel plate. The spots were prepared by spotting 1 µl of matrix/sample solution (CHCA concentration: a, b: 2 mg/ml; c,: 5 mg/ml). (a) SEM image after MALDI analyses. (b) Higher magnification SEM image of one trace, showing that the laser ablated virtually the entire sample material in its path. (c) Light microscope image of a section of the spot. (d) Cross section of the same area as seen in (c) obtained from image analysis. (Note that only the x,y-plane is calibrated. The z-axis is expressed in contrast (gray) values from the digital image, but with no specific physical meaning describing the actual dimension in the z-direction.)

The analytes chosen for this study were quinidine, an antiarrhythmic agent, danofloxacin, a fluoroquinolone used as a broad-spectrum antibacterial agent in veterinary applications, ramipril, an angiotensin-converting enzyme (ACE) inhibitor, and nadolol, a beta-adrenergic blocker. Structures for all the analytes and their internal standards, as well as their corresponding product ions monitored in the MRM experiments, are shown in Figure 5.5. Each internal standard exhibits a very similar structure to its analyte and produces an analogous fragmentation pathway. Since small molecule MALDI is still a rather new technique, this report represents the first MALDI analysis method for these drugs. α-Cyano-4-hydroxycinnamic acid (CHCA), 2,5-dihydroxybenzoic acid (DHB) and sinapinic acid (SA) were tested as organic matrices and, based on sensitivity, CHCA yielded the best results for all compounds analyzed.

Of note, the three above-mentioned matrices were also tested for suitability for the quantitative assays described here. Figure 5.6 shows that the crystallization behaviors for the different matrices are quite different. Light microscope images are shown for each matrix at concentrations of 1.0 and 2.5 mg/ml with 50% ACN, 0.1% TFA. The average % relative standard deviation (RSD) values for the measurements using the three different matrices at these two concentrations are also given in this figure. It is clear that CHCA is the only matrix, of those tested, which yields acceptable reproducibilities of measurement. These data were collected for both quinidine and danofloxacin at concentrations of 0.05, 0.25, 1.0 μM with 0.5 μM internal standard. The % RSD values noted in the table are average values for 10 spots each of the three concentrations of analyte (n = 30 total). Both DHB and SA gave very irreproducible results, potentially due to problems with spot size and shape, as well as lack of co-crystallization of the organic matrix with the analyte and internal standard.

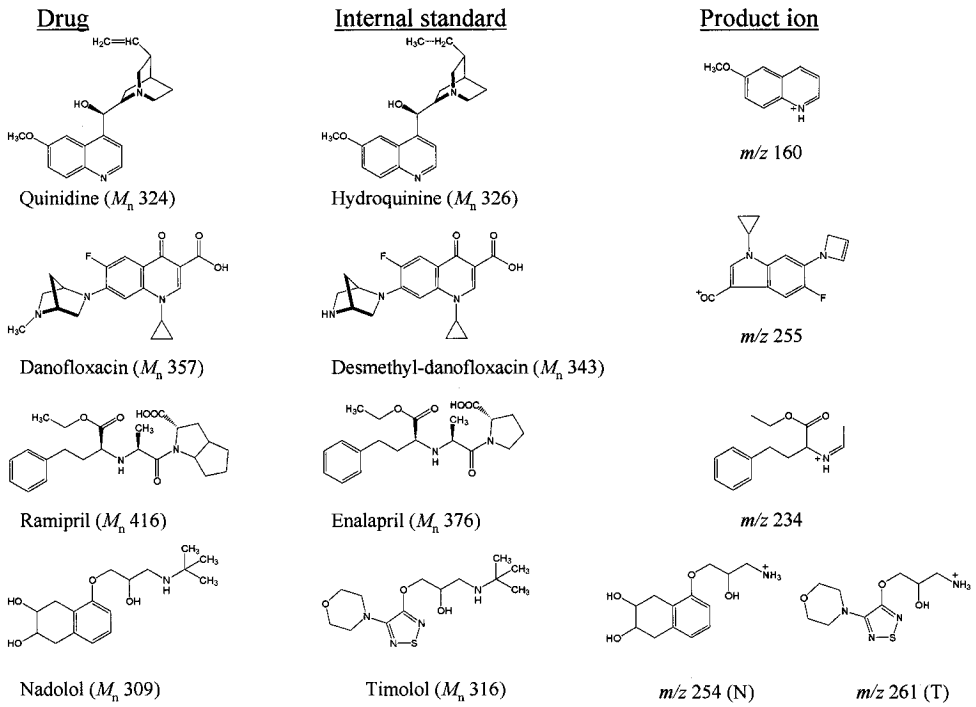

Figure 5.5 Chemical structures and nominal molecular weights of the investigated drug molecules and their internal standards, as well as the structures proposed for the chosen product ions for MRM analyses

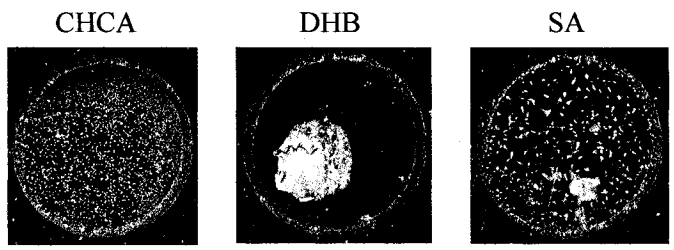

Matrix	%RSD$_{avg}$ (Quinidine)	%RSD$_{avg}$ (Danofloxacin)
CHCA 1 mg/ml	9.4	15.0
CHCA 2.5 mg/ml	5.8	12.2
DHB 1 mg/ml	46.3	90.4
DHB 2.5 mg/ml	42.2	53.6
SA 1 mg/ml	39.7	41.2
SA 2.5 mg/ml	22.9	22.9

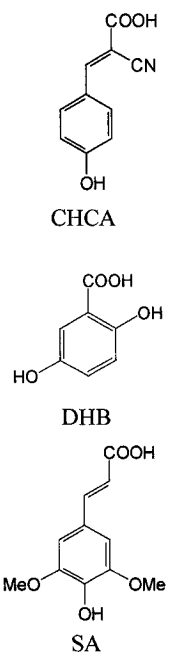

Figure 5.6 Light microscope images of crystal spots after air-drying of one microliter of three different MALDI matrix solutions at 1.0 mg/ml in 50:50 acetonitrile/water + 0.1% TFA (above). (Note: diameter of the circular spot on the MALDI plate is 2.6 mm.) Comparison of the measurement reproducibilities for quinidine and danofloxacin using the three investigated MALDI matrices at two different concentration levels (below). Structures of three matrices shown on the right.

For the quantitative studies, collision energies for each MRM transition were optimized and the corresponding product ion scans for each analyte and internal standard are shown in Figure 5.7. Table 5.1 summarizes the results of the MALDI quantitation for the four investigated drugs. All data shown represent averages from three separate calibration curves for each analyte. Each standard was spotted three times and each spot was sampled twice for a total of 6 data points for each concentration. Limit of detection (LOD) and lower limit of quantitation (LLOQ) values were determined by adding the signal of the analyte blank to 3× and 10× its standard deviation, respectively. All concentrations lower than the calculated LLOQ, except for the analyte blank, were omitted from the calibration curves.

For the case of quinidine, the background signal for the analyte blank seemed comparatively high and could therefore mask the signal for lower amounts of analyte. After verifying that the background signal was not from the CHCA matrix, it was presumed that the internal standard used in the quinidine assays was not completely pure and contained a small amount of quinidine. When the concentration of the hydroquinine internal standard was decreased 5-fold, LOD and LOQ values were decreased to 0.007 and 0.022 μM, respectively. Subsequently, another analog of quinidine, hydroquinine 4-methyl-2-quinolyl ether (structure shown in Figure 5.8), was investigated as an internal standard. The same assay was performed using an MRM transition of 468→160 for the ether derivative. The LOD and LLOQ values in this case were 0.005 and 0.013 μM, respectively, representing an improvement over the results with hydroquinine. Of note, the slope of the calibration curves using this second internal standard are much higher due to the fact that the monitored transition did not represent the base peak under the MRM conditions used and therefore the ratios of intensities are correspondingly higher.

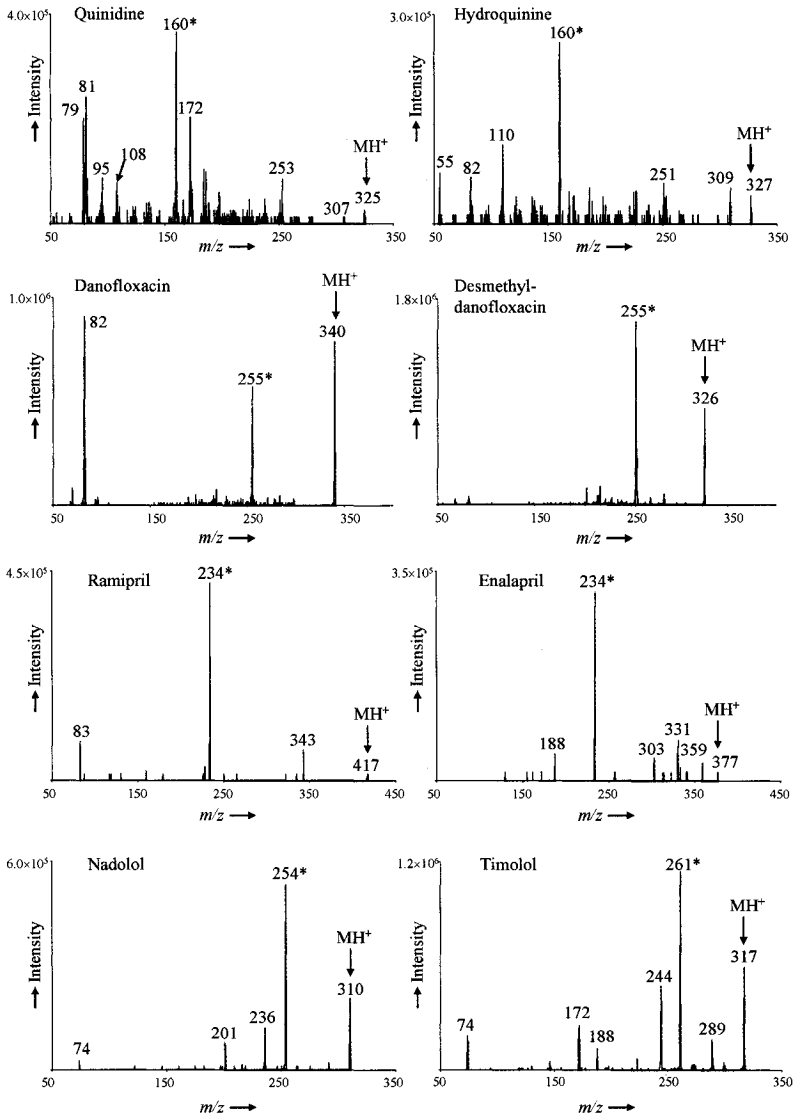

Figure 5.7 Product ion spectra of the investigated drug molecules and their internal standards obtained from MALDI-QqQ analyses. The chosen product ions for the MRM transitions are indicated with *.

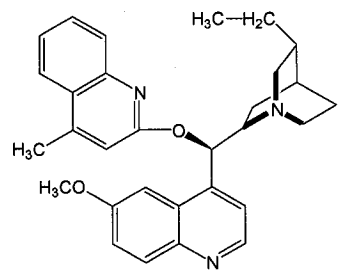

M_n 467

Figure 5.8 Chemical structure and nominal molecular weight of the internal standard hydroquinine 4-methyl-2-quinolyl ether.

Table 5.1 Summary of quantitation results for the investigated pharmaceutical drugs

	Equation	R^2	LOD(μM)	LOQ(μM)	dynamic range	% RSD_{avg}
Quinidine	$y = 0.4807x + 0.0208$ (RSD_{slope} 5.1%)	0.9971 (RSD 0.3%)	0.015	0.033	0.033-2.5 μM	10.1
hydroquinine (IS)						
quinidine-ether analog (IS)	$y = 6.1735x + 0.0392$ (RSD_{slope} 9.9%)	0.9975 (RSD 0.05%)	0.005	0.013	0.013-1.5 μM	12.0
Danofloxacin	$y = 1.4424x + 0.0066$ (RSD_{slope} 3.1%)	0.9972 (RSD 0.4%)	0.0005	0.0025	0.0025-2.5μM	9.6
Ramipril	$y = 0.7906x - 0.0089$ (RSD_{slope} 6.3%)	0.9974 (RSD 0.3%)	<0.0005	0.0007	0.0007-2.5μM	14.0
Nadolol	$y = 0.0359x + 0.0023$ (RSD_{slope} 8.1%)	0.9990 (RSD 0.0%)	<0.01	0.015	0.015-20 μM	10.3

Additionally, LC/MS experiments were performed in order to verify the purities of the two internal standards used in the quinidine assays. Hydroquinine did indeed have a corresponding signal for the MRM transition for quinidine at the expected retention time, as well as two closely eluting smaller peaks. When these contributions are summed, this accounts for a 4.2% contamination of the hydroquinine standard; and if we consider only the quinidine peak itself, we still have a 2.5% contamination peak. For the case of hydroquinine 4-methyl-2-quinolyl ether, a small impurity corresponding to quinidine was also present. Based on relative areas of the quinidine peak for the ether analog and hydroquinine, there is a 0.7% contribution for quinidine in the ether standard. The purity of the internal standard is particularly important for MALDI applications, where no prior chromatography is used to eliminate isobaric interferences.

The MALDI-QqQ combination seems to be an excellent instrument for high-throughput quantitative analyses of small molecules since it represents the highest sensitivity MS/MS configuration currently available. It has been reported that QqTOF instruments have seen recent advances, which allow them to increase their duty cycle to get closer to the performance of the triple quadrupole in MRM mode. While there is no dedicated MRM or precursor ion mode on a QqTOF mass spectrometer, Chernushevich demonstrated [262] that the duty cycle of the oaTOF analyzer can be increased to 100% for very small *m/z* ranges that are monitored simultaneously. There are nevertheless some ion transmission losses taking place in the QqTOF instrument after the collision cell q_2,

for instance, between the exit lens and the TOF accelerator. Also, there are losses through the grids in the TOF itself. In contrast, the transmission efficiency in the QqQ instrument after the exit lens to the detector is assumed to be close to 100%.

In these experiments, the effect of different laser parameters on measurable properties such as % ablation and signal intensities was studied in order to find optimized settings for extremely sensitive quantitative assays for small molecule MALDI. If we consider the LOD for ramipril of 0.5 nM, and assume homogeneous distribution of the sample throughout the spot area, this corresponds to a total of 0.5 fmol of analyte per spot, 3.9% of which is 19.5 attomoles with total ablation. If we go one step further and estimate each analysis to run for approximately three seconds, corresponding to 3000 laser shots, we can then estimate that an average of 6.5 zeptomoles of compound is ablated per laser shot at the detection limit for this analyte. An LLOQ value of 0.025 μM, for example, which is well above the value for most of these analyses using the MALDI-triple quadrupole, would translate into a total of 975 attomoles of analyte ablated per analysis. This corresponds to extremely low levels and definitely competes and even surpasses most electrospray analyses, based on material consumed in the analysis.

Assessing properties of internal standards

It is generally desired that an internal standard compound be as chemically similar as possible to the analyte molecule of interest, to compensate for detrimental variations during sample preparation or the instrumental measurement of the analyte. It is often not possible, however, to obtain isotope-labeled compounds and structurally similar analogs must then be employed. It is important that in MALDI, the chosen internal standard compound co-crystallizes with the matrix in the same way as the analyte molecule. Subsequently, it must exhibit the same or very similar properties in the gas phase, after laser desorption from the crystal matrix.

The suitability of different internal standards for quantitative MALDI of small molecules has been evaluated in two separate studies. In all experiments, the general strategy was to start with a structurally almost identical analog of the analyte and then successively vary the structure and physicochemical properties and monitor differences in their appropriateness as internal standards. Quantitation using structurally different

internal standards has previously been demonstrated [241]; the experiments required a constant molar ratio of (analyte + IS)/matrix over the quantitation range, however, which is impractical for samples with unknown concentration of analyte. It has been reported [241] that keeping the internal standard's concentration close to that of the highest standard in the calibration curve was advantageous since it minimizes the change in (analyte+IS)-to-matrix ratio without having problems due to ion suppression of the analyte by a large molar excess of the IS. Similarly, better precisions were obtained for molar ratios of internal standard to analyte between 0.2 to 5 than for the range from 0.1 to 10 within the calibration curve for the determination of phenylethylamine [251]. In our experiments, the internal standard was therefore used at a concentration level close to the highest analyte concentration investigated.

The first study involved the investigation of a series of acylcarnitines with a fixed charge site and increasing alkyl chain length to systematically determine the effect of molecular weight as a parameter. Fifteen different acylcarnitines, ranging from acetyl-carnitine (M_n=203 g/mol) to octadecanoyl-carnitine (427 g/mol) were used. These compounds as well as their corresponding *m/z* values are shown in Figure 5.9. Initially, the quantitation of acetyl-carnitine was considered with the other acylcarnitines as internal standards, including its d_3-labeled analog. As the mass of the internal standard increases, the overall precision of the quantitative assay deteriorates. This is illustrated in Figure 5.10a, showing the average % RSDs of measurements throughout the calibration curve as a function of the % change in molecular weight of the IS relative to that of acetyl-carnitine ($\Delta M_n/M_n \cdot 100\%$). Acceptable values (<15%) are only seen with the isotope-labeled derivative and propionyl-carnitine. These numbers increase rapidly to over 40% RSD for the molecules having a 12-carbon chain or more, corresponding to a ≥60% increase in mass as compared to the analyte. A similar trend was seen in the MALDI quantitation of phenylethylamine (PEA) [251] using either d_5-PEA or phenylmethylamine as internal standards. Despite the subtle change in chemical structure (methyl vs. ethyl), the difference corresponds to a significant relative change in mass and, accordingly, the precision of the PEA determination was considerably worse with PMA than with the d_5-analog (19% vs. 4%). Another good parameter for assessing the suitability of an IS is the linearity of the calibration curve (R^2, Figure 5.10b), of which

only acceptable values (>0.99) are seen in the case of d_3-acetyl, propionyl, butyryl, isobutyryl and isovaleryl carnitines. In the region from d_3-acetyl to octanoyl-carnitine in the graph in Figure 5.10b (blown-up region), an interesting phenomenon is also noted. Both isobutyryl and isovaleryl yield better linearities than their unbranched counterparts. This suggests that reducing the length of the alkyl chain by branching could cause the IS in question to become more similar to the smaller acetyl-carnitine analyte.

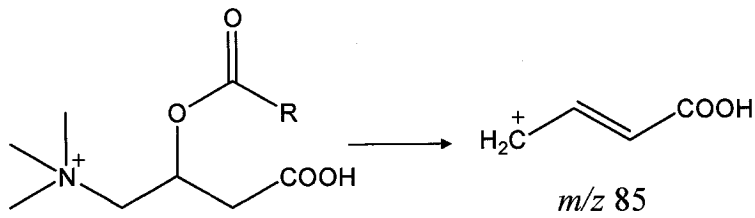

Compound	R group	m/z
acetyl-L-carnitine	CH_3	204
[d_3]acetyl-L-carnitine	CD_3	207
propionyl-L-carnitine	CH_2CH_3	218
butyryl-L-carnitine	$(CH_2)_2CH_3$	232
isobutyryl-L-carnitine	$CH(CH_3)_2$	232
valeryl-L-carnitine	$(CH_2)_3CH_3$	246
isovaleryl-L-carnitine	$CH(CH_3)CH_2CH_3$	246
hexanoyl-L-carnitine	$(CH_2)_5CH_3$	260
[d_3]hexanoyl-L-carnitine	$(CH_2)_5CD_3$	263
octanoyl-L-carnitine	$(CH_2)_7CH_3$	288
decanoyl-L-carnitine	$(CH_2)_9CH_3$	316
dodecanoyl-L-carnitine	$(CH_2)_{11}CH_3$	344
tetradecanoyl-L-carnitine	$(CH_2)_{13}CH_3$	372
hexadecanoyl-L-carnitine	$(CH_2)_{15}CH_3$	400
octadecanoyl-L-carnitine	$(CH_2)_{17}CH_3$	428

Figure 5.9 Acylcarnitine structures with corresponding *m/z* values and common product ion (*m/z* 85) monitored in MRM experiments.

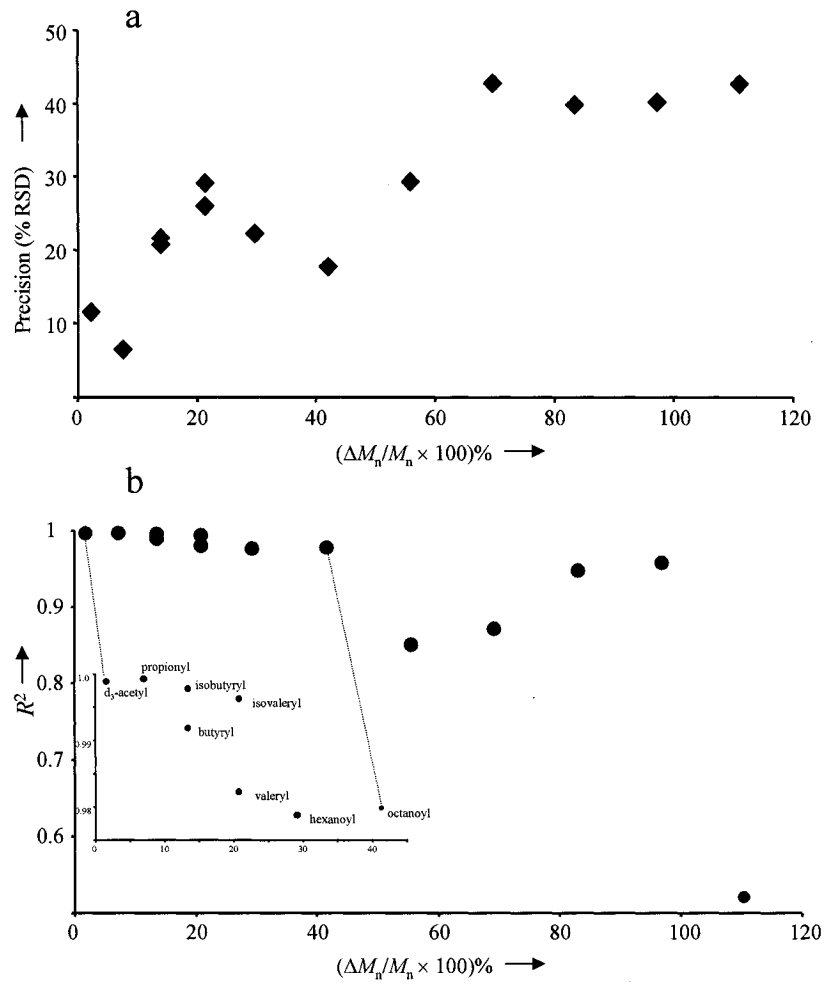

Figure 5.10 Average % RSD values (a) and linearities (R^2) (b) for calibration curves in the quantitation of acetyl-carnitine (M_n 203) plotted as a function of relative change in nominal mass between the analyte and the internal standard.

An important trend is observed when the quantitation of hexanoyl-carnitine was assessed. Figure 5.11 clearly displays that the effect of the % change in molecular weight is much more marked for increasingly heavier molecules. The precision and R^2 values remain within a relatively narrow range for all of the smaller acylcarnitines, however increasing the molecular weight of the IS shows an increase in % RSD and a sharp deterioration in standard curve linearity. A possible explanation for this phenomenon involves the matrix compound CHCA, potentially promoting more homogeneous co-crystallization with the smaller acyl-carnitines because of their closer chemical similarity to CHCA than with the larger compounds.

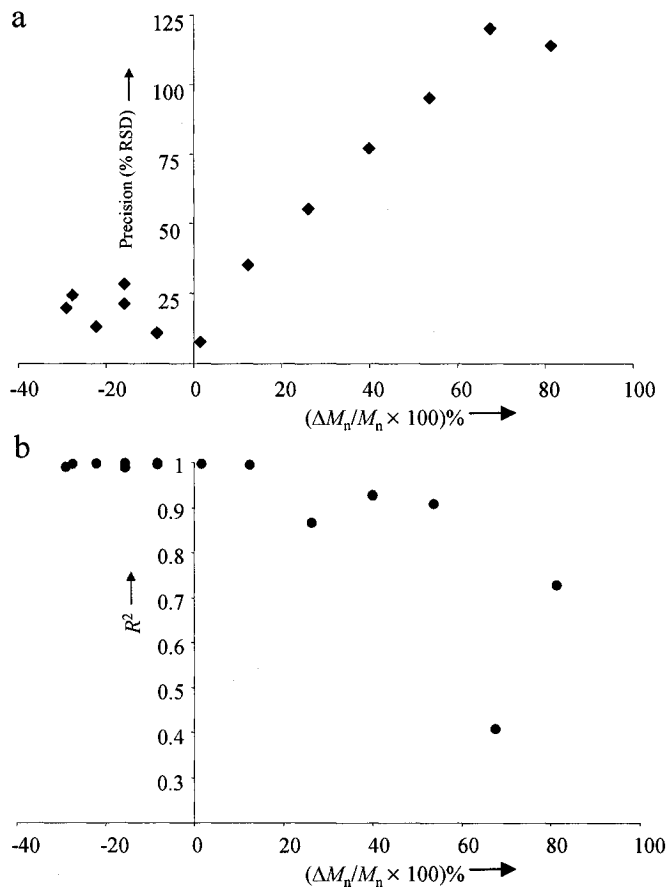

Figure 5.11 Average % RSD values (a) and linearities (R^2) (b) for calibration curves in the quantitation of hexanoyl-carnitine (M_n 259) plotted as a function of relative change in nominal mass between the analyte and the internal standard.

It was therefore seen that increasing the difference in molecular weight between an analyte and its IS, even with a fixed charge site, has an important impact on the results for quantitation by MALDI-MS. Figure 5.12 illustrates the difference between the isotope-labeled standard and octadecanoyl-carnitine in the quantitation of acetyl-carnitine. It is obvious by these representative ion current traces that the distribution of analyte and IS within the crystallized matrix is very similar in the case of the isotope standard (Figure 5.12a) and vastly different when octadecanoyl-carnitine is employed (Figure 5.12b).

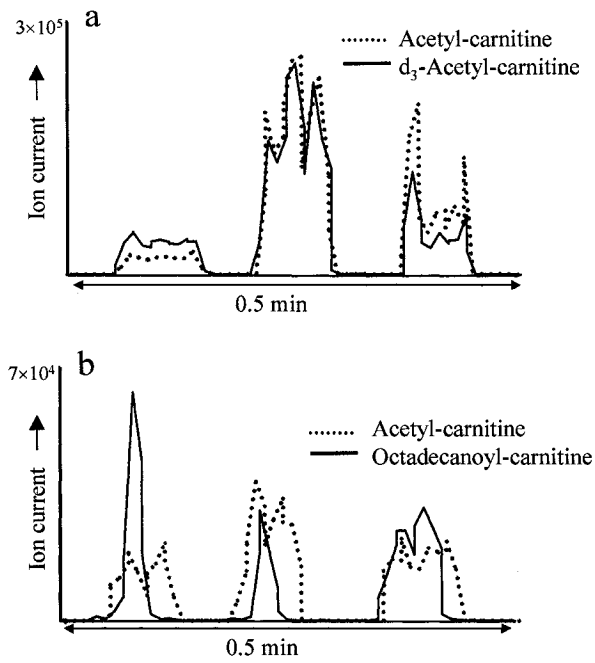

Figure 5.12 Representative ion current traces for three spots from vertical rastering down a MALDI plate for acetyl-carnitine with d_3-acetyl-carnitine (a) and octadecanoyl-carnitine (b) as internal standards. The ion currents for the analyte/internal standard pair are very consistent for d_3-acetyl-carnitine, however it is clear that octadecanoyl-carnitine does not have similar distribution as this analyte within the MALDI spot.

Owens and co-workers suggest that sample segregation occurs during the crystallization phase when the solubilities of matrix and analyte are not properly matched [249]. A similar conclusion can be drawn from our experiments by looking at cross-sections of the laser ablation traces (Figure 5.12). Ion currents from ablated segments are noticeably more evenly distributed along the ion current trace when matrix (CHCA) and analyte are closer in polarity than for mismatched pairs, such as seen, for example, from the acetyl-carnitine trace in comparison to the octadecanoyl-carnitine trace. In the context of this study, it is very important, however, that these mismatches do not seem to influence the analysis to any significant degree as long as analyte and internal standard are properly matched. This was seen when we used hexadecanoyl-carnitine as the analyte with its two most closely matched derivatives, namely tetradecanoyl-carnitine and octadecanoyl-carnitine as internal standards. Very good linearities (R^2=0.992) and precisions of 12.1 and 12.8 %, respectively, were seen for these two internal standards. Thus, the most important aspect in choosing an appropriate internal standard for

quantitative MALDI assays is that it matches the crystallization behavior of the analyte and not necessarily that it exhibits homogeneous distribution throughout the sample spot.

In another study, a group of 4-quinolone antibiotics and several other compounds were examined to investigate the influence of solution phase ionization equilibria and hydrophobicity on the relative response of analyte and internal standard. The chosen 4-quinolones were ten amphoteric and four acidic compounds, including the amphoteric ciprofloxacin as the model analyte in all cases. At the pH of the spotted sample solutions, the amphoteric 4-quinolones (**1-10**, Figure 5.13) are predominantly in their protonated MH^+ form, and all acidic quinolones (**11-14**, Figure 5.13) are in their neutral M form. Predicted apparent octanol/water partition coefficients *D* (=distribution coefficients, usually quoted as log *D*) and aqueous dissociation constants, pK_a, were used to assess the importance of the hydrophobicity and ionic species in solution as characteristics for an ideal internal standard in quantitative MALDI assays. The idea of using octanol/water partition coefficients *P* for describing relative polarities was previously mentioned by Owens and co-workers [249] as a possible way of looking at analyte/matrix compatibilities. These types of calculations have been reported [263] for the 4-quinolones in an earlier study, and are used here in order to investigate their usefulness for predicting good matches between analyte and internal standard for MALDI of small molecules. Several of the investigated molecules are distributed into multiple species at a given pH. The distribution coefficient log *D* was therefore used rather than the partition coefficient log *P* to describe the hydrophobicity of the analytes and internal standards at the investigated pH value of 2.0. For many compounds, values for partition or distribution coefficients are not available from the literature and their experimental determination is time-consuming. Commercial software was employed to calculate log *D* and pK_a, based on the structural formulae of the test compounds.

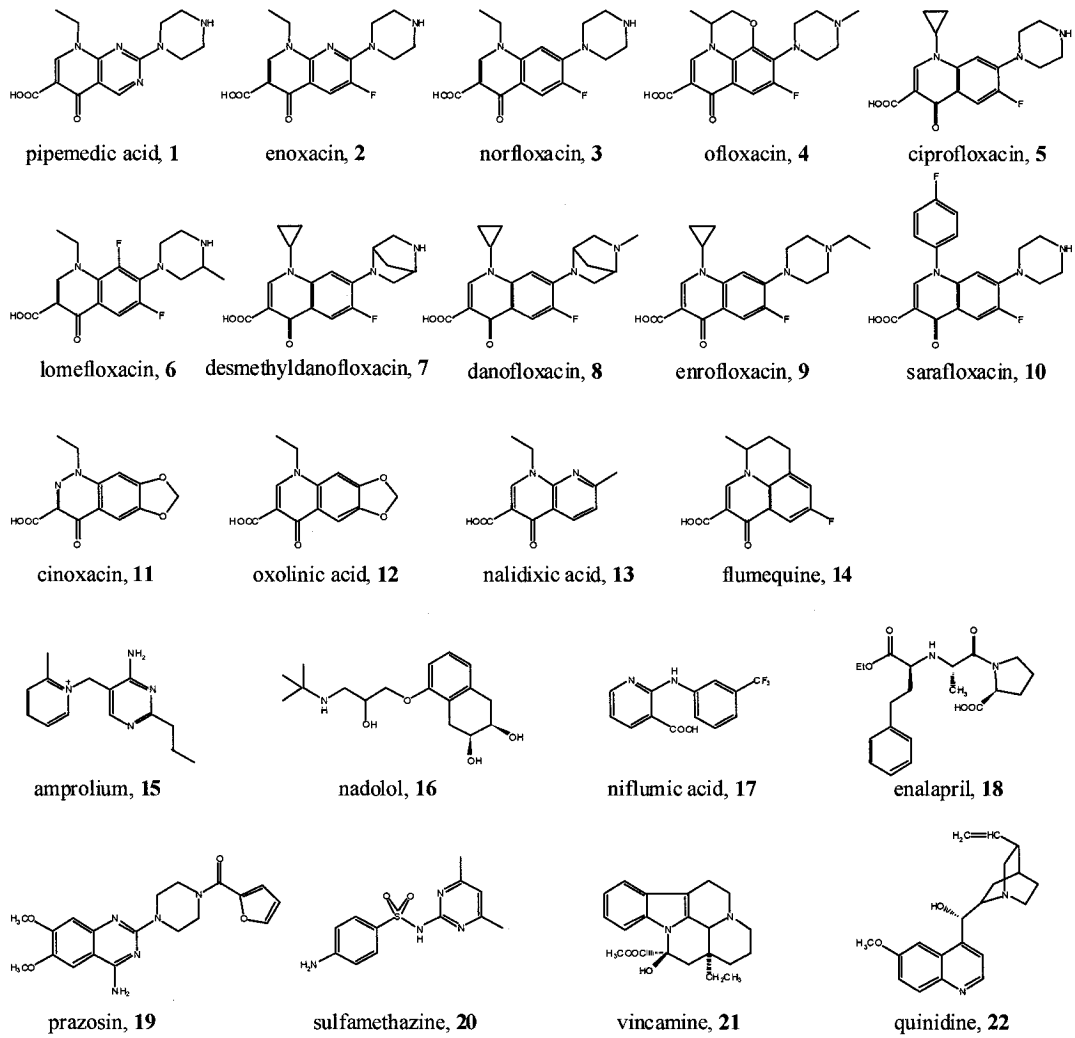

Figure 5.13 Structures of fluoroquinolone antibiotics (**1-14**) and other pharmaceutical drugs (**15-22**) employed in the quantitation study of ciprofloxacin.

Table 5.2 lists the nominal masses (M_n) and calculated log D values for the compounds used in this study as well as the pK_a's for the 4-quinolones. For the few compounds for which comparable experimental data were available, the calculated pK_{a2} values (referring to the basic site in the molecule) are in reasonably good agreement with the literature [263], thus establishing some confidence in the theoretical model. There exists a range of log D values from –4.06 (for pipemedic acid) to +2.35 (for cinoxacin) for the different internal standards investigated. In Figure 5.14, it is demonstrated that a large difference in log D between an analyte and its internal standard can lead to

detrimental effects on the quantitation of the analyte by MALDI. Compounds **1-10** (where compound **5** is the analyte, ciprofloxacin) all represent amphoteric compounds with virtually identical carboxyl groups and very similar basic functionalities. All of these compounds give acceptable relative standard deviations of measurements (Figure 5.14a) and excellent linearities with R^2 values above 0.99 (Figure 5.14b), throughout the dynamic range. Compounds **11-14**, however, have no basic group in their structures (no pKa_2), the importance of which is demonstrated in the increase in % RSD values and suboptimal linearities for the calibration curves. These compounds are in their neutral form at the sample pH during crystallization with the matrix compound, whereas the analyte ciprofloxacin is predominantly in its ionic form. Different crystallization behavior between analyte and internal standard can therefore be expected. The acidic quinolones were also investigated in quantitative assays with similarly paired analyte and internal standards. Table 5.3 summarizes the results for oxolinic acid paired with either cinoxacin and nalidixic acid. The results are in good agreement with our hypothesis that quantitation can easily be performed using different types of analytes with CHCA as the organic matrix, as long as the IS is chosen carefully in order to give similar distribution within the sample spot.

A series of unrelated pharmaceutical drugs was also tested as internal standards in the quantitation of ciprofloxacin. These compounds (**15-22**, Figure 5.13) show a large variety in structure and represent several classes of small molecules. Their log *D* values were also calculated and compared in a similar fashion as the 4-quinolones based on their ability to yield linear calibration curves with satisfactory relative standard deviations of measurement. The results for these drugs are compiled in Figure 5.14(c,d). In general, these unrelated drugs do not act as good internal standards in the quantitation of ciprofloxacin, with one exception. Quinidine seems to allow reasonable precision of measurement (10% RSD) and a linearity of 0.99. Importantly, this compound also has the most similar log *D* as calculated using the prediction software (Table 5.2). This again shows the importance of similar physicochemical properties between the analyte/internal standard pair and also reflects the fact that a different compound can be used if these characteristics are matched properly.

Table 5.2 Physicochemical properties of compounds used in quantitative analysis of ciprofloxacin*

Compound	M_n (g/mol)	log D (pH 2)	pKa_1	pKa_2
1. Pipemedic acid	303	-4.1	6.3	9.0
2. Enoxacin	320	-3.6	5.8	9.0
3. Norfloxacin	319	-3.6	6.3	9.1
4. Ofloxacin	361	-3.4	6.0	7.9
5. Ciprofloxacin	331	-3.4	6.3	9.1
6. Lomefloxacin	351	-3.6	5.9	9.1
7. Desmethyl-danofloxacin	343	-3.1	6.3	9.6
8. Danofloxacin	357	-2.8	6.2	9.0
9. Enrofloxacin	359	-2.7	6.2	9.5
10. Sarafloxacin	385	-2.9	6.2	9.1
11. Cinoxacin	262	2.4	3.1	
12. Oxolinic acid	261	1.5	6.3	
13. Nalidixic acid	232	-0.6	6.1	
14. Flumequine	261	1.7	6.3	
15. Amprolium	243	-5.3		
16. Nadolol	309	-0.4		
17. Niflumic acid	282	0.0		
18. Enalapril	376	-1.6		
19. Prazosin	382	-1.2		
20. Sulfamethazine	278	-0.4		
21. Vincamine	354	-1.3		
22. Quinidine	324	-3.6		

* pK_a values are shown for the 4-quinolone compounds as they have comparable groups. pK_{a1} relates to the acidic COOH group and pK_{a2} corresponds to the basic 4'-N on the piperazinyl ring, which is missing for the acidic fluroquinolones.

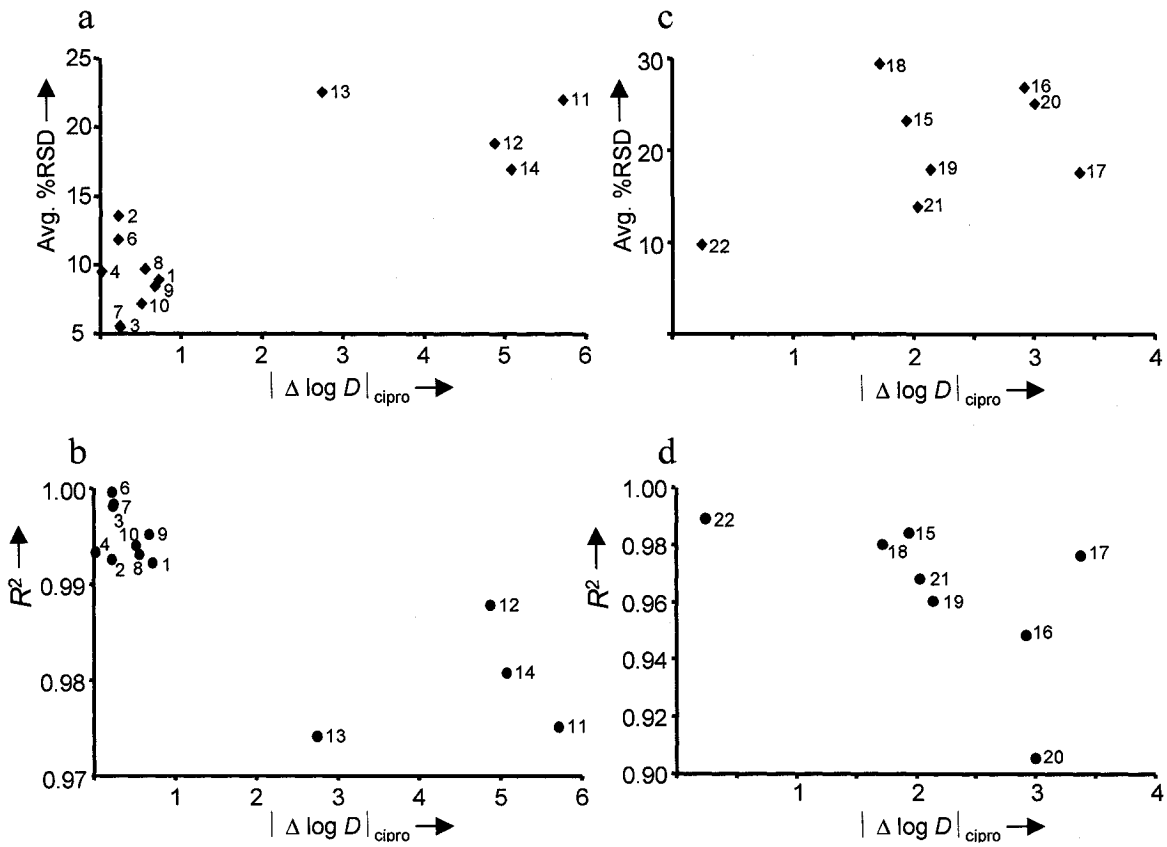

Figure 5.14 Results from ciprofloxacin quantitation study. Thirteen different 4-quinolones and eight other pharmaceutical drugs were investigated as internal standards. The average % RSD values and corresponding linearities for the calibration curves are represented above as a function of the difference in log *D* values between the IS in question and that of ciprofloxacin. Graphs a, b illustrate the results for the 4-quinolones and c, d show those for the other eight compounds employed in this study.

Table 5.3 Quantitation results for acidic quinolones

Analyte	Internal Standard	R^2	% RSD
Cinoxacin	Oxolinic acid	0.9996	10.4
Oxolinic acid	Cinoxacin	0.9997	10.8
Nalidixic acid	Oxolinic acid	0.9990	10.2
Oxolinic acid	Nalidixic acid	0.9981	11.5

Note: MRM transition for cinoxacin in these experiments was *m/z* 263-189.

Screening of toxin samples using MALDI-QqQ

The analysis of marine toxins in complex samples was investigated using the MALDI-triple quadrupole system. A quantitative study was performed for the analyte 13-desmethyl spirolide C (Des-C), the main toxin component present in the crude extract (see Chapter 2) and the only spirolide compound for which a pure, reference standard is obtainable. In order to validate the quantitative results for MALDI, the same samples were also subjected to LC/MS analysis with electrospray ionization. A comparison of these two methods provided good evidence for the possibility of obtaining accurate quantitative data from MALDI experiments. Also, the unique features possible from the combination of MALDI with a triple quadrupole instrument are illustrated with results from specialized scan functions, such as precursor ion and neutral loss experiments. Species from the same compound class can be detected through the use of these specific scans. Moreover, it is possible to obtain CID spectra from low abundant species in complex samples with good signal-to-noise ratios, without tedious and time-consuming chromatographic steps prior to analysis.

The internal standard chosen for the quantitative experiments was gymnodimine (GYM, refer to Figure 2.4 for structure), a marine toxin with important structural similarities to the spirolides. Gymnodimine was thought to act similarly to Des-C in the crystallization process and subsequent MALDI analysis. It was also shown that Des-C and GYM exhibit similar ionization efficiencies under ESI conditions (Chapter 2). This compound has been used successfully in the quantitative LC/MS analysis of Des-C with electrospray ionization.

Since spirolide toxins had never before been analyzed by MALDI, several factors both in sample preparation and instrumention were initially optimized. For sample preparation, three different organic matrices were tested, namely CHCA, DHB and SA, with different organic solvents as well as % organic content. After selecting the matrix and solvent composition, different matrix concentrations and matrix-to-analyte ratios were compared. During these experiments, CHCA gave the highest signal intensities for Des-C and GYM. Both methanol and acetonitrile were investigated as organic solvent for preparing the samples and methanol samples exhibited higher signals for Des-C and

GYM. Better sensitivity was achieved for the 75% methanol samples, when compared to 25 and 50% content.

For further optimization of the sample preparation procedure, Des-C and GYM MH^+ peak intensities were monitored using matrix-to-analyte ratios of 10, 100, 1000 and 10000. The best analyte sensitivity vs. matrix interference was achieved using a ratio of 1000. Also, constant matrix concentrations of 2.5 and 5 mg/ml were employed for a three-point analysis of Des-C samples at 1, 2 and 5 μg/ml prepared with a final composition of 75% methanol (+ 0.1% TFA). Ultimately, 2.5 mg/ml CHCA gave more intense signals for both analyte and internal standard. When these results were compared, it was noticed that the GYM signal was suppressed as the concentration of Des-C was increased above the concentration of the internal standard. This phenomenon of IS signal suppression at high analyte concentration was not important unless the concentration of Des-C was in great excess (~10x) compared to gymnodimine. Therefore, this trend was carefully considered when concentrations were chosen for the quantitative analysis experiments. The highest ratio of GYM/Des-C in this study was 2.8, at which the ion suppression effect was not apparent. Additionally, certain instrumental parameters were important for the MALDI analysis, namely laser pulse frequency and energy. The laser was run at 1000 Hz for the quantitative experiments in order to ensure maximal ion currents. Laser energies were similar to those used in the quantitative assays described previously in this chapter, in order to have full ablation with minimal in-source fragmentation.

Quantitative experiments were performed with a constant matrix concentration of 2.5 mg/ml for different analyte concentrations as well as with a constant matrix-to-analyte ratio of 1000, in order to compare the potential importance of maintaining a constant ratio throughout the analyte concentration range on quantitative results. It has been suggested previously that this does in fact play an important role in quantitative data for MALDI [264]. Figure 5.15 illustrates a summary of the results from the quantitation of Des-C with and without the use of the internal standard. The SIM calibration curves are shown using a constant matrix concentration in Figure 5.15a, with an inset exhibiting the curves using absolute signal intensities for Des-C. The same is shown in Figure 5.15b, but a constant matrix-to-analyte ratio was maintained throughout the entire

concentration range. It is clearly seen that linearities were improved when the ratios of Des-C/GYM peak areas were considered vs. the absolute intensities of Des-C. Also, inter-day variations are decreased when an internal standard is employed in the analysis. It is therefore imperative that the internal standard be used, especially in the case of MALDI analysis, which is continuously plagued with signal irreproducibilities due to inhomogeneous sample spots [265, 266]. The calibration curves using the constant matrix ratio gave slightly better R^2 values (average values of 0.998 vs. 0.993); however, the constant matrix concentration curves still yielded excellent results. A constant matrix concentration was employed, as otherwise, the quantitation of unknown samples would be much more difficult.

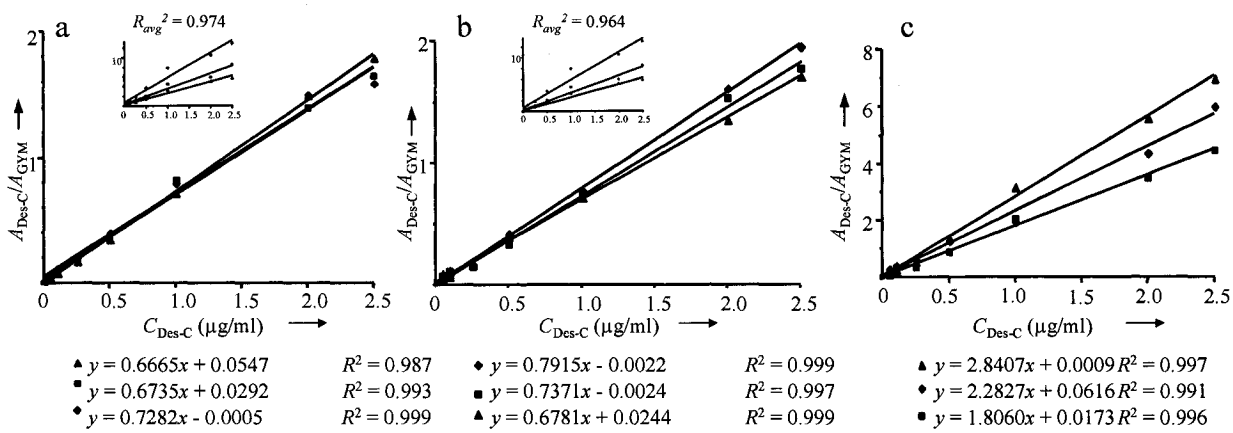

Figure 5.15 Optimization of MALDI quantitation of 13-desmethyl spirolide C. Each experiment was performed in triplicate (inter-day variation). a) SIM detection with constant matrix concentration (inset without IS). b) SIM detection with constant analyte:matrix ratio (inset without IS). c) MRM detection with constant matrix concentration.

Subsequent quantitative experiments were performed using MRM conditions. The CID spectra of the protonated molecule of Des-C (*m/z* 692) exhibited very similar fragment ions from both MALDI and ESI (Figure 5.16(a,b)). Two structurally significant ions are present at *m/z* 164 and 444. For the MRM experiments, the collision offset voltage was optimized at 60 V for the transition from *m/z* 692 to *m/z* 164. Above this collision energy, scattering losses increase and the signal for this transition was consequently reduced. Under the same CID conditions, the most predominant fragment ion in the product ion spectra of GYM (*m/z* 508) was seen at *m/z* 174; therefore, the

transition from *m/z* 508 to *m/z* 174 was monitored as the internal standard signal for quantitative results. The MRM method is much more selective than SIM detection for the quantitative analysis of complex samples. Figure 5.15c shows three inter-day analyses of Des-C standard curves with GYM as the internal standard and a constant matrix concentration. Linearities were excellent and very consistent with an averaged R^2 value of 0.995.

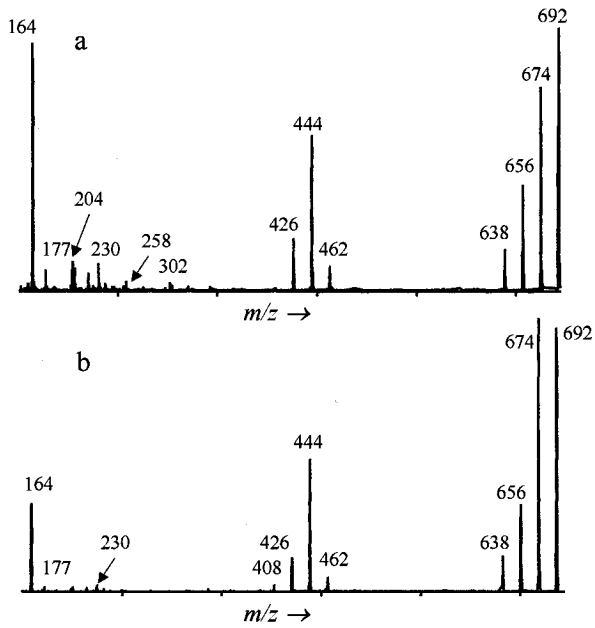

Figure 5.16 Product ion spectra following CID in triple quadrupole instrument with MALDI (a) and electrospray ionization (b). Spectra shown are at collision offset voltage of 45 V.

A quantitative study was performed for several unknown samples derived from a crude extract. The samples employed in this study were prepared with semi-preparative mass-triggered LC fractionation of a crude methanolic extract prepared from a culture of *Alexandrium ostenfeldii* (refer to Chapter 2). Several fractions resulted with different concentrations and compositions of spirolide toxins. All fractions (samples 1-7) with substantial Des-C concentrations were chosen as unknown samples for obtaining quantitative results. The concentration of Des-C was also determined in the crude extract with two separate dilution factors (samples 9-10). All samples contained other spirolide analogs, however, these did not interfere with the Des-C measurements. Also, four fractions (samples 8, 11-14) were chosen and cleaned-up with an additional solid-phase

extraction procedure (see Experimental). The resulting calibration curve, covering the concentration range of 0.01 to 1.75 μg/ml Des-C, seen in Figure 5.17a, exhibited excellent linearity (R^2=0.999). Average values for the ratio of Des-C/GYM peak areas from six repetitive measurements gave very good relative standard deviations for each of the unknown samples, all but one of which were under 10%. The corresponding concentrations for the undiluted samples were calculated and are represented in Table 5.4. In order to further validate the results from this method, the samples were also quantified using an LC/MS method with electrospray ionization. The same MRM transitions were monitored as for the MALDI analysis while also maintaining identical CID conditions. The ESI standard curve extended from 0.0005 to 0.15 μg/ml and all samples were diluted an extra 10-fold compared to the MALDI samples. Des-C and GYM were well separated with elution times of 1.5 and 0.9 minutes, respectively, as seen in the chromatogram from an LC/MS run in Figure 5.18. The ESI calibration curve is shown in Figure 5.17b and also displays excellent linearity (R^2=0.998). A significant correlation between these two methods would allow the conclusion that accurate data could be achieved with MALDI even with complex samples without prior chromatography. The calculated concentrations obtained from the ESI data are summarized alongside those from the MALDI results in Table 5.4. The average % RSD for the MALDI analysis was 7.4 ± 2.4 %. The cross-correlation plot in Figure 5.19 illustrates good agreement between the two methods. Ideally, the comparison would result in a linear plot with a slope of 1. The corresponding curve deviates only slightly from the ideal situation, thus providing excellent confidence in the accuracy of the MALDI method. The correlation between the two methods did not improve when the SPE samples were considered alone. It was therefore concluded that the SPE step was not required for obtaining quantitative MALDI data.

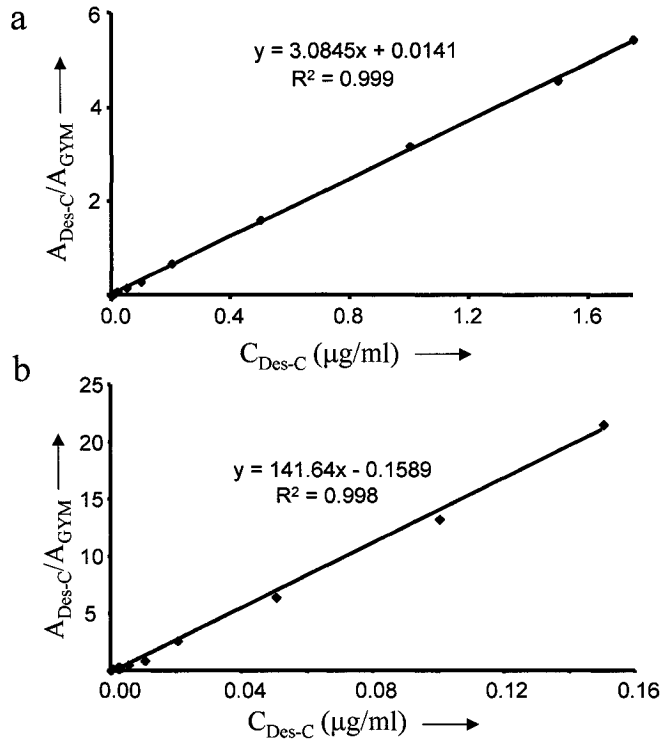

Figure 5.17 Quantitative results from MALDI and ESI experiments. Calibration curves are shown for MALDI (a) and electrospray (b) analyses.

Table 5.4 Summary of quantitative results for unknown samples from MALDI and ESI experiments

	MALDI quantitation		ESI quantitation	
Sample	Concentration of run sample (µg/ml)	Concentration of original sample[a] (µg/ml)	Concentration of run sample (µg/ml)	Concentration of original sample[a] (µg/ml)
1	0.01	**0.05**	0.0028	**0.07**
2	0.45	**90.4**	0.039	**83.5**
3	0.22	**44.2**	0.019	**38.2**
4	0.21	**20.6**	0.018	**18.3**
5	0.28	**27.6**	0.022	**22.4**
6	0.25	**1.00**	0.023	**0.94**
7	0.13	**2.63**	0.012	**2.4**
8	0.34	**3.41**	0.027	**2.8**
9	0.07	**7.21**	0.0079	**7.3**
10	0.15	**7.41**	0.014	**6.8**
11	0.58	**23.2**	0.063	**27.2**
12	0.39	**15.6**	0.054	**22.9**
13	1.04	**41.7**	0.135	**58.6**
14	0.12	**4.70**	0.015	**5.81**

[a] Different dilution factors were applied in order to have the samples fall within the dynamic range of each method.

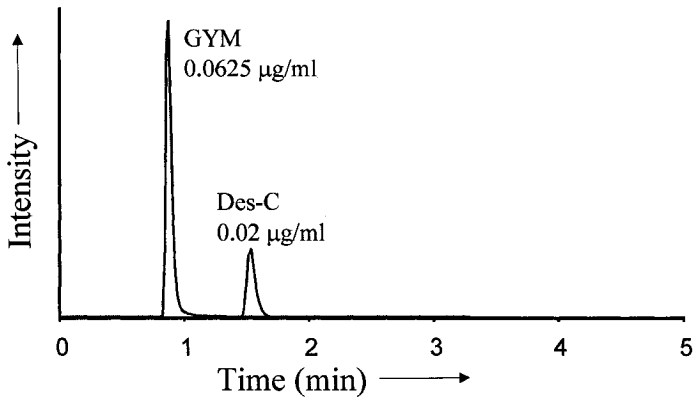

Figure 5.18 Representative chromatogram from electrospray MRM experiment. Des-C (*m/z* 692 → 164) and GYM (*m/z* 508 → 174) elute at 1.5 and 0.9 min, respectively, during the chromatographic run.

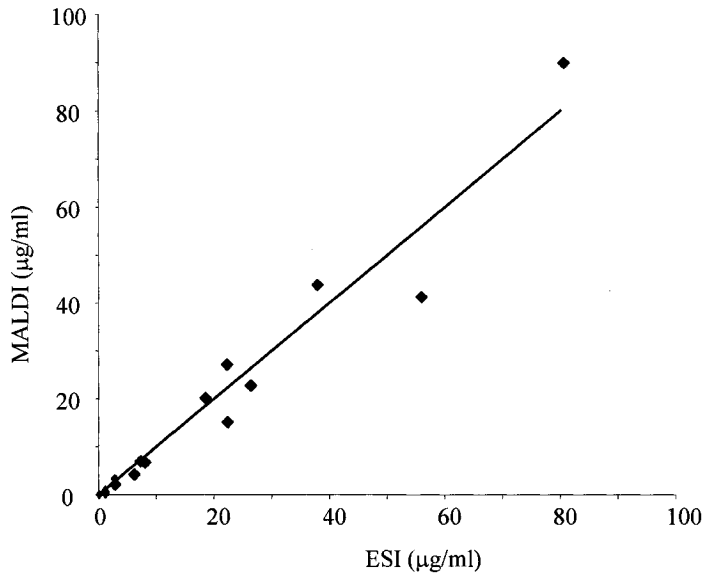

Figure 5.19 Cross-correlation diagram comparing MALDI and ESI quantitation results and accuracy of methods. (Note that the line in the diagram represents the ideal behavior; slope = 1.)

Additionally, this method benefits from the inherent advantages of MALDI over electrospray. It has been reported that this ionization method is much more tolerant to buffers and salts than ESI, and therefore, is potentially more amenable to the direct analysis of biological samples [233, 234]. Also, repetitive sampling is a clear advantage for MALDI. For example, one could readily run a data-dependent experiment, starting with an initial full scan, followed by targeted product ion scan analyses on precursor ions of interest, as well as precursor ion and neutral loss scans, all on the same spot. We could

therefore easily obtain much more information from one MALDI spot than is possible for a single sample injection in ESI LC/MS, since after the elution of the chromatographic peak, the analyte is no longer present and a further injection would be required. Both MALDI and ESI calibration curves yield excellent linearities, however, the ESI curve extends to concentrations an order of magnitude lower. Therefore, the ESI method is perceived as having lower detection limits. Yet, the absolute amount sampled is much less for the MALDI analysis. The electrospray method consumes 100% of 3 µl sample with each analysis whereas the MALDI method samples a very minimal area (~4%) of the dried spot from a 1 µl sample (see previous section).

Previous analyses of spirolides in *A. ostenfeldii* cultures have estimated 13-desmethyl spirolide C to have a concentration of 54 pg/cell [98]. Therefore, we predict that single cell analysis would be feasible with the present method, since 10 pg on target was easily detected and quantified. Single cell analysis is of great interest, as it would allow the differential toxin profiles and spirolide content to be studied for different cells in the same culture. Moreover, the limit of detection for the MALDI method could be improved substantially with a longer sampling time on each spot; this would, however, decrease the throughput of the method. Ultimately, the high-throughput nature of MALDI is the most important advantage over electrospray. The present method sampled each spot within approximately 3 seconds with the entire sample set being analyzed in under one hour. Conversely, the ESI method needed over 10 minutes for each sample due to chromatographic separation, column equilibration and other overhead steps. As a result, analyzing the entire set of samples using the ESI method required approximately 12 hours. Of course, slight improvements on the throughput of the ESI method could be achieved, however it would still need a much longer analysis time than the MALDI experiment. Similar methods for the quantitation of small molecules in complex biological matrices would be extremely attractive for the pharmaceutical industry, where there exists a great need for increased productivity and efficiency.

Another important advantage of MALDI-QqQ is the use of dedicated scan functions. Some unique features of the triple quadrupole are quite interesting for the study of natural products and related compounds in complex mixtures. Precursor ion and neutral loss scans are particularly useful for the identification of specific compound

classes. Several common fragment ions and neutral losses are observed within the spirolide toxin family. Their characteristic fragmentation behavior can aid in their detection as well as elucidating their structure. Both precursor ion and neutral loss scans have been performed using the most informative ions in the CID spectra of Des-C, at *m/z* 164 and *m/z* 444. Spirolide-type compounds are easily detected in a crude extract using these ions for specific linked scans. A full scan spectrum, shown in Figure 5.20a, exhibits a wide range of ions, including those related to the organic matrix as well as other interferences present in the extract. Precursor ion scans were performed for both *m/z* 164 and *m/z* 444 ions (Figure 5.20b). For the precursor ion spectrum of *m/z* 164, we can identify peaks at *m/z* values of 692, 694, 706 and 708, which represent previously identified spirolide compounds (seen in bold in the figure), as well as some other peaks as a result of in-source water loss fragmentation of either *m/z* 692 or *m/z* 706. A precursor ion at *m/z* 598 was also identified in this experiment, which represents an unknown compound thought to be a spirolide analog present in the phytoplankton extract. A similar experiment for identifying precursors of the fragment ion at *m/z* 444 gave signals for the protonated molecule of Des-C (m/z 692), a fragment ion corresponding to a single water loss (*m/z* 674), and a very small signal for *m/z* 694. The latter corresponds to that of 13-desmethyl spirolide D, a minor component present in the extract. None of the other spirolide species present in the crude extract yield a product ion at *m/z* 444. Instead, spirolide C and D give analogous peaks at *m/z* values of 458, for their protonated molecules at *m/z* 706 and 708, respectively. Two other minor spirolide toxins, with *m/z* values of 694 and 708, have previously been detected in the extract and exhibit fragment ions at *m/z* 460 (Chapter 2). Corresponding neutral loss scans were also monitored for the dissociation pathways forming the two main structurally informative ions of Des-C. A neutral loss scan of 528 Da gave a sole signal at *m/z* 692, however, different spirolides were detected through a neutral loss scan of 248 Da. The experiment for detecting precursors exhibiting neutral losses for 528 Da would allow the identification of spirolide analogs with structural changes on the cyclic imine portion of the molecule. The latter experiment, for the neutral loss of 248 Da, revealed precursor ions at *m/z* values of 692, 706 and 604, corresponding to the protonated molecules of 13-desmethyl spirolide C, spirolide C and an unknown spirolide analog, respectively.

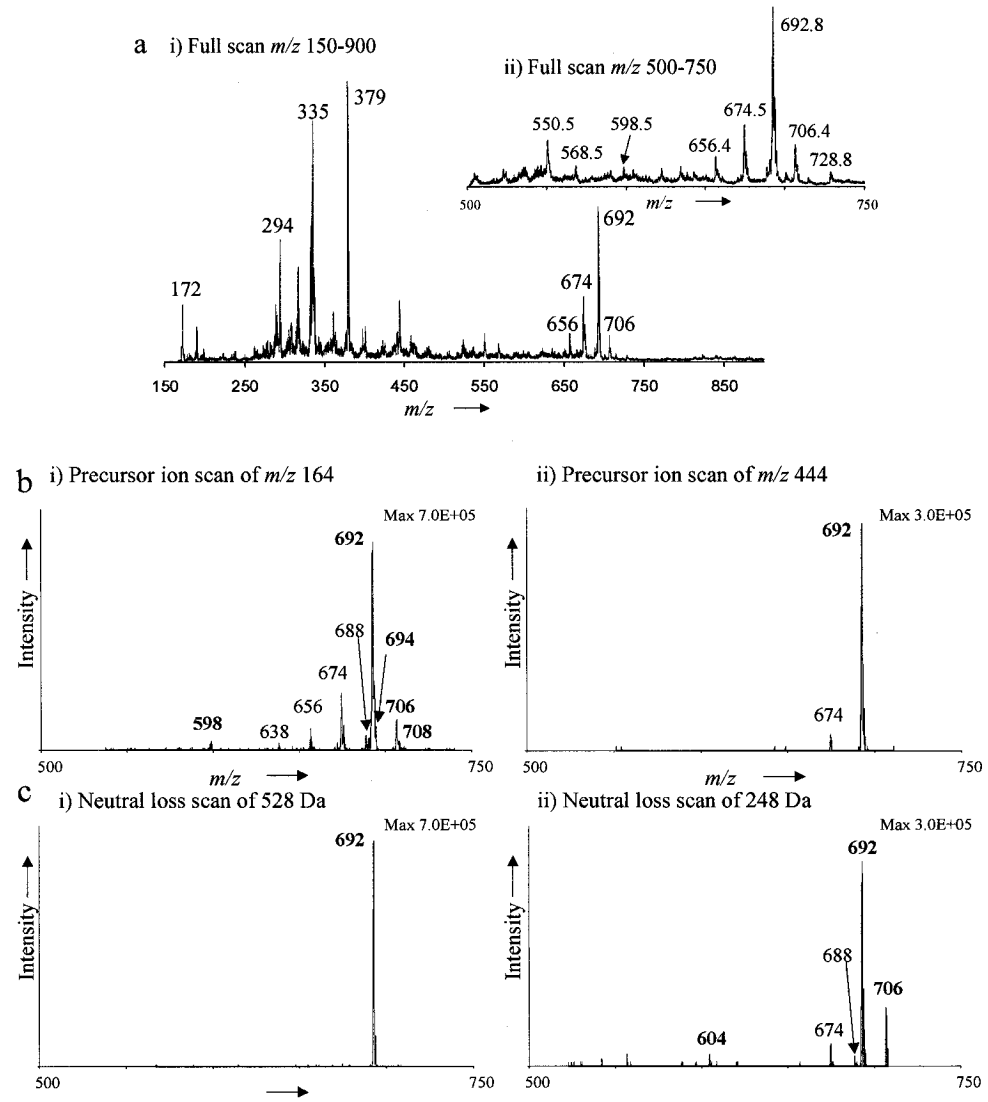

Figure 5.20 MALDI experiments on crude phytoplankton extract. a) Full scan experiment i) *m/z* 150-900 and ii) *m/z* 500-750, b) precursor ion scans for fragment ions at i) *m/z* 164 (at 60 V) and ii) *m/z* 444 (at 45 V) and (c) neutral loss scans of i) 528 Da and ii) 248 Da. The bolded *m/z* values represent protonated spirolide molecules, whereas the others are derived from water losses occuring in the MALDI source.

The MALDI-QqQ also provided high-quality CID spectra for the spirolides present in complex mixtures. A full scan spectrum (*m/z* 500-750) for one of the fractions containing several of the toxins is shown in Figure 5.21a. Protonated spirolide compounds were detected at m/z 692, 694, 706 and 708 and were present at very different concentration levels. Each component was selected to undergo CID and the resulting product ion spectra are represented in Figure 5.21b. Even the minor components

resulted in structurally informative CID spectra with excellent signal-to-noise ratios. The spectra consequently classified the different spirolide species as 13-desmethyl spirolide C (*m/z* 692), spirolide C (*m/z* 706) and spirolide D (*m/z* 708). Unfortunately, since 13-desmethyl spirolide C was present in much higher amounts than the other spirolides, the CID spectrum of *m/z* 694 corresponds to that of the M+2 isotope of the *m/z* 692 peak and not 13-desmethyl spirolide D (*m/z* 694). This represents an important limitation of the MALDI-triple quadrupole technique, as no chromatographic separation prior to the MS analysis is performed. This must therefore be kept in mind for certain applications where isomeric or isobaric interferences may be present.

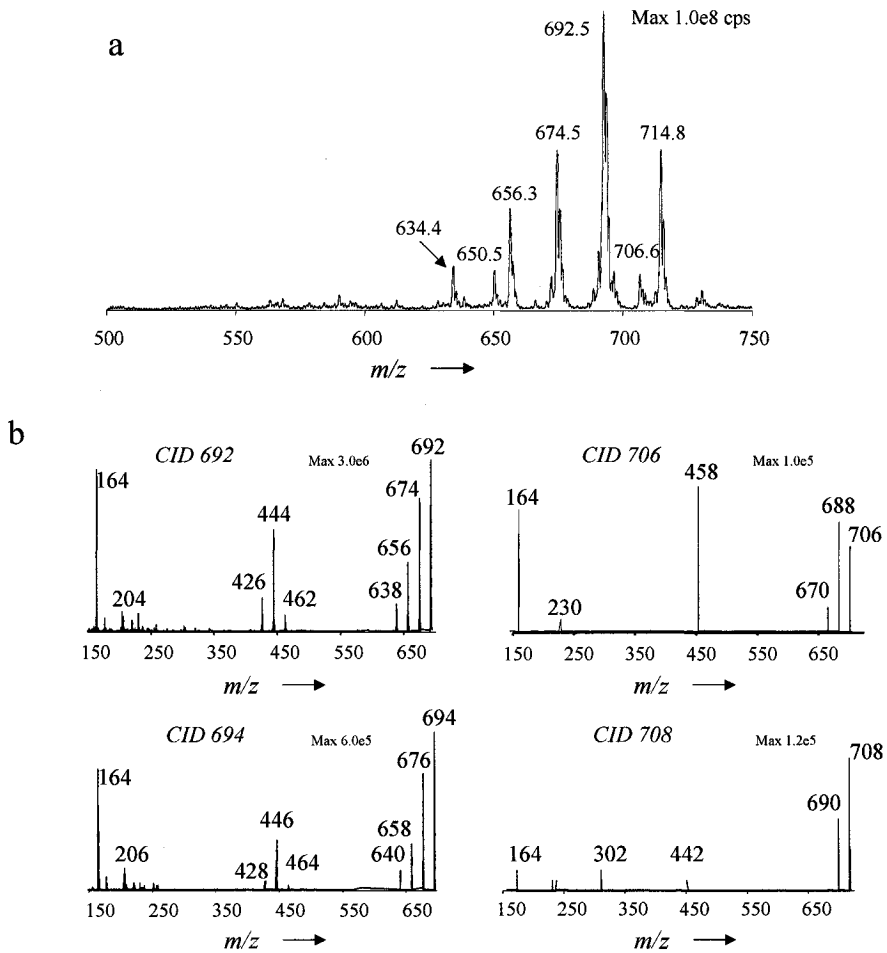

Figure 5.21 a) Full scan experiment (*m/z* 500-750) from purified fraction of phytoplankton extract. b) Product ion scans from individual spirolide components at *m/z* 692, 694, 706 and 708 with collision offset voltage of 45 V.

Conclusions

Quantitative small molecule MALDI shows great promise for becoming an established technique, mainly due to the combination of a high-repetition rate MALDI source with a triple quadrupole mass spectrometer. The focus here was mainly to investigate underlying phenomena associated with this technique and to assess the validity of the generated results.

MALDI has long suffered from several limiting factors for the analysis of small molecules, including large matrix interferences for *m/z* values less than 1000. In these studies analytes in this mass range were easily measured using CHCA as the organic matrix and selecting specific fragmentation pathways of each analyte/internal standard pair for increased selectivity. An important element was the imaging of spots using both light microscope and SEM images. Imaging software was employed to examine the ablated areas and calculate the amount of sample consumed. Several parameters needed to be addressed in order to operate at optimal conditions for these quantitative MALDI experiments. The laser power and frequency settings were extremely important in terms of amount ablated and sensitivity. Impressive detection limits and linearities were seen for the chosen pharmaceutical compounds, which would easily surpass most of the electrospray methods presently used.

Certain aspects of internal standard selection were evaluated for quantitative MALDI. The important factors for selecting an appropriate internal standard and the resulting analytical figures of merit (precision, linearity of calibration curve) can be summarized as follows: choosing an isotope standard of the analyte naturally leads to optimal results. If isotope-labeled compounds are not available, however, structural analogs can be successfully used as long as important solution-phase properties are appropriately matched. With a group of acyl-carnitines, it was shown that molecular weight, and thus solubility, remains very important even in the case of molecules having a fixed charge site. In addition, matching the solubility of the analyte or the internal standard with the matrix compound is also essential for improved co-crystallization. More important, however, is a close match of the crystallization behavior of internal standard and analyte. These results show that if this condition is met, a homogeneous

distribution throughout the sample spot is not necessarily required. Such a match in crystallization behaviour can be obtained when the relative polarities of analyte and internal standard are similar. This is particularly important for compounds with multiple ionization sites in solution.

Experimental evidence has also been shown here, exemplifying the fact that we can even use an internal standard of a different compound class, if its solution-phase properties match that of the analyte. This is explained by a similar distribution of analyte and internal standard in the crystal matrix. Naturally, further work would aid in the understanding of these underlying mechanisms for segregation of different molecules within the matrix. For example, it would be interesting to see how compounds with similar solution-phase (log *D*) but increasingly different gas-phase properties (*e.g.*, proton affinity) behave in an analogous comparison.

With certain advanced crystallization techniques such as electrospray sample deposition, it may be possible to "force" the analyte and internal standard into a more homogeneous co-crystallization pattern, even though they may segregate under dried droplet sample preparation conditions. Also, different solvent systems or matrices could reduce segregation effects in some cases. Importantly, the sample preparation conditions were deliberately chosen, in order to describe a simple procedure for the applicability of high-throughput analyses for small molecule quantitation.

The analysis of spirolide toxins was assessed using the MALDI-triple quadrupole system. A quantitative study with 13-desmethyl spirolide C demonstrated the feasibility of this system for accurate determination of toxin concentrations in complex samples. Furthermore, precursor ion and neutral loss scans can be employed for the screening of certain compound classes in order to simplify the MALDI spectra.

Additionally, several high-throughput applications exist in the pharmaceutical industry, including metabolism and pharmacokinetic studies as well as combinatorial library screening which would also benefit from the MALDI-QqQ technique. The number of samples can be enormous, and their analyses often represent an important bottleneck for the introduction of a new drug. Current collaborative efforts are ongoing in the application of these assays for pharmaceutical samples.

Chapter VI. Conclusion

The rapid advancement of biological mass spectrometry has been largely driven by increasingly demanding applications from pharmaceutical, proteomics and metabolomics laboratories. Very often, the goal of mass spectrometry research is to make method development faster and simpler. Increasingly, however, scientists also require the measurement of molecules at very low, biologically active levels, while simultaneously maintaining fragile secondary or tertiary structural conformations or, sometimes, even important non-covalent interactions. A range of interesting technological concepts has resulted from recent developments. The subject of this thesis was the investigation of some of these new technologies for analyzing small molecules.

One of the most important applications of mass spectrometry is the structural characterization of novel biologically-relevant compounds such as natural products or drug metabolites. Using multistage tandem MS methods often allows pinpointing the sites of structural modification by comparing the fragmentation behaviour of the unknown to that of a known precursor or analog. This can be further supported by the use of accurate mass measurements. With high mass accuracy, a small number of possible empirical formulae can be calculated from the data, aiding greatly in characterizing the unknown compound. In this work, the spirolide and paralytic shellfish poison (PSP) toxin families were extensively studied by MS/MS and high-resolution FT-ICR. Several new analogs of the spirolide toxins were discovered, which were subsequently confirmed by FT-ICR accurate mass data. A comparative study of QqTOF and FT-ICR instruments was additionally performed using the complex CID spectra of two PSP toxins, for the investigation of the mass accuracy requirements needed in these applications. It was found that for most full scan or simple MS/MS spectra, medium-resolution TOF instruments yielded excellent mass accuracies. This was subsequently confirmed for elemental formula assignments of product ions from anthracycline antibiotics. In turn, the importance of certain functional groups in the fragmentation of these drug molecules could be demonstrated and was employed for the rationalization of metabolic routes. For overlapping isobaric peaks, however, FT-ICR-MS was needed to fully resolve individual species. It should be pointed out that only high mass resolution can give reliable results

for unknown samples, since one never knows in advance whether potential interferences are present. Unfortunately, FT-ICR-MS is very expensive and out of reach for many laboratories, because of the immense initial purchase price as well as the substantial regular maintenance cost, mostly for cryogens required for the superconducting magnet. Recently, an interesting instrument, the "Orbitrap", has been introduced, which promises a similar resolving power to the FT-ICR, without the need for a superconducting magnet. The verdict on this new technology, however, will only be out in several years, as only very few instruments have been installed in research laboratories.

A second important current application of mass spectrometry is high-throughput pharmaceutical and clinical analyses. Throughput enhancements in these fields have largely been achieved by developing multiplexed sample introduction interfaces to LC/MS instruments. In this thesis, we have assessed a new alternative approach for small molecules, namely quantitative MALDI by means of a prototype MALDI-QqQ instrument. Initially, several fundamental studies demonstrated the importance of laser parameters, organic matrix selection and the use of internal standards for obtaining reliable results. It was then shown that the monitoring and quantitation of pharmaceutical drugs and toxins represent important areas which could benefit tremendously from this technique.

There is no question that developments in mass spectrometry instrumentation in the near future will further improve the sensitivity and reliability of biological analyses. It can also be readily anticipated that the application range of today's mass spectrometers will further expand, allowing more compounds with a wider range of polarities to be analyzed simultaneously. What is significantly lacking, however, is the availability of intelligent processing software for the experimental results, for example; automated interpretation of fragmentation patterns or structure assignments and algorithms for classification of identified biological compounds according to their function rather than only on their chemical structure. This work has demonstrated that the latest generation mass spectrometers can be successfully applied to very demanding biological analyses, yielding a tremendous amount of relevant analytical data. A similar effort in the research on MS software developments as has recently been seen for the instrumentation, would therefore greatly advance the biological mass spectrometry field.

References

1. Mei H. "Matrix effects: Causes and solutions". In: *Using Mass Spectrometry for Drug Metabolism Studies*, Korfmacher WA (ed), CRC Press, Boca Raton, 2005: 103.

2. James C. "Solid-phase extraction". In: *Principles and Practice of Bioanalysis*, Venn RF (ed), Taylor and Francis, London, 2000: 28.

3. Wiltshire H. " Physico-chemical properties of drugs and metabolites and their extraction from biological material". In: *Principles and Practice of Bioanalysis*, Venn RF (ed), Taylor and Francis, London, 2000: 1.

4. Van Deemter JJ, Zuiderweg FJ, Klinkenberg A. Longitudinal diffusion and resistance to mass transfer as causes of nonideality in chromatography. *Chem. Eng. Sci.* 1956; **5**: 271.

5. Miller JM. In: *Chromatography. Concepts and Contrasts.* Wiley-Interscience, Hoboken, NJ, 2005: 75.

6. Tanaka N, Kobayashi H, Nakanishi K, Minakuchi H, Ishizuka N. Monolithic LC columns. *Anal. Chem.* 2001; **73**: 420A.

7. Wilson ID, Nicholson JK, Castro-Perez J, Granger JH, Johnson KA, Smith BW, Plumb RS. High resolution "ultra performance" liquid chromatography coupled to oa-TOF mass spectrometry as a tool for differential metabolic pathway profiling in functional genomic studies. *J. Proteome Res.* 2005; **4**: 591.

8. Barber M, Bordoli RS, Sedgwick RD. "Fast atom bombardment". In: *Soft Ionization Biological Mass Spectrometry*, Morris HR (ed), Heyden, London, 1981: 137.

9. Yamashita M, Fenn JB. Electrospray ion source. Another variation on the free-jet theme. *J. Phys. Chem.* 1984; **88**: 4451.

10. Yamashita M, Fenn JB. Negative ion production with the electrospray source. *J. Phys. Chem.* 1984; **88**: 4671.

11. Bruins AP. Mass spectrometry with ion sources operating at atmospheric pressure. *Mass Spectrom. Rev.* 1991; **10**: 53.

12. Karas M, Bachmann D, Bahr U, Hillenkamp F. Matrix-assisted ultraviolet laser desorption of non-volatile compounds. *Int. J. Mass Spectrom.* 1987; **78**: 53.

13. Nguyen DN, Becker GW, Riggin RM. Protein mass spectrometry: Applications to analytical biotechnology. *J. Chrom. A* 1995; **705**: 21.

14. Winston RL, Fitzgerald MC. Mass spectrometry as a readout of protein structure and function. *Mass Spectrom. Rev.* 1997; **16**: 165.

15. Bergquist J, Palmblad M, Wetterhall M, Håkansson P, Markides KE. Peptide mapping of proteins in human body fluids using electrospray ionization Fourier transform ion cyclotron resonance mass spectrometry. *Mass Spectrom. Rev.* 2002; **21**: 2.

16. Crain PF, McCloskey JA. Applications of mass spectrometry to the characterization of oligonucleotides and nucleic acids. *Curr. Opin. Biotechnol.* 1998; **9**: 25.

17. Beck JL, Colgrave ML, Ralph SF, Sheil MM. Electrospray ionization mass spectrometry of oligonucleotide complexes with drugs, metals, and proteins. *Mass Spectrom. Rev.* 2001; **20**: 61.

18. Stöckigt J, Sheludko Y, Unger M, Gerasimenko I, Warzecha H, Stöckigt D. High-performance liquid chromatographic, capillary electrophoretic and capillary electrophoretic-electrospray ionization mass spectrometric analysis of selected alkaloid groups. *J. Chrom. A* 2002; **967**: 85.

19. Kostiainen R, Kotiaho T, Kuuranne T, Auriola S. Liquid chromatography/ atmospheric pressure ionization-mass spectrometry in drug metabolism studies. *J. Mass Spectrom.* 2003; **38**: 357.

20. Cech NB, Enke CG. Practical implications of some recent studies in electrospray fundamentals. *Mass Spectrom. Rev.* 2001; **20**: 362.

21. Taflin DC, Ward TL, Davis EJ. Electrified droplet fission and the Raleigh limit. *Langmuir* 1989; **5**: 376.

22. Dole M, Mack LL, Hines RL, Mobley RC, Ferguson LD, Alice MB. Molecular beams of macroions. *J. Chem. Phys.* 1968; **49**: 2240.

23. Iribarne JV, Thomson BA. On the evaporation of charged ions from small droplets. *J. Chem. Phys.* 1976; **64**: 2287.

24. Loo JA. Studying noncovalent protein complexes by electrospray ionization mass spectrometry. *Mass Spectrom. Rev.* 1997; **16**: 1.

25. Gelpí E. Biomedical and biochemical applications of liquid chromatography - mass spectrometry. *J. Chrom. A* 1995; **703**: 59.

26. Von Brocke A, Nicholson G, Bayer E. Recent advances in capillary electrophoresis -electrospray-mass spectrometry. *Electrophoresis* 2001; **22**: 1251.

27. Fenn JB, Mann M, Meng CK, Wong SF, Whitehouse CM. Electrospray ionization for mass spectrometry of large biomolecules. *Science* 1989; **246**: 64.

28. Karas M, Bachmann D, Hillenkamp F. Influence of the wavelength in high-irradiance ultraviolet laser desorption-MS of organic molecules. *Anal. Chem.* 1985; **57**: 2935.

29. Juhasz P, Costello CE, Biemann K. MALDI-MS with 2-(4-hydroxyphenylazo)benzoic acid acid matrix. *J. Am. Soc. Mass Spectrom.* 1993; **4**: 399.

30. Zenobi R, Knochenmuss R. Ion formation in MALDI-MS. *Mass Spectrom. Rev.* 1998; **17**: 337.

31. Karas M, Bahr U, Giessmann U. MALDI-MS. *Mass Spectrom. Rev.* 1991; **10**: 335.

32. Westmacott G, Ens W, Hillenkamp F, Dreisewerd K, Schürenberg M. The influence of laser fluence on ion yield in MALDI-MS. *Int. J. Mass Spectrom.* 2002; **221**: 67.

33. Westman A, Huth-Fehre T, Demirev P, Sundqvist BUR. Sample morphology effects in matrix-assisted laser desorption/ionization of proteins. *J. Mass Spectrom.* 1995; **30**: 206.

34. Kussmann M, Roepstorff P. Sample preparation techniques for peptides and proteins analyzed by MALDI-MS. *Methods Mol. Biol.* 2000; **146**: 405.

35. Fenselau C. MALDI MS and strategies for protein analysis. *Anal. Chem.* 1997; **69**: 661A.

36. Paul W, Steinwedel HS. Ein neues Massenspektrometer ohne Magnetfeld. *Z. Naturforsch.* 1953; **8a**: 448.

37. Ferguson RE, McCulloh KE, Rosenstock HM. Observation of the products of ionic collision processes and ion decompositions in a linear, pulsed time-of-flight mass spectrometer. *J. Chem. Phys.* 1965; **42**: 100.

38. Barker J. *Mass Spectrometry.* 2nd edition, John Wiley & Sons, Chichester, 1999: 75.

39. de Hoffmann E, Stroobant V. *Mass Spectrometry. Principles and Application.* 2nd edition, John Wiley & Sons, Chichester, 2002: 66.

40. Jemal M, Ouyang Z, Zhao W, Zhu M, Wu WW. A strategy for metabolite identification using triple-quadrupole mass spectrometry with enhanced resolution and accurate mass capability. *Rapid Commun. Mass Spectrom.* 2003; **17**: 2732-2740.

41. Yost RA, Enke CG. Selected ion fragmentation with a tandem quadrupole mass spectrometer. *J. Am. Chem. Soc.* 1978; **100**: 2274.

42. March RE. "Quadrupole ion trap mass spectrometer". In: *Encyclopedia of Analytical Chemistry,* Meyers RA (ed). John Wiley & Sons, Chichester, 2000: 11848.

43. Paul W, Steinwedel H. Apparatus for separating charged particles of different specific charges, German Patent 944,900,1956; US Patent 2,939,952,1960.

44. Stafford GC Jr, Kelley PE, Syka JEP, Reynolds WE, Todd JFJ. Recent improvements in and analytical applications of advanced ion trap technology. *Int. J. Mass Spectrom. Ion Processes.* 1984; **60**: 85.

45. Kaiser RE, Cooks RG, Stafford GC, Syka JEP, Hemberger PH. Operation of a quadrupole ion trap mass spectrometer to achieve high mass/charge ratios. *Int. J. Mass Spectrom. Ion Processes* 1991; **106**: 79.

46. Cleven CD, Cox KA, Cooks RG, Bier ME. Mass shifts due to ion/ion interactions in a quadrupole ion trap mass spectrometer. *Rapid Commun. Mass Spectrom.* 1994; **8**: 451.

47. Cox KA, Cleven CD, Cooks RG. Mass shifts and local space charge effects observed in the quadrupole ion trap at higher resolution. *Int. J. Mass Spectrom. Ion Processes.* 1995; **144**: 47.

48. Douglas DJ, Frank AJ, Mao D. Linear ion traps in mass spectrometry. *Mass Spectrom. Rev.* 2005; **24**: 1.

49. Gross ML, Rempel DL. Fourier transform mass spectrometry. *Science.* 1984; **226**: 261.

50. Comisarow MB, Marshall AG. The early development of Fourier transform ion cyclotron resonance (FT-ICR) spectroscopy. *J. Mass Spectrom.* 1996; **31**: 581.

51. Comisarow MB, Marshall AG. Fourier transform ion cyclotron resonance spectrometry. *Chem. Phys. Lett.* 1974; **25**: 282.

52. Comisarow MB, Marshall AG. Frequency-sweep Fourier transform ion cyclotron resonance spectrometry. *Chem. Phys. Lett.* 1974; **26**: 489.

53. Marshall AG, Hendrickson CL, Jackson GS. Fourier transform ion cyclotron resonance mass spectrometry: A primer. *Mass Spectrom. Rev.* 1998; **17**: 1.

54. de Hoffmann E, Stroobant V. *Mass Spectrometry. Principles and Applications.* 2nd edition, John Wiley & Sons: Chichester 2002: 121.

55. Hager JW, Le Blanc JCY. Product ion scanning using a Q-q-Q linear ion trap (Q TRAP) mass spectrometer. *Rapid Commun. Mass Spectrom.* 2003; **17**: 1056.

56. Hopfgartner G, Husser C, Zell M. Rapid screening and characterization of drug metabolites using a new quadrupole-linear ion trap mass spectrometer. *J. Mass Spectrom.* 2003; **38**: 138.

57. Clarke NJ, Rindgen D, Korfmacher WA, Cox KA. Systematic LC/MS metabolite identification in drug discovery. *Anal. Chem.* 2001; **73**: 430A.

58. Warscheid, B, Jackson K, Sutton C, Fenselau C. MALDI analysis of *Bacilli* in spore mixtures by applying a quadrupole ion trap time-of-flight tandem mass spectrometer. *Anal. Chem.* 2003; **75**: 5608.

59. Patrie SM, Charlebois JP, Whipple D, Kelleher NL, Hendrickson CL, Quinn JP, Marshall AG, Mukhopadhyay B. Construction of a hybrid quadrupole/Fourier transform ion cyclotron resonance mass spectrometer for versatile MS/MS above 10 kDa. *J. Am. Soc. Mass Spectrom.* 2004; **15**: 1099.

60. Belov ME, Nikolaev EN, Anderson GA, Auberry KJ, Harkewicz R, Smith RD. Electrospray ionization-Fourier transform ion cyclotron mass spectrometry using ion preselection and external accumulation for ultrahigh sensitivity. *J. Am. Soc. Mass Spectrom.* 2001; **12**: 38.

61. McLuckey SA. Principles of collisional activation in analytical mass spectrometry. *J. Am. Soc. Mass Spectrom.* 1992; **3**: 599.

62. Shukla AK, Futrell JH. Tandem mass spectrometry: Dissociation of ions by collisional activation. *J. Mass Spectrom.* 2000; **35**: 1069.

63. Jennings KR. The changing impact of the collision-induced decomposition of ions on mass spectrometry. *Int. J. Mass Spectrom.* 2000; **200**: 479.

64. Levsen K. *Fundamental Aspects of Organic Mass Spectrometry*, Verlag Chemie, Weinheim, 1978: 138.

65. Busch KL, Glish GL, McLuckey SA. *Mass Spectrometry/ Mass Spectrometry: Techniques and Applications of Tandem Mass Spectrometry,* VCH Publishers Inc., New York, 1988: 64.

66. Durup J. "Mechanisms of collision-induced dissociation of fast ions". In: *Recent Developments in Mass Spectrometry,* Ogata K, Hawakawa T (eds). University Park Press, Baltimore, 1970: 921.

67. Cooks RG. "Collision-induced dissociation of polyatomic ions". In: *Collision Spectroscopy,* Cooks RG (ed). Plenum Press, New York and London, 1979: 372.

68. McLuckey SA, Goeringer DE. Slow heating methods in tandem mass spectrometry. *J. Mass Spectrom.* 1997; **32**: 461.

69. Gauthier JW, Trautman TR, Jacobson DB. Sustained off-resonance irradiation for collision-activated dissociation involving Fourier transform mass spectrometry. Collision-activated dissociation technique that emulates infrared multiphoton dissociation. *Anal. Chim. Acta* 1991; **246**: 211.

70. Schwartz RN, Slawsky ZI, Herzfeld KF. Calculation of vibrational relaxation times in gases. *J. Chem. Phys.* 1952; **20**: 1591.

71. Thorne LR, Beauchamp JL. "Infrared photochemistry of gas phase ions". In: *Gas Phase Ion Chemistry. Vol. 3: Ions and Light*, MT Bowers (ed). Academic Press, London, 1984: 41.

72. van der Hart WJ. Studies of ion structures by photodissociation. *Int. J. Mass Spectrom. Ion Processes* 1992; **118/119**: 617.

73. Uechi GT, Dunbar RC. The kinetics of infrared laser photodissociation of n-butylbenzene ions at low pressure. *J. Chem. Phys.* 1992; **96**: 8897.

74. Brodbelt J. "Effects of collisional cooling on ion detection". In: *Practical Aspects of Ion Trap Mass Spectrometry.* Volume I: Fundamentals of Ion Trap Mass Spectrometry. March RE, Todd JFJ (eds). CRC Press, Boca Raton, FL, 1995: 209.

75. Colorado A, Shen JX, Vartanian VH, Brodbelt J. Use of infrared multiphoton photodissociation with SWIFT for electrospray ionization and laser desorption applications in a quadrupole ion trap mass spectrometer. *Anal. Chem.* 1996; **68**: 4033.

76. Sleno L, Volmer DA, Kovačević B, Maksić ZB. Gas-phase dissociation reactions of protonated saxitoxin and neosaxitoxin. *J. Am. Soc. Mass Spectrom.* 2004; **15**: 462.

77. Little DP, Speir JP, Senko MW, O'Connor PB, McLafferty FW. Infrared multiphoton dissociation of large multiply charged ions for biomolecule sequencing. *Anal. Chem.* 1994; **66**: 2809.

78. Li W, Hendrickson CL, Emmett MR, Marshall AG. Identification of intact proteins in mixtures by alternated capillary liquid chromatography electrospray ionization and LC ESI infrared multiphoton dissociation Fourier transform ion cyclotron resonance mass spectrometry. *Anal. Chem.* 1999; **71**: 4397.

79. Xie Y, Lebrilla CB. Infrared multiphoton dissociation of alkali metal-coordinated oligosaccharides. *Anal. Chem.* 2003; **75**: 1590.

80. Little DP, Aaserud DJ, Valaskovic GA, McLafferty FW. Sequence information from 42-108-mer DNAs (complete for a 50-mer) by tandem mass spectrometry. *J. Am. Chem. Soc.* 1996; **118**: 9352.

81. Sannes-Lowery KA, Hofstadler SA. Sequence confirmation of modified oligonucleotides using IRMPD in the external ion reservoir of an electrospray ionization Fourier transform ion cyclotron mass spectrometer. *J. Am. Soc. Mass Spectrom.* 2003; **14**: 825.

82. Goolsby BJ, Brodbelt JS. Analysis of protonated and alkali metal cationized aminoglycoside antibiotics by collision-activated dissociation and infrared multiphoton dissociation in the quadrupole ion trap. *J. Mass Spectrom.* 2000; **35**: 1011.

83. Crowe MC, Brodbelt JS, Goolsby BJ, Hergenrother P. Characterization of erythromycin analogs by collisional activated dissociation and infrared multiphoton dissociation in a quadrupole ion trap. *J. Am. Soc. Mass Spectrom.* 2002; **13**: 630.

84. Hallegraeff GM. A review of harmful algal blooms and their apparent global increase. *Phycologia* 1993; **32**: 79.

85. Van Dolah FM. Marine algal toxins: Origins, health effects, and their increased occurrence. *Environ. Health Perspect. Supp.* 2000; **108**: 133.

86. Shimizu Y. "The chemistry of paralytic shellfish toxins". In: *Marine Toxins and Venoms. Handbook of Natural Toxins: Volume 3.* Tu AT (ed). Marcell Dekker Inc., New York, 1988: 63.

87. Hu T, Doyle J, Jackson D, Marr J, Nixon E, Pleasance S, Quilliam MA, Walter JA, Wright JLC. Isolation of a new diarrhetic shellfish poison from Irish mussels. *J. Chem. Soc. Chem. Commun.* 1992: 39.

88. Bird CJ, Wright JLC. The shellfish toxin domoic acid. *World Aquaculture* 1989; **20**: 40.

89. Baden DG. Brevetoxins: unique polyether dinoflagellate toxins. *FASEB J.* 1989; **3**: 1807.

90. Hu T, Curtis JM, Oshima Y, Quilliam MA, Walter JA, Watson-Wright WM, Wright JLC. Spirolides B and D, two novel macrocycles isolated from the digestive glands of shellfish. *J. Chem. Soc. Chem. Commun.* 1995; 2159.

91. Cembella AD, Quilliam MA, Lewis NI, Bauder AG, Wright JLC. "Identifying the planktonic origin and distribution of spirolides in coastal Nova Scotia". In: *Harmful Algae. Proceedings of the VIIIth International Conference on Harmful Algae.* Reguera B, Blanco J, Fernandez ML, Wyatt T (eds). Xunta de Galicia and Intergovernmental Oceanographic Commission (UNESCO), Santiago de Compostela, Spain, 1998: 481.

92. Cembella AD, Bauder AG, Lewis NI, Quilliam MA. Association of gonyaulacoid dinoflagellate *Alexandrium ostenfeldii* with spirolide toxins in size-fractionated plankton. *J. Plankton Res.* 2001; **23**: 1413.

93. Gribble KE, Keafer BA, Quilliam MA, Cembella AD, Kulis DM, Manahan A, Anderson DM. Distribution and toxicity of *Alexandrium ostenfeldii* (Dinophyceae) in the Gulf of Maine, USA. *Deep-Sea Res. II* 2005; **52**: 2745.

94. MacKinnon SL, Cembella AD, Quilliam MA, LeBlanc P, Lewis NI, Hardstaff WR, Burton IW, Walter JA. "The characterization of two new spirolides isolated from Danish strains of the toxigenic dinoflagellate *Alexandrium ostenfeldii*". In: *Harmful Algae. Proceedings of the Xth International Conference on Harmful Algae.* Steidinger KA, Landsberg JH, Tomas CR, Vargo GA (eds). Florida fish and Wildlife Conservation Commission and Intergovernmental Oceanographic Commission of UNESCO, St. Pete Beach, FL, 2003: 186.

95. Luckas B, Dahlmann J, Erler K, Gerdts G, Wasmund N, Hummert C, Hansen PD. Overview of key phytoplankton toxins and their recent occurrence in the North and Baltic Seas. *Environ. Toxicol.* 2005; **20**: 1.

96. Richard D, Arsenault E, Cembella A, Quilliam M. "Investigations into the toxicology and pharmacology of spirolides, a novel group of shellfish toxins." In: *Harmful Algal Blooms,* Hallegraeff GM, Blackburn SI, Bolch CJ, Lewis RJ (eds). Intergovernmental Oceanographic Commission of UNESCO, 2001: 383.

97. Cembella AD, Lewis NI, Quilliam MA. Spirolide composition of micro-extracted pooled cells isolated from natural plankton assemblages and from cultures of the dinoflagellate *Alexandrium ostenfeldii. Nat. Toxins* 1999; **7**: 197.

98. Cembella AD, Lewis NI, Quilliam MA. The marine dinoflagellate *Alexandrium ostenfeldii* (dinophyceae) as the causative organism of spirolide shellfish toxins. *Phycologia* 2000; **39**: 67.

99. Cembella AD, Bauder AG, Lewis NI, Quilliam MA. "Population dynamics and spirolide composition of the toxigenic dinoflagellate *Alexandrium ostenfeldii* in coastal embayments of Nova Scotia". In: *Harmful Algal Blooms,* Hallegraeff GM, Blackburn SI, Bolch CJ, Lewis RJ (eds). Intergovernmental Oceanographic Commission of UNESCO, 2001: 173.

100. Hu T, Burton IW, Cembella AD, Curtis JM, Quilliam MA, Walter JA, Wright JLC. Characterization of spirolides A, C, and 13-desmethyl C, new marine toxins isolated from toxic plankton and contaminated shellfish. *J. Nat. Prod.* 2001; **64**: 308.

101. Hu T, Curtis JM, Walter JA, Wright JLC. Characterization of biologically inactive spirolides E and F: Identification of the spirolide pharmacophore. *Tetrahedron Lett.* 1996; **37**: 7671.

102. Uemura D, Chou T, Haino T, Nagatsu A, Fukuzawa S, Zheng S, Chen H. Pinnatoxin A: A toxic amphoteric macrocycle from the Okinawan bivalve *Pinna muricata. J. Am. Chem. Soc.* 1995; **117**: 1155.

103. Seki T, Satake M, Mackenzie L, Kaspar HF, Yasumoto T. Gymnodimine, a new marine toxin of unprecedented structure isolated from New Zealand oysters and the dinoflagellate, *Gymnodium* sp. *Tetrahedron Lett.* 1995; **36**: 7093.

104. Chou T, Haino T, Kuramoto M, Uemura D. Isolation and structure of pinnatoxin D, a new shellfish poison from the Okinawan bivalve *Pinna muricata. Tetrahedron Lett.* 1996; **37**: 4027.

105. Munday R, Towers NR, Mackenzie L, Beuzenberg V, Holland PT, Miles CO. Acute toxicity of gymnodimine to mice. *Toxicon* 2004; **44**: 173.

106. Falk M, Burton IW, Hu T, Walter JA, Wright JLC. Assignment of the relative stereochemistry of the spirolides, macrocyclic toxins isolated from shellfish and from the cultured dinoflagellate *Alexandrium ostenfeldii. Tetrahedron* 2001; **57**: 8659.

107. Naoki H, Murata M, Yasumoto T. Negative-ion fast-atom bombardment tandem mass spectrometry for the structural study on polyether compounds: Structural verification of yessotoxin. *Rapid Commun. Mass Spectrom.* 1993; **7**: 179.

108. Ukena T, Satake M, Usami M, Oshima Y, Fujita T, Naoki H, Yasumoto T. Structural confirmation of ostreocin-D by application of negative-ion fast-atom bombardment collision-induced dissociation tandem mass spectrometric methods. *Rapid Commun. Mass Spectrom.* 2002; **16**: 2387.

109. Premstaller A, Ongania K-H, Huber CG. Factors determining the performance of triple quadrupole, quadrupole ion trap and sector field mass spectrometers in electrospray ionization tandem mass spectrometry of oligonucleotides. 1. Comparison of performance characteristics. *Rapid Commun. Mass Spectrom.* 2001; **15**: 1045.

110. Triolo A, Altamura M, Cardinali F, Sisto A, Maggi CA. Mass spectrometry and combinatorial chemistry: A short outline. *J. Mass Spectrom.* 2001; **36**: 1249.

111. Bier ME, Schwartz JC. "Electrospray-ionization quadrupole ion-trap mass spectrometry." In: *Electrospray Ionization Mass Spectrometry. Fundamentals, Instrumentation and Applications.* Cole RB (ed). John Wiley & Sons Inc., New York, 1997: 235.

112. Strife RJ, Robosky LC, Garrett G, Ketcha MM, Scaffer JD, Zhang N. Ion trap MS^n genealogical mapping – approaches for structure elucidation of novel products of consecutive fragmentations of morphinans. *Rapid Commun. Mass Spectrom.* 2000; **14**: 250.

113. Guillard RRL, Hargraves PE. *Stichochrysis immobilis* is a diatom, not a chrysophyte. *Phycologia* 1993; **32**: 234.

114. Marshall AG, Verdun FR. "Fourier transforms of digital (discrete) waveforms". In: *Fourier Transforms in NMR, Optimal, and Mass Spectrometry: A User's Handbook.* Elsevier, Amsterdam, 1990: 69.

115. Shi, SD-H, Drader JJ, Freitas MA, Hendrickson CL, Marshall AG. Comparison and interconversion of the two most common frequency-to-mass calibration functions for Fourier transform ion cyclotron resonance mass spectrometry. *Int. J. Mass. Spectrom.* 2000; **195/196**: 591.

116. Ledford EB Jr, Rempel DL, Gross ML. Space charge effects in Fourier transform mass spectrometry. Mass calibration. *Anal. Chem.* 1984; **56**: 2744.

117. Marshall AG, Wang T-CL, Ricca TL. Tailored excitation for Fourier transform ion cyclotron resonance mass spectrometry. *J. Am. Chem. Soc.* 1985; **107**: 7893.

118. Guan S, Marshall AG. Stored waveform inverse Fourier transform (SWIFT) ion excitation in trapped-ion mass spectrometry: Theory and applications. *Int. J. Mass Spectrom. Ion Processes* 1996; **157/158**: 5.

119. Senko MW, Canterbury JD, Guan S, Marshall AG. A high-performance modular data system for Fourier transform ion cyclotron resonance mass spectrometry. *Rapid Commun. Mass Spectrom.* 1996; **10**:1839.

120. Lowry OH, Rosebrough NJ, Farr AL, Randall RJ. Protein measurement with the Folin phenol reagent. *J. Biol. Chem.* 1951; **193**: 265.

121. Fitzgerald RL, O'Neal CL, Hart BJ, Poklis A, Harold DA. Comparison of an ion trap and a quadrupole mass spectrometer using diazepam as a model compound. *J. Anal. Toxicol.* 1997; **21**: 445.

122. Yates NA, Booth MM, Stephenson JL Jr, Yost RA. "Practical ion trap technology: GC/MS and GC/MS/MS". In: *Practical Aspects of Ion Trap Mass Spectrometry*

Volume III Chemical, Environmental and Biomedical Applications. March RE, Todd JFJ (eds). CRC Press Inc., Boca Raton, FL, 1995: 121.

123. Brombacher S, Edmonds S, Volmer DA. Studies on azaspiracid biotoxins. II. Mass spectral behavior and structural elucidation of azaspiracid analogs. *Rapid Commun. Mass Spectrom.* 2002; **16**: 2306.

124. Volmer DA, Lock CM. Electrospray ionization and collision-induced dissociation of antibiotic polyether ionophores. *Rapid Commun. Mass Spectrom.* 1998; **12**: 157.

125. Quilliam MA. Analysis of diarrhetic shellfish poisoning toxins in shellfish tissue by liquid chromatography with fluorometric and mass spectrometric detection. *J AOAC Int.* 1995; **78**: 555.

126. Lewis RJ, Holmes MJ, Alewood PF, Jones A. Ionspray mass spectrometry of ciguatoxin-1, maitotoxin-2 and –3 and related marine polyether toxins. *Nat. Toxins* 1994; **2**:56.

127. Adams J. Charge-remote fragmentations: Analytical applications and fundamental studies. *Mass Spectrom. Rev.* 1990; **9**: 141.

128. Cheng C, Gross ML. Applications and mechanisms of charge-remote fragmentation. *Mass Spectrom. Rev.* 2000; **19**: 398.

129. Adams J, Gross ML. Energy requirements for remote charge site ion decompositions and structural information from collisional activation of alkali metal cationized fatty alcohols. *J. Am. Chem. Soc.* 1986; **108**: 6915.

130. Adams J, Gross ML. Charge-remote fragmentations from closed-shell ions: A thermolytic analogy. *J. Am. Chem. Soc.* 1989; **111**: 435.

131. Tureček F, Hanuš V. Retro-Diels-Alder reaction in mass spectrometry. *Mass Spectrom. Rev.* 1984; **3**: 85.

132. Takada N, Umemura N, Suenaga K, Chou T, Nagatsu A, Haino T, Yamada K, Uemura D. Pinnatoxins B and C, the most toxic components in the pinnatoxin series from the Okinawan bivalve *Pinna muricata*. *Tetrahedron Lett.* 2001; **42**: 3491.

133. Luckas B. Phycotoxins in seafood – Toxicological and chromatographic aspects. *J. Chromatogr.* 1992; **624**: 439.

134. van Egmond HP, Aune T, Lassus P, Speijers GJA, Waldock M. Paralytic and diarrhetic shellfish poisons: Occurrence in Europe, toxicity, analysis and regulation. *J. Nat. Toxins* 1993; **2**: 41.

135. Favre I, Moczydlowski E, Schild L. Specificity for block by saxitoxin and divalent cations at a residue which determines sensitivity of sodium channel subtypes to guanidinium toxins. *J. Gen. Physiol.* 1995; **106**: 203.

136. Hille B. An essential ionized acid group in sodium channels. *Fed. Proc.* 1975; **34**: 1318.

137. Spalding BC. Properties of toxin-resistant sodium channels produced by chemical modification in frog skeletal muscle. *J. Physiol.* 1980; **305**: 485.

138. Sakamoto Y, Lockey RF, Krzanowski JJ Jr. Shellfish and fish poisoning related to the toxic dinoflagellates. *South. Med. J.* 1987; **80**: 866.

139. de Carvalho M, Jacinto J, Ramos N, de Oliveira V, Pinho e Melo T, de Sá J. Paralytic shellfish poisoning: Clinical and electrophysiological observations. *J. Neurol.* 1998; **245**: 551.

140. Llewellyn LE, Dodd MJ, Robertson A, Ericson G, de Koning C, Negri AP. Post-mortem analysis of samples from a human victim of a fatal poisoning caused by the xanthid crab, *Zosimus aeneus*. *Toxicon* 2002; **40**: 1463.

141. Shimizu Y, Hsu C, Fallon WE, Oshima Y, Miura I, Nakanishi K. Structure of neosaxitoxin. *J. Am. Chem. Soc.* 1978; **100**: 6791.

142. Boyer GL, Schantz EJ, Schnoes HK. Characterization of 11-hydroxysaxitoxin sulphate, a major toxin in scallops exposed to blooms of the poisonous dinoflagellate *Gonyaulax tamarensis*. *J. Chem. Soc. Chem. Comm.* 1978: 889.

143. van Egmond HP, van den Top HJ, Paulsch WE, Goenaga X, Vieytes MR. Paralytic shellfish poison reference materials: An intercomparison of methods for the determination of saxitoxin. *Food Add. Contam.* 1994; **11**: 39.

144. Krogh P. Measurements of paralytic shellfish poisons. *Nord. Vet.-Med.* 1979; **31**: 302.

145. Quilliam MA. "Liquid chromatography-mass spectrometry of seafood toxins". In: *Applications of LC-MS in Environmental Chemistry*, Barcelo D (ed). Elsevier, Amsterdam, 1996: 415.

146. Quilliam MA, Hess P, Dell'Aversano C. "Recent developments in the analysis of phycotoxins by liquid chromatography-mass spectrometry". In: *Mycotoxins and Phycotoxins in Perspective at the Turn of the Millenium*, deKoe WJ, Samson RA, van Egmond HP, Gilbert J, Sabino M (eds). Proc. Xth Intl. IUPAC Symp. Mycotoxins Phycotoxins, Sao Paulo, Brazil, 2000: 383.

147. Quilliam MA. The role of chromatography in the hunt for red tide toxins. *J. Chromatogr. A* 2003; **1000**: 527.

148. Thibault P, Pleasance S, Laycock MV. Analysis of paralytic shellfish poisons by capillary electrophoresis. *J. Chromatogr.* 1991; **542**: 483.

149. Kawatsu K, Hamano Y, Sugiyama A, Hashizume K, Noguchi T. Development and application of an enzyme immunoassay based on a monoclonal antibody against gonyautoxin components of paralytic shellfish poisoning toxins. *J. Food Prot.* 2002; **65**: 1304.

150. Sphon JA. Use of mass spectrometry for confirmation of animal drug residues. *JAOAC.* 1978; **61**: 1247.

151. Nakamura M, Oshima Y, Yasumoto T. Occurrence of saxitoxin in pufferfish. *Toxicon* 1984; **22**: 381.

152. White KD, Sphon JA, Hall S. Fast atom bombardment mass spectrometry of 12 marine toxins isolated from *Protogonyaulax*. *Anal. Chem.* 1986; **58**: 562.

153. Mirocha CJ, Cheong W, Mirza U, Kim YB. Analysis of saxitoxin in urine by continuous-flow fast atom bombardment mass spectrometry. *Rapid Commun. Mass Spectrom.* 1992; **6**: 128.

154. Quilliam MA, Janeček M, Lawrence JF. Characterization of the oxidation products of paralytic shellfish poisoning toxins by liquid chromatography/mass spectrometry. *Rapid Commun. Mass Spectrom.* 1993; **7**: 482.

155. Dahlmann J, Budakowski WR, Luckas B. Liquid chromatography-electrospray ionization-mass spectrometry based methods for the simultaneous determination of algal and cyanobacterial toxins in phytoplankton from marine waters and lakes followed by tentative structural elucidation of microcystins. *J. Chromatogr. A* 2003; **994**: 45.

156. Arakawa O, Noguchi T, Shida Y, Onoue Y. Occurrence of carbamoyl-N-hydroxy derivatives of saxitoxin and neosaxitoxin in a xanthid crab Zosimus aeneus. *Toxicon* 1994; **32**: 175.

157. Pleasance S, Thibault P, Kelly J. Comparison of liquid-junction and coaxial interfaces for capillary electrophoresis-mass spectrometry with application to compounds of concern to the aquaculture industry. *J. Chromatogr.* 1992; **591**: 325.

158. Hashimoto T, Nishio S, Nishibori N, Yoshioka S, Noguchi T. A new analytical method for gonyautoxins based on postcolumn HPLC. *J. Food Hyg. Soc. Japan* 2002; **43**: 144.

159. Andrinolo D, Michea LF, Lagos N. Toxic effects, pharmacokinetics and clearance of saxitoxin, a component of paralytic shellfish poison (PSP), in cats. *Toxicon* 1999; **37**: 447.

160. Wils ERJ, Hulst AG. Determination of saxitoxin by liquid chromatography/thermospray-mass spectrometry. *Rapid Commun. Mass Spectrom.* 1993; **7**: 413.

161. Pleasance S, Ayer SW, Laycock MV, Thibault P. Ionspray mass spectrometry of marine toxins. III. Analysis of paralytic shellfish poisoning toxins by flow-injection analysis, liquid chromatography/mass spectrometry and capillary electrophoresis/mass spectrometry. *Rapid Commun. Mass Spectrom.* 1992; **6**: 14.

162. Buzy A, Thibault P, Laycock MV. Development of a capillary electrophoresis method for the characterization of enzymatic products arising from the carbamoylase digestion of paralytic shellfish poisoning toxins. *J. Chromatogr. A* 1994; **688**: 301.

163. Locke SJ, Thibault P. Improvement in detection limits for the determination of paralytic shellfish poisoning toxins in shellfish tissues using capillary electrophoresis/electrospray mass spectrometry and discontinuous buffer systems. *Anal. Chem.* 1994; **66**: 3436.

164. Quilliam MA, Thomson BA, Scott GJ, Siu KWM. Ion-spray mass spectrometry of marine neurotoxins. *Rapid Commun. Mass Spectrom.* 1989; **3**: 145.

165. Reyero M, Cacho E, Martínez A, Vázquez J, Marina A, Fraga S, Franco JM. Evidence of saxitoxin derivatives as causative agents in the 1997 mass mortality of monk seals in the Cape Blanc Peninsula. *Nat. Toxins* 1999; **7**: 311.

166. Ito K, Asakawa M, Sida Y, Miyazawa K. Occurrence of paralytic shellfish poison (PSP) in the starfish *Asterina pectinifera* collected from the Kure Bay, Hiroshima Prefecture, Japan. *Toxicon* 2003; **41**: 291.

167. Senko MW, Hendrickson CL, Paša-Tolić L, Marto JA, White FM, Guan S, Marshall AG. Electrospray ionization Fourier transform ion cyclotron resonance at 9.4 T. *Rapid Commun. Mass Spectrom.* 1996; **10**: 1824.

168. Chowdhury SK, Katta V, Chait BT. An electrospray-ionization mass spectrometer with new features. *Rapid Commun. Mass Spectrom.* 1990; **4**: 81.

169. Wilcox BE, Hendrickson CL, Marshall AG. Improved ion extraction from a linear octopole ion trap: SIMION analysis and experimental demonstration. *J. Am. Soc. Mass Spectrom.* 2002; **13**: 1304.

170. Maksić ZB, Kovačević B. Absolute proton affinity of some polyguanides. *J. Org. Chem.* 2000; **65**: 3303.

171. Kovačević B, Maksić ZB, Vianello R. The proton affinity of some extended π-systems involving guanidine and cyclopropenimine subunits. *J. Chem Soc. Perkin 2.* 2001: 886.

172. Vianello R, Kovačević B, Maksić ZB. In search of neutral organic superbases - iminopolyenes and their amino derivatives. *New J. Chem.* 2002; **26**: 1324.

173. See for example: Koch W, Holthausen MC. *A Chemist Guide to Density Functional Theory.* Wiley-VCH, Weinheim-New York, 2000 and references cited therein.

174. Alcamí M, Mó O, Yáñez M. Computational chemistry: A useful (sometimes mandatory) tool in mass spectrometry studies. *Mass Spectrom. Rev.* 2001; **20**: 195.

175. Gaussian 98 (Revision A.*10*): Frisch MJ, Trucks GW, Schlegel HB, Scuseria GE, Robb MA, Cheeseman JR, Zakrzewski VG, Montgomery, Jr JA, Stratmann RE, Burant JC, Dapprich S, Millam JM, Daniels AD, Kudin KN, Strain MC, Farkas O, Tomasi J, Barone V, Cossi M, Cammi R, Mennucci B, Pomelli C, Adamo C, Clifford S, Ochterski J, Petersson GA, Ayala PY, Cui Q, Morokuma K, Malick DK, Rabuck AD, Raghavachari K, Foresman JB, Cioslowski J, Ortiz JV, Baboul AG, Stefanov BB, Liu G, Liashenko A, Piskorz P, Komaromi I, Gomperts R, Martin RL, Fox DJ, Keith T, Al-Laham MA, Peng CY, Nanayakkara A, Gonzalez C, Challacombe M, Gill PMW, Johnson BG, Chen W, Wong MW, Andres JL, Head-Gordon M, Replogle ES, Pople JA. Gaussian Inc., Pittsburgh PA, 1998.

176. Shimizu Y. "Paralytic shellfish poisons". In: *Progress in the Chemistry of Organic Natural Products*, Herz W, Grisebach H, Kirby GW (eds). Springer-Verlag, New York, 1984: 235.

177. Rogers RS, Rapoport H. The pKa's of saxitoxin. *J. Am. Chem. Soc.* 1980; **102**: 7335.

178. Watt AP, Mortishire-Smith RJ, Gerhard U, Thomas SR. Metabolite identification in drug discovery. *Current Opinion in Drug Discovery & Development* 2003; **6**: 57.

179. Papac DI, Shahrokh Z. Mass spectrometry innovations in drug discovery and development. *Pharmaceutical Research* 2001; **18**: 131.

180. Hoke SH II, Morand KL, Greis KD, Baker TR, Harbol KL, Dobson RLM. Transformations in pharmaceutical research and development, driven by innovations in multidimensional mass spectrometry-based technologies. *Int. J. Mass Spectrom.* 2001; **212**: 135.

181. Lee MS, Kerns EH. LC/MS applications in drug development. *Mass Spectrom. Rev.* 1999; **18**: 187.

182. Cody RB, Freiser BS. High-resolution detection of collision-induced dissociation fragments by Fourier transform mass spectrometry. *Anal. Chem.* 1982; **54**: 1431.

183. Colombo M, Sirtori FR, Rizzo V. A fully automated method for accurate mass determination using high-performance liquid chromatography with a quadrupole/orthogonal acceleration time-of-flight mass spectrometer. *Rapid Commun. Mass Spectrom.* 2004; **18**: 511.

184. Fang L, Demee M, Cournoyer J, Sierra T, Young C, Yan B. Parallel high-throughput accurate mass measurement using a nine-channel multiplexed electrospray liquid chromatography ultraviolet time-of-flight mass spectrometry system. *Rapid Commun. Mass Spectrom.* 2003; **17**: 1425.

185. Belov ME, Anderson GA, Wingerd MA, Udseth HR, Tang K, Prior DC, Swanson KR, Buschbach MA, Strittmatter EF, Moore RJ, Smith RD. An automated high performance capillary liquid chromatography-Fourier transform ion cyclotron resonance mass spectrometer for high-throughput proteomics, *J. Am. Soc. Mass Spectrom.* 2004; **15**: 212.

186. Sleno L, Windust AJ, Volmer DA. Structural study of spirolide marine toxins by mass spectrometry. Part I. Fragmentation pathways of 13-desmethyl spirolide C by collision-induced dissociation and infrared multiphoton dissociation mass spectrometry. *Anal. Bioanal. Chem.* 2004; **378**: 969.

187. Sleno L, Chalmers MJ, Volmer DA. Structural study of spirolide marine toxins by mass spectrometry. Part II. Mass spectrometric characterization of unknown spirolides and related compounds in cultured phytoplankton extract. *Anal. Bioanal. Chem.* 2004; **378**: 977.

188. Fiehn O, Kopka J, Trethewey RN, Willmitzer L. Identification of uncommon plant metabolites based on calculation of elemental compositions using gas chromatography and quadrupole mass spectrometry. *Anal. Chem.* 2000; **72**: 3573.

189. Eckers C, Wolff JC, Haskins NJ, Sage AB, Giles K, Bateman R. Accurate mass liquid chromatography/mass spectrometry on orthogonal acceleration time-of-flight mass analyzers using switching between separate sample and reference sprays. 1. Proof of concept. *Anal. Chem.* 2000; **72**: 3683.

190. Charles L. Flow injection of the lock mass standard for accurate mass measurement in electrospray ionization time-of-flight mass spectrometry coupled with liquid chromatography. *Rapid Commun. Mass Spectrom.* 2003; **17**: 1383.

191. Pelander A, Ojanperä I, Laks S, Rasanen I, Vuori E. Toxicological screening with formula-based metabolite identification by liquid chromatography/time-of-flight mass spectrometry. *Anal. Chem.* 2003; **75**: 5710.

192. Marshall AG, Rodgers RP. Petroleomics: The next grand challenge for chemical analysis. *Acc. Chem. Res.* 2004: **37**: 53.

193. Stenson AC, Marshall AG, Cooper WT. Exact masses and chemical formulas of individual Suwannee river fulvic acids from ultrahigh resolution electrospray ionization Fourier transform ion cyclotron resonance mass spectra. *Anal. Chem.* 2003; **75**: 1275.

194. Thompson CM, Richards DS, Fancy S-A, Perkins GL, Pullen FS, Thom C. A comparison of accurate mass techniques for the structural elucidation of fluconazole. *Rapid Commun. Mass Spectrom.* 2003; **17**: 2804.

195. Hau J, Stadler R, Jenny TA, Fay LB. Tandem mass spectrometric accurate mass performance of time-of-flight and Fourier transform ion cyclotron resonance mass spectrometry: a case study with pyridine derivatives. *Rapid Commun. Mass Spectrom.* 2001; **15**: 1840.

196. Bristow AWT, Webb KS. Intercomparison study on accurate mass measurement of small molecules in mass spectrometry. *J. Am. Soc. Mass Spectrom.* 2003; **14**: 1086.

197. Lee HN, Marshall AG. Theoretical maximal precision for mass-to-charge ratio, amplitude, and width measurement in ion-counting mass analyzers. *Anal. Chem.* 2000; **72**: 2256.

198. Meija J, Caruso JA. Deconvolution of isobaric interferences in mass spectra, *J. Am. Soc. Mass Spectrom.* 2004; **15**: 654.

199. Limbach PA, Grosshans PB, Marshall AG. Experimental determination of the number of trapped ions, detection limit, and dynamic range in FT/ICR/MS. *Anal. Chem.* 1993; **65**: 135.

200. Olsen JV, Ong S-E, Mann M. Trypsin cleaves exclusively C-terminal to arginine and lysine residues. *Mol. Cell. Proteomics* 2004; **3**: 608.

201. Grange AH, Genicola FA, Sovocool GW. Utility of three types of mass spectrometers for determining elemental compositions of ions formed from chromatographically separated compounds. *Rapid Commun. Mass Spectrom.* 2002; **16**: 2356.

202. Sweatman TW, Israel M. "Anthracyclines". In: *Cancer Therapeutics: Experimental and Clinical Agents*, Teicher BA (ed). Humana Press, Totowa, NJ, 1997: 113.

203. Monneret C. Recent developments in the field of antitumour anthracyclines. *Eur. J. Med. Chem.* 2001; **36**: 483.

204. Gewirtz DA. A critical evaluation of the mechanisms of action proposed for the antitumour effects of the anthracycline antibiotics adriamycin and daunorubicin. *Biochem. Pharmacol.* 1999; **57**: 727.

205. Coukell AJ, Faulds D. Epirubicin. An updated review of its pharmacodynamic and pharmacokinetic properties and therapeutic efficacy in the management of breast cancer. *Drugs* 1997; **53**: 453.

206. Arcamone F, Bernardi L, Giardino P, Patelli B, Di Marco A, Casazza AM, Pratesi G, Reggiani P. Synthesis and antitumor activity of 4-demethoxydaunorubicin, 4-demethoxy-7,9-diepidaunorubicin, and their β anomers. *Cancer Treat. Rep.* 1976; **60**: 829.

207. Lachâtre F, Marquet P, Ragot S, Gaulier JM, Cardot P, Dupuy JL. Simultaneous determination of four anthracyclines and three metabolites in human serum by liquid chromatography-electrospray mass spectrometry. *J. Chrom. B.* 2000; **738**: 281.

208. Sottani C, Tranfo G, Bettinelli M, Faranda P, Spagnoli M, Minoia C. Trace determination of anthracyclines in urine: A new high-performance liquid chromatography/tandem mass spectrometry method for assessing exposure of hospital personnel. *Rapid Commun. Mass Spectrom.* 2004; **18**: 2426.

209. Arnold RD, Slack JE, Straubinger RM. Quantification of doxorubicin and metabolites in rat plasma and small volume tissue samples by liquid chromatography/electrospray tandem mass spectrometry. *J. Chrom. B.* 2004; **808**: 141.

210. Taatjes DJ, Gaudiano G, Resing K, Koch TH. Alkylation of DNA by the anthracycline, antitumour drugs adriamycin and daunomycin. *J. Med. Chem.* 1996; **39**: 4135.

211. Luce RA, Hopkins PB. Chemical cross-linking of drugs to DNA. *Methods Enzymol.* 2001; **340**: 396.

212. Cutts SM, Nudelman A, Rephaeli A, Phillips DR. The power and potential of doxorubicin-DNA adducts. *IUBMB Life* 2005; **57**: 73.

213. Takanashi S, Bachur NR. Daunorubicin metabolites in human urine. *J. Pharmacol. Exp. Ther.* 1975; **195**: 41.

214. Takanashi S, Bachur NR. Adriamycin metabolism in man: Evidence from urinary metabolites. *Drug Metab. Dispos.* 1976; **4**: 79.

215. Cassinelli G, Confligliacchi E, Penco S, Rivola G, Arcamone F, Ferrari L. Separation, characterization, and analysis of epirubicin (4'-epidoxorubicin) and its metabolites from human urine. *Drug Metab. Dispos.* 1984; **12**: 506.

216. Quintieri L, Geroni C, Fantin M, Battaglia R, Rosato A, Speed W, Zanovello P, Floreani M. Formation and antitumor activity of PNU-159682, a major metabolite of nemorubicin in human liver microsomes. *Clin. Cancer Res.* 2005; **11**: 1608.

217. Bachur NR. Daunorubicinol, a major metabolite of daunorubicin: Isolation from human urine and enzymatic reactions. *J. Pharmacol. Exp. Ther.* 1971; **177**: 573.

218. Chan KE, Watson E. GLC-mass spectrometry of several important anticancer drugs II: doxorubicin and daunorubicin aglycone analogs. *J. Pharm. Sci.* 1978; **67**: 1748.

219. Bloom J, Lehman P, Israel M, Rosario O, Korfmacher W. Mass spectral characterization of three anthracycline antibiotics: A comparison of thermospray mass spectrometry to particle beam mass spectrometry. *J. Anal. Tox.* 1992; **16**: 223.

220. Smith RG. Characterization of anthracycline antibiotics by desorption chemical ionization mass spectrometry. *Anal. Chem.* 1982; **54**: 2006.

221. Monneret C, Sellier N. Desorption chemical ionization mass spectrometry of anthracyclines and of trisaccharides related to aclacinomycin A and marcellomycin. *Biomed. Environ. Mass Spectrom.* 1986; **13**: 319.

222. Maurer KH, Rapp U. "Possible applications of quantitative field desorption mass fragmentography to pharmacokinetic studies of antineoplastic drugs". In: *Advances in Mass Spectrometry in Biochemistry and Medicine*, Volume I. Frigerio A, Castagnoli N (eds). Spectrum Publications Inc., New York, 1976: 541.

223. Gioia B, Arlandini E, Vigevani A. Field desorption mass spectrometry of anthracyclines. Comparison with other soft ionization techniques. *Biomed. Mass Spectrom.* 1984; **11**: 35.

224. Dass C, Sehadri R, Israel M, Desiderio DM. Fast atom bombardment mass spectrometric analysis of anthracyclines and anthracyclinones. *Biomed. Environ. Mass Spectrom.* 1988; **17**: 37.

225. Chandler CJ, Brownlee RT, Hook RJ, Phillips DR, Reiss JA, Edgar JA. Fast atom bombardment mass spectrometry of some anthracycline and bisanthracycline derivatives. *Biomed. Environ. Mass Spectrom.* 1988; **17**: 21.

226. Tozuka Z, Kaneko H, Shiraga T, Mitani Y, Beppu M, Terashita S, Kawamura A, Kagayama A. Strategy for structural elucidation of drugs and drug metabolites using $(MS)^n$ fragmentation in an electrospray ion trap. *J. Mass Spectrom.* 2003; **38**: 793.

227. Hopfgartner G, Varesio E, Tschäppät V, Grivet C, Bourgogne E, Leuthold LA. Triple quadrupole linear ion trap mass spectrometer for the analysis of small molecules and macromolecules. *J. Mass Spectrom.* 2004; **39**: 845.

228. Weinmann W, Stoertzel M, Vogt S, Wendt J. Tune compounds for electrospray ionisation/in-source collision-induced dissociation with mass spectral library searching. *J. Chromatogr. A* 2001; **926**: 199.

229. Cohen LH, Gusev AI. Small molecule analysis by MALDI mass spectrometry. *Anal. Bioanal. Chem.* 2002; **373**: 571.

230. Hatsis P, Brombacher S, Corr J, Kovarik P, Volmer DA. Quantitative analysis of small pharmaceutical drugs using a high repetition rate laser matrix-assisted laser desorption/ionization source. *Rapid Commun. Mass Spectrom.* 2003; **17**: 2303.

231. Reyzer ML, Hsieh Y, Ng K, Korfmacher WA, Caprioli RM. Direct analysis of drug candidates in tissue by matrix-assisted laser desorption/ionization mass spectrometry. *J. Mass Spectrom.* 2003; **38**: 1081.

232. Laiko VV, Moyer SC, Cotter RJ. Atmospheric pressure MALDI/ion trap mass spectrometry. *Anal. Chem.* 2000; **72:** 5239.

233. Kast J, Parker CE, van der Drift K, Dial JM, Milgram SL, Wilm M, Howell M, Borchers CH. Matrix-assisted laser desorption/ionization directed nano-electrospray ionization tandem mass spectrometric analysis for protein identification. *Rapid Commun. Mass Spectrom.* 2003; **17**: 1825.

234. Jonsson AP. Mass spectrometry for protein and peptide characterization. *Cell. Mol. Life Sci.* 2001; **58**: 868.

235. Shen Z, Thomas JJ, Averbuj C, Broo KM, Engelhard M, Crowell JE, Finn MG, Siuzdak G. Porous silicon as a versatile platform for laser desorption/ionization mass spectrometry. *Anal. Chem.* 2001; **73**: 612.

236. McLean JA, Russell WK, Russell DH. A high repetition rate (1 kHz) microcrystal laser for high throughput atmospheric pressure MALDI-quadrupole-time-of-flight mass spectrometry. *Anal Chem.* 2003; **75**: 648.

237. Cui M, McCooeye MA, Fraser C, Mester Z. Quantitation of lysergic acid diethylamide in urine using atmospheric pressure matrix-assisted laser desorption/ionization ion trap mass spectrometry. *Anal. Chem.* 2004; **76**: 7143.

238. Alterman MA, Gogichayeva NV, Kornilayev BA. Matrix-assisted laser desorption/ionization time-of-flight mass spectrometry-based amino acid analysis. *Anal. Biochem.* 2004; **335**: 184.

239. Lidgard R, Duncan MW. Utility of matrix-assisted laser desorption/ionization time-of-flight mass spectrometry for the analysis of low molecular weight compounds. *Rapid Commun. Mass Spectrom.* 1995, **9**: 128.

240. Duncan MW, Matanovic G, Cerpa-Poljak A. Quantitative analysis of low molecular weight componds of biological interest by matrix-assisted laser desorption ionization. *Rapid Commun. Mass Spectrom.* 1993; **7**: 1090.

241. Gusev AI, Wilkinson WR, Proctor A, Hercules DM. Direct quantitative analysis of peptides using matrix-assisted laser desorption ionization. *Fresenius J. Anal. Chem.* 1996; **354**: 455.

242. Hensel RR, King RC, Owens KG. Electrospray sample preparation for improved quantitation in matrix-assisted laser desorption/ionization time-of-flight mass spectrometry. *Rapid Commun. Mass Spectrom.* 1997; **11**: 1785.

243. Hoteling AJ, Mourey TH, Owens KG. Importance of solubility in the sample preparation of poly(ethylene terephthalate) for MALDI TOFMS. *Anal. Chem.* 2005; **77**: 750.

244. Chen H, Guo B. Use of binary solvent systems in the MALDI-TOF analysis of poly(methyl methacrylate). *Anal. Chem.* 1997; **69**: 4399.

245. Vorm O, Roepstorff P, Mann M. Improved resolution and very high sensitivity in MALDI TOF of matrix surfaces made by fast evaporation. *Anal. Chem.* 1994; **66**: 3281.

246. Zheng J, Li N, Ridyard M, Dai H, Robbins SM, Li L. Simple and robust two-layer matrix/sample preparation method for MALDI MS/MS analysis of peptides. *J. Proteome Res.* 2004; **4**: 1709.

247. Xiong S, Ding Q, Zhao Z, Chen W, Wang G, Liu S. A new method to improve sensitivity and resolution in matrix-assisted laser desorption/ionization time of flight mass spectrometry. *Proteomics* 2003; **3**: 265.

248. Wei H, Nolkrantz K, Powell DH, Woods JH, Ko M-C, Kennedy RT. Electrospray sample deposition for matrix-assisted laser desorption/ionization (MALDI) and atmospheric pressure MALDI mass spectrometry with attomole detection limits. *Rapid Commun. Mass Spectrom.* 2004; **18**: 1193.

249. Hoteling AJ, Erb WJ, Tyson RJ, Owens KG. Exploring the importance of the relative solubility of matrix and analyte in MALDI sample preparation using HPLC. *Anal. Chem.* 2004; **76**: 5157.

250. Wilkinson WR, Gusev AI, Proctor A, Houalla M, Hercules DM. Selection of internal standards for quantitative analysis by matrix-assisted laser desorption-ionization (MALDI) time-of-flight mass spectrometry. *Fresenius J. Anal. Chem.* 1997; **357**: 241.

251. Kang M-J, Tholey A, Heinzle E. Application of automated matrix-assisted laser desorption/ionization time-of-flight mass spectrometry for the measurement of enzyme activities. *Rapid Commun. Mass Spectrom.* 2001; **15**: 1327.

252. Zabet-Moghaddam M, Heinzle E, Tholey A. Qualitative and quantitative analysis of low molecular weight compounds by ultraviolet matrix-assisted laser desorption/ionization mass spectrometry using ionic liquid matrices. *Rapid Commun. Mass Spectrom.* 2004; **18**: 141.

253. Bungert D, Heinzle E, Tholey A. Quantitative matrix-assisted laser desorption/ionization mass spectrometry for the determination of enzyme activities. *Anal. Biochem.* 2004; **326**: 167.

254. Horak J, Werther W, Schmid ER. Optimisation of the quantitative determination of chlormequat by matrix-assisted laser desorption/ionisation mass spectrometry. *Rapid Commun. Mass Spectrom.* 2001; **15**: 241.

255. Gusev AI, Muddiman DC, Proctor A, Sharkey AG, Hercules DM, Tata PNV, Venkataramanan R. A quantitative study of *in vitro* hepatic metabolism of tacrolimus (FK506) using secondary ion and matrix-assisted laser desorption/ionization mass spectrometry. *Rapid Commun. Mass Spectrom.* 1996; **10**: 1215.

256. Ranasinghe C, Akhurst RJ. Matrix assisted laser desorption ionisation time of flight mass spectrometry (MALDI-TOF MS) for detecting novel Bt toxins. *J. Invertebrate Pathology* 2002; **79**: 51.

257. Welker M, Fastner J, Erhard M, von Döhren H. Applications of MALDI-TOF MS analysis in cyanotoxin research. *Environ. Toxicol.* 2002; **17**: 367.

258. Nasri AB, Bouaicha N, Fastner J. First report of a microcystin-containing bloom of the cyanobacteria Microcystis spp. in Lake Oubeira, eastern Algeria. *Arch. Environ. Contam. Toxicol.* 2004; **46**: 197.

259. Oliveira JS, Pires Junior OR, Morales RAV, Bloch Junior C, Schwartz CA, Freitas JC. Toxicity of puffer fish - two species (*Lagocephalus laevigatus*, linaeus 1766 and *Sphoeroides spengleri*, Bloch 1785) from the Southeastern Brazilian coast. *J. Venom. Anim. Toxins incl. Trop. Dis.* 2003; **9**: 76.

260. Kalume DE, Stenflo J, Czerwiec E, Hambe B, Furie B, Furie BC, Roepstorff P. Structure determination of two conotoxins from *Conus textile* by a combination of

matrix-assisted laser desorption/ionization time-of-flight and electrospray ionization mass spectrometry and biochemical methods. *J. Mass Spectrom.* 2000; **35**: 145.

261. Rigby AC, Lucas-Meunier E, Kalume DE, Czerwiec E, Hambe B, Dahlqvist I, Fossier P, Baux G, Roepstorff P, Baleja JD, Furie BC, Furie B, Stenflo J. A conotoxin from *Conus textile* with unusual posttranslational modifications reduces presynaptic Ca21 influx. *Proc. Natl. Acad. Sci. USA* 1999; **96**: 5758.

262. Chernushevich IV. Duty cycle improvement for a quadrupole-time-of-flight mass spectrometer and its use for precursor ion scans. *Eur. J. Mass Spectrom.* 2000; **6**: 471.

263. Volmer DA, Mansoori B, Locke SJ. Study of 4-quinolone antibiotics in biological samples by short-column liquid chromatography coupled with electrospray ionization tandem mass spectrometry. *Anal. Chem.* 1997; **69**: 4143.

264. Kang M-J, Tholey A, Heinzle E. Quantitation of low molecular mass substrates and products of enzyme catalyzed reactions using matrix-assisted laser desorption/ionization time-of-flight mass spectrometry. *Rapid Commun. Mass Spectrom.* 2000; **14**: 1972.

265. Cheng Y, Hercules DM. Quantitative estimation of geometric isomers by post-source decay MALDI MS. *Microchem. J.* 2002; **72**: 255.

266. Mims D, Hercules D. Quantification of bile acids directly from urine by MALDI-TOF-MS. *Anal. Bioanal. Chem.* 2003; **375**: 609.